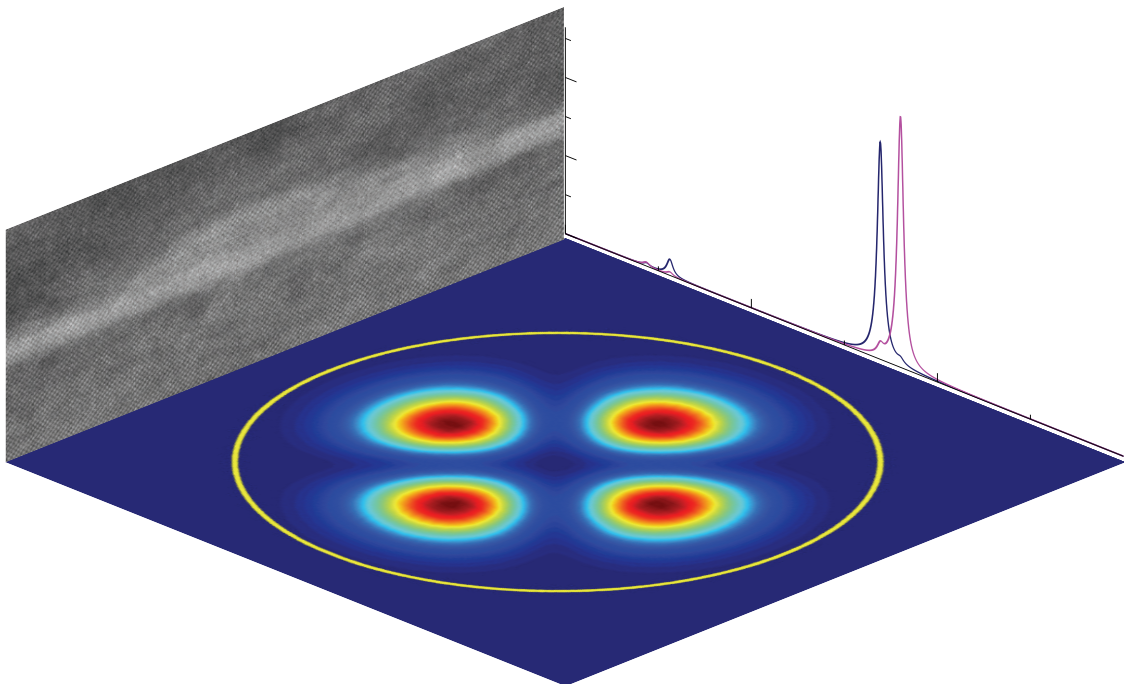


From Structure to Spectra: Tight-Binding Theory of InGaAs Quantum Dots



Elias Goldmann, Master of Science

From Structure to Spectra: Tight-Binding Theory of InGaAs Quantum Dots

Vom Fachbereich Physik und Elektrotechnik
der Universität Bremen

zur Erlangung des akademischen Grades eines
Doktors der Naturwissenschaften (Dr. rer. nat)
genehmigte Dissertation

von
Elias Goldmann, Master of Science
aus Duisburg

1. Gutachter: Prof. Dr. rer. nat. Frank Jahnke
2. Gutachter: Prof. Dr. rer. nat. Gerd Czycholl

Eingereicht am: 25.06.2014
Tag des Promotionskolloquiums: 23.07.2014

For Sonja & Nora Marie.

Self-assembled semiconductor quantum dots have raised considerable interest in the last decades due to a multitude of possible applications ranging from carrier storage to light emitters, lasers and future quantum communication devices. Quantum dots offer unique electronic and photonic properties due to the three-dimensional confinement of charge carriers and the coupling to a quasi-continuum of wetting layer and barrier states.

In this work we investigate the electronic structure of $\text{In}_x\text{Ga}_{1-x}\text{As}$ quantum dots embedded in GaAs, considering realistic quantum dot geometries and Indium concentrations. We utilize a next-neighbour sp^3s^* tight-binding model for the calculation of electronic single-particle energies and wave functions bound in the nanostructure and account for strain arising from lattice mismatch of the constituent materials atomistically. With the calculated single-particle wave functions we derive Coulomb matrix elements and include them into a configuration interaction treatment, yielding many-particle states and energies of the interacting many-carrier system. Also from the tight-binding single-particle wave functions we derive dipole transition strengths to obtain optical quantum dot emission and absorption spectra with Fermi's golden rule. Excitonic fine-structure splittings are obtained, which play an important role for future quantum cryptography and quantum communication devices for entanglement swapping or quantum repeating.

For light emission suited for long-range quantum-crypted fiber communication InAs quantum dots are embedded in an $\text{In}_x\text{Ga}_{1-x}\text{As}$ strain-reducing layer, shifting the emission wavelength into telecom low-absorption windows. We investigate the influence of the strain-reducing layer Indium concentration on the excitonic fine-structure splitting. The fine-structure splitting is found to saturate and, in some cases, even reduce with strain-reducing layer Indium concentration, a result being counterintuitively. Our result demonstrates the applicability of InGaAs quantum dots for quantum telecommunication at the desired telecom wavelengths, offering good growth controllability.

For the application in lasers, quantum based active media are known to offer superior properties to common quantum well lasers such as low threshold currents or temperature stability. For device design, the knowledge about the saturation behaviour of optical gain with excitation density is of major importance. In the present work we combine quantum-kinetic models for the calculation of the optical gain of quantum dot active media with our atomistic tight-binding model for the calculation of single-particle energies and wave functions. We investigate the interplay between structural properties of the quantum dots and many-body effects in the optical gain spectra and identify different regimes of saturation behaviour. Either phase-space filling dominates the excitation dependence of the optical gain, leading to saturation, or excitation-induced dephasing dominates the excitation dependence of the optical gain, resulting in a negative differential gain.

Contents

1. Introduction	1
1.1. Quantum dots (QDs)	2
1.2. Topics	6
1.3. Brief description of content	7
2. Single-particle theory	9
2.1. Calculation of electronic bulk band structures	10
2.1.1. The $\mathbf{k}\cdot\mathbf{p}$ model	10
2.1.2. Empirical pseudopotentials	11
2.2. Empirical tight-binding (TB)	12
2.2.1. Introduction	12
2.2.2. Tight-binding fundamentals	13
2.2.3. Two-center approximation	16
2.2.4. Spin-orbit coupling	20
2.2.5. Strain	22
2.2.6. Piezoelectricity	27
2.3. Modelling semiconductor nanostructures	29
2.3.1. Bulk band structures	30
2.3.2. Quantum wells	38
2.3.3. Quantum dots	46
2.4. Supercell requirements	53
2.5. Diagonalization of large sparse matrices	54
2.6. Benchmarks	55
2.7. Geometry and single-particle properties	57
2.8. Choice of valence band offset	66
2.9. Number of bound states	68
3. Many-particle theory	71
3.1. Full Configuration Interaction	73
3.1.1. Coulomb matrix elements from TB wave functions	76
3.1.2. Many-particle states	78
3.1.3. Dipole matrix elements from TB wave functions	79
3.1.4. Excitonic spectrum	84
3.2. Excitonic fine-structure splitting	86

4. QDs in single-photon emitters and laser devices	91
4.1. Evolution of FSS under SRL influence	93
4.1.1. Introduction	93
4.1.2. System	94
4.1.3. Results and discussion	95
4.2. Optical gain in QD active media	99
4.2.1. Optical gain	99
4.2.2. Envelope approximation	100
4.2.3. Realistic envelopes	103
4.2.4. Negative differential gain in QD systems	107
4.2.5. Results and discussion	108
4.3. Conclusion	113
5. Summary and outlook	115
A. Appendix	119
A.1. Quantum dot growth	120
A.2. LAMMPS best practice parameters	122
A.3. PETSc/SLEPc best practice parameters	123
A.4. TB parametrizations	126
Publications and conference contributions	129
Bibliography	132
List of figures	154
List of tables	160
Acknowledgements	162
Acknowledgements	163

1. Introduction

Contents

1.1. Quantum dots (QDs)	2
1.2. Topics	6
1.3. Brief description of content	7

1.1. Quantum dots (QDs)

According to [1] and references therein, the global market for quantum dot (QD) technology grew from an estimated value of \$28 million in 2008 to an estimated value of \$67 million in revenues in 2010. The study predicts an annual growth rate of around 60%. Given this impressive data, a closer look on quantum dot technology and what the prospects are seems legitimate.

The term *quantum dot* usually refers to nanoscaled structures of semiconductor material, typically with physical dimensions of 1-100nm in all three directions of space. These QDs can either be in solution (called *nanocrystallites*), or epitaxially grown on other semiconductor materials (called *self-assembled QDs*). Both geometries cause three-dimensional confinement of charge carriers inside the QD, giving a density of states (DOS, the number of states in an energy interval) as shown schematically in Fig. 1.1. For QDs, the DOS becomes δ -like, resulting in discrete ("quantized", giving the name) energy levels of carriers inside the nanostructure. Due to this discrete level structure, QDs have similarities to single atoms and therefore offer unique physical properties. Especially, tunability of absorption/emission energies with the nanostructure size leads to multiple possible applications as detectors and emitters at tailorable energy windows. Consequentially, QDs have received enormous attention and still are subject of intense research.

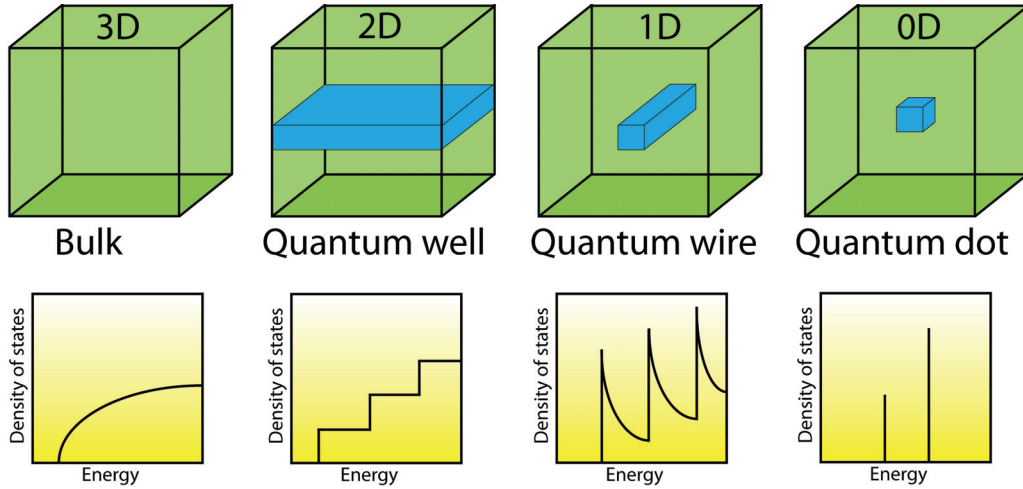


Figure 1.1.: Reduction of translational degrees of freedom affects the electronic density of states. In bulk semiconductors, the DOS is square-root like and becomes a step function for quantum wells. For consecutive loss of translational symmetry (three-dimensionally confined nanostructures) the DOS becomes δ -like, resulting in discrete energy levels.

Quantum dots emerged as subject to academic research in the early 1980s, following its technological predecessor, the quantum well (QW). Carrier trapping and

electron level quantization in the two dimensions perpendicular to the growth direction was first observed in 1974 for QWs [2]. One decade later, quantization of energy levels in spherical CdS nanocrystallites was reported, together with a remarkable shift of the fundamental absorption edge with nanocrystallite radius [3]. This shift gave rise to various different applications, because it demonstrated the tunability of emission energy with the nanocrystallite size. In CdSe nanocrystallites, for example, the ground state energy gap can be tuned between 1.8 eV and 3 eV, covering almost the entire visible part of the electromagnetic spectrum [4], optimally suited for applications in optoelectronics. Nowadays, applications for nanocrystallites range from solar cells (Intermediate Band Solar Cells, [5]) to QD television [6] with the nanocrystallites enhancing resolution and color brilliance. Recently, CdS/CdSe nanocrystallites have been utilized as light harvesters in polymer glasses, guiding the way to photovoltaic windows by concentrating light onto solar cells [7]. Probably the largest field of application for nanocrystallites in solution is the medical sector. In cancer therapy, nanocrystallite surfaces are functionalized with active pharmaceutical ingredients in order to target cancer cells in vivo and visualize them via characteristic fluorescence signals [8], as can be seen in figure 1.2. Also, functionalized nanocrystallites are used as carriers for targeted gene silencing

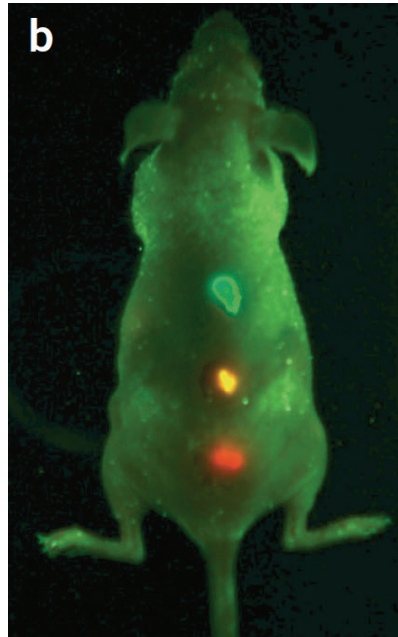


Figure 1.2.: Fluorescence signals from functionalized CdSe nanocrystallites for in-vivo tumor targeting. Different colors show different nanocrystallite sizes, used to encode different functionalizations, which target cancer cells. Picture adopted from [8].

[9] and offer, in general, bright technological future prospects. See the review of Cheki et al. [10] for more information.

Since nanocrystallites are synthesized mainly in solution or as powder, they are a poor choice when device integration is needed. This is where self-assembled QDs become interesting because well-defined epitaxial layer-by-layer growth of embedded QD layers and electrical contacting are possible. Following the early technique of etching of monolayer-sized quantum lattices to manufacture quantum dots, growth of self-assembled quantum dots in molecular beam epitaxy (MBE) was reported in the late 1980s [11, 12] and still is the state-of-the-art growth technique for high quality QD samples.

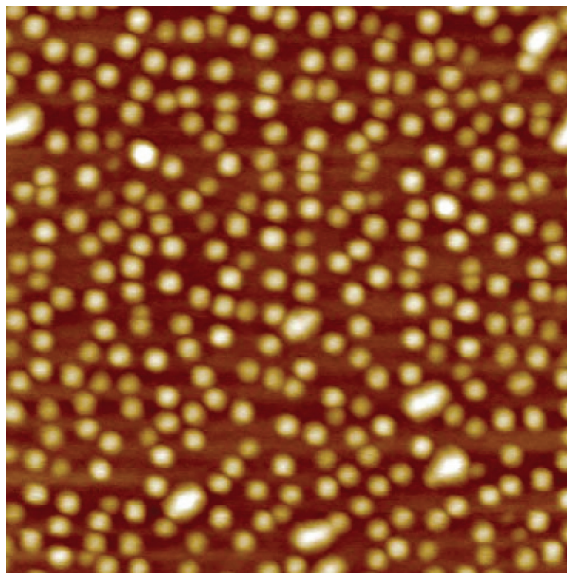


Figure 1.3.: Atomic force microscope (AFM) picture of a quantum dot layer before overgrowth, from [13]. The area is $500 \times 500 \text{ nm}^2$. Brighter colors translate to higher QD elevation.

In Fig. 1.3 and Fig. 1.4 typical self-assembled QDs are shown. A short introduction to QD growth-modes and -techniques can be found in the appendix A.1.

Ever since the 1990s the discrete level structure of QDs and tunability of emission properties with QD geometry gave rise to many device proposals using QDs as active material or as key components, leading to superior device functionality. Considering lasers with QDs as active material, superior properties such as enhanced temperature stability and reduced threshold currents were predicted theoretically [16]. This received great attention, because lasers built with quantum well structures as active material suffer performance deterioration by temperature effects. A review can be found in [17]. The conventional QD laser has a large ensemble of QDs inside the active region¹.

New physics arises, when the active material consists of only a few QDs or in the ultimate limit of miniaturization of only one QD inside an optical cavity, introducing

¹Typical QD densities are of the order 10^{11} per centimeter squared.

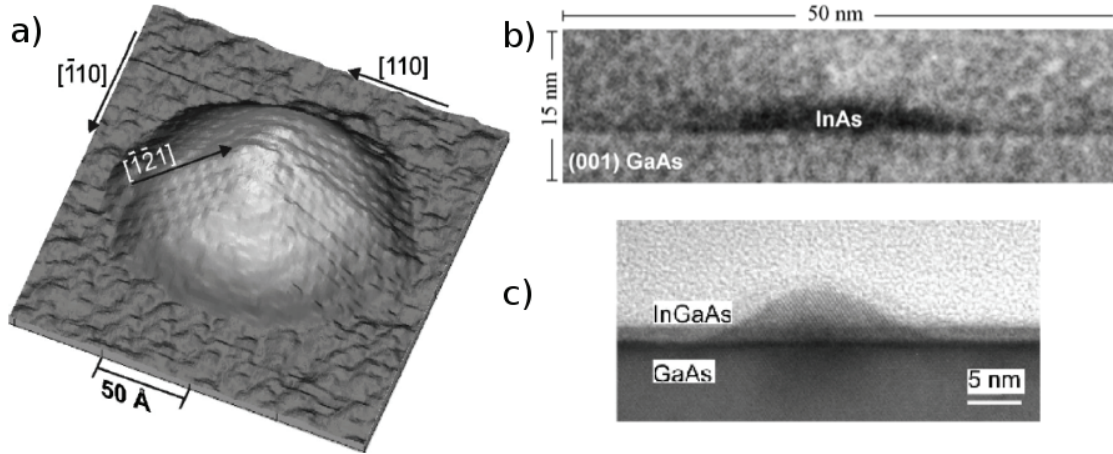


Figure 1.4.: a) Scanning electron microscope (SEM) picture of an InAs QD on a GaAs substrate before overgrowth, from [14]. b) Transmission electron microscope (TEM) picture of a GaAs-overgrown InAs QD in cross section view (Courtesy of Gilles Patriarche, CNRS). c) TEM-picture of an overgrown alloyed InGaAs QD, from [15].

the single-QD laser [18–20], as can be fabricated in VCSEL² geometry for example [21]. In a single-QD laser, the regime of strong light-matter coupling can be achieved as well as non-classical light emission [22]. The latter allows for new applications, because single-photon sources showing anti-bunching or emission of entangled photon pairs can be designed. Single photons can be used in various scopes, from quantum information applications such as transmission of information via polarization states of single photons or quantum cryptography protocols to quantum storage devices [23–25]. The origin of those single photons, the single quantum dot, plays the role of the storage medium therein, accessible via optical write and readout processes, since photonic excitations can be converted into quantum dot electronic states and vice versa.

Electronic and optical properties of semiconductor quantum dots still are a very active field of research, though entering the stage of bringing quantum dot technology to market. Nevertheless, many questions related to QD physics are to be answered in the future, arising from the dawn of quantum computing and cryptography as well as the ongoing need for miniaturization and enhancement of device efficiency.

²Vertical-cavity surface-emitting laser: an etched pillar-shaped structure containing a single active layer between two pairs of Bragg reflectors formed by alternating layers of semiconductor material. By using low QD density layers and pre-etching selection techniques, the situation of only one QD coupled to the cavity can be achieved.

1.2. Topics

In this thesis, an introduction into the description of single-particle energies and wave functions of carriers bound in the QD via the empirical tight-binding model will be given. Structural properties such as the shape and composition of the QDs enter these calculations. Also, consecutive derivation of many-particle states of the interacting system of bound carriers in the configuration interaction scheme will be presented by usage of the previously calculated single-particle wave functions and energies. By combining these approaches we link the structural and optical properties such as emission spectra and excitonic fine-structure splittings and emphasize questions regarding the applicability of QDs as optical components in modern communication and laser devices.

The III-V Indium-Arsenide (InAs) Gallium-Arsenide (GaAs) material system is well appreciated in semiconductor research due to low cost of constituent materials and good controllability during growth, as well as less toxicity compared to other materials. Nevertheless, typical emission wavelengths of InGaAs QDs are around or below $1.0\ \mu\text{m}$, far away from telecom low absorption windows at 1.3 and $1.5\ \mu\text{m}$, respectively. Various attempts have been undertaken to shift the emission wavelengths into those windows, one of which being the application of a strain-reducing layer (SRL). The latter consists of an additional InGaAs quantum well embedding the QDs in order to incorporate more Indium into the QDs and to relieve compressive strain. Both effects are known to enlarge carrier binding energies and therefore shift QD emission to larger wavelengths. When it comes to quantum cryptography, high-degree entanglement of photons emitted by QDs is needed for successful error correction and transport of the entangled photons over large distances. Those (polarization-) entangled photon pairs usually are created by the cascaded biexciton-exciton decay. Nevertheless, the excitonic fine-structure splitting (FSS) between the two bright excitonic emission lines reduces the degree of entanglement, if it is larger or comparable to the linewidth of the emission, because it adds a “which-path” information to the spectrum. In this thesis, we will answer the question if the utilization of a SRL to shift the emission wavelength to the telecom windows has an effect on the size of the FSS and how this effect impacts the device functionality. Furthermore we investigate the statistical nature of the FSS.

Active materials of conventional lasers usually consist of semiconductor quantum wells. Superior laser properties such as low threshold currents or temperature stability have been proposed for using InGaAs QDs as active material. In difference to quantum well lasers, QDs as active materials have been discovered to show reduction of the differential gain for high excitation power for some QD samples. This happens due to the interplay of dephasing and Coulomb-induced phase-state filling. We investigate this topic combining realistic QD wave functions from our tight-binding model with quantum-kinetic calculations of the differential gain. We identify re-

gimes where either dephasing or phase-state filling dominates the behaviour of the peak gain with excitation density, leading to reduction or saturation of the peak gain.

1.3. Brief description of content

This thesis is structured as follows.

In chapter 2 we develop in detail a theory for the calculation of *single-particle* properties of quantum dots using the method of semiempirical tight-binding. The theoretical concepts of including strain arising from lattice mismatch of constituent materials, spin-orbit interaction and piezoelectricity in the tight-binding model are presented. Single-particle wave functions and corresponding energies are shown for bulk band structures of III-V semiconductor materials in zinkblende lattices, for quantum wells, and quantum dots. Common quantum dot structures are reviewed from literature and results of the corresponding calculations are presented. We study the influence of various parameters on single-particle properties, such as the QD geometry, composition, and valence band offset.

In Chapter 3 the calculation of *many-particle* properties of quantum dots based on the single-particle tight-binding results is described. The method of configuration interaction is explained, giving eigenstates of the interacting many-particle system by diagonalization of the many-particle Hamiltonian including Coulomb interaction. The derivation of Coulomb and dipole matrix elements from tight-binding expansion coefficients is described. The related excitonic spectrum is explained, introducing the excitonic fine-structure splitting. Results for the most common QD structures identified in the previous chapter are shown exemplarily.

In Chapter 4 applications of the introduced theoretical framework are presented, regarding the aforementioned topics. The first section is about the effect the SRL has on the excitonic fine-structure splitting and the statistical nature of this value, connected to individual atomic realizations of the SRL. The second section pays attention to the effect of gain reduction for increasing excitation power in QD active materials. Combined results of tight-binding calculations and gain spectra derived from quantum-kinetic calculations are presented.

A summary of the thesis and an outlook are given in chapter 5, followed by the appendix.

2. Single-particle theory

Contents

2.1. Calculation of electronic bulk band structures	10
2.1.1. The $\mathbf{k}\cdot\mathbf{p}$ model	10
2.1.2. Empirical pseudopotentials	11
2.2. Empirical tight-binding (TB)	12
2.2.1. Introduction	12
2.2.2. Tight-binding fundamentals	13
2.2.3. Two-center approximation	16
2.2.4. Spin-orbit coupling	20
2.2.5. Strain	22
2.2.6. Piezoelectricity	27
2.3. Modelling semiconductor nanostructures	29
2.3.1. Bulk band structures	30
2.3.2. Quantum wells	38
2.3.3. Quantum dots	46
2.4. Supercell requirements	53
2.5. Diagonalization of large sparse matrices	54
2.6. Benchmarks	55
2.7. Geometry and single-particle properties	57
2.8. Choice of valence band offset	66
2.9. Number of bound states	68

This chapter is devoted to the calculation of single-particle properties of semiconductor nanostructures. After a short introduction to alternative methods for the calculation of electronic single-particle properties, the tight-binding fundamentals are discussed. This is followed by a detailed description of modelling three-dimensional semiconductor nanostructures within the empirical tight-binding formalism. After a benchmark of our theory we review common quantum dot structures and present calculations regarding the influence of various QD parameters in QD single-particle properties.

2.1. Calculation of electronic bulk band structures

Three main approaches can be found in the literature for the calculation of band structures of semiconductors or single-particle energies and wave functions of semiconductor heterostructures beyond simple effective mass theory: the $\mathbf{k}\cdot\mathbf{p}$ formalism, the empirical pseudopotential theory and the tight-binding theory, each of which being advantageous in certain respects. Also, for the calculation of bulk band structures, ab-initio methods like density functional theory (DFT) are available. However, those methods fail for large structures containing more than around thousand atoms because of the problem size and therefore are not discussed further. In this section the $\mathbf{k}\cdot\mathbf{p}$ formalism and the pseudopotential theory will be outlined, before the TB model will be introduced.

2.1.1. The $\mathbf{k}\cdot\mathbf{p}$ model

The $\mathbf{k}\cdot\mathbf{p}$ model was proposed for the calculation of the band structure of semiconductor bulk materials in momentum space [26] and has been used for calculations of three-dimensional nanostructures as well (see [27] for an overview). It describes band structures in the vicinity of the Brillouin zone center at $\mathbf{k} = \mathbf{0}$ in a perturbative manner. In the single-particle picture, the energy E of an electron with mass m is given by the Schrödinger equation with the Hamiltonian H :

$$H\psi(\mathbf{r}) = \left[\frac{p^2}{2m} + V \right] \psi(\mathbf{r}) = E\psi(\mathbf{r}). \quad (2.1)$$

V is the (unknown) periodic potential of the crystal and p is the momentum operator. In the periodic crystal the electronic wave functions are products of plane waves with wave vector \mathbf{k} and Bloch functions $u_{n\mathbf{k}}$ with index n

$$\psi(\mathbf{r}) = e^{i\mathbf{k}\mathbf{r}} u_{n\mathbf{k}}, \quad (2.2)$$

which leads to the eigenvalue equation

$$\left[\frac{\hbar^2 k^2}{2m} + \frac{\mathbf{k} \cdot \mathbf{p}}{m} + \frac{p^2}{2m} + V \right] u_{n\mathbf{k}} = E_n u_{n\mathbf{k}}, \quad (2.3)$$

in which the cross-term $\frac{\mathbf{k} \cdot \mathbf{p}}{m}$ can be treated as a perturbation. Under the assumption that for a known reciprocal vector $\mathbf{k}_0 = \mathbf{0}$ (Γ -point) the solution is known, the \mathbf{k} -dependence of the energy can be calculated in the basis of the unknown Bloch functions. This yields for the n -th energy band:

$$E_n(\mathbf{k}) = E_n(\mathbf{0}) + \frac{\hbar^2 k^2}{2m} + \frac{\hbar^2}{m^2} \sum_{n' \neq n} \frac{|\langle u_n | \mathbf{k} \cdot \mathbf{p} | u_{n'} \rangle|^2}{E_n(\mathbf{0}) - E_{n'}(\mathbf{0})}. \quad (2.4)$$

The resulting energy dispersion is parabolic with corrections from the matrix elements

$$\langle u_n | \mathbf{k} \cdot \mathbf{p} | u_{n'} \rangle. \quad (2.5)$$

Similar to tight-binding calculations, the actual form of the basis functions is neither known nor needed for the calculation. The only requirement is the Bloch function symmetries being equal to the symmetries of the energy bands to which the functions are related. The values of these energies can be taken from experiments and inserted into the calculation, which produces good results in reproducing experimental data. Depending on the number of Bloch functions used as basis, one speaks about 8-band-, 14-band or even 20-band $\mathbf{k} \cdot \mathbf{p}$ modelling. For example in the 8-band model three valence bands and one conduction band are featured, each being spin degenerate. Additional to band structure calculations, the $\mathbf{k} \cdot \mathbf{p}$ formalism has been used to derive the energies and envelopes of the wave functions of bound carriers in semiconductor nanostructures such as quantum dots or wires very successfully [28, 29]. Since the structure of the crystal lattice does not enter the calculation, only envelopes of the wave functions, lacking the symmetry of the underlying crystal structure, can be calculated. Nevertheless, the $\mathbf{k} \cdot \mathbf{p}$ model is widely used.

2.1.2. Empirical pseudopotentials

The empirical pseudopotential method [30–32] has received much attention lately and was developed to simplify band structure calculations from the Schrödinger equation

$$\left[-\frac{1}{2} \nabla^2 + V(r) \right] \psi_i(\mathbf{r}) = E_i \psi_i(\mathbf{r}) \quad (2.6)$$

using the potentials

$$V(\mathbf{r}) = \sum_{j,\alpha} v_j(|\mathbf{r} - \mathbf{R}_{j,\alpha}|). \quad (2.7)$$

Here, the index j runs over all atoms in the unit cell and v_j are the atomic potentials centered at the atomic sites \mathbf{R}_j of atom type α . In general, the v_j include both core and valence electrons as well as the potential of the nucleus. Usually, the wave functions ψ_i are expanded using a plane wave basis. The above eigenvalue problem results in the diagonalization of the Hamilton matrix, which has to be evaluated in the plane wave basis too. Within the empirical pseudopotential method,

it turns out, only a small number of the potentials v_j are non-zero, which are used as parameters to fit the desired band structure to experimentally known properties. Like the $\mathbf{k}\cdot\mathbf{p}$ method, the empirical pseudopotential method has been extended very successfully from band structure calculations to the calculation of electronic wave functions of heterostructures like quantum wires [33], colloidal quantum dots [34] and embedded quantum dots [35–37] in various material systems. With the inclusion of strain, piezoelectricity and screening into the pseudopotentials, the empirical pseudopotential method has become an accurate and trusted method for the calculation of electronic properties of semiconductor nanostructures. Because of the underlying atomic lattice entering the calculation, the correct point symmetries are captured, in contrast to continuum methods like $\mathbf{k}\cdot\mathbf{p}$. Together with the tight-binding method, it has become the up-to-date method for systems containing a few hundred up to many million atoms, which is where ab-initio methods fail due to the large basis required. The interested reader may be referred to the excellent topical review article [38]. Empirical pseudopotential calculations are believed to be very accurate and therefore are often used as benchmarks for other theories. We also use pseudopotential calculations to benchmark our results in chapter 2.6.

2.2. Empirical tight-binding (TB)

In this section, the theoretical framework of the empirical tight-binding model will be explained in detail, including a detailed discussion of the widely used two-center approximation, spin-orbit coupling and the incorporation of strain into the formalism. The section is closed with a short discussion about the necessity of the inclusion of piezoelectric effects into the calculations regarding bound states and energies in QDs.

2.2.1. Introduction

Empirical tight-binding (TB), as formulated in the 1980s by Vogl et al. [39, 40], is a common method to calculate single-particle electronic properties of solids which is both accurate and efficient.

TB follows the assumption of isolated atoms in a solid which all have distinct orbitals. Since every atom is accounted for separately, the TB method holds a microscopic description of the crystal. The calculation consists of the diagonalization of a Hamiltonian matrix that in general describes two physical properties: the energies of carriers in the atomic orbitals at each individual atom of the solid as well as the process of electrons hopping between orbitals at different atoms. This is a sufficient description if two assumptions can be made:

1. The dominant electronic features can be described by a relatively small number of orbitals per atom.
2. The spatial overlap of atomic orbitals at different atomic sites decays fast with increasing distance of the atoms.

The first point means that mainly electrons in outer shells contribute to the binding. Therefore, core electrons can be neglected. The second assumption can be understood as a tight binding of the electrons to the atoms, which is where the name of the method originates from. The orbital energies enter the Hamiltonian as diagonal elements, while the hopping probabilities are accounted for as off-diagonal elements. To take several other processes into account, such as spin-orbit interaction of electrons at the same atomic site or external electromagnetic fields, corresponding matrix elements can be added both diagonal and off-diagonal.

The method of empirical tight-binding is mainly used to calculate band structures of solids and the energies and occupation probabilities of electrons and holes in nanostructures without full translational invariance like quantum wells and quantum dots. Since band structures are experimentally well known properties for most usual bulk semiconductor materials, a TB model is first built to reproduce the band structure of all materials that occur in a certain nanostructure before it is used to calculate the electronic properties of the nanostructure itself. Astonishingly, this generalization of bulk parameters to the atomic parameters of the nanostructure works very well.

Depending on the number of atomic orbitals that describe the tight-binding basis and on the choice of parameters the band structure can be reproduced in smaller or larger intervals of the Brillouin zone. Often it is sufficient to reproduce the band structure for a certain interval of \mathbf{k} -vectors, for example around the Γ -point for optical problems. In general, the basis of atomic orbitals can be classified by $|\mathbf{R}, \alpha\nu\sigma\rangle$ with the orbital ν being localized at the atom type α (if the solid consists of more than one atom type like Gallium and Arsen atoms in the semiconductor GaAs or for systems with more than one atom in the unit cell such as Silicon or graphene) at location \mathbf{R} with spin σ .

2.2.2. Tight-binding fundamentals

For a single free atom located at position \mathbf{R}_n , the Schrödinger equation reads

$$H^{\text{atom}} |\mathbf{R}_n, \alpha\nu\sigma\rangle = E_{\alpha,\nu}^{\text{atom}} |\mathbf{R}_n, \alpha\nu\sigma\rangle \quad (2.8)$$

with $|\mathbf{R}_n, \alpha\nu\sigma\rangle$ being the basis of atomic orbitals and $E_{\alpha,\nu}^{\text{atom}}$ being the atomic orbital energies. The Hamiltonian is given by

$$H^{\text{atom}} = \frac{p^2}{2m} + V(\mathbf{R}_n, \alpha), \quad (2.9)$$

where $V(\mathbf{R}_n, \alpha)$ is the atomic potential of the single atom and m is the electron or hole mass, respectively. Schrödinger's equation of the periodic crystal is then given by

$$H^{\text{crystal}} |\mathbf{k}\rangle = E(\mathbf{k}) |\mathbf{k}\rangle \quad (2.10)$$

with \mathbf{k} being the reciprocal lattice vector and $\psi(\mathbf{r}) = \langle \mathbf{r} | \mathbf{k} \rangle$ being the wave functions of electrons in the periodic lattice potential of the crystal. Here the Hamiltonian is

$$H^{\text{crystal}} = H^{\text{atom}} + \sum_{m \neq n, \alpha} V(\mathbf{R}_m, \alpha) \quad (2.11)$$

because of the presence of the potentials of all other atoms in the crystal located at positions $\mathbf{R}_m \neq \mathbf{R}_n$.

For the solution of this eigenproblem the electronic wave functions are expressed as linear combinations of the atomic orbitals:

$$|\mathbf{k}\rangle = \sqrt{\frac{V_{uc}}{V}} \sum_{\alpha\nu\sigma} \sum_n e^{i\mathbf{k} \cdot \mathbf{R}_n} u_{\alpha\nu\sigma}(\mathbf{k}) |\mathbf{R}_n, \alpha\nu\sigma\rangle. \quad (2.12)$$

The position of atom α is given by \mathbf{R}_n and V_{uc}/V is the ratio in volume of one unit cell to the whole crystal. The $|\mathbf{k}\rangle$ are not orthonormal, an attribute which usually is necessary for a good choice of basis, because atomic orbitals of different atoms are not orthogonal in general. The overlap matrix of states $\langle \mathbf{k}' |$ and $|\mathbf{k}\rangle$ reads:

$$O_{\alpha', \nu', \sigma', \alpha, \nu, \sigma}(\mathbf{k}) = \frac{V_{uc}}{V} \sum_{n, m} e^{i\mathbf{k}(\mathbf{R}_m - \mathbf{R}_n)} \langle \mathbf{R}_m, \alpha', \nu', \sigma' | \mathbf{R}_n, \alpha, \nu, \sigma \rangle. \quad (2.13)$$

The bra-ket expressions translate to real-space integrals such as

$$\langle \mathbf{R}_m, \alpha', \nu', \sigma' | \mathbf{R}_n, \alpha, \nu, \sigma \rangle = \int d^3\mathbf{r} \psi^*(\mathbf{R}_m - \mathbf{r}, \alpha' \nu' \sigma') \psi(\mathbf{R}_n - \mathbf{r}, \alpha \nu \sigma) \quad (2.14)$$

with $\psi(\mathbf{r})$ being the electronic wave functions.

For the situation of orthogonal basis states the matrix $O(\mathbf{k})$ in Eqn. (2.13) would be the identity matrix. Since it is a basic assumption of the tight-binding model that the electrons are tightly bound to the atoms, the overlap matrix elements are assumed to be small compared to the matrix elements of the Hamiltonian. In fact the basis orbitals can be treated as orthogonal since for the case that the overlap matrix $O(\mathbf{k})$ is positive definite (which is indeed fulfilled for the usually assumed basis states) a so-called Löwdin transformation exists which transforms the basis into an orthogonal representation [41]. Moreover, this transformation does not even need to be carried out explicitly because it preserves the original symmetry and localization properties of the basis. It is sufficient to assume that the transformation has been carried out implicitly. For a discussion of the Löwdin transformation see [42]. This

assumption reduces the former generalized eigenproblem to a usual eigenproblem, which is numerically easier to tackle. The remaining equation to be solved in the orthogonalized basis is:

$$\sum_{\alpha, \nu, \sigma} H_{\alpha', \nu', \sigma', \alpha, \nu, \sigma}^{\text{crystal}}(\mathbf{k}) u_{\alpha, \nu, \sigma}(\mathbf{k}) = E(\mathbf{k}) u_{\alpha', \nu', \sigma'}(\mathbf{k}). \quad (2.15)$$

The solution of this equation gives the energy bands of the crystal. The matrix elements $\langle \mathbf{R}_m, \alpha', \nu', \sigma' | H | \mathbf{R}_n, \alpha, \nu, \sigma \rangle$ can either be calculated numerically by explicit knowledge of the atomic potentials (e.g. in DFT treatment [43]) or they can be treated as empirical parameters to be determined by fitting the calculated band structure to experimentally available band structures, effective masses and band gaps. The use of these empirical parameters is the reason why the method is called *empirical* tight-binding. The best calculations for comparison are based on pseudo-potentials (for example see [32] for GaAs band structure calculations) as introduced in chapter 2.1.2.

As mentioned earlier, there are two main contributions of matrix elements in the Hamiltonian. In the expression $\langle \mathbf{R}_m, \alpha', \nu', \sigma' | H | \mathbf{R}_n, \alpha, \nu, \sigma \rangle$ the real space lattice vectors \mathbf{R}_m and \mathbf{R}_n can either be equal or different. In the first case the matrix element is called "on-site" and represents the energy of an atomic orbital. The corresponding contributions are diagonal in the tight-binding Hamiltonian, so by dropping the "crystal" index the on-site matrix elements can be written as

$$\begin{aligned} H_{\alpha', \nu', \sigma', \alpha, \nu, \sigma}^{\text{on-site}} &= \langle \mathbf{R}_m, \alpha' \nu' \sigma' | H | \mathbf{R}_n, \alpha \nu \sigma \rangle \delta_{m,n} \delta_{\alpha', \alpha} \delta_{\nu', \nu} \delta_{\sigma', \sigma} \\ &=: E_{\alpha, \nu}. \end{aligned} \quad (2.16)$$

The orbital energies are spin-independent, so the index σ is dropped in the last line. The second case holds the situation where \mathbf{R}_m and \mathbf{R}_n are not equal. With $\mathbf{R}_m - \mathbf{R}_n$ being the distance between nearest neighbours in the crystal lattice, (second next neighbours, third next neighbours etc.) these matrix elements are called "nearest neighbour hopping matrix elements" and so on. They describe the probability for an electron to "hop" from one atom of type α' at the position \mathbf{R}_m in an orbital ν' with spin σ' to another atom of type α at position \mathbf{R}_n into the orbital ν with spin σ . These matrix elements are off-diagonal in the Hamiltonian matrix and will be written as

$$H_{\alpha', \nu', \sigma', \alpha, \nu, \sigma}^{\text{neighbour}} = \langle \mathbf{R}_m, \alpha', \nu', \sigma' | H | \mathbf{R}_n, \alpha, \nu, \sigma \rangle \delta_{\sigma, \sigma'} \quad (2.17)$$

$$=: V(\mathbf{R}_m - \mathbf{R}_n)_{\alpha, \alpha', \nu, \nu'} \quad (2.18)$$

from here on. No spin-flip processes are mediated through the Hamiltonian, so the hopping matrix elements are diagonal in the electron spin. It is obvious from a physical point of view that these integrals decay rapidly with the distance $\mathbf{R}_m - \mathbf{R}_n$ between the two atoms, so it is usual to set these matrix elements to zero for a distance larger than some cut-off radius. Also from a computational point of view

it makes sense to restrict the order of hopping matrix elements since a higher order results in a higher bandwidth of the matrix to be diagonalized. The bandwidth in turn has a strong influence on the time needed for numerical diagonalization. In many cases it is sufficient to take only nearest-neighbour hoppings into account and drop the higher orders.

So how does the tight-binding Hamiltonian look like? The most general representation of the TB-Hamiltonian has the size of the matrix being the number of basis states multiplied by the number of atoms assumed. Depending on the needed accuracy of the calculations and the physical properties to be highlighted, different numbers of atomic orbitals are taken into account. Assuming single atom orbital symmetry properties (labelled s, p, d, \dots as shown in Fig. 2.1) for the tight-binding orbitals different features can be addressed. Many different models can be found in the literature: from simple two-band models (one s -like orbital at each atom in the unit cell for both electrons and holes) over intermediate models accounting for different bands for anions and cations (sp_a^3 , [44]) and the often used model accounting for a basis of one s -like and three p -like orbitals at each atom ($sp_x p_y p_z = sp^3$, [45]) to more advanced models such as $sp^3 s^*$ [39] or even $sp^3 d^5 s^*$ [46, 47]. See [48] for a review of different models and parametrizations. For means of keeping the basis size as small as possible, so-called s^* -orbitals were introduced by Vogl et al. [39]. These orbitals are artificial entities holding s -like symmetry and are used to account for the influence of energetically higher orbitals without taking them into account explicitly. Since in the scope of this thesis we are interested in optical properties of semiconductor nanostructures it is sufficient to reproduce the band structure features around the Γ -point. Throughout this thesis a $sp^3 s^*$ -basis in a nearest-neighbour model is used, so in this case the s^* -orbitals represent the d -like orbitals. For other tasks, e.g. transport problems, it is necessary to reproduce the band structure accurately also at the X -point where a $sp^3 s^*$ model fails to reproduce correct effective masses. This can be achieved with a basis including d -like orbitals.

2.2.3. Two-center approximation

A famous approach for the simplification of the treatment of tight-binding hopping matrix elements is given by the so-called two-center approximation, which was proposed by Slater and Koster [49] and stems from the idea of keeping the actual calculation of the matrix elements simple. Even though we are dealing with the matrix elements as empirical parameters, this ansatz is very fruitful because of its implications for the incorporation of strain into the tight-binding model. This will be shown in section 2.2.5. The general form of the orbital part of the matrix elements

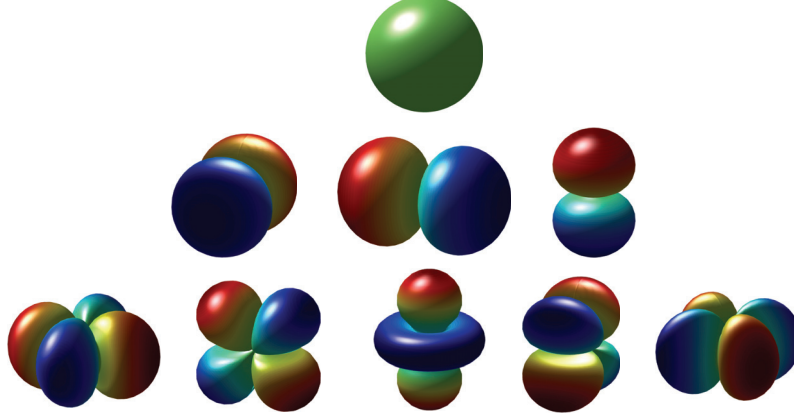


Figure 2.1.: Representations of atomic orbitals via the angular parts of the spherical harmonics. First line: orbital with s -symmetry; second line: orbitals with p -symmetry; last line: orbitals with d -symmetry.

is given by

$$\langle k' | H | k \rangle = \sum_{m,n} \sum_{\alpha', \nu', \sigma'} \sum_{\alpha, \nu, \sigma} \langle \mathbf{R}_m, \alpha', \nu', \sigma' | H | \mathbf{R}_n, \alpha, \nu, \sigma \rangle \quad (2.19)$$

Each summand above includes two orbitals localized at position \mathbf{R}_m and \mathbf{R}_n as well as one atomic potential V localized at position \mathbf{R}_l as part of the Hamiltonian, because

$$H \sim \sum_{l, \alpha} V(\mathbf{R}_l, \alpha). \quad (2.20)$$

In a nearest neighbour tight-binding model only $|\mathbf{R}_m - \mathbf{R}_n| \leq d_{NN}$ is considered, whereas \mathbf{R}_l can undergo each atomic position in the crystal. Slater and Koster call this a three-center integral, where $m \neq n \neq l$. Their proposal was to only take two-center integrals into account, where either $l = m$ or $l = n$. These integrals describe the situation that the atomic potential is localized at one of the orbital positions and all other situations are neglected. This so-called two-center approximation is a reasonable approach for the case that the atomic potential decays fast with the distance to the orbital positions. This is feasible due to physical intuition: the potential at \mathbf{R}_l mediates the hopping of a carrier between positions \mathbf{R}_m and \mathbf{R}_n . The more distant the potential is, the smaller the probability of a hopping. integrals.

Given the two-center approximation, the effective potential for a hopping process is rotationally symmetric with respect to the vector $\mathbf{d} = \mathbf{R}_m - \mathbf{R}_n$ between two atoms. In that case, the angular momentum with respect to \mathbf{d} , $L_{\mathbf{d}} = L_{|\mathbf{d}|}$, is a good quantum number. Since $L_{\mathbf{d}}$ and the effective two-center Hamiltonian commute, all hopping matrix elements vanish which contain orbitals with different eigenvalues $\hbar m'_{\mathbf{d}} \neq \hbar m_{\mathbf{d}}$ with respect to the angular momentum operator $L_{\mathbf{d}}$. Therefore it is a better choice to decompose the $p_{x,y,z}$ -like orbitals along a cartesian axis \mathbf{e}_i with

respect to \mathbf{d} into bond-parallel and bond-normal orbitals:

$$|p_{\mathbf{e}_i}\rangle = \mathbf{e}_i \mathbf{d} |p_\sigma\rangle + \mathbf{e}_i \mathbf{n} |p_\pi\rangle \quad (2.21)$$

as sketched in Fig. 2.2. Here, \mathbf{n} is a unit vector normal to the plane spanned by

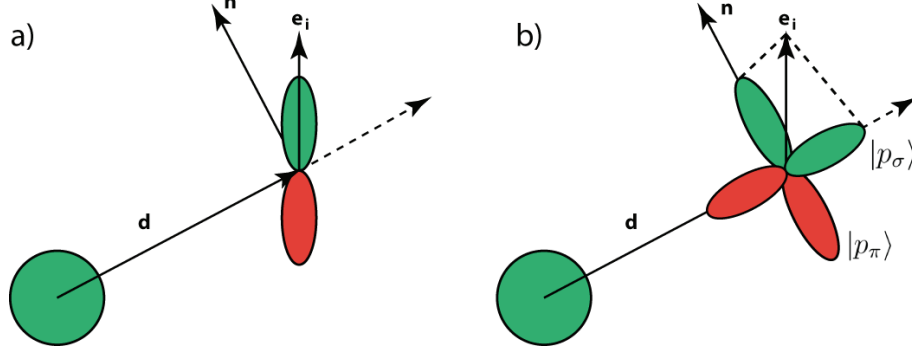


Figure 2.2.: a) Definition of the vectors. b) Decomposition of a p -like atomic orbital into σ and π parts, weighted by the projection of \mathbf{e}_i onto the bond-parallel and bond-normal vectors, respectively.

\mathbf{d} and \mathbf{e}_i . The orbital components are labelled corresponding to the eigenvalue of the angular momentum operator with respect to \mathbf{d} : $|p_\sigma\rangle$ corresponds to $m_{\mathbf{d}} = 0$, $|p_\pi\rangle$ to $m_{\mathbf{d}} = \pm 1$, respectively. The reader may note, that the index σ here is in no relation to the spin-index used before to label atomic orbitals. What is meant by σ should be clear contextually anyway. The different labels for bonds between atomic orbitals are shown in Fig. 2.3.

Now for example a hopping matrix element between a s -like and a p -like orbital can be written as (neglecting all other indices for the moment):

$$\langle s | H | p \rangle = \mathbf{e}_i \mathbf{d} \langle s | H | p_\sigma \rangle + \mathbf{e}_i \mathbf{n} \langle s | H | p_\pi \rangle \quad (2.22)$$

$$= \mathbf{e}_i \mathbf{d} \langle s | H | p_\sigma \rangle \quad (2.23)$$

$$= V_{sp\sigma}. \quad (2.24)$$

Due to the different angular momenta of the atomic orbitals, and due to the symmetry of the p_π -orbital with respect to \mathbf{d} , the matrix element $\langle s | H | p_\pi \rangle = V_{sp\pi}$ equals zero. Introducing the directional cosines d_x, d_y and d_z along the cartesian axes via

$$\mathbf{d} = |\mathbf{d}|(d_x, d_y, d_z), \quad (2.25)$$

so that

$$d_x = \frac{\mathbf{e}_i \cdot \mathbf{d}}{|\mathbf{d}|}, \quad (2.26)$$

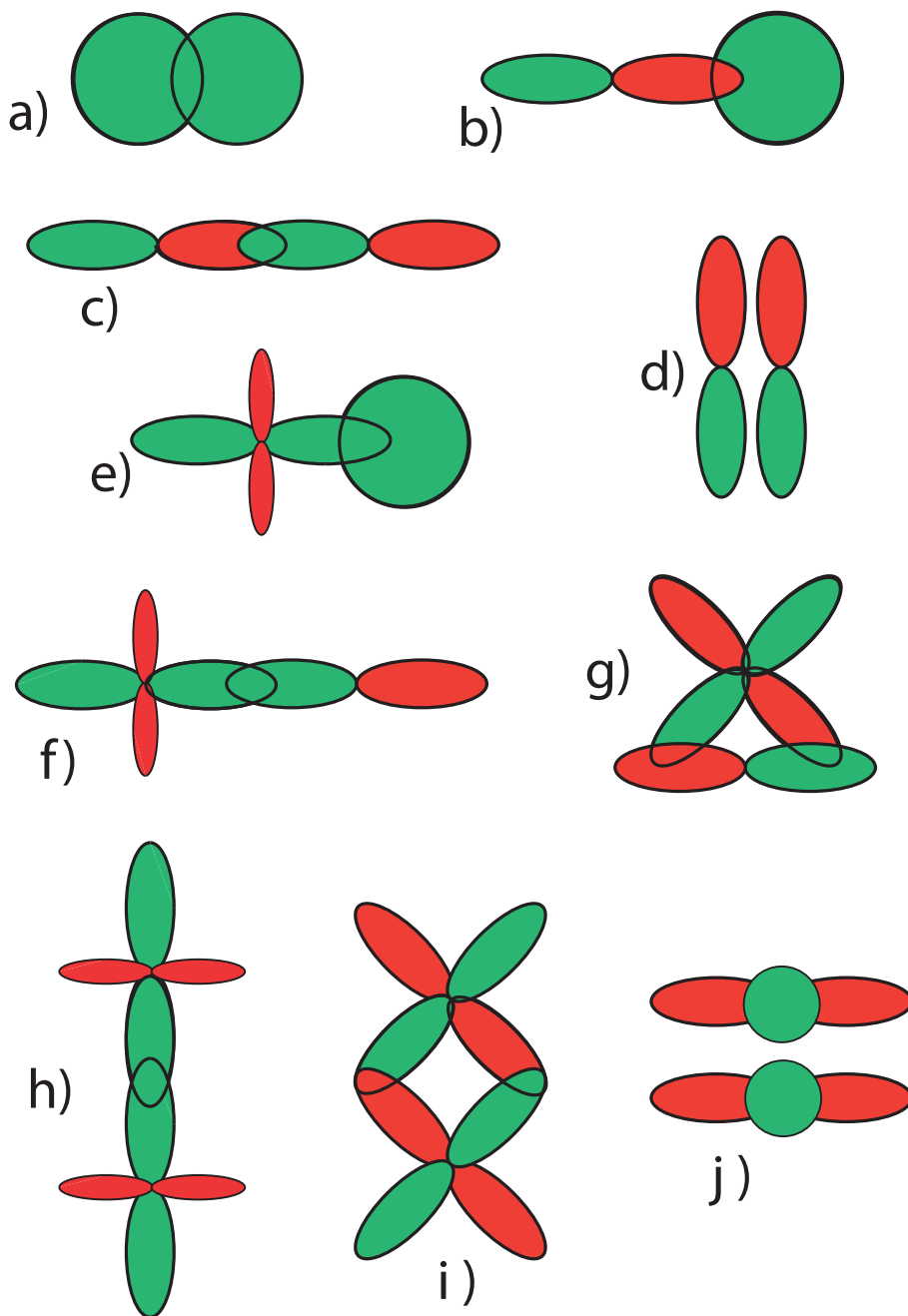


Figure 2.3.: Different types of bonds between orbitals in projection view. Red/green colors describe negative/positive sign of the wave function. a) $ss\sigma$ bond, b) $sp\sigma$, c) $pp\sigma$, d) $pp\pi$, e) $sd\sigma$, f) $pd\sigma$, g) $pd\pi$, h) $dd\sigma$, i) $dd\pi$, j) $dd\delta$.

gives the relations between the old p_x, p_y, p_z orbitals and the new matrix elements in the two-center approximation [49]:

$$\langle s | H | p_x \rangle = d_x V_{sp\sigma} \quad (2.27)$$

$$\langle s | H | p_y \rangle = d_y V_{sp\sigma} \quad (2.28)$$

$$\langle s | H | p_z \rangle = d_z V_{sp\sigma} \quad (2.29)$$

$$\langle s^* | H | p_x \rangle = d_x V_{s^*p\sigma} \quad (2.30)$$

$$\langle s^* | H | p_y \rangle = d_y V_{s^*p\sigma} \quad (2.31)$$

$$\langle s^* | H | p_z \rangle = d_z V_{s^*p\sigma} \quad (2.32)$$

$$\langle p_x | H | p_x \rangle = d_x^2 V_{pp\sigma} + (1 - d_x^2) V_{pp\pi} \quad (2.33)$$

$$\langle p_x | H | p_y \rangle = d_x d_y V_{pp\sigma} - d_x d_y V_{pp\pi} \quad (2.34)$$

$$\langle p_y | H | p_z \rangle = d_y d_z V_{pp\sigma} - d_y d_z V_{pp\pi}. \quad (2.35)$$

All other matrix elements can be calculated by cyclical permutation of the cartesian indices.

Due to symmetry reasons, interchanging the order of the orbitals changes the sign of the matrix element if the sum of the orbital parities equals an odd number and leaves the sign unaffected if the sum of the parities is even. This results in relations

$$\langle s | H | p_x \rangle = - \langle p_x | H | s \rangle \quad (2.36)$$

and

$$\langle p_x | H | p_y \rangle = \langle p_y | H | p_x \rangle. \quad (2.37)$$

2.2.4. Spin-orbit coupling

The effect of spin-orbit coupling is known to alter the energy bands of semiconductors by shifting energies and inducing a splitting Δ_{so} of heavy- and light-hole bands at the center of the Brillouin-zone. This splitting typically is of the order of tens up to a hundred meV for common semiconductors.

For an accurate description of semiconductors spin-orbit coupling needs to be included. The common approach to include spin-orbit coupling into the tight-binding model is the strategy proposed by Chadi [45], which has the advantage of not increasing the size of the basis. The spin-orbit Hamiltonian H_{so} can be added to the Hamiltonian of the crystal H_0 (what was H in the sections before):

$$H = H_0 + H_{so}. \quad (2.38)$$

Nevertheless, it turns out the spin-orbit coupling matrix elements are complex, which makes the diagonalization more complicated because the solution of the complex eigenvalue problem is numerically much more difficult than the standard eigenvalue

problem with real coefficients. In general, matrix elements of the Hamiltonian can be complex anyway, only hermiticity of the Hamiltonian is required. For three-dimensional heterostructures, however, the matrix elements all are real except those of the spin-orbit interaction.

The approach of Chadi starts with the assumptions that the atomic spin-orbit operator is well suited for the tight-binding problem and describes the influence of spin-orbit coupling on the tight-binding basis states properly. Only p -like orbitals at the same atom are coupled via spin-orbit interaction. Interatomic spin-orbit couplings can be taken into account [50], but it turns out that already the on-site spin-orbit interaction is sufficient to reproduce the splitting of heavy-hole and light-hole bands in the band structure of common semiconductor materials.

The atomic spin-orbit Hamiltonian is given by:

$$H_{so} = \frac{1}{2m^2c^2} \frac{1}{r} \frac{\partial V_{atom}}{\partial r} \mathbf{L} \cdot \mathbf{s}, \quad (2.39)$$

where \mathbf{L} is the operator of angular momentum, \mathbf{s} is the spin operator, V_{atom} is the atomic potential and m and c are the electron mass and the speed of light, respectively. r is the spatial coordinate. As mentioned above, only matrix elements between p -like orbitals at the same atom are considered. It turns out the only non-vanishing matrix elements of the spin-orbit Hamiltonian are:

$$\langle p_x \pm | H_{so} | p_z \mp \rangle = \pm \lambda \quad (2.40)$$

$$\langle p_x \pm | H_{so} | p_y \pm \rangle = \mp i \lambda \quad (2.41)$$

$$\langle p_y \pm | H_{so} | p_z \mp \rangle = -i \lambda \quad (2.42)$$

and their complex conjugates [45]. In the above equations, $+$ and $-$ denote spin up and down, respectively. Surprisingly, the complete influence of the spin-orbit coupling on the band structure can be traced back to one single parameter λ per atom type in the crystal, which is defined by:

$$\lambda = \langle p_x | \frac{\hbar^2}{4m^2c^2} \frac{1}{r} \frac{\partial V_{atom}}{\partial r} | p_x \rangle. \quad (2.43)$$

The parameter λ can be used as an additional fitting parameter to reproduce the valence-band splitting correctly around the Γ -point. The parameters for λ used in this thesis can be found in the appendix A.4.

2.2.5. Strain

As described in the introductory section, in the Stranski-Krastanov growth mode quantum dots form due to strain induced by the lattice-mismatch between the two (or more) competing lattice constants. For example for InAs quantum dots in a GaAs host material the lattice mismatch is about 7%¹. Due to the arising strain the individual atoms are no longer in the bulk lattice positions of the host material but are displaced into strained equilibrium positions which minimize the global strain energy. Examples for displacements for a pure InAs-QD and an alloyed InGaAs-QD inside the supercell are shown in Figs. 2.4 and 2.5. There are different approaches to calculate the strain-induced displacements in the crystal. Since hundreds of thousands up to several millions of atoms have to be accounted for in the strain calculations, ab-initio methods clearly fail due to the sheer problem size. There are several methods found to be applicable for QD calculations. The three most promising and most applied methods are introduced in the following. For a review of the methods for the calculation of strain in nanostructures see [51].

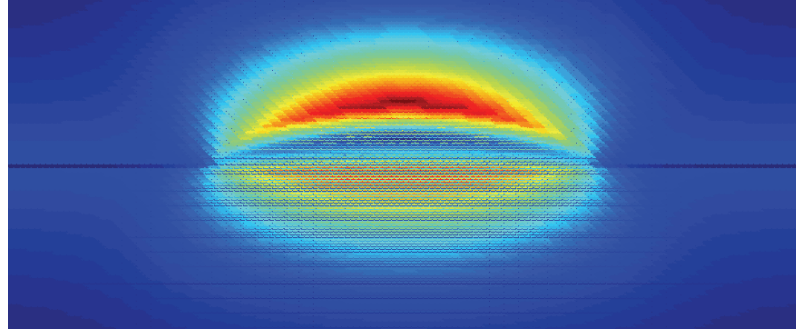


Figure 2.4.: Example for atomic displacements due to lattice-mismatch-induced strain. Shown is a small part of the many-million atom supercell containing the WL and the QD, cut vertically through the middle of the QD and seen from the side of the supercell. Colors correspond to absolute value (blue = small, red = large) of displacement with respect to the GaAs bulk nearest-neighbour distance.

FEM

One approach to model the strain arising in semiconductor nanostructures is the finite element analysis (FEM, see [52–54] for InAs/GaAs,[55] for Ge(Si)/Si). The main idea in FEM is to discretize a continuous domain into a mesh of smaller subdomains, called elements. The behaviour of those elements can be treated mathematically in a stiffness matrix. Elements are connected by nodes and through

¹The lattice constants are: $a_{\text{GaAs}} = 5.65 \text{ \AA}$ and $a_{\text{InAs}} = 6.06 \text{ \AA}$, respectively.

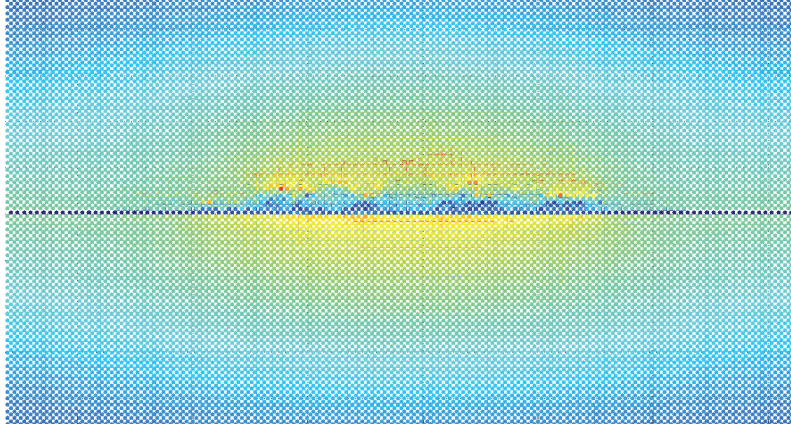


Figure 2.5.: Example for atomic displacements due to strain for a reduced quantum dot Indium content of 20%. The color scale for the displacements does not correspond to the scale in Fig. 2.4.

these nodes, an approximate system of (partial differential) equations for the whole system of the form

$$K\mathbf{u} = \mathbf{f} \quad (2.44)$$

arises. Here, K is the so-called stiffness matrix, \mathbf{u} is a global displacement vector to be solved for and \mathbf{f} is the force vector. The lattice mismatch is treated via application of a thermal expansion coefficient to the elements inside the dot and a consecutive raise of temperature. The value of the expansion coefficient is given by the lattice mismatch in percent (0.067 for InAs/GaAs). This results in thermal strain that defines the force vector. Of course, the accuracy of the calculated nodal displacements depends on the choice of the finite elements (meshing). The shortcoming of this model is that atomic effects such as local clustering and random alloy fluctuations as well as shape asymmetries cannot be considered because usually only a symmetric slice of the simulation domain is accounted for, i.e., only one corner of a pyramidally shaped QD or only one circular segment of a spherically shaped QD.

Continuum elasticity

Another method to calculate the strain-induced displacements is the continuum-elasticity model (CE) [56]. As implied by the name, the CE model treats the strain-induced displacement of a continuum within the harmonic approximation of classical elasticity. The strain energy per atom is given by

$$E_{CE} = \frac{V}{2}C_{11}(\epsilon_{xx}^2 + \epsilon_{yy}^2 + \epsilon_{zz}^2) + \frac{V}{2}C_{44}(\epsilon_{yz}^2 + \epsilon_{zx}^2 + \epsilon_{xy}^2) + VC_{12}(\epsilon_{yy}\epsilon_{zz} + \epsilon_{yy}\epsilon_{xx} + \epsilon_{zz}\epsilon_{xx}) \quad (2.45)$$

for a cubic system. Here, C_{ij} are the cubic elastic constants, V is the equilibrium volume and ϵ_{ij} is the strain tensor, yielding

$$\epsilon_{ij} = \frac{1}{2} \left(\frac{d\mathbf{u}_i}{d\mathbf{x}_j} + \frac{d\mathbf{u}_j}{d\mathbf{x}_i} \right), \quad (2.46)$$

where \mathbf{u}_i is the displacement and \mathbf{x}_i are coordinates. Indices i and j run over the three independent spatial directions. The strained equilibrium configuration is determined by finding the minimum of the global strain energy by adjusting the displacement vectors (not the atomic positions but displacements on a discretized grid which has to be chosen accurately). In both the FEM and the CEM it is not clear how to map the calculated displacement-fields onto the atoms in the TB model.

Valence force fields

A third method for the calculation of strain-induced atomic displacements and the method of choice for TB is the atomistic Valence Force Field (VFF) [57] method of Keating [58] and Martin [59] in its generalized version for zincblende alloy crystals [60, 61]. It appears to be natural to use the VFF method in our context because it treats the strain atomistically like the tight-binding method is intrinsically. Therefore we will use this model to calculate the strain-induced atomic displacements entering the tight-binding Hamiltonian.

In the VFF approach using the original Keating potential the global strain energy (elastic energy) for zincblende-type crystals can be described as a function of the atomic positions \mathbf{R}_i :

$$E_{strain} = \sum_i \sum_{j=1}^4 \frac{3\alpha_{ij}}{16(d_{ij}^0)^2} \left((\mathbf{R}_j - \mathbf{R}_i)^2 - (d_{ij}^0)^2 \right)^2 + \sum_i \sum_{j,k>j} \frac{3\beta_{ijk}}{8d_{ij}^0 d_{jk}^0} \left((\mathbf{R}_j - \mathbf{R}_i)(\mathbf{R}_k - \mathbf{R}_i) - \cos \theta_0 d_{ij}^0 d_{jk}^0 \right)^2. \quad (2.47)$$

Here, d_{ij}^0 and d_{jk}^0 is the bulk equilibrium bond length between nearest neighbours i and j or k , respectively, $\cos \theta_0 = -\frac{1}{3}$ is the ideal bulk bond angle and α_{ij} and β_{ijk} are material-dependent parameters. The first term is a sum over all atoms i and their four nearest neighbours. Since it is zero if $\mathbf{R}_j - \mathbf{R}_i$ equals the bulk equilibrium bond length this term describes bond-stretching. The second term includes the angle between two of the bonds between three atoms i , j and k and describes the influence of bond-bending on the total strain energy. In the Keating model, the material parameters entering Eqn. (2.47) are given as functions of the stiffness parameters

Material	C_{11}	C_{12}	C_{44}
GaAs	11.88	5.38	5.94
InAs	8.34	4.54	3.95

Table 2.1.: Stiffness parameters used in this thesis, scaled by $10^{11} \cdot \text{dyn}/(\text{cm}^2)$

[62]:

$$\alpha_{ij} = (C_{11} + 3C_{12}) \frac{a_0}{4} \quad (2.48)$$

$$\beta_{ijk} = (C_{11} - C_{12}) \frac{a_0}{4}, \quad (2.49)$$

where the C_{ij} are experimental values of the stiffness coefficients taken from [63] for GaAs and [64] for InAs, given in Tab. 2.1. The constant a_0 is the equilibrium lattice constant. The third stiffness parameter C_{44} is not independent but related to the other parameters by

$$\frac{2C_{44}(C_{11} + C_{12})}{(C_{11} - C_{12})(C_{11} + 3C_{12})} = 1. \quad (2.50)$$

The above formulas are valid if the constituent atoms i and j or i , j and k are of the same binary compound. If the atoms belong to different atomic species, e.g. i denotes an Indium atom and k is a Gallium atom, the α_{ij} and β_{ijk} parameters are taken as the arithmetic average of the parameters for the related compounds. The influence of different stiffness parametrizations in the VFF model onto the electronic states in the TB model is discussed in [65].

Different model potentials, such as the Tersoff potential [66] or the Stillinger-Weber potential [67], can be used to improve anharmonicity effects or to include not only nearest neighbours. Nevertheless we will use the Keating potential in this work because it captures the main aspects of lattice deformation caused by strain. The calculations of the equilibrium atomic positions due to strain relaxation are carried out throughout this thesis using the program package LAMMPS ("Large-scale Atomic/Molecular Massively Parallel Simulator", [68]). A typical relaxation procedure starts with all atoms at the bulk positions of the host material in the supercell. First, the global strain energy is calculated from Eqn. (2.47). Second, the residual forces acting on the atoms are calculated and the atoms are moved along their individual force vectors. These two steps are iterated using a Hessian-free truncated Newton algorithm [69–71] which is a more robust variant of the conjugate gradient method [72]. After convergence, the output consists of the relaxed atomic positions, which can be used to calculate the new distances and angles between the atoms. At this point it appears natural to formulate the TB Hamiltonian in the two-center approximation introduced earlier since it directly implies how to incorporate

the displacements from equilibrium positions and equilibrium bond angles into the tight-binding Hamiltonian. It is a common assumption that the influence of strain only has minor impact on the on-site energies, although there are some approaches to include these effects into TB calculations [73–75].

In the present model only the coupling parameters (off-diagonal matrix elements) are modified by strain in the following way:

$$V_{ss}(i, j) = V_{ss\sigma} \left(\frac{d_{ij}^0}{d_{ij}} \right)^\eta \quad (2.51)$$

$$V_{sp_x}(i, j) = d_x V_{pp\sigma} \left(\frac{d_{ij}^0}{d_{ij}} \right)^\eta \quad (2.52)$$

$$V_{p_x p_y}(i, j) = d_x d_y V_{pp\sigma} \left(\frac{d_{ij}^0}{d_{ij}} \right)^\eta - d_x d_y V_{pp\pi} \left(\frac{d_{ij}^0}{d_{ij}} \right)^\eta \quad (2.53)$$

and likewise for all other coupling matrix elements. Here, the factor $d_x = \frac{\mathbf{e}_x \cdot \mathbf{d}_{ij}}{d_{ij}}$ is the strain-affected directional cosine (compare Eqn. (2.26)) and therefore accounts for strain-induced bond-angle deformations, where \mathbf{d}_{ij} is the strain-altered distance vector between atoms i and j with $d_{ij} = |\mathbf{d}_{ij}|$.

The bond-length distortions are included as well in the second term $\left(\frac{d_{ij}^0}{d_{ij}} \right)^\eta$, where d_{ij}^0 is the equilibrium distance between atoms i and j . The physical idea behind this term is that the coupling strength between two atoms scales with the interatomic distance with a power η . So if the distance d_{ij} altered by strain equals the atomic distance in the unstrained lattice, the coupling matrix element is not changed because $\left(\frac{d_{ij}^0}{d_{ij}} \right)^\eta$ equals unity. If the distance is actually smaller/larger than in the unstrained lattice, the matrix element gets larger/smaller (for the very reasonable assumption $\eta > 0$). There are several proposals in the literature how to treat this additional parameter η of which the so-called d^{-2} -ansatz or Harrison-rule [76] is the most simple and common. It assumes a general scaling parameter of $\eta = 2$ for all coupling matrix elements. Other proposals assume either another value for η (3.4 as proposed in [40] or 2.9 in [77]) or an individual η according to the atomic orbitals participating in the coupling [78], i.e. $\eta_{pp\sigma}, \eta_{pp\pi}$ and so on. In the literature even more sophisticated proposals on scaling interatomic orbital interactions can be found. For example a special treatment was proposed for the s^*-p orbital interaction to include the correct behaviour of d -states under biaxial strain [78, 79]:

$$(s^* x \sigma) = (s^* p \sigma) \left(\frac{d_0}{d} \right)^\eta [(1 + 2F)|l| - F(|m| + |n|)] \frac{1}{|l|} \quad (2.54)$$

with $F = -0.63$ being a constant and l, m, n being the directional cosines. Other approaches include the calculation of the band-dependence on volume effects and fits to deformation potentials [46, 75, 80]. We will restrict our model to using the

modified Harrison-rule $\eta = 2.9$ from [77] for the coupling parameters and no strain-dependence of the on-site parameters due to simplicity and the small differences found by using the advanced models. The value of $\eta = 2.9$ gives better results for the single-particle properties than the original value of 2.0.

A comparison between the CE and VFF approaches can be found in [81] for InAs/GaAs superlattices or in [82] for InAs/GaAs QDs. It was found that in general both methods are applicable to calculate the strain distribution (CE grid points were chosen as cation positions of the ideal GaAs lattice). The methods gave good agreement in the buffer region but revealed differences in regions of the dot interfaces and inside the dot. In [82] these differences were attributed to the loss of the atomic symmetry in the CE and to violation of the linearity regime of CE due to the large strain arising through the QD geometry.

The reliability of the calculations carried out by the VFF method using the Keating potential in LAMMPS was investigated by Müller et al. [83] through comparison to ab-initio DFT calculations, which is possible for supercells containing only a small number of atoms. A good agreement in terms of the residual forces on the atoms after the relaxation procedure was found. Additionally, no differences in the atomic displacements from the two methods were larger than 2.6 pm, a length which is in the order of the thermal vibrations of the crystal.

2.2.6. Piezoelectricity

The III-V semiconductors GaAs and InAs are polar materials in the sense that the single constituents are charged (Ga^{3+} , As^{3-}) and therefore the bonds are ionic. If the atoms are in the unstrained bulk lattice positions there is no net charge distribution in the system. If strain comes into play and displaces the atoms into new positions that minimize the strain energy, the local charge distribution can be non-vanishing and gives rise to a polarization in certain directions. This interplay is called the piezoelectric effect and arises in pseudomorphically grown zinkblende semiconductors caused by shear strain. It was first discovered by the Curie brothers [84] in 1880. It turns out that for semiconductor quantum wells and superlattices grown along the [001] direction the shear strain can be neglected and therefore no piezoelectric polarization is expected [85]. Due to the reduction of point-group symmetry in strained QDs, piezoelectric effects in general are present and need to be considered in electronic calculations. Since in general piezoelectricity is much stronger in GaAs than in InAs in terms of the piezoelectric module e_{14} , the piezoelectric potential is considerably smaller inside the quantum dot than in the barrier [86] and only small corrections to energy levels and states are expected due to the piezoelectric effect. While at first only linear terms in strain were taken into account for the modelling of quantum wells [87] and QDs [28, 88–93], Bester [94] pointed out that the inclusion of the second order term is necessary since it is of the same order of magnitude as

the linear term but of opposite sign, although there was ongoing discussion [29, 95].

Even more Bester suggested that it is better to neglect the piezoelectric effect altogether than to include only linear terms. Following Bester's arguments, the piezoelectric effects are considerably small compared to intraband or confinement energies (confinement energies reach some hundred meV for large QDs; the magnitude of the piezoelectric effects is in the order of a few meV, [96]) and will be neglected in our model. Additionally the piezoelectric effect was shown to be small in zincblende crystals compared to wurtzite grown QDs [97].

For the sake of completeness we will outline how to account for the piezoelectric effect in a tight-binding calculation [98]. In this approach the piezoelectric electrostatic potential is included into the tight-binding Hamiltonian as an additional on-site potential V_{piezo} that locally shifts the orbital energies. The calculation of this potential includes four steps. First, the piezoelectric coefficients for the strained bulk materials have to be determined by measurement [99, 100] or by ab-initio calculations [94]. Together with the strain tensor ϵ , that can be deduced via the atomic displacements, in a second step the piezoelectric polarization P_{piezo} [101] along the i -th spatial coordinate can be calculated using

$$P_{piezo}^i = \sum_j e_{ij} \epsilon_j + \frac{1}{2} \sum_{jk} B_{ijk} \epsilon_j \epsilon_k + \dots \quad (2.55)$$

with e_{ij} and B_{ijk} being the linear and quadratic piezoelectric coefficients, respectively.

Having calculated the piezoelectric potential, in the third step the piezoelectric charge density ρ_{piezo} can be calculated following classical electrodynamics as the divergence of the polarization:

$$\rho_{piezo} = -\text{div} P_{piezo}. \quad (2.56)$$

In a last step, the local electrostatic potential φ_{piezo} can be calculated via

$$\rho_{piezo} = \epsilon_0 \nabla (\epsilon_r(r) \nabla \varphi_{piezo}) \quad (2.57)$$

$$\Delta \varphi_{piezo} = \frac{\rho_{piezo}}{\epsilon_0 \epsilon_r} - \frac{1}{\epsilon_r(r)} \nabla \varphi_{piezo}(r) \nabla \epsilon_r(r). \quad (2.58)$$

Here, $\epsilon_r(r)$ is the local dielectric constant at the position r , depending on the material occupying the corresponding lattice site. Having determined the electrostatic potential φ_{piezo} it can be included into the tight-binding Hamiltonian as an additional term

$$V_{piezo} = -e \varphi_{piezo}(r) \quad (2.59)$$

that is added to the on-site energies.

2.3. Modelling semiconductor nanostructures

In this section we will explain in detail how to adopt the TB model introduced in the last section for the simulation of electronic properties of semiconductor nanostructures. We explicitly write down the Hamiltonian for the calculation of band structures and show results for InAs and GaAs. The changes in the Hamiltonian for the consecutive loss of translational invariance when modelling quantum wells and quantum dots are discussed. Common quantum dot geometries are identified and the influence of various structural dot parameters is reviewed.

When it comes to semiconductor nanostructures such as quantum wells, wires or dots, several compound materials come together like GaAs and InAs for example. In some structures it is even three or more compounds grown on the same sample, for example InGaNaNs superlattices. For most of the on-site energies the inclusion of different materials is quite straightforward because every lattice site is directly represented by a certain sub-block of the tight-binding Hamiltonian. So in principle each diagonal sub-block holds the on-site bulk parameters of the compound assigned to the corresponding lattice site. In regions consisting only of atoms related to one compound material this works well. A problem arises for material combinations such as InAs in GaAs where the compound materials have common atom types (the Arsenic anions in this example). Then there is no way to tell whether a common atom belongs to one of the two compounds or the other at interfaces. There are several ways to deal with this problem, the most common being the virtual-crystal approximation (VCA, [102]) and the direct assignment of the atom type in doubt to one of the two materials. The VCA is mostly used in modelling alloy materials such as $A_xB_{1-x}C$ where $x \in [0, 1]$ is the concentration of A-atoms. It makes the assumption that the atomic potential $V(ABC)$ of the alloy can be described by a linear dependency on the concentration $V(AC)$ and $V(BC)$ of the constituents:

$$V(ABC) = xV(AC) + (1 - x)V(BC) \quad (2.60)$$

without considering any correlations and is an averaging over bulk properties of the single compounds. This idea can be directly carried forward to the tight-binding parameters. But since the VCA represents a non-local ansatz and we are dealing with a local tight-binding model it appears natural that the VCA should not be used here. So in our model for each atom it is decided which compound it is related to and based on this the corresponding bulk parameters are used for this atom. This ansatz somehow decides between anions related to GaAs and InAs material. This is certainly wrong for isolated atoms but seems to be a good treatment in compounds since the atomic orbital energies are influenced by the surrounding atoms. Additionally, in our way of treating strain it is necessary to assign a dedicated type of atom to every lattice site to calculate the strain energy which makes the VCA impossible to incorporate here. To treat alloys in our model we do what is called exact disorder [103] for the atomistic material definition: in a domain of

space where a certain alloy material shall be included, for example an $In_xGa_{1-x}As$ quantum dot with a certain shape, we call a random number generator for a random number r between 0 and 1 for each lattice site inside the domain. By comparison of the resulting random number to the target concentration $x \in [0, 1]$ we define each lattice site as related to the InAs ($r < x$) or GaAs ($r > x$) compound. With this approach we reach the target concentration only by the law of large numbers and therefore account for the statistical nature of the growth process, allowing for random clustering. Nevertheless, for the coupling parameters there is no known way of treating them besides via averaging. At couplings between atoms belonging to the same compound the compound bulk coupling parameters are used in the tight-binding Hamiltonian. Due to the lack of a better treatment, for couplings between atoms belonging to different compounds the coupling parameters enter averaged as

$$V_{pp\sigma}^{InAs-GaAs} = \frac{1}{2} (V_{pp\sigma}^{InAs} + V_{pp\sigma}^{GaAs}) \quad (2.61)$$

into the tight-binding Hamiltonian.

Having set up the tight-binding Hamiltonian for a nanostructure the Hamiltonian has to be diagonalized to obtain the bound electronic single-particle energies and states of the nanostructure. The numerical diagonalization of such a matrix (very large, sparse², self-adjoint, complex) in parallel is a very difficult task and the field of numerical algorithms is in vivid progress. A more accurate description of the programs for diagonalization used throughout this thesis for diagonalization is provided in section 2.5. In the following we will go from the simplest case of modeling (bulk band structure) to the most general case of a three-dimensionally shaped nanostructure in a large supercell.

2.3.1. Bulk band structures

Describing a bulk crystal with the tight-binding method is a simple task due to the translational invariance holding in all three dimensions of space. It is sufficient to describe only the atoms in one unit cell of the crystal as well as their couplings and to make use of Bloch's theorem for taking all other atoms into account. As shown before Schrödinger's equation of the periodic crystal is given by

$$H^{\text{BULK}} |\mathbf{k}\rangle = E(\mathbf{k}) |\mathbf{k}\rangle \quad (2.62)$$

with \mathbf{k} being the reciprocal lattice vector. For the solution of this eigenproblem in case of the bulk material the electronic wave functions are expressed as linear

²Sparse here means that the number of non-zero elements in the matrix is small compared to the number of matrix elements which are zero. The relation between those numbers is called the sparsity of the matrix and is in the order of approximately 10^{-7} for the quantum dot Hamiltonian.

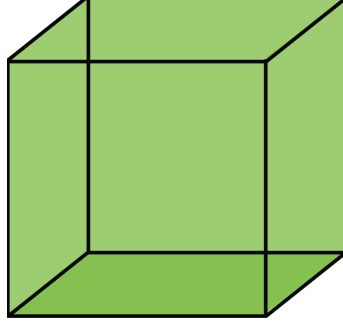


Figure 2.6.: Scheme of the empty supercell representing the bulk system, provided that periodic boundary conditions are applied.

combinations of the atomic orbitals:

$$|\mathbf{k}\rangle = \sqrt{\frac{V_{uc}}{V}} \sum_n \sum_{\alpha\nu\sigma} e^{i\mathbf{k}\mathbf{R}_n} u_{\alpha\nu\sigma}(\mathbf{k}) |\mathbf{R}_n\alpha\nu\sigma\rangle, \quad (2.63)$$

where $u_{\alpha\nu\sigma}$ are the Bloch factors. In difference to the case of a nanostructure without any translational symmetry, the influence of the symmetry here is incorporated through the Bloch sums. As before, $\frac{V_{uc}}{V}$ is the ratio in volume of one unit cell to the whole crystal volume, α is the atom type, ν the atomic orbital and σ denotes the spin. \mathbf{R}_n describes the position of the unit cell. It is assumed here that the $|\mathbf{R}_n\alpha\nu\sigma\rangle$ are Löwdin-orthogonalized basis states. Applying $\langle\mathbf{k}'|$ from the left to both sides of Eqn. (2.62) results in an eigenproblem. The left hand side reads:

$$\begin{aligned} \langle\mathbf{k}'| H^{\text{BULK}} |\mathbf{k}\rangle &= \frac{V_{uc}}{V} \sum_{n,m} \sum_{\alpha\nu\sigma,\alpha'\nu'\sigma'} e^{i\mathbf{k}(\mathbf{R}_n-\mathbf{R}_m)} u_{\alpha\nu\sigma} u_{\alpha'\nu'\sigma'} \langle\mathbf{R}_m\alpha'\nu'\sigma'| H^{\text{BULK}} |\mathbf{R}_n\alpha\nu\sigma\rangle \\ &= \frac{V_{uc}}{V} \sum_{\alpha\nu\sigma,\alpha'\nu'\sigma'} \left[\sum_{n,m} e^{i\mathbf{k}(\mathbf{R}_n-\mathbf{R}_m)} \langle\mathbf{R}_m\alpha'\nu'\sigma'| H^{\text{BULK}} |\mathbf{R}_n\alpha\nu\sigma\rangle \right] u_{\alpha\nu\sigma} u_{\alpha'\nu'\sigma'} \\ &= \frac{V_{uc}}{V} \sum_{\alpha\nu\sigma,\alpha'\nu'\sigma'} \left[N \sum_j e^{i\mathbf{k}\mathbf{R}_j} \langle\mathbf{0}\alpha'\nu'\sigma'| H^{\text{BULK}} |\mathbf{R}_j\alpha\nu\sigma\rangle \right] u_{\alpha\nu\sigma} u_{\alpha'\nu'\sigma'} \\ &= \sum_{\alpha\nu\sigma,\alpha'\nu'\sigma'} \left[H_{\alpha\nu\sigma,\alpha'\nu'\sigma'}^{\text{BULK}} \right] u_{\alpha\nu\sigma} u_{\alpha'\nu'\sigma'}. \end{aligned} \quad (2.64)$$

In the second to last step, one inner sum was carried out with shifting \mathbf{R}_m into the origin, giving $N = \frac{V}{V_{uc}}$ times the same sum over all vectors, and the relative vector

$\mathbf{R}_n - \mathbf{R}_m$ was relabelled \mathbf{R}_j . The right hand side is given by:

$$\begin{aligned}
\langle \mathbf{k}' | E(\mathbf{k}) | \mathbf{k} \rangle &= \frac{V_{uc}}{V} \sum_{n,m} \sum_{\alpha\nu\sigma, \alpha'\nu'\sigma'} e^{i\mathbf{k}(\mathbf{R}_n - \mathbf{R}_m)} u_{\alpha\nu\sigma} u_{\alpha'\nu'\sigma'} \langle \mathbf{R}_m \alpha' \nu' \sigma' | E(\mathbf{k}) | \mathbf{R}_n \alpha \nu \sigma \rangle \\
&= E(\mathbf{k}) \frac{V_{uc}}{V} \sum_{\alpha\nu\sigma, \alpha'\nu'\sigma'} \left[\sum_{n,m} e^{i\mathbf{k}(\mathbf{R}_n - \mathbf{R}_m)} \langle \mathbf{R}_m \alpha' \nu' \sigma' | \mathbf{R}_n \alpha \nu \sigma \rangle \right] u_{\alpha\nu\sigma} u_{\alpha'\nu'\sigma'} \\
&= E(\mathbf{k}) \sum_{\alpha\nu\sigma, \alpha'\nu'\sigma'} \left[\sum_j e^{i\mathbf{k}\mathbf{R}_j} \langle \mathbf{0} \alpha' \nu' \sigma' | \mathbf{R}_j \alpha \nu \sigma \rangle \right] u_{\alpha\nu\sigma} u_{\alpha'\nu'\sigma'}.
\end{aligned} \tag{2.65}$$

As before, one inner sum was carried out, resulting in the same simplifications. In general, the wave functions are not orthogonal, as pointed out before. Assuming Löwdin-orthogonalized basis functions, the overlap integrals become

$$\langle \mathbf{0} \alpha' \nu' \sigma' | \mathbf{R}_j \alpha \nu \sigma \rangle = \delta_{\mathbf{R}_j, \mathbf{0}} \delta_{\alpha, \alpha'} \delta_{\nu, \nu'} \delta_{\sigma, \sigma'}. \tag{2.66}$$

Now the right hand side is

$$\langle \mathbf{k}' | E(\mathbf{k}) | \mathbf{k} \rangle = E(\mathbf{k}) \sum_{\alpha\nu\sigma} u_{\alpha\nu\sigma} u_{\alpha\nu\sigma} \tag{2.67}$$

by carrying out the sum over the primed indices. Combination of both equations yields

$$\sum_{\alpha\nu\sigma} \sum_{\alpha'\nu'\sigma'} H_{\alpha\nu\sigma, \alpha'\nu'\sigma'}^{\text{BULK}} u_{\alpha\nu\sigma} u_{\alpha'\nu'\sigma'} = E(\mathbf{k}) \sum_{\alpha\nu\sigma} u_{\alpha\nu\sigma} u_{\alpha\nu\sigma} \tag{2.68}$$

and, accordingly,

$$\boxed{\sum_{\alpha'\nu'\sigma'} H_{\alpha\nu\sigma, \alpha'\nu'\sigma'}^{\text{BULK}} u_{\alpha'\nu'\sigma'} = E(\mathbf{k}) u_{\alpha\nu\sigma}.} \tag{2.69}$$

This is the energy band equation to be solved by diagonalization. The band structure is given by the eigenvalues of the matrix with elements

$$H_{\alpha\nu\sigma, \alpha'\nu'\sigma'}^{\text{BULK}} = \sum_j e^{i\mathbf{k}\mathbf{R}_j} \langle \mathbf{0} \alpha' \nu' \sigma' | H^{\text{BULK}} | \mathbf{R}_j \alpha \nu \sigma \rangle \tag{2.70}$$

for each reciprocal vector \mathbf{k} . Depending on the required degree of accuracy the sum over j covers the nearest neighbours, second-nearest neighbours or even more distant neighbours for each atom. Due to the spacial decay of the wave functions, the contributions from nearest neighbours are more important than the contributions from second-nearest neighbours due to a reduced wave function overlap with increasing distance of the atoms. In many cases, even by choosing only nearest neighbours to be taken into account, good approximations of the band structure can be obtained. In empirical tight-binding theory, the integrals

$$\langle \mathbf{0} \alpha' \nu' \sigma' | H^{\text{BULK}} | \mathbf{R}_j \alpha \nu \sigma \rangle \tag{2.71}$$

are taken as fitting parameters to adjust the calculated band structure to experimentally measured properties of the crystal like band gaps at high symmetry points and the curvature of the bands (effective masses). Following the notation of [39], those integrals are abbreviated by either

$$\langle \mathbf{0} \alpha \nu \sigma | H^{\text{BULK}} | \mathbf{R}_j \alpha \nu \sigma \rangle = E_{\alpha \nu \sigma}(klm) \quad (2.72)$$

for integrals at the same atom, giving the orbital energies or

$$\langle \mathbf{0} \alpha' \nu' \sigma' | H^{\text{BULK}} | \mathbf{R}_j \alpha \nu \sigma \rangle = V_{\alpha' \nu' \sigma', \alpha \nu \sigma}(klm) \quad (2.73)$$

if $\alpha' \neq \alpha$, representing the hopping elements between orbitals located at different atoms. The use of the indices (klm) was introduced in [49] and represents the projection of the relative vector between the two atoms onto the cartesian grid:

$$\mathbf{R} = \frac{ka}{4} \mathbf{e}_x + \frac{la}{4} \mathbf{e}_y + \frac{ma}{4} \mathbf{e}_z \quad (2.74)$$

with a being the lattice constant of the semiconductor. For example the hopping integral for the hopping of an electron in an s -like orbital located at a cation at the origin with spin up into a p -like orbital at an anion located at the position $(111)a/4$ with spin up reads

$$\langle \frac{a}{4}(111)pA \uparrow | H^{\text{BULK}} | \mathbf{0}sC \uparrow \rangle = V_{sC,pA}(111). \quad (2.75)$$

The spin index can be dropped here, because no spin-flip processes are mediated through of H^{BULK} in the tight-binding formalism.

Zincblende structure

The two semiconductor material systems most often used for optical applications, InAs and GaAs, crystallize in the zincblende lattice, which is shown in Fig. 2.7. Each atom of one type has a tetrahedral coordination of four atoms belonging to the other atom type. Therefore, nearest neighbours (NN) always are of the respective other atom type, next nearest neighbours are of the same atom type. The nearest-neighbour vectors for an atom in the origin with a being the lattice constant are

$$\mathbf{R}_1 = \frac{a}{4} \begin{pmatrix} 1 \\ 1 \\ 1 \end{pmatrix} \quad \mathbf{R}_2 = \frac{a}{4} \begin{pmatrix} -1 \\ -1 \\ 1 \end{pmatrix} \quad \mathbf{R}_3 = \frac{a}{4} \begin{pmatrix} 1 \\ -1 \\ -1 \end{pmatrix} \quad \mathbf{R}_4 = \frac{a}{4} \begin{pmatrix} -1 \\ 1 \\ -1 \end{pmatrix}. \quad (2.76)$$

Depending on the actual position of the atom, the NN vectors may be rotated by $\pi/2$.

In Tab. 2.2 the characteristic points of high symmetry inside the first Brillouin zone of the reciprocal lattice are given for a zincblende crystal as depicted in Fig. 2.8.

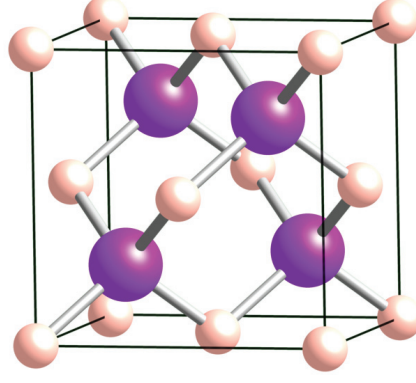


Figure 2.7.: Sketch of the zincblende lattice structure, which is the superposition of two face-centered lattices for anions and cations. Large spheres indicate cations, small spheres the anions. Picture taken from <http://nanophysics.pbworks.com/>.

L	Γ	X	U	K
$\frac{\pi}{a} \begin{pmatrix} 1 \\ 1 \\ 1 \end{pmatrix}$	$\begin{pmatrix} 0 \\ 0 \\ 0 \end{pmatrix}$	$\frac{2\pi}{a} \begin{pmatrix} 0 \\ 1 \\ 0 \end{pmatrix}$	$\frac{2\pi}{a} \begin{pmatrix} \frac{1}{4} \\ 1 \\ \frac{1}{4} \end{pmatrix}$	$\frac{3\pi}{2a} \begin{pmatrix} 1 \\ 1 \\ 0 \end{pmatrix}$

Table 2.2.: Points of high symmetry in the Brillouin zone of the zincblende lattice structure. a is the lattice constant and reciprocal vectors read (k_x, k_y, k_z) .

The sp^3s^* basis

A widely-used model to calculate semiconductor band structures is given by the famous nearest-neighbour sp^3s^* model proposed by Vogl et al. in 1983 [39]. At every atom site one s -like and three p -like orbitals are localized as well as an additional s^* -like orbital. This additional orbital simulates the influence of the energetically higher-lying d -like orbitals and therefore this model provides a better description of the energy bands of the crystal than other models such as $s_C p_A^3$ or sp^3 [44]. Technically, the s^* -like orbital provides more fitting parameters, which results in better band structure fit at valleys far away the Γ -point. Also, taking more distant neighbours into account could provide this additional degree of freedom. Nevertheless, we will employ the popular original nearest-neighbour sp^3s^* model. Without the inclusion of spin-orbit coupling, the Hamiltonian to diagonalize has the dimensions 10×10 and can be formulated best in the Löwdin-orthogonalized basis

$$\begin{aligned} &|sA\rangle, |sC\rangle, |p_xA\rangle, |p_yA\rangle, |p_zA\rangle, \\ &|p_xC\rangle, |p_yC\rangle, |p_zC\rangle, |s^*A\rangle, |s^*C\rangle. \end{aligned}$$

The Hamiltonian reads [39]:

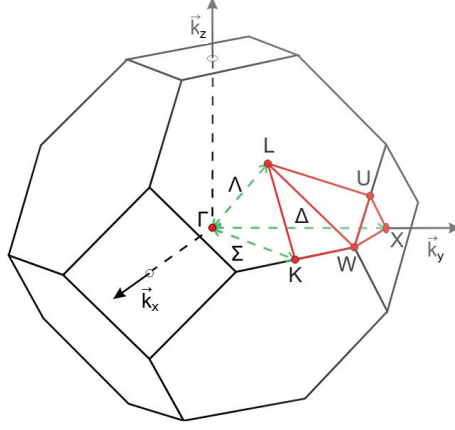


Figure 2.8.: Brillouin zone and high-symmetry points of the zincblende lattice. Image from IPV Stuttgart (<http://www.ipv.uni-stuttgart.de/lehre/-vorlesungen/festkoerperelektronik.html>).

$$H = \begin{pmatrix}
 E_{sA} & V_{ss}g_0 & 0 & 0 & 0 \\
 V_{ss}g_0^* & E_{sC} & -V_{pAsC}g_1^* & -V_{pAsC}g_2^* & -V_{pAsC}g_3^* \\
 0 & -V_{pScA}g_1 & E_{pA} & 0 & 0 \\
 0 & -V_{pScA}g_2 & 0 & E_{pA} & 0 \\
 0 & -V_{pScA}g_3 & 0 & 0 & E_{pA} \\
 V_{sApC}g_1^* & 0 & V_{xx}g_0^* & V_{xy}g_3^* & V_{xy}g_2^* \\
 V_{sApC}g_2^* & 0 & V_{xy}g_3^* & V_{xx}g_0^* & V_{xy}g_1^* \\
 V_{sApC}g_3^* & 0 & V_{xy}g_2^* & V_{xy}g_1^* & V_{xx}g_0^* \\
 0 & 0 & 0 & 0 & 0 \\
 0 & 0 & -V_{pAs^*C}g_1^* & -V_{pAs^*C}g_2^* & -V_{pAs^*C}g_3^*
 \end{pmatrix}$$

$$\begin{pmatrix}
 V_{sApC}g_1 & V_{sApC}g_2 & V_{sApC}g_3 & 0 & 0 \\
 0 & 0 & 0 & 0 & 0 \\
 V_{xx}g_0 & V_{xy}g_3 & V_{xy}g_2 & 0 & -V_{pAs^*C}g_1 \\
 V_{xy}g_3 & V_{xx}g_0 & V_{xy}g_1 & 0 & -V_{pAs^*C}g_2 \\
 V_{xy}g_2 & V_{xy}g_1 & V_{xx}g_0 & 0 & -V_{pAs^*C}g_3 \\
 E_{pC} & 0 & 0 & V_{s^*ApC}g_1^* & 0 \\
 0 & E_{pC} & 0 & V_{s^*ApC}g_2^* & 0 \\
 0 & 0 & E_{pC} & V_{s^*ApC}g_3^* & 0 \\
 V_{s^*ApC}g_1 & V_{s^*ApC}g_2 & V_{s^*ApC}g_3 & E_{s^*A} & V_{s^*s^*}g_0 \\
 0 & 0 & 0 & V_{s^*s^*}g_0^* & E_{s^*C}
 \end{pmatrix} \quad (2.77)$$

in the corrected version of Boykin [104], where minor typographical errors were corrected. The crystal structure is introduced via the Bloch-sums (structure factors) as follows:

$$g_0(\mathbf{k}) = \cos\left(\frac{k_x a}{4}\right) \cos\left(\frac{k_y a}{4}\right) \cos\left(\frac{k_z a}{4}\right) - i \sin\left(\frac{k_x a}{4}\right) \sin\left(\frac{k_y a}{4}\right) \sin\left(\frac{k_z a}{4}\right) \quad (2.78)$$

$$g_1(\mathbf{k}) = -\cos\left(\frac{k_x a}{4}\right) \sin\left(\frac{k_y a}{4}\right) \sin\left(\frac{k_z a}{4}\right) + i \sin\left(\frac{k_x a}{4}\right) \cos\left(\frac{k_y a}{4}\right) \cos\left(\frac{k_z a}{4}\right) \quad (2.79)$$

$$g_2(\mathbf{k}) = -\sin\left(\frac{k_x a}{4}\right) \cos\left(\frac{k_y a}{4}\right) \sin\left(\frac{k_z a}{4}\right) + i \cos\left(\frac{k_x a}{4}\right) \sin\left(\frac{k_y a}{4}\right) \cos\left(\frac{k_z a}{4}\right) \quad (2.80)$$

$$g_3(\mathbf{k}) = -\sin\left(\frac{k_x a}{4}\right) \sin\left(\frac{k_y a}{4}\right) \cos\left(\frac{k_z a}{4}\right) + i \cos\left(\frac{k_x a}{4}\right) \cos\left(\frac{k_y a}{4}\right) \sin\left(\frac{k_z a}{4}\right) \quad (2.81)$$

with a being the lattice constant and $\mathbf{k} = (k_x, k_y, k_z)$ being the reciprocal lattice vector.

The diagonal matrix elements are defined as

$$E_{s\alpha} = \langle \mathbf{R}s\alpha | H | \mathbf{R}s\alpha \rangle \quad (2.82)$$

$$E_{p\alpha} = \langle \mathbf{R}p\alpha | H | \mathbf{R}p\alpha \rangle \quad (2.83)$$

$$E_{s^*\alpha} = \langle \mathbf{R}s^*\alpha | H | \mathbf{R}s^*\alpha \rangle \quad (2.84)$$

with $\alpha = (A, C)$ and can be understood as the orbital energies. The off-diagonal matrix elements are given by

$$V_{ss} = 4 \langle \mathbf{R}s\alpha | H | \mathbf{0}s\alpha \rangle \quad (2.85)$$

$$V_{xx} = 4 \langle \mathbf{R}p_x\alpha | H | \mathbf{0}p_x\alpha \rangle \quad (2.86)$$

$$V_{xy} = 4 \langle \mathbf{R}p_x\alpha | H | \mathbf{0}p_y\alpha \rangle \quad (2.87)$$

$$V_{sApC} = 4 \langle \mathbf{R}sA | H | \mathbf{0}p_xC \rangle \quad (2.88)$$

$$V_{pAsC} = 4 \langle \mathbf{R}p_xA | H | \mathbf{0}sC \rangle \quad (2.89)$$

$$V_{s^*ApC} = 4 \langle \mathbf{R}s^*A | H | \mathbf{0}p_xC \rangle \quad (2.90)$$

$$V_{pAs^*C} = 4 \langle \mathbf{R}p_xA | H | \mathbf{0}s^*C \rangle \quad (2.91)$$

$$V_{s^*s^*} = 4 \langle \mathbf{R}s\alpha | H | \mathbf{0}s^*\alpha \rangle, \quad (2.92)$$

where the prefactor of 4 reflects the tetragonal coordination of atoms in a zincblende lattice.

From the Hamiltonian (2.77), already some properties can be identified as introduced in section 2.2.2: The Hamiltonian is hermitian, i.e., the lower triangular matrix is the complex conjugate of the upper triangular matrix³. The orbital energies appear at the main diagonal, while hopping matrix elements appear off-diagonal. The model assumptions of no hoppings between s (s^*)- and p -like orbitals at the same atom to be taken into account are visible. Moreover, no hoppings between p -like orbitals at the same atom are assumed. Because of the symmetries of the p -like orbitals, all interactions between p -like orbitals can be traced back to only

³This is of particular interest when setting up the Hamiltonian matrix numerically.

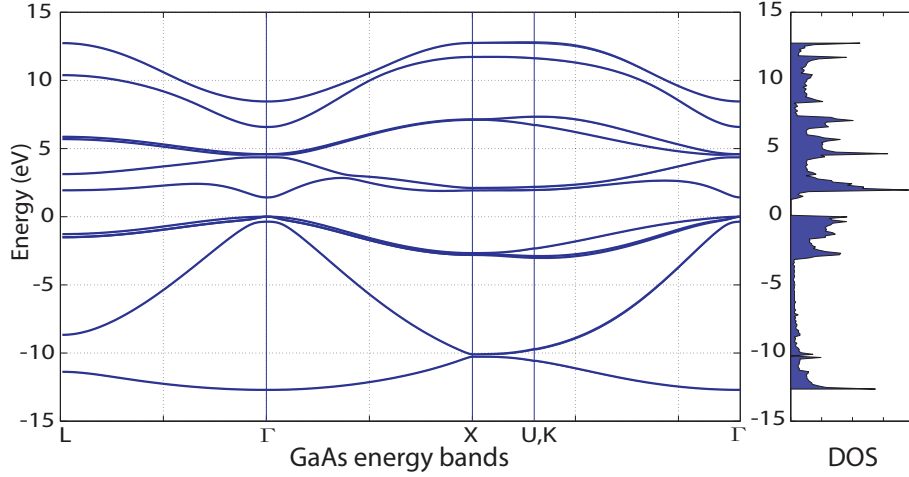


Figure 2.9.: The left-hand figure shows the bulk band structure in the sp^3s^* TB model for GaAs. Right-hand figures show the corresponding DOS.

two situations, p_x - p_x (V_{xx}) and p_x - p_y (V_{xy}). Also, the rule for the sum of orbital parities can be observed to be present at the Hamiltonian.

In the form of Eqn. (2.77), this Hamiltonian does not include spin-orbit coupling yet. It can be included as shown in section 2.2.4, with the mentioned increase of basis size. For a formulation of the NN sp^3s^* -Hamiltonian in the basis of angular momentum including spin-orbit coupling, see [105]. Additionally, for a three-dimensional supercell formulation including strain, the Hamiltonian will be formulated in the two-center approximation as introduced in section 2.2.3.

For zincblende structures several tight-binding parameter sets can be found in the literature, for example [39, 104, 106, 107] for GaAs with and without inclusion of spin-orbit coupling and [39, 106–108] for InAs and InAs including spin-orbit coupling, even though there are many more parametrizations available in the literature. A well-written overview of models and parameter sets can be found in the topical review of Di Carlo [48]. There are even larger models like $sp^3d^5s^*$ [46] discussed in the literature, but of course these models have an increased basis size (40x40) because the Hamiltonian dimensions directly depend on the number of basis states. The nearest-neighbour sp^3s^* model seems to be a good compromise between memory requirements throughout the diagonalization procedure and accuracy in the reproduction of the band structure. Also, the number of neighbours to be taken into account is of importance for accuracy. In [109] a comparison of the sp^3s^* nearest-neighbour and next-nearest-neighbour models was carried out with the result holding only slight differences in the binding energies of electrons and holes in superlattices. Therefore, we restrict our tight-binding model to the nearest neighbours. In Figs. 2.9 and 2.10 the calculated band structures using the sp^3s^* nearest neighbour tight-binding model are shown for InAs and GaAs over \mathbf{k} -vectors con-

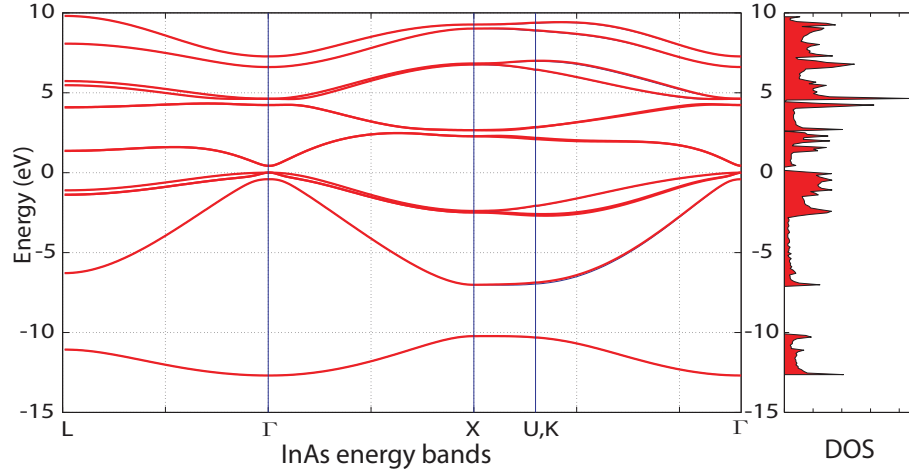


Figure 2.10.: The left-hand figure shows the bulk band structure in the sp^3s^* model for InAs.

necting points of high symmetry in the Brillouin zone (see Tab. 2.2). Additionally, the calculated density of states (DOS) is shown as calculated as a sum over the number of states in a finite energy interval in the corresponding band structure. In the band structures, parabolic dispersions around the center of the Brillouin zone, the Γ -point, can be seen, altered by corrections in the vicinity of Γ . The characteristic band gaps are reproduced, being 1.51 eV for GaAs and 0.42 eV for InAs at the Γ -point. The parametrizations used throughout this thesis can be found in the appendix.

2.3.2. Quantum wells

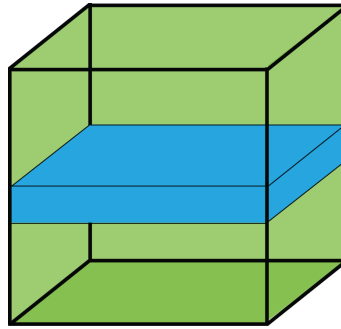


Figure 2.11.: Scheme of the supercell representing a quantum well. Periodic boundary conditions have to be applied in all spatial directions, taking care of a minimal distance of layers in growth direction.

Quantum wells (QWs) are examples for nanostructures with a huge variety of applications in optoelectronics. They consist of one or more atomic layers of a semi-

conductor material inside another semiconductor host material, for example InAs layers embedded in GaAs. Quantum wells are used as active laser material, switches, photodetectors and several other applications in modern telecommunication and electronic devices. Because of the layer structure, the translational symmetry is lifted in growth direction (typically the [001]-direction in zincblende semiconductors) but still remains in the other two directions. In terms of our tight-binding model this means compared to the bulk case the Bloch-sums run only over these two directions [110]. The structure in growth direction is represented in the Hamiltonian in which every layer is represented by a sub-block similar to the bulk matrix. The matrix elements are given by:

$$H_{m\nu'\alpha',n\nu\alpha}^{\text{QW}} = \sum_{\mathbf{R}_\perp} e^{i\mathbf{k}^\perp \cdot \mathbf{R}_\perp} \langle \mathbf{R}_m^\parallel \nu' \alpha' | H | \mathbf{R}_n^\parallel + \mathbf{R}_\perp \nu \alpha \rangle. \quad (2.93)$$

Here \mathbf{R}_m^\parallel and \mathbf{R}_n^\parallel represent the z-positions of the atomic layers, \mathbf{R}_\perp are the x- and y-components for nearest neighbours and $\mathbf{k}^\perp = (k_x, k_y, 0)$. The Hamiltonian then includes the layer-wise resolution and covers the anion-cation structure:

$$\left(\begin{array}{c|ccccc} & A & C & A & C & A \\ & n=0 & n=1 & n=2 & n=3 & n=4 \\ \hline A \ m=0 & \boxed{AA} & \boxed{AC \uparrow} & & & \\ C \ m=1 & \boxed{CA \downarrow} & \boxed{CC} & \boxed{CA \uparrow} & & \\ A \ m=2 & & \boxed{AC \downarrow} & \boxed{AA} & \boxed{AC \uparrow} & \\ C \ m=3 & & & \boxed{CA \downarrow} & \boxed{CC} & \boxed{CA \uparrow} \\ & & & & & \ddots \end{array} \right). \quad (2.94)$$

Here the blocks $\boxed{\alpha\alpha}$ with $m = n$ and $\alpha \in \{A, C\}$ describe the on-site energies (and the couplings inside a layer if second next nearest neighbours are considered), $\boxed{\alpha\alpha' \uparrow}$ with $n - m = 1$ describes the inter-layer coupling with the next higher layer and $\boxed{\alpha\alpha' \downarrow}$ describes the coupling with the next lower layer. It should be clear in this context, that \downarrow and \uparrow do indicate couplings and are not related to spin degrees of freedom. The single sub-blocks still include the structure factors and the tight-binding parameters, in a NN sp^3s^* model they have dimensions of 5x5 with 13 independent empirical parameters. The relations between matrix elements and parameters are given by:

$$E_{sA} = \langle \mathbf{R}_m^\parallel sA | H | \mathbf{R}_m^\parallel + \mathbf{R}_\perp sA \rangle \quad (2.95)$$

$$V_{sApC} = 4 \langle \mathbf{R}_m^\parallel sA | H | \mathbf{R}_m^\parallel + \mathbf{R}_\perp pC \rangle \quad (2.96)$$

and likewise for all other elements [39]. As shown earlier, the directional cosines as given in Eqn. (2.27) and following equations weight the coupling parameters. This weighting stems from the decomposition of the orbitals into components of σ and π -bonds in the two-center approximation. To trace back the matrix elements to

common parameters, their order has to be changed for certain elements. With that an additional sign enters the matrix elements according to the parity of the according atomic orbitals. s -, and s^* -like orbitals have even parity, p -like orbitals have odd parity. If the sum of the parity of the orbitals is even, changing the order of the orbitals does not change the sign of the matrix element. If the sum of the parity of the orbitals is odd, which is the case for couplings between s - and p -like orbitals for example, changing the order of orbitals does change the sign of the matrix element:

$$\langle \nu | H | \nu' \rangle = \begin{cases} + \langle \nu' | H | \nu \rangle & \text{even parity sum of orbitals} \\ - \langle \nu' | H | \nu \rangle & \text{odd parity sum of orbitals.} \end{cases} \quad (2.97)$$

In the sp^3s^* -basis neglecting spin ($|\alpha, s\rangle, |\alpha, p_x\rangle, |\alpha, p_y\rangle, |\alpha, p_z\rangle, |\alpha, s^*\rangle$) the sub-matrices read:

$$\boxed{AC \uparrow} = AC_{param} \cdot \begin{pmatrix} s_1 & s_2 & s_2 & s_1 & 0 \\ -s_2 & s_1 & s_1 & s_2 & -s_2 \\ -s_2 & s_1 & s_1 & s_2 & -s_2 \\ -s_1 & s_2 & s_2 & s_1 & -s_1 \\ 0 & s_2 & s_2 & s_1 & 0 \end{pmatrix} \quad (2.98)$$

$$\boxed{CA \downarrow} = AC'_{param} \cdot \begin{pmatrix} s_1 & s_2 & s_2 & -s_1 & 0 \\ -s_2 & s_1 & s_1 & -s_2 & -s_2 \\ -s_2 & s_1 & s_1 & -s_2 & -s_2 \\ s_1 & -s_2 & -s_2 & s_1 & s_1 \\ 0 & s_2 & s_2 & -s_1 & 0 \end{pmatrix} \quad (2.99)$$

$$\boxed{AC \downarrow} = AC_{param} \cdot \begin{pmatrix} s_3 & s_4 & -s_4 & -s_3 & 0 \\ -s_4 & s_3 & -s_3 & -s_4 & -s_4 \\ s_4 & -s_3 & s_3 & s_4 & s_4 \\ s_3 & -s_4 & s_4 & s_3 & s_3 \\ 0 & s_4 & -s_4 & -s_3 & 0 \end{pmatrix} \quad (2.100)$$

$$\boxed{CA \uparrow} = AC'_{param} \cdot \begin{pmatrix} s_3 & s_4 & -s_4 & s_3 & 0 \\ -s_4 & s_3 & -s_3 & s_4 & -s_4 \\ s_4 & -s_3 & s_3 & -s_4 & s_4 \\ -s_3 & s_4 & -s_4 & s_3 & -s_3 \\ 0 & s_4 & -s_4 & s_3 & 0 \end{pmatrix} \quad (2.101)$$

with the abbreviations

$$s_1 = e^{i\mathbf{k}^\perp \mathbf{R}_1^\perp} + e^{i\mathbf{k}^\perp \mathbf{R}_2^\perp} \quad (2.102)$$

$$s_2 = e^{i\mathbf{k}^\perp \mathbf{R}_1^\perp} - e^{i\mathbf{k}^\perp \mathbf{R}_2^\perp} \quad (2.103)$$

$$s_3 = e^{i\mathbf{k}^\perp \mathbf{R}_3^\perp} + e^{i\mathbf{k}^\perp \mathbf{R}_4^\perp} \quad (2.104)$$

$$s_4 = e^{i\mathbf{k}^\perp \mathbf{R}_3^\perp} - e^{i\mathbf{k}^\perp \mathbf{R}_4^\perp} \quad (2.105)$$

and

$$AC_{param} = \frac{1}{4} \begin{pmatrix} V_{ss} & V_{sApC} & V_{sApC} & V_{sApC} & 0 \\ V_{pAsC} & V_{xx} & V_{xy} & V_{xy} & V_{pAs^*C} \\ V_{pAsC} & V_{xy} & V_{xx} & V_{xy} & V_{pAs^*C} \\ V_{pAsC} & V_{xy} & V_{xy} & V_{xx} & V_{pAs^*C} \\ 0 & V_{s^*ApC} & V_{s^*ApC} & V_{s^*ApC} & 0 \end{pmatrix} \quad (2.106)$$

to be multiplied elementwise. Here, \mathbf{R}_1 to \mathbf{R}_4 are the NN locations and the zeros express the assumption, that no couplings between s^* - and s -like-orbitals appear in the model of [39].

Under inclusion of periodic boundary conditions this Hamiltonian still describes the bulk material. To use periodic boundary conditions means periodicity at the surfaces up to a phase factor given by $e^{ik_z Na/4} = 1$, $N \in \mathbb{N}$ being the number of layers. Therefore the band structure consists of many sub-bands each with $k_z = Na\pi/4$ as shown in Fig. 2.12.

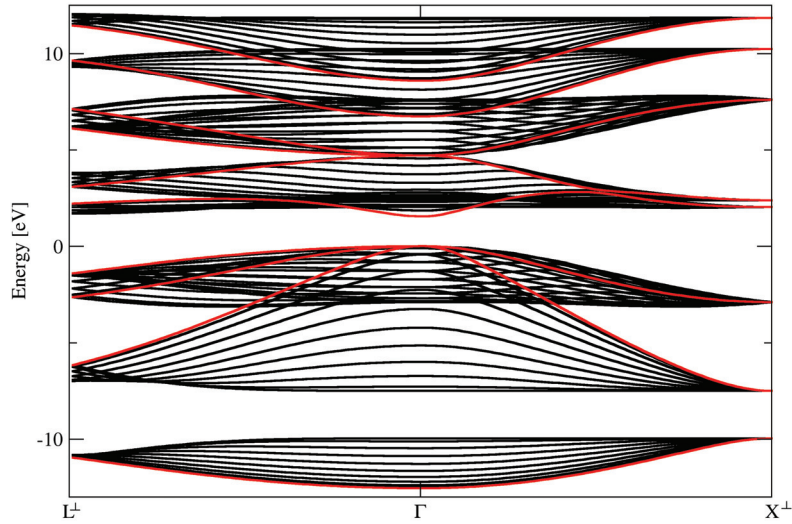


Figure 2.12.: Sub-bands for GaAs bulk material from the diagonalization of the QW Hamiltonian for $N = 11$ layers. Colored in red are the bulk bands as calculated in the previous chapter. Deviations from the bulk bands stem from the different paths through the Brillouin-zone as indicated by L^\perp and X^\perp .

The consideration of spin-orbit coupling into the Hamiltonian follows exactly the same steps as in the bulk case and therefore it doubles the Hamiltonian matrix size.

Since it is assumed that only p -orbitals at the same atom are coupled via spin-orbit interaction, the off-diagonal parts of the Hamiltonian stay the same, just accounting for the bigger basis size:

$$\boxed{AC \uparrow}^{so} = \begin{pmatrix} \boxed{AC \uparrow} & 0 \\ 0 & \boxed{AC \uparrow} \end{pmatrix} \quad (2.107)$$

The diagonal blocks become

$$\boxed{\alpha\alpha} = \begin{pmatrix} \boxed{\alpha\alpha} & 0 \\ 0 & \boxed{\alpha\alpha} \end{pmatrix} + \boxed{SO}_\alpha \quad (2.108)$$

with

$$\boxed{SO}_\alpha = \lambda_\alpha \cdot \begin{pmatrix} 0 & 0 & 0 & 0 & 0 & 0 & 0 & 0 & 0 & 0 \\ 0 & 0 & -i & 0 & 0 & 0 & 0 & 0 & 1 & 0 \\ 0 & i & 0 & 0 & 0 & 0 & 0 & 0 & -i & 0 \\ 0 & 0 & 0 & 0 & 0 & 0 & -1 & i & 0 & 0 \\ 0 & 0 & 0 & 0 & 0 & 0 & 0 & 0 & 0 & 0 \\ 0 & 0 & 0 & 0 & 0 & 0 & 0 & 0 & 0 & 0 \\ 0 & 0 & 0 & -1 & 0 & 0 & 0 & i & 0 & 0 \\ 0 & 0 & 0 & -i & 0 & 0 & -i & 0 & 0 & 0 \\ 0 & 1 & i & 0 & 0 & 0 & 0 & 0 & 0 & 0 \\ 0 & 0 & 0 & 0 & 0 & 0 & 0 & 0 & 0 & 0 \end{pmatrix}. \quad (2.109)$$

The parameter λ_α is defined by Eqn. (2.43).

Until this point it is just another and more complicated description of the bulk band structure; there is no quantum well included. The quantum well (let's assume an InAs well in GaAs host material) is simulated by using the tight-binding InAs bulk parameters at the diagonal and off-diagonal Hamiltonian sub-blocks corresponding to the layers that form the quantum well and their couplings, respectively. Depending on which atom types form the surfaces between the two materials, the parameters are averaged as given by Eqn. (2.61). See [111] for a discussion of different shapes and symmetries. In the case of InAs/GaAs quantum wells the two materials have common anions (the arsenic atoms). This situation is implemented by averaging the on-site parameters at the arsenic layers at the boundaries between the quantum well and the host material. Couplings between this arsenic layer and the surrounding layers hold InAs-related coupling parameters at the InAs-related sites and GaAs-related coupling parameters at the GaAs-related sites. In this special system no averaging of off-diagonal parameters is necessary. The part of the

Hamiltonian describing the quantum well reads as follows:

$$H^{QW} = \begin{pmatrix} \boxed{AA} & \boxed{AC \uparrow} & & & & & \\ \boxed{CA \downarrow} & \boxed{CC} & \boxed{CA \uparrow} & & & & \\ & \boxed{AC \downarrow} & \boxed{AA} & \boxed{AC \uparrow} & & & \\ & & \boxed{CA \downarrow} & \boxed{CC} & \boxed{CA \uparrow} & & \\ & & & \boxed{AC \downarrow} & \boxed{AA} & \boxed{AC \uparrow} & \\ & & & & \boxed{CA \downarrow} & \boxed{CC} & \boxed{CA \uparrow} \\ & & & & & \boxed{AC \downarrow} & \boxed{AA} \end{pmatrix}. \quad (2.110)$$

Each block $\boxed{\alpha\alpha}$ represents one layer of atoms (cations for $\alpha = C$ and anions for $\alpha = A$) and each block $\boxed{\alpha\beta}$ represents the coupling between two atomic layers. According to the parameters to be used in this model these blocks have different colours: GaAs-parameters are yellow, InAs-parameters are green. The blue blocks represent the common anion layers, where the parameters get averaged as

$$\boxed{AA} = \frac{1}{2} \left(\boxed{AA} + \boxed{AA} \right). \quad (2.111)$$

Another important fact to be accounted for in the tight-binding model stems from the situation that the energy bands of the different materials have to be aligned. The energy zero of band structure is generally free to be chosen as the valence band maximum. In the case of two or more materials coming together these two energy scales have to be energetically related to each other. To incorporate this, a single factor called the valence band offset ΔE_v is introduced into the model which is added to the on-site parameters of the well-material. This factor describes the energetic distance of the valence band maxima of the materials⁴. In the literature, many values of ΔE_v can be found, showing some controversy because of the huge differences. For the InAs/GaAs material system these values are between $\Delta E_v = 0.05$ eV and $\Delta E_v = 0.5$ eV ([113–117]). Throughout this thesis we will use the value of $\Delta E_v = 0.06$ eV as suggested in [113]. A more detailed discussion of the valence band offset and its influence on electronic binding energies is given in Section 2.8.

In Figs. 2.13 and 2.14, the energy bands of a symmetric InAs quantum well consisting of 3 monolayers InAs inside a GaAs host matrix are shown. The quantum well creates new sub-bands inside the bulk energy gap.

⁴In principle it does not matter if the energetic distance of the valence band maxima or at the conduction band minima is considered because one value sets the other and vice versa, see [112].

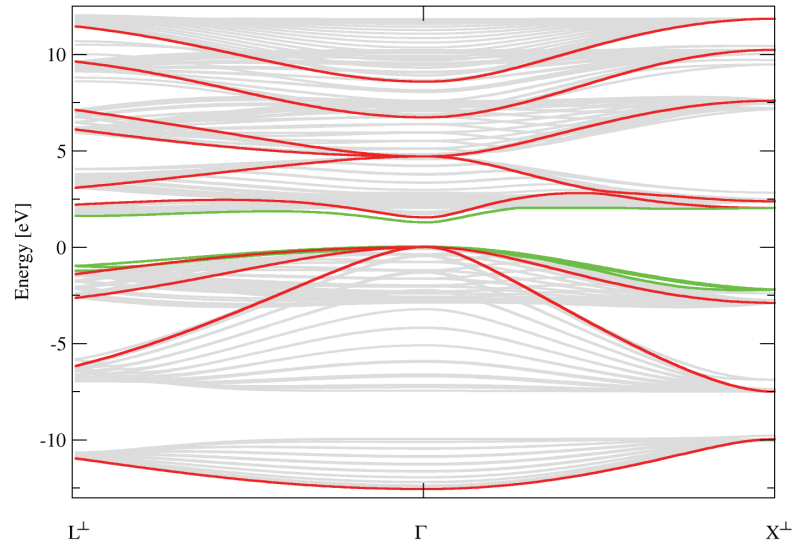


Figure 2.13.: Energy bands of an InAs quantum well of three monolayers (green) in GaAs bulk material (red bands and grey sub-bands).

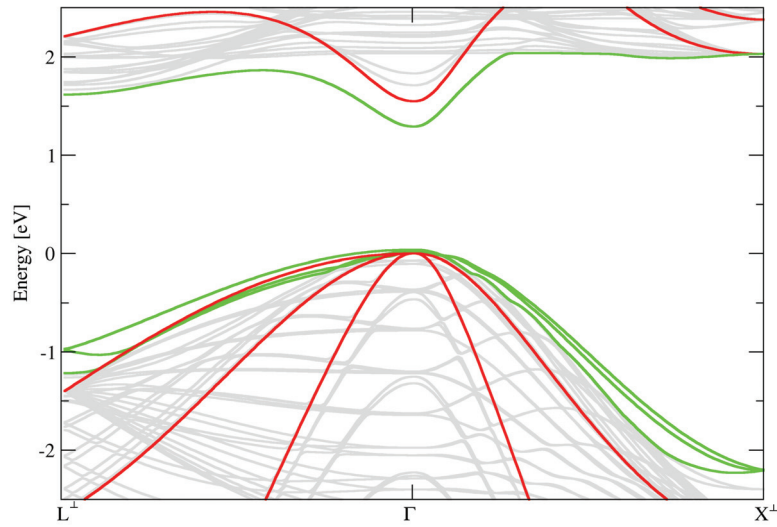


Figure 2.14.: As above, but a narrowed energy scale around energy zero is shown to emphasize the InAs quantum well bound energy bands (green) in the vicinity of the Γ -point.

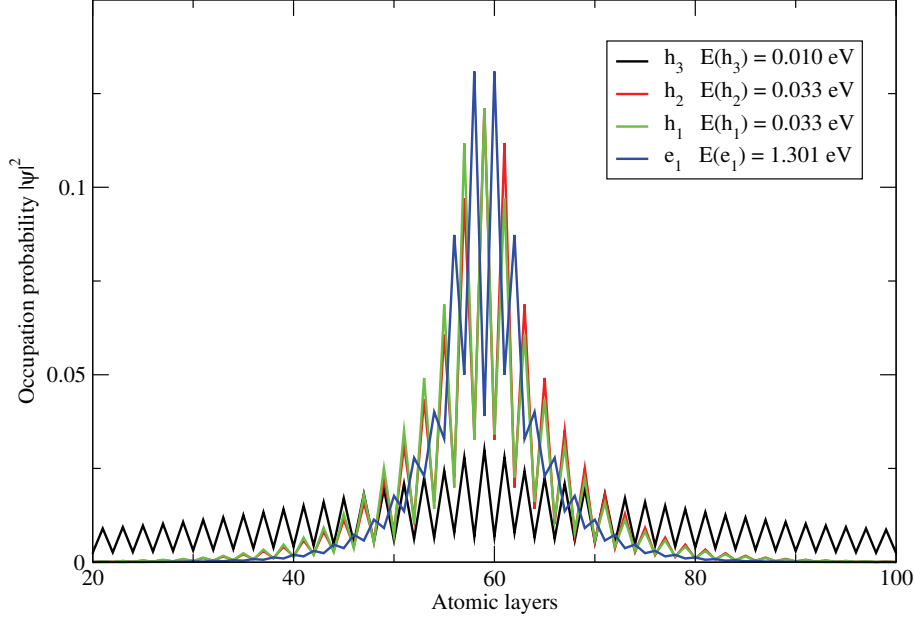


Figure 2.15.: Occupation probability at the Γ -point for bound electron and hole states of an InAs QW in a GaAs host matrix.

From Fig. 2.14 it can be seen, that only one electron state is bound (i.e. it has an energy below the GaAs bulk conduction band edge), while three hole states are bound at the Γ -point (with energies above the GaAs bulk valence band edge). This can be understood via the different effective masses of electrons and holes: while the electron effective mass in InAs is $0.023m_0$ with m_0 being the bare electron mass, the hole effective mass is $0.41m_0$, which is considerably heavier [118]. From a simple potential well picture it is clear that the heavier the particles are, the stronger they are bound in the potential. The calculated energies of the bound states are given in Fig. 2.15 in the inset, together with their corresponding occupation probability $|\psi|^2$ as a function of the atomic layer index in growth direction. From the occupation probabilities of the holes it can be seen, that the probabilities are smeared out for small binding energies (h_3). Additionally, the typical zig-zag form of the occupation probability can be seen, representing the alternating layers of anions and cations, having different potentials and therefore attracting the electrons and holes more and less, respectively.

2.3.3. Quantum dots

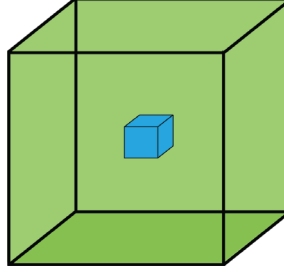


Figure 2.16.: Scheme of a three-dimensionally confined area of material in the supercell, representing the QD.

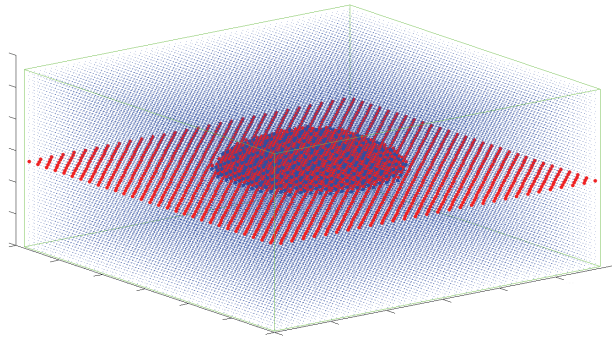


Figure 2.17.: Exemplary supercell realization of a pure lens-shaped InAs QD. Red dots indicate Indium atoms, small blue dots indicate atoms belonging to the GaAs buffer.

In this chapter the calculation of bound single-particle energies and wave functions of quantum dots on top of a wetting layer in a host matrix is explained in detail. Included is an overview of common quantum dot structures, benchmarks of our results as well as analysis of the influences of the different geometrical aspects of quantum dots on the electronic structure. Additionally the influences of Indium concentration, the choice of valence band offset and individual realizations is discussed.

When it comes to modelling quantum dots in the tight-binding approach, no more spatial periodicities can be used to simplify the corresponding Hamiltonian. For the description of three-dimensional nanostructures, each and every single atom in the spatial domain of interest has to appear as an individual subblock in the Hamiltonian, a fact that blows up the computational needs drastically. The general structure of the Hamiltonian corresponds to the structure of the Hamiltonian used in the quantum well case, Eqn. (2.94). The difference is, that each subblock that belonged to a single layer in the quantum well case now consists of numerous subblocks itself, each representing an individual atom inside the layer. The atomic subblocks hold the on-site energies and the spin-orbit terms of each individual atom.

In second quantization, the unstrained TB Hamiltonian in its most general form reads as follows:

$$H^{TB} = \sum_{\mathbf{R}\nu\alpha\sigma} E_{\alpha\nu} |\mathbf{R}\nu\alpha\sigma\rangle \langle \mathbf{R}\nu\alpha\sigma| + \sum_{\mathbf{R}'\nu'\alpha'\sigma', \mathbf{R}\nu\alpha\sigma} V_{\mathbf{R}'\alpha'\nu'\mathbf{R}\alpha\nu} |\mathbf{R}'\nu'\alpha'\sigma'\rangle \langle \mathbf{R}\nu\alpha\sigma| \quad (2.112)$$

with $E_{\alpha\nu}$ being the on-site energy of orbital ν at atom type α and $V_{\mathbf{R}'\alpha'\nu'\mathbf{R}\alpha\nu}$ being the hopping parameters between orbitals ν' and ν at atom type α' at the atomic site \mathbf{R}' and α at \mathbf{R} , respectively.

The electronic wave functions are expressed as linear combinations of the atomic orbitals with complex expansion coefficients to be determined by diagonalization of the TB Hamiltonian:

$$\psi = \sum_{\mathbf{R}\alpha\nu\sigma} c_{\mathbf{R}\alpha\nu\sigma} |\mathbf{R}\alpha\nu\sigma\rangle. \quad (2.113)$$

In the sp^3s^* model including spin-orbit coupling five basis orbitals per atom per spin direction are assumed, which makes the size of the Hamiltonian $10N \times 10N$ with N being the number of atoms in the computational domain for three-dimensional calculations. Without assuming the effect of spin-orbit coupling, the Hamiltonian is spin-independent and has the dimension $5N \times 5N$. For sake of simplicity we will drop the spin-part for the moment. In that case the Hamiltonian looks like:

$$H = \begin{pmatrix} H_{\alpha}^{on-site} & H_{\alpha,\alpha'}^{NN} & 0 & 0 & \dots \\ H_{\alpha',\alpha}^{NN} & H_{\alpha'}^{on-site} & H_{\alpha',\alpha}^{NN} & 0 & \dots \\ 0 & H_{\alpha,\alpha'}^{NN} & H_{\alpha}^{on-site} & H_{\alpha,\alpha'}^{NN} & \dots \\ 0 & 0 & H_{\alpha',\alpha}^{NN} & H_{\alpha'}^{on-site} & \dots \\ \vdots & \vdots & \vdots & \vdots & \ddots \end{pmatrix} \quad (2.114)$$

with the diagonal part holding the orbital energies

$$H_{\alpha}^{on-site} = \begin{pmatrix} E_{\alpha,s} & 0 & 0 & 0 & 0 \\ 0 & E_{\alpha,p_x} & 0 & 0 & 0 \\ 0 & 0 & E_{\alpha,p_y} & 0 & 0 \\ 0 & 0 & 0 & E_{\alpha,p_z} & 0 \\ 0 & 0 & 0 & 0 & E_{\alpha,s^*} \end{pmatrix} \quad (2.115)$$

and the off-diagonal parts containing the NN hopping matrix elements

$$H_{\alpha,\alpha'}^{NN} = \begin{pmatrix} V_{s,\alpha,s,\alpha'}^{NN} & V_{s,\alpha,p_x,\alpha'}^{NN} & V_{s,\alpha,p_y,\alpha'}^{NN} & V_{s,\alpha,p_z,\alpha'}^{NN} & V_{s,\alpha,s^*,\alpha'}^{NN} \\ V_{p_x,\alpha,s,\alpha'}^{NN} & V_{p_x,\alpha,p_x,\alpha'}^{NN} & V_{p_x,\alpha,p_y,\alpha'}^{NN} & V_{p_x,\alpha,p_z,\alpha'}^{NN} & V_{p_x,\alpha,s^*,\alpha'}^{NN} \\ V_{p_y,\alpha,s,\alpha'}^{NN} & V_{p_y,\alpha,p_x,\alpha'}^{NN} & V_{p_y,\alpha,p_y,\alpha'}^{NN} & V_{p_y,\alpha,p_z,\alpha'}^{NN} & V_{p_y,\alpha,s^*,\alpha'}^{NN} \\ V_{p_z,\alpha,s,\alpha'}^{NN} & V_{p_z,\alpha,p_x,\alpha'}^{NN} & V_{p_z,\alpha,p_y,\alpha'}^{NN} & V_{p_z,\alpha,p_z,\alpha'}^{NN} & V_{p_z,\alpha,s,\alpha'}^{NN} \\ V_{s^*,\alpha,s,\alpha'}^{NN} & V_{s^*,\alpha,p_x,\alpha'}^{NN} & V_{s^*,\alpha,p_y,\alpha'}^{NN} & V_{s^*,\alpha,p_z,\alpha'}^{NN} & V_{s^*,\alpha,s^*,\alpha'}^{NN} \end{pmatrix}. \quad (2.116)$$

In general a NN sp^3s^* TB model yields 5 independent diagonal elements per atom type and 25 hopping matrix elements per atom type as well as 25 matrix elements per intertype coupling. So for GaAs (Gallium and Arsenic atoms) for example the model would need $5 + 5 + 25 + 25 + 25 = 85$ different matrix elements to be determined empirically by fitting to an experimentally determined band structure already in a nearest neighbour model. Luckily, in reality this is not the case. Due to the assumed symmetry properties of the atomic orbitals (s -like, p -like symmetry etc.) and due to the model restrictions the number of free hopping parameters can be reduced drastically. First, by limiting the distance up to which couplings are taken into account, not every combination of couplings of atom types is allowed. Second, because of the orbital symmetries, several couplings are identical or zero:

$$V_{s^*,\alpha,s,\alpha'} = V_{s,\alpha,s^*,\alpha'} = V_{s^*,\alpha,s^*,\alpha'} = 0. \quad (2.117)$$

Because of the odd symmetry of p -like orbitals, simplifications as

$$V_{p_x,\alpha,p_x,\alpha'} = V_{p_y,\alpha,p_y,\alpha'} = V_{p_z,\alpha,p_z,\alpha'} \quad (2.118)$$

$$V_{s,\alpha,p_x,\alpha'} = -V_{p_x,\alpha,s,\alpha'} \quad (2.119)$$

$$V_{s,\alpha,p_y,\alpha'} = -V_{p_y,\alpha,s,\alpha'} \quad (2.120)$$

$$V_{s,\alpha,p_z,\alpha'} = -V_{p_z,\alpha,s,\alpha'} \quad (2.121)$$

$$V_{s^*,\alpha,p_x,\alpha'} = -V_{p_x,\alpha,s^*,\alpha'} \quad (2.122)$$

$$V_{s^*,\alpha,p_y,\alpha'} = -V_{p_y,\alpha,s^*,\alpha'} \quad (2.123)$$

$$V_{s^*,\alpha,p_z,\alpha'} = -V_{p_z,\alpha,s^*,\alpha'} \quad (2.124)$$

$$V_{p_x,\alpha,p_y,\alpha'} = -V_{p_y,\alpha,p_x,\alpha'} \quad (2.125)$$

$$V_{p_x,\alpha,p_y,\alpha'} = V_{p_y,\alpha,p_x,\alpha'} \quad (2.126)$$

can be used.

Then the nearest neighbour hopping submatrices can be written as:

$$H_{\alpha,\alpha'}^{NN} = \begin{pmatrix} V_{s,\alpha,s,\alpha'}^{NN} & V_{s,\alpha,p_x,\alpha'}^{NN} & V_{s,\alpha,p_y,\alpha'}^{NN} & V_{s,\alpha,p_z,\alpha'}^{NN} & 0 \\ -V_{s,\alpha,p_x,\alpha'}^{NN} & V_{p_x,\alpha,p_x,\alpha'}^{NN} & V_{p_x,\alpha,p_y,\alpha'}^{NN} & V_{p_x,\alpha,p_z,\alpha'}^{NN} & V_{p_x,\alpha,s^*,\alpha'}^{NN} \\ -V_{s,\alpha,p_y,\alpha'}^{NN} & V_{p_x,\alpha,p_y,\alpha'}^{NN} & V_{p_x,\alpha,p_x,\alpha'}^{NN} & V_{p_x,\alpha,p_y,\alpha'}^{NN} & V_{p_y,\alpha,s^*,\alpha'}^{NN} \\ -V_{s,\alpha,p_z,\alpha'}^{NN} & V_{p_x,\alpha,p_z,\alpha'}^{NN} & V_{p_x,\alpha,p_y,\alpha'}^{NN} & V_{p_x,\alpha,p_x,\alpha'}^{NN} & V_{p_z,\alpha,s^*,\alpha'}^{NN} \\ 0 & -V_{p_x,\alpha,s^*,\alpha'}^{NN} & -V_{p_y,\alpha,s^*,\alpha'}^{NN} & -V_{p_z,\alpha,s^*,\alpha'}^{NN} & 0 \end{pmatrix}. \quad (2.127)$$

These considerations reduce the number of independent parameters to $5 + 5 + 7 + 7 + 7 = 31$. We have assumed, that three of the basis orbitals hold p -like symmetry: p_x, p_y and p_z where the index x, y, z represents the different realizations of the angular momentum quantum number. Since this has no influence on the orbital energy, the energies of these three orbitals equal each other. So per atom type there are only three free parameters left for the orbital energies. Additionally, in a nearest-neighbour model for a common semiconductor material such as GaAs,

there are no couplings between Gallium atoms themselves or between Arsen atoms themselves because they always have at least second next neighbour distances to each other, as can be seen in Fig. 2.7. Thus the only coupling parameters needed are the ones between Gallium and Arsen atoms or, put more general, between anions and cations. In the end, to describe a semiconductor material in a NN sp^3s^* model $3+3+7 = 13$ independent matrix elements are required. As said before, these can be obtained by fitting to a given band structure. An overview of parametrizations can be found at [48]. TB parametrizations used in this thesis are given in the appendix A.4.

Steps of building a QD

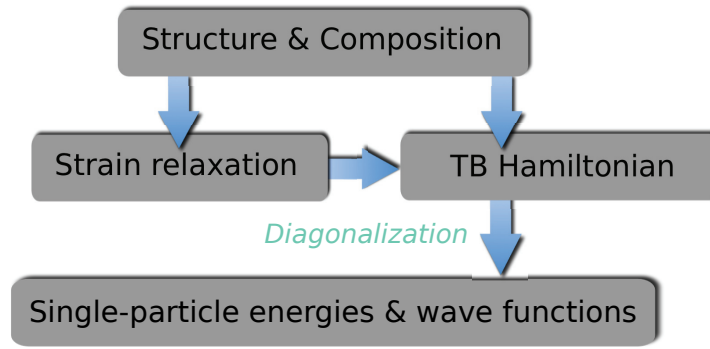


Figure 2.18.: Scheme representing the workflow for the calculation of electronic single-particle states. After having setup the geometry and composition, the structure is relaxed in order to find the strained equilibrium atomic positions. This information enters the TB-Hamiltonian, the eigenenergies and eigenstates of which give the electron and hole single-particle energies and wave functions by diagonalization.

In Fig. 2.18 the general workflow for the tight-binding calculation of the electronic structure of a three-dimensional nanostructure is shown. The first step consists of assuming the geometrical parameters of the structure. In the case of a QD this would include the shape, diameter, height, material composition and composition gradients. These informations can be taken from experiments, for example TEM or AFM measurements, or can be assumed theoretically. After this has been done, the tight-binding Hamiltonian needs to be constructed.

Building the Hamiltonian of the computational domain starts with the definition of a bulk crystal matrix of the host material, e.g. GaAs. The number of included atoms is calculated and according to that a sparse diagonal matrix holding all on-site energies is constructed. In a next step, the wetting layer, if assumed, is constructed by overwriting one or more layers with the onsite energies of the confined material, e.g. InAs. The WL is a small layer, typically consisting of only a few monolayers

of the QD material, which is the central element in the Stranski-Krastanov growth mode, see appendix A.1.

On top of the wetting layer the quantum dot is built according to the chosen geometry. The most common geometries for InAs or InGaAs QDs on [001]-GaAs are lens-, disk- and pyramidal-shaped dots, sketched in Figs. 2.19, 2.20 and 2.21 and discussed in the following. We will concentrate on lens-shaped dots here and show results for the other shapes only for comparison. Those shapes are more or less roughly estimated: Often the dot-shapes are measured before overgrowth and multiple steps of annealing, both effects of which are known as to change the shape drastically due to several effects like interdiffusion, reordering and changes in the strain-distribution. In a true atomistic model these effects have to be included at least in considering InGaAs-QDs instead of pure InAs QDs: in reality no such thing like a pure InAs QD would be realized because of the phenomena mentioned above. So in a realistic structure a QD always exhibits some fraction of the host material inside the QD region. This effect is treated statistically: for a given target Indium concentration inside the dot region each cation atomic site is occupied with either an Indium or Gallium atom with a probability reflecting the target concentrations. The effect of this random alloy realization on single-particle energies and wave functions is discussed in section 2.7.

After the QD is defined properly, new equilibrium positions for each atom due to the arising lattice-mismatch induced strain are calculated employing molecular dynamics simulation software⁵ via minimization of the global strain energy using the VFF as discussed in section 2.2.5. Afterwards, the strain-altered coupling matrix elements are introduced into the tight-binding Hamiltonian according to the actual distribution of atoms and their equilibrium positions. As mentioned in section 2.2.3 the couplings are treated in the two-center approximation. First, the bulk coupling matrix elements are set according to which atoms are coupled, then the strain-affected directional cosines are calculated (bond-bending term) and in the end the product of both is multiplied with a factor that includes the new bond-length (bond-stretching term) to the power of the factor η . In a last step prior to the diagonalization the strain-independent spin-orbit splitting terms are included into the Hamiltonian and the boundaries are set.

Common QD structures

In this Section, the three most common InAs quantum dot structures are discussed in terms of morphology and composition, as given in the literature. High-quality samples are often grown in MBE (molecular beam epitaxy), while low-cost samples are grown in the MOVPE (metal organic vapor phase epitaxy) growth mode. Both

⁵See the appendix for a short introduction, LAMMPS material parameters for InAs and GaAs and best practice parameters.

methods are sketched in the appendix A.1. During MBE, the growth can be monitored in-situ by XPS methods (x-ray photoelectron spectroscopy), which give information about the quantum dot formation and morphology for freestanding QDs. During overgrowth strain distributions change, lattice distortions arise and inter-diffusion of materials occurs due to different annealing steps [119–121]. Structures of overgrown QDs can be investigated by TEM or related techniques, although for transmission experiments a sample has to be cut in a thin slice to allow for transmission of electrons. So TEM-pictures as given in [15] do not provide three-dimensional data about the QD morphology as it would be necessary as an input for a three-dimensional theory like tight-binding.

Likewise material concentrations inside and around the QD can only be measured to a certain degree by TEM and averaging in direction of transmission over the whole QD region cannot be avoided. Since complete knowledge about the QD features is not achievable it appears a good idea simulating different structures in theory to conclude to a most likely QD morphology by comparison of QD features like energy levels of bound states or exciton lines in the emission spectra [122–124]. Nevertheless, some information, at least in good approximation, is given about the QDs. What should be kept in mind is that QD growth always is subject to fluctuations due to temperature variations, local lattice imperfections or local strain changes and due to the statistical nature of the growth itself. As a result of this, no QD is completely equal to another QD. There always are small deviations in size and composition which can be seen in comparing luminescence spectra of single quantum dots from the same sample or by high resolution spectroscopy of QD ensembles [125] which lead to slightly varying excitonic emission lines, both in energetic position and height. One of the consequences of these small differences of energy levels and wave functions are slight changes in Coulomb interaction of carriers inside the QD, which is the reason for the individual fine-structure splitting occurring in entanglement experiments [124, 126]. This problem will be addressed in section 3.2.

Keeping the statistical nature of the growth process in mind, three main geometries of InAs QDs can be identified, which are shown in the next sections.

Lens-shaped QDs

QDs indicating a lens-shape as shown in Fig. 2.19 can be assumed as the most common QDs for InAs grown on a [001] GaAs substrate [35, 36, 75, 93, 127–138]. To condense the information given in the literature, a typical lens-shaped InAs QD is believed to have a diameter of approximately 25 nm and a height of 2.3 nm to 3.3 nm. Indium concentrations range from In-rich (100-85% InAs in the QD region) to highly annealed (60-10% InAs). Pure 100% InAs QDs are not believed to exist in nature but are useful model assumptions for a comparison between different theories because statistical fluctuations due to random alloying are avoided. Therefore, benchmarking

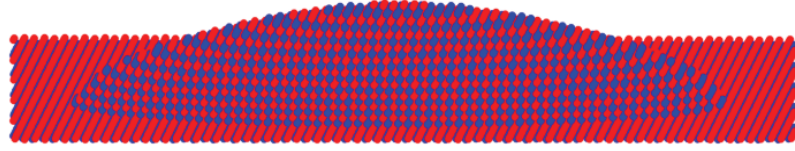


Figure 2.19.: Atomistic supercell representation of a lens-shaped QD of pure InAs on top of a wetting layer, consisting of two monolayers InAs. Red and blue atoms are Indium and Arsenic atoms, respectively. Atoms belonging to the GaAs buffer are not shown for illustration purposes and only a small part of the original supercell is shown.

will be done with pure InAs QDs.

Truncated pyramid-shaped QDs

QDs exhibiting the shape of a (truncated) pyramid as shown in Fig. 2.20 are assumed to have a side-length of about 20 nm and the height of 2.3 nm [86, 126, 139–141]. These dots host a large percentage of Indium (approximately 100% InAs in the QD region). Truncated pyramid-shaped QDs were often used for early $\mathbf{k} \cdot \mathbf{p}$ and TB calculations.

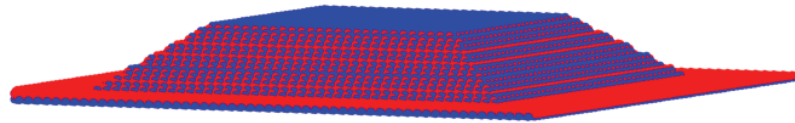


Figure 2.20.: Atomistic supercell representation of a truncated pyramid-shaped QD of pure InAs on top of a wetting layer, consisting of two monolayers InAs. Atoms belonging to the GaAs buffer are not shown for illustration purposes. Only a small part of the original supercell is shown.

Disk-shaped QDs

Cylindrical QDs with a disklike shape are assumed to have a diameter of around 20 nm and height of approximately 2.3 nm [128, 134, 142–148]. The InAs content in these QDs is assumed to be around 60%. A model of the atomistic supercell representation is shown in Fig. 2.21.

Also, combinations of the three geometries were observed, for example a disk-shaped dot with a reduction in diameter with increasing height [149].



Figure 2.21.: Atomistic supercell representation of a disk-shaped QD of pure InAs on top of a wetting layer, consisting of two monolayers InAs. Atoms belonging to the GaAs buffer are not shown for illustration purposes. Only a small part of the original supercell is shown.

2.4. Supercell requirements

As fabricated, QD sample and device sizes are in the order of centimeters, with realistic quantum dot densities between 10^9 and 10^{12} per centimeter squared. Depending on the aperture size, in photoluminescence measurements for example, a signal often comes from a large ensemble of QDs. Simultaneous atomistic simulation of the whole ensemble can only be treated by simple models such as the effective mass model, if the wavefunctions of individual QDs overlap and therefore influence each other. Three-dimensional models fail due to the problem size. For calculation of the optical properties of the ensemble Cluster-expansion methods can be used [150, 151]. Most recent supercomputer calculations for the electronic structure feature quantum dot stacks with computational domains of around $(110 \text{ nm})^3$ [152]. In more recent experiments, quantum dot densities can be lowered down experimentally to ultra low densities such as 10^7 QDs per centimeter squared [153], and techniques such as post-growth spatial selection and site-selective QD growth [154] allow for measurements on single QDs, integrated into devices like photonic or VCSEL-cavities.

In a tight-binding model this situation of a single QD with sizes ranging between 5 and around 40 nanometers in diameter can be addressed. In recent years it became possible to even simulate QD molecules [77] and stacks of QDs [152] by means of tight-binding. Nevertheless, simulating a single QD can only cover a finite spatial region, so it is necessary to treat the boundaries of the simulation domain appropriately.

As discussed in [155] there are different boundary conditions (BCs) possible to be imposed on the Hamiltonian: open BCs, surface passivation and periodic BCs. Open BCs treat the surface of the tight-binding supercell as a transition from the crystal to vacuum. This technique is known to produce unphysical surface states which energetically lie inside the band gap [103]. Some effort is necessary to identify and remove these states from the calculation, which is the reason why open BCs are used only in special geometries. One attempt to remove these states directly is to passivate the surfaces with hydrogen atoms. In the tight-binding formalism this means that all coupling matrix elements from surface atoms to atoms outside the simulation domain are raised by several eV which shifts the energy of the surface states out of the band gap. Nevertheless, neither are the energies of the passivation

atoms known, nor is it physically intuitive to passivate at all in a region of space where the bulk material is located at. Another way of treating the surfaces is to impose periodic BCs, so that the atoms at one surface of the domain are coupled to the atoms at the opposing surface of the domain. This approach corresponds to the physical situation of placing QDs besides, on top and below each other with a distance of approximately the size of the simulation domain side-length. It appears intuitive that in this case of BCs the simulation domain needs to be large enough that the QDs do not influence each other. This and the fact that the numerical bandwidth of the Hamiltonian matrix increases with using periodic BCs makes this choice the computationally most demanding. Nevertheless, periodic BCs are used in our model because it is the most realistic case and unphysical surface states do not appear.

2.5. Diagonalization of large sparse matrices

In general, the diagonalization of a matrix is a very basic piece of algebra as long as the matrix is small and fulfills some features such as invertibility. However, as problems (matrix sizes) are getting larger and more complicated, the search for eigenstates and eigenvalues can be very difficult. Therefore the field of mathematical research on efficient diagonalization algorithms is in neverending progress [156]. Luckily, the Hamiltonian matrices arising in a tight-binding model fall in a class which fulfills some symmetries and characteristics that make the problem traceable and guarantee the existence of solutions. First of all, after Löwdin-orthogonalization the basis states are orthogonal and a standard eigenvalue problem has to be solved, yielding eigenpairs (eigenvalues and eigenstates):

$$\begin{aligned} H\psi &= E\psi && \text{standard} \\ H\psi &= EB\psi && \text{generalized,} \end{aligned}$$

where H is the Hamiltonian matrix, E are eigenvalues and ψ are the corresponding complex eigenstates. B would be another matrix which could arise for example in stability analysis in fluid dynamics. The TB Hamiltonian matrix usually is hermitian (real eigenvalues), very sparse with a small bandwidth, complex (if spin-orbit splitting is considered) and very large (of the order of $10^8 \times 10^8$). The sparsity usually is around 10^{-7} .

In semiconductor nanostructures, only a few states are bound which lie in a defined region of energy, most likely to be located inside the energy gap. So here we do not need the information about all eigenpairs of the Hamiltonian matrix but only about a very few eigenpairs with eigenvalues in the middle of the spectrum. Since the diagonalization of such a large matrix is not an easy task and convergence time is a crucial parameter, we use freely available software packages for efficient diagonalization. There are many different packages provided (for an overview see [157]), each

suited for one or more special cases. We chose to use SLEPc [158], the "Scalable Library for Eigenvalue Problem Computations". This framework provides several parallel spectral transformations and state-of-the-art eigensolvers based on PETSc [159], the "Portable, Extensible Toolkit for Scientific Computation" which provides "a suite of data structures and routines that provide the building blocks for the implementation of large-scale application codes on parallel (and serial) computers" [160, 161]. In our case it turned out that using the standard Krylov-Schur algorithm [162] in combination with the harmonic extraction technique [163, 164] is the best choice to find eigenpairs closest to a desired energy in terms of convergence speed. Best practice parameters for the use of PETSc and SLEPc are given in the appendix.

2.6. Benchmarks

In Fig. 2.22 GaAs band structures obtained from different TB models are compared. It can be seen, that the main differences occur in the conduction band far away from the Γ -point. The sp^3s^* model appears to be a good compromise between the sp^3 and the $sp^3d^5s^*$ models. It captures the correct band gap and effective masses in the vicinity of the Γ -point and resembles the splitting at X - and L -points quite well. Definitely, the $sp^3d^5s^*$ model captures more band structure features, but since we are interested in optical properties, the sp^3s^* model is well suited because optical transitions mainly occur between states around the smallest direct band gap, which is at the Γ -point in conventional semiconductors. The band structure at the X -point for example becomes important for transport properties.

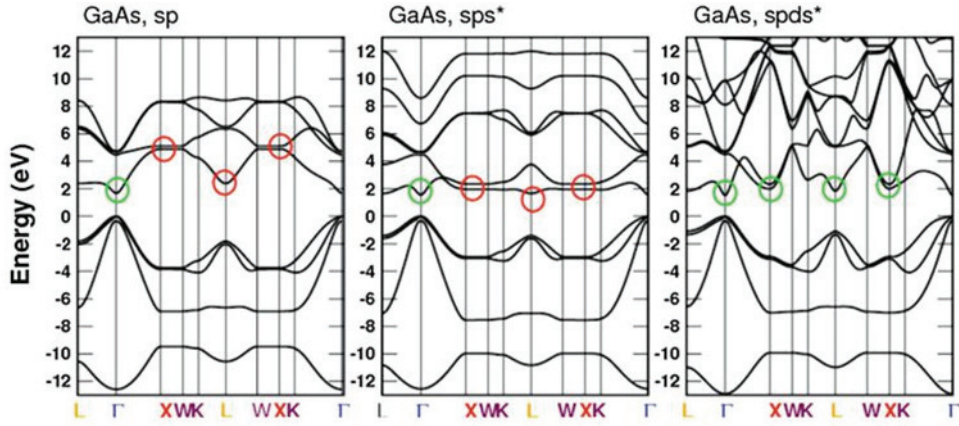


Figure 2.22.: GaAs band structure fits using different basis sizes in the empirical tight-binding model, from [165]. Red and green circles show discrepancy and agreement with experiment, respectively. The $sp^3d^5s^*$ model clearly resembles the band structure best, but for applications happening mainly at the Γ -point, the sp^3s^* -basis is already sufficient.

In Tab. 2.3 a comparison of QD single-particle energy gap (energetic distance of ground electron and hole states) and corresponding level splittings with results from different calculations from the literature using empirical pseudopotentials and the $sp^3d^5s^*$ TB model are shown. All calculations were carried out for a standard lens-shaped pure InAs QD with height of 3.5 nm and a diameter of 25 nm on top of a wetting layer inside a GaAs host matrix, as displayed in Fig. 2.23.

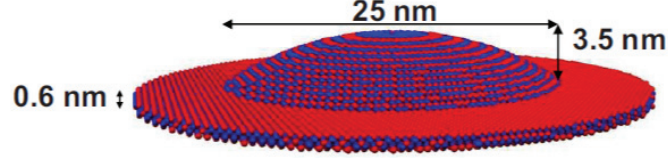


Figure 2.23.: Atomistic representation of the pure InAs QD exhibiting lens-shape used to benchmark our TB model. From [75] for comparison.

Splitting	EPP 1	EPP 2	Experiment	TB 1	TB 2	Our results
	[35]	[166]	[167, 168]	[75]	[65]	
$e_2 - e_1$	65	57	50	52.7	59.9	59.3
$e_3 - e_2$	2	2.1	2	1.28	4.2	3.4
$e_4 - e_3$	68	58	48	51.7	55.1	55.6
$h_1 - h_2$	8	11		14.4	14.5	13.5
$h_2 - h_3$	7	9		9.8	9.8	8.6
$h_3 - h_4$	6	2.4		5.5	5.3	7.9
E_{Gap}				796	732	749

Table 2.3.: Benchmark of our sp^3s^* TB model with results from different other calculations (EPP 1, EPP 2, TB 1, TB 2) and with experimental data. Splittings between bound electron ($e_1..e_4$) and hole states ($h_1..h_4$) are compared as well as the single-particle energy gap $E_{Gap} = e_1 - h_1$. All values are given in meV.

EPP 1 and EPP 2 are calculations using the empirical pseudopotential model with different parametrizations, while TB 1 and TB 2 are tight-binding calculations within the $sp^3d^5s^*$ model including spin-orbit coupling and strain modifications via valence force field strain minimization. From comparison of the energy splittings it can be seen that the sp^3s^* TB model used in this thesis can compete with both, the advanced $sp^3d^5s^*$ TB models as well as the pseudopotential models. Even between the EPP and TB models themselves, differences of several meV between the energy splittings are observed, stemming from differences in the band structure parametrizations and strain parameters. This defines the accuracy of the energy levels to be of the order of meV. Additionally, the EPP models use a modified valence force field including higher-order bond-stretching terms, while the TB models use an additional modification of on-site parameters due to the strain-altered atomic positions.

Nevertheless, the basic energy level structure of the model QD is already covered in our more simple sp^3s^* TB model. Moreover, an astonishing agreement of our data with the TB 2 results can be observed.

2.7. Geometry and single-particle properties

Having benchmarked the sp^3s^* -TB model, in this section the single-particle electron and hole wave functions as calculated by our tight-binding model will be presented and discussed for the common QD shapes, compositions and parameters. For comparison, we assume a height of 2.2 nm and a diameter of 25 nm at QD base for all lens-shaped, truncated pyramid-shaped and disk-shaped geometry, respectively. All QDs consist of pure InAs. After this comparison regarding the QD shape, we study the influence of QD diameter and height as well as the Indium concentration for a lens-shaped QD. Additionally, the variation of the single-particle properties with different individual atomic realizations is investigated.

Lens-shaped QDs

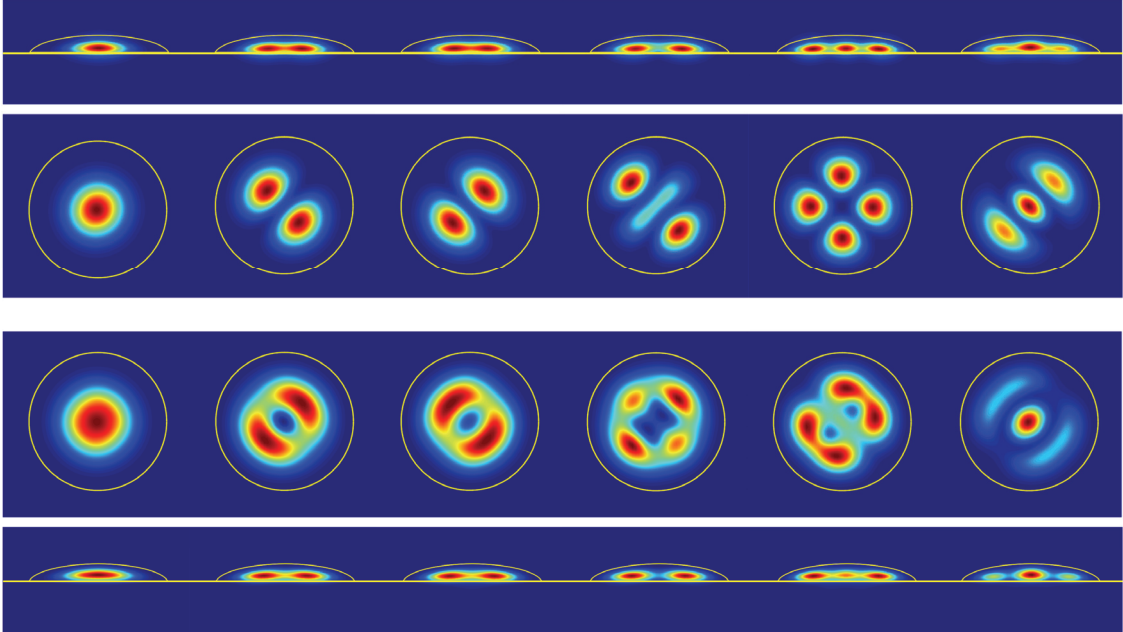


Figure 2.24.: Squared wave functions of the first 12 bound electrons (top) and holes (bottom) for a pure lens-shaped InAs QD. Each state is twofold degenerate due to spin degree of freedom. Yellow lines indicate QD geometry.

In Fig. 2.24 the squared single-particle wave functions of electrons and holes for

the standard lens-shaped pure InAs QD are shown. In the upper half, the squared electron wave functions are depicted in side-view (first row) and in top-view (second row), while in the lower half the squared hole wave functions are given again in top-view (third row) and in side-view (fourth row). Occupation probabilities vary from low probability (dark blue) to high probability (dark red) on a color scale normalized to the maximum occupation probability. Plots show summation over squared lattice-site eigenstate coefficients from the diagonalization of the TB Hamiltonian along growth-direction for the top-view plots and along [010]-direction for side-view plots, respectively. Consequently, no absolute scale is given.

For the electrons, the lowest bound state is shown at the left side, having *s*-like symmetry, followed by two perpendicular *p*-like states in the second and third column from the left. The first three bound states having *d*-like symmetries are given in the three columns on the right. All of these electron states show clear signatures of the quantum harmonic oscillator states with increasing number of nodes of the wave functions with energy.

For the hole states, the deepest bound state is given in the left column, having *s*-like symmetry, followed, again, by two perpendicular aligned states with a somehow *p*-like symmetry. However, state mixing is larger for the holes, so the characteristics of the quantum harmonic oscillator states are less pronounced. This can be seen even better for the three states in the right columns.

From the side-view plots of both electron and hole squared wave functions it is visible, that electron and hole states appear quite similar in this projection and that the center of the wave function tends to be closer to the base of the QD than to the top, which can be interpreted as the influence of the wetting layer and QD shape. Note the difference in z-axis and x-axis: the z-axis has been magnified to show the wave functions properly.

Spin degeneracy is not shown, so each of the given states is doubly Kramers degenerate resulting in a total of twelve bound states given here. The total number of bound states in this very geometry is very large indeed because of the maximum Indium concentration of 100 % assumed inside the QD.

In Tab. 2.4 the binding energies E_B as defined by the energetic distance between the energy corresponding to the state and the respective electron or hole wetting layer band edge are given. Large binding energies are reached for both electrons and holes because of the large Indium concentration. Some general trends can be identified from the energies. Because of the difference in effective mass but depending on the valence band offset, electrons usually have larger binding energies than holes, while the intraband splittings are larger for electrons than for holes. Because of this, usually more hole states are bound despite their smaller binding energies. The intraband splittings of electrons usually exhibit a large-small-large-small structure which corresponds to the splittings between states with different

	Electrons	Holes		Electrons	Holes
$E_B(n_1)$	385	259	$n_1 - n_2$	64.8	19.6
$E_B(n_2)$	321	239	$n_2 - n_3$	3.0	8.5
$E_B(n_3)$	318	230	$n_3 - n_4$	58.5	12.2
$E_B(n_4)$	259	218	$n_4 - n_5$	2.5	11.3
$E_B(n_5)$	257	207	$n_5 - n_6$	1.0	2.6
$E_B(n_6)$	256	204			
E_{Gap}	759.65				

Table 2.4.: In the left hand table the binding energies of the ground and first few excited bound electron and hole states for the standard lens-shaped pure InAs QD are shown. The index n corresponds to electrons ($n = e$) and holes ($n = h$). The right hand table shows the intraband splittings. Additionally the single-particle energy gap $E_{Gap} = e_1 - h_1$ is given. All energies are in units of meV.

symmetry being large and splittings between states with the same symmetry being small. For example between the second and third electron state, both having p -like symmetry, the splitting is small (3 meV), as well as between the states having d -like symmetry (2.5 and 1 meV). This energetic structure can be found in simple two-dimensional harmonic oscillator models, whereas the p - and d -like states are degenerate there and the large splittings between these shells are equivalent. For holes, this structure is spoiled. Splittings in general have a smaller amplitude and no clear large-small structure can be identified. Moreover, all splittings have similar values. In the last row of Tab. 2.4 the single-particle energy gap as defined by $E_{Gap} = e_1 - h_1 = 759$ meV is given, in good agreement with the literature, see Tab. 2.3.

Truncated pyramid-shaped QDs

In Fig. 2.25 the squared wave functions of the pure InAs QD with 2.2 nm height and 25 nm diameter having the shape of a truncated pyramid are shown. The electron and hole wave functions appear quite similar to the ones from the lens-shaped QD but account for the changes in geometry.

From the binding energies and intraband splittings for this geometry in Tab. 2.5 it can be observed, that the confinement from the pyramid-shaped QD is larger than from a lens-shaped QD, yielding larger binding energies for electrons (474 meV) and holes (290 meV). This results in a much smaller single-particle energy gap of 639 meV, 120 meV smaller than for the lens-shaped QD. The bound state splittings reveal an opposite trend for electrons and holes: electron splittings are smaller for the pyramidal shaped QD than for the lens-shaped QD, while hole splittings show

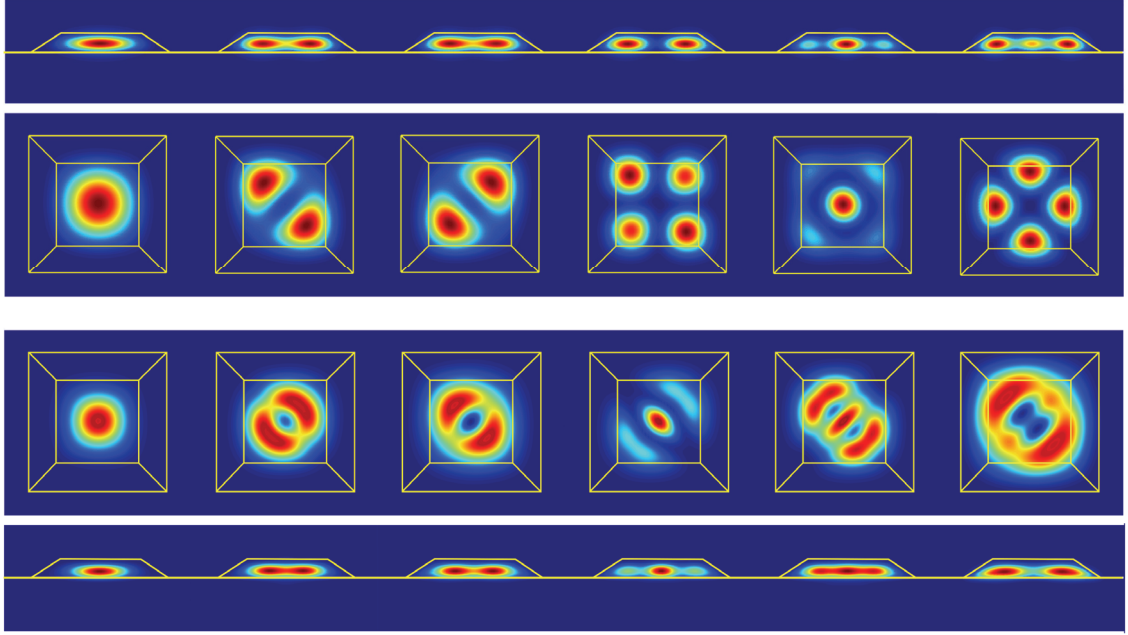


Figure 2.25.: Squared wave functions of the first 12 bound electrons (top) and holes (bottom) for a pure InAs QD with the shape of a truncated pyramid. Each state is twofold degenerate due to spin degree of freedom. Yellow lines indicate QD geometry.

	Electrons	Holes		Electrons	Holes
$E_B(n_1)$	474	290	$n_1 - n_2$	51.8	29.9
$E_B(n_2)$	422	260	$n_2 - n_3$	1.4	6.4
$E_B(n_3)$	420	254	$n_3 - n_4$	44.8	19.4
$E_B(n_4)$	376	234	$n_4 - n_5$	19.7	2.7
$E_B(n_5)$	356	232	$n_5 - n_6$	1.3	7.1
$E_B(n_6)$	355	225			
E_{Gap}	639.82				

Table 2.5.: In the left hand table the binding energies of the lowest bound electron and highest bound hole states for the standard pure InAs QD with truncated pyramid-shape are shown. The index n corresponds to electrons ($n = e$) and holes ($n = h$). The right hand table shows the intraband splittings. Additionally the single-particle energy gap $E_{Gap} = e_1 - h_1$ is given. All energies are in units of meV.

the opposite behaviour. Also, the splitting between the two first electron d -like states is largely increased. The hole states show a tendency of behaving more like in the harmonic oscillator case described above, resulting in the large-small-large splitting energy structure.

Disk-shaped QDs

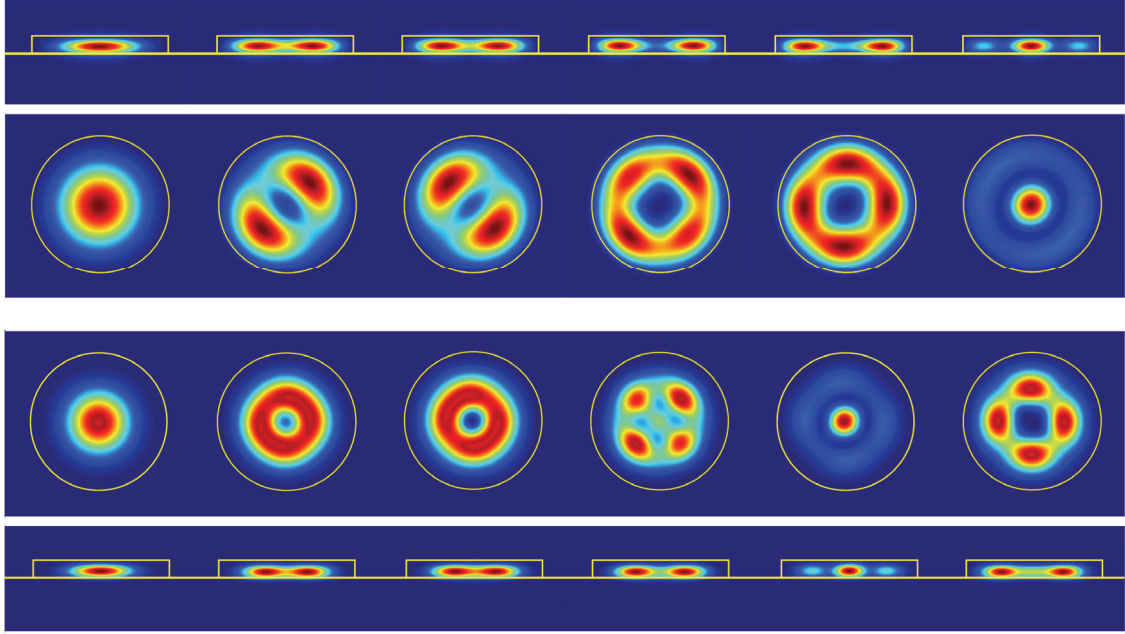


Figure 2.26.: Squared wave functions of the first 12 bound electrons (top) and holes (bottom) for a pure disk-shaped InAs QD. Each state is twofold degenerate due to spin degree of freedom. Yellow lines indicate QD geometry.

In Fig. 2.26 the single-particle squared wave functions of electrons and holes are shown for the QD having disk-like shape. The symmetric geometry is clearly reflected in the shape of the wave functions, for example the hole p -like states are nearly rotationally symmetric.

Observing the binding energies and intraband splitting of the disk-shaped QD in Tab. 2.6 reveals the trend from lens-shape to pyramid-shape ongoing to the disk-shape. Electron binding energies are enlarged further when compared to the pyramid shape, as well as hole binding energies. This leads to a further reduction in the single-particle energy gap to 604 meV. Electron splittings are also reduced further, while hole splittings remain comparable to the hole splittings of the pyramid-shaped QD. The trend of hole splittings to a large-small-large energy structure is also further extended.

Variation of QD diameter

In Fig. 2.27 the variation of the first few bound electron and hole single-particle energies with QD diameter are shown for a typical pure InAs QD having lens-shape with a fixed height of 2.0 nm, which is lower than the previous QDs. The states

	Electrons	Holes		Electrons	Holes
$E_B(n_1)$	491	309	$n_1 - n_2$	41.4	28.8
$E_B(n_2)$	449	280	$n_2 - n_3$	1.3	3.5
$E_B(n_3)$	448	276	$n_3 - n_4$	44.0	22.3
$E_B(n_4)$	404	254	$n_4 - n_5$	1.9	2.9
$E_B(n_5)$	402	251	$n_5 - n_6$	9.5	5.9
$E_B(n_6)$	393	245			
E_{Gap}	604.20				

Table 2.6.: In the left hand table the binding energies of the lowest bound electron and highest bound hole states for the standard disk-shaped pure InAs QD are shown. The index n corresponds to electrons ($n = e$) and holes ($n = h$). The right hand table shows the intraband splittings. Additionally the single-particle energy gap $E_{Gap} = e_1 - h_1$ is given. All energies are in units of meV.

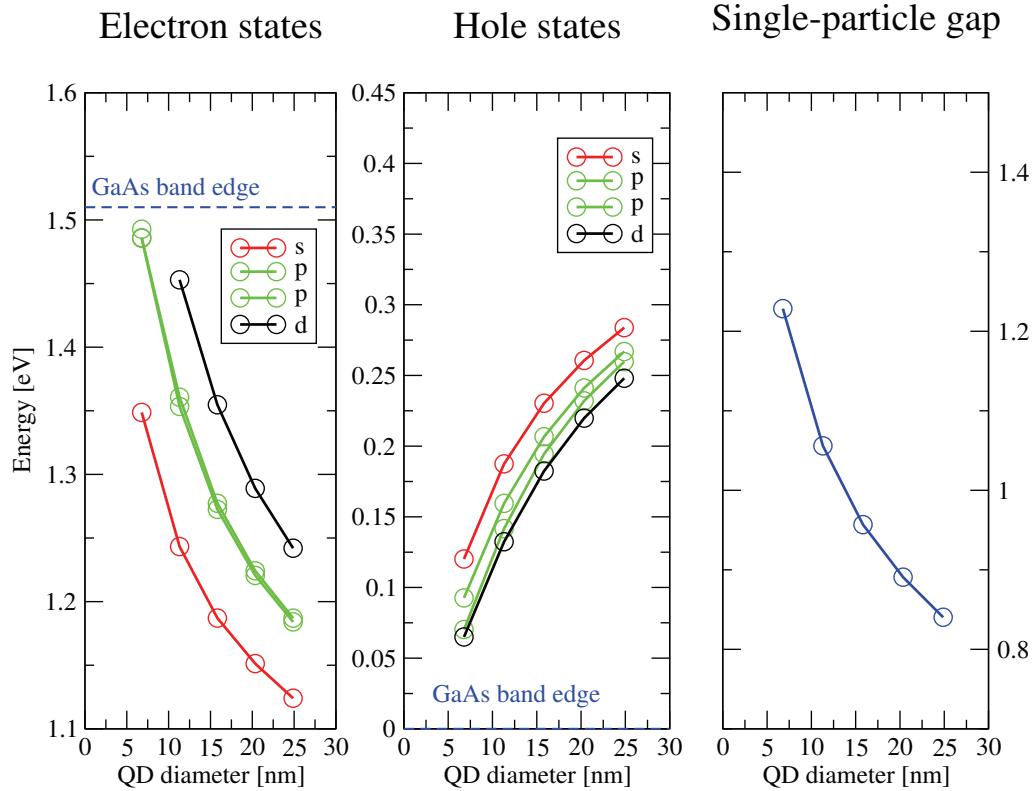


Figure 2.27.: Variation of electron and hole single-particle total energies with QD diameter (left hand and middle panel). In the right hand panel the variation of the single-particle energy gap $E_{Gap} = e_1 - h_1$ is depicted.

having s, p, d -like orbital symmetry are labelled s, p and d , respectively. As expected from a simple quantum harmonic oscillator potential, the electron single-particle

energies are lowered with QD diameter and additional bound states appear, while hole single-particle energies are raised. The overall energy gap as the difference of electron and hole energies is lowered in a non-linear way while raising the QD diameter. Note that the single-particle gap energies are raised in comparison to the QDs before due to the smaller QD height, resulting in a weaker confinement potential.

Variation of QD height

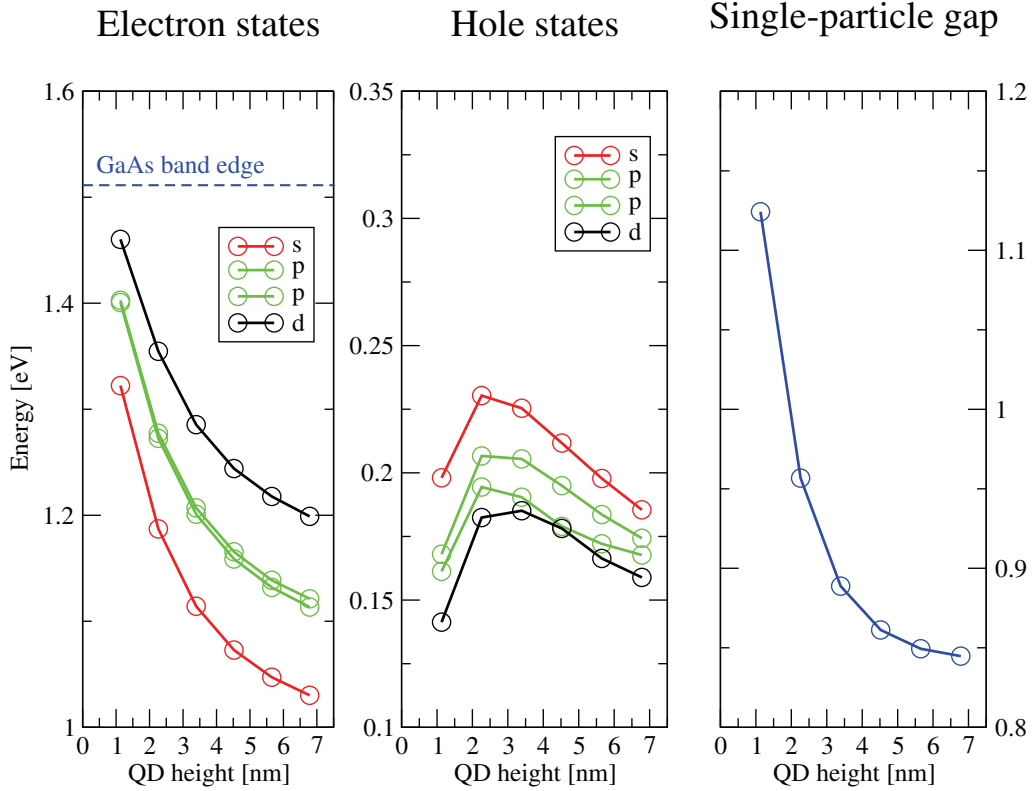


Figure 2.28.: Variation of electron and hole single-particle energies with QD height (left hand and middle panel). In the right hand panel the variation of the single-particle energy gap $E_{Gap} = e_1 - h_1$ is depicted.

In Fig. 2.28 the variation of electron and hole single-particle energies with QD height is shown for typical heights ranging from one to seven nm with a fixed diameter of 15.8 nm. While the evolution of electron energies again can be explained by the increase in confinement in growth direction, the behaviour of the hole energies is more complex. First, the hole energies are raised for QD height changes from one to two nm, followed by an energetic decrease for larger QD heights. This behaviour appears because of the complex interplay between strain distribution and carrier confinement due to QD geometry. Nevertheless, the resulting single-particle

energy gap has a smooth evolution with QD height, which shows convergence-like behaviour to values of 0.84 eV. At a closer look, the energetic splittings catch the eye. While the splittings between electronic states increase monotonic for larger QD height, the splittings between hole states follow no trend, and also the nearly degeneracy between the two p -like hole states is lifted to some extent⁶. Again, this effect is due to the interplay of strain and confinement changes.

Variation of Indium concentration

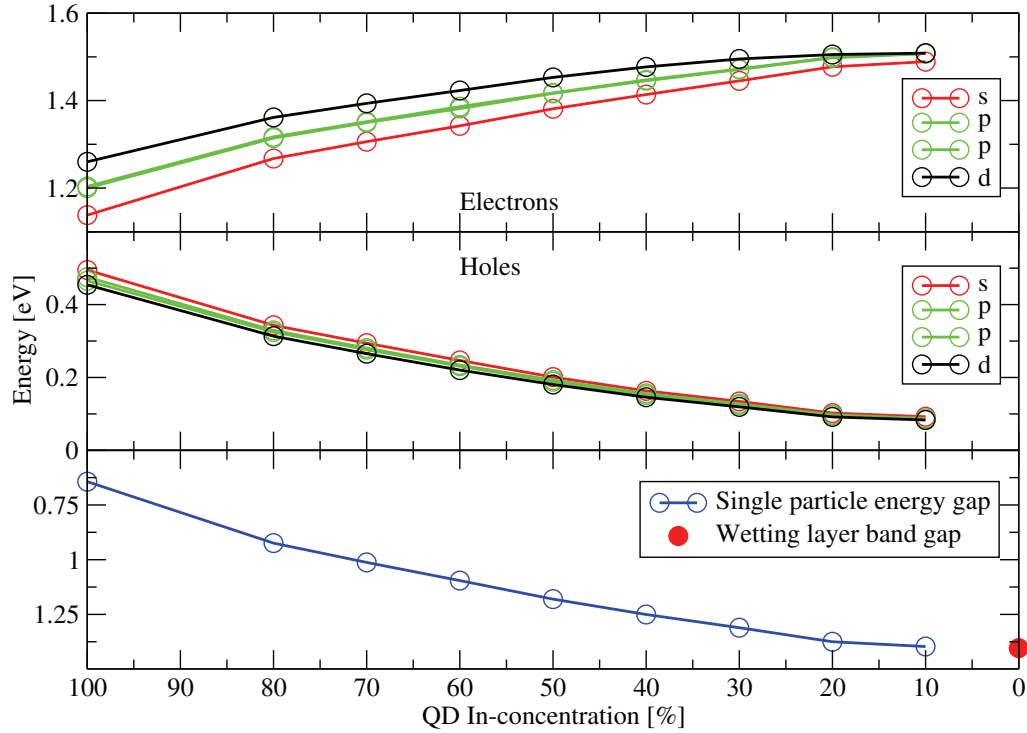


Figure 2.29.: Variation of electron and hole single-particle energies with QD Indium concentration (upper and middle panel). In the lower panel the variation of the single-particle energy gap is depicted.

The evolution of the single-particle electron and hole energies with Indium concentration in the QD and the resulting single-particle energy gap is shown in Fig. 2.29 for an InGaAs QD with lens-shape having 3.4 nm height and a diameter of 25 nm. Starting from a pure InAs QD with deeply bound electron and hole single-particle states, the energies approach the WL band edges for consecutive loss of confinement. Consequently, the single-particle energy gap approaches the WL band gap energy

⁶Not to be mixed up with the spin degeneracy, which still holds. Each of the displayed energy appears twice in the diagonalization of the Hamiltonian, corresponding to two orthogonal eigenstates with the same energy.

for the complete absence of the QD. The WL Indium concentration is not changed in this calculations.

Averaging random realizations

As mentioned above, alloyed materials like InGaAs are modelled atomistically by random statistic distribution of the atoms. To illustrate the influence of these alloy fluctuations on the bound state energies, calculations for three random realizations of a lens-shaped InGaAs QD with a nominal concentration of 30% Indium inside the QD are summarized in Tab. 2.7.

Splitting	Realization #1	Realization #2	Realization #3
$E_B(e_1)$	74.9	74.6	74.2
$E_B(h_1)$	32.4	34.5	32.6
$e_1 - h_1$	1357.3	1355.5	1357.8
$e_2 - e_1$	47.6	44.6	45.2
$e_3 - e_2$	5.2	3	5.4
$e_4 - e_3$	17.2	22.9	19.5
$h_2 - h_1$	7.5	7.7	7.3
$h_3 - h_2$	3.2	3.5	3.3
$h_4 - h_3$	3.4	3.7	3.3

Table 2.7.: Influence of alloy fluctuations on lowest electron and hole binding energies ($E_B(e_1)$ and $E_B(h_1)$), the single-particle energy gap $e_1 - h_1$ and the interband splittings. All values are in meV.

It can be seen that the fluctuations in binding energies and the single-particle gap are of the order of 1-2 meV. Fluctuations of the intraband splittings show a tendency of being larger, where the largest fluctuation is between e_3 and e_2 (5 meV). These results can be compared with the literature for justification: in [169], a nearest neighbour $sp^3d^5s^*$ TB model was utilized for the repeated calculation of single-particle energies of dome-shaped InGaAs QDs with 60% Indium content, a diameter of 30 nm and a height of 5.4 nm. The energetic variation at the band edges was calculated to have a distribution with width ± 0.5 meV for holes and ± 1 meV for electrons, respectively, which is in very good agreement with our calculations. Nevertheless, the typical linewidth broadening measured in photoluminescence experiments on quantum dot ensembles [170, 171] is much higher because not only alloy fluctuations at the same Indium concentration occur but also size and composition fluctuations due to the statistical nature of QD growth.

2.8. Choice of valence band offset

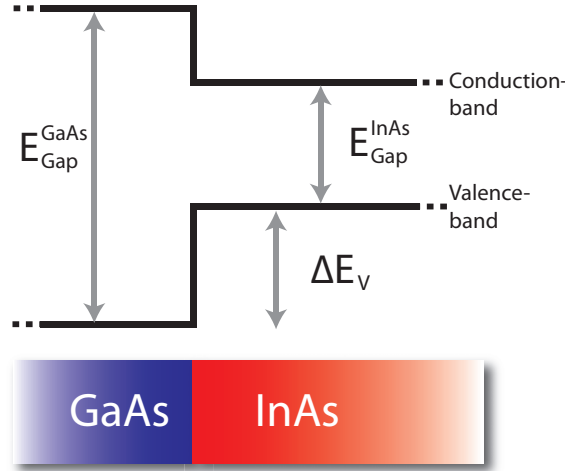


Figure 2.30.: Schematic energy diagram showing the band alignment at interfaces between GaAs and InAs by means of the valence band offset ΔE_v . The vertical axis labels energy, horizontal axis labels a spatial dimension, e.g. growth direction.

In a tight-binding calculation, the choice of the (unstrained) valence-band offset ΔE_v seems to be a crucial parameter, because it determines the depth of the confinement potential of both electrons and holes at once (see Fig. 2.30).

At a closer look, the choice of valence-band offset appears to be less important: as long as the number of confined states is high anyway, e.g. the Indium content is high, the influence of the choice of ΔE_v on the band gap and the level splittings is negligible. This was shown for example in [75], where a change of only 2% of the effective gap was reported while going from $\Delta E_v = 0.22$ eV to $\Delta E_v = 0.06$ eV. In the present NN sp^3s^* TB model a change of 1.2% in the band gap was calculated between $\Delta E_v = 60$ meV and $\Delta E_v = 120$ meV, in very good agreement with the literature. On the other hand the choice of ΔE_v becomes important in cases where QDs have low Indium content, because in this case the number of confined states is affected. This can lead to changes in the optical spectra due to a change in the configuration-interaction-basis⁷.

In the case of InAs QDs grown on GaAs the two materials form a type I interface (as sketched in Fig. 2.30). Since both materials share the same anions, the band offset tends to be rather small, according to the popular "common-anion-rule" [172–174]. The values of ΔE_v between GaAs and InAs interfaces in the literature span a large range from only a few meV up to several hundreds of meV [113–115]. See [117]

⁷The CI basis consists of all bound quantum dot states, at least in a full-CI treatment, to be introduced in section 3.1

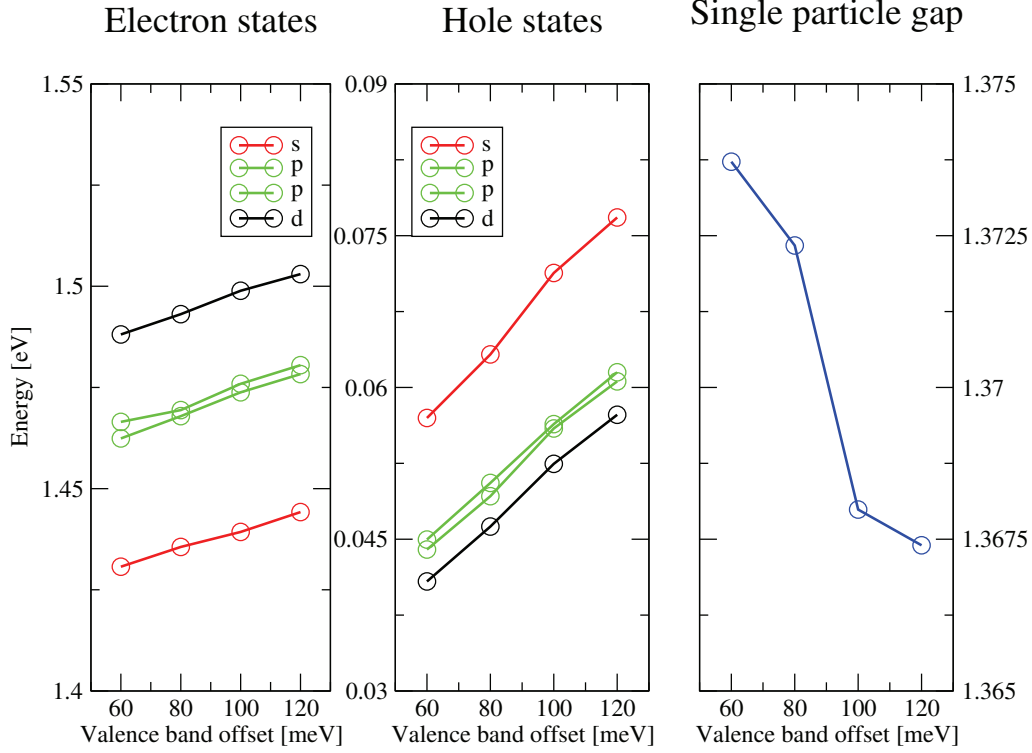


Figure 2.31.: Dependence of electron and hole single-particle energies (left hand and middle panel) and energy gap (right hand panel) on the choice of valence band offset ΔE_v .

and [175] for reviews. Since there is no accepted value for the valence band offset between GaAs and InAs we use a rather small value of 60 meV from [113], providing the best agreement with other calculations for the benchmark given in section 2.6.

In Fig. 2.31 the dependence of the single-particle electron and hole energies on the valence band offset ΔE_v is shown as well as the single-particle energy gap. ΔE_v was varied between 60 meV and 120 meV and a disk-shaped QD with diameter of 18 nm, height of 2.0 nm and an Indium concentration of 30% was assumed, similar to [176]. Bound electron and hole energies both show only a small dependence on the offset. While the raise of electron energies with the valence-band offset leads to smaller binding energies, the raise of hole energies leads to larger binding energies. This behaviour simply reflects the increase and decrease in depth of the confinement potentials for electrons and holes, respectively, as mediated by the valence-band offset.

2.9. Number of bound states

The number of bound electron and hole states is an important parameter for applications. It is mainly influenced by the depth of confinement (the Indium concentration in InGaAs QDs) and the geometry of the QD. Following the picture of a quantum harmonic oscillator, the number of confined hole states should always outnumber the number of confined electron states if the potential is equally deep, which would be the case for valence band offset and conduction band offset being equal. The reason for this is the larger effective mass of holes in the crystal, bringing the hole states closer together. In general, the two band-offsets are not equal, so the numbers of confined electron and hole states are independent. As the criterion for an electron (hole) state being confined in the nanostructure, two different methods can be applied.

As a first method the part of the occupation probability $|\psi|^2$ of the state under consideration inside the QD can be used as a measure for the state being bound or unbound. A certain number has to be defined as a threshold: If the part of the occupation probability inside the QD is larger (smaller) than the threshold, the state is considered as bound (not bound).

The second method utilizes the energy of the state to define whether it is bound or not. To do this, an independent calculation has to be carried out considering an empty system without the QD, only consisting of the WL inside the supercell. The band edges of this system, which are the highest WL hole state and the lowest WL electron state, are used to define the binding energies of the QD system. An electron (hole) is considered bound, if the corresponding energy is lower (higher) than the WL electron (hole) band edge. This energetic difference defines the binding energy of the bound states. Intuitively, a state with a positive binding energy is bound, while negative binding energies define unbound states.

Here, we use the second criterion since it introduces no artificial threshold and therefore appears natural to use.



Figure 2.32.: WL system consisting of two monolayers of InAs. Anions and cations of InAs are shown red and blue, while atoms belonging to the GaAs buffer are not shown for illustration.

In the following, calculations of the number of bound states were carried out for typical InGaAs QDs with low Indium concentration between 15% and 30%. The QDs are modelled lens-shaped with a height of 2.2 nm and a diameter of approximately 25 nm. The WL is assumed to have a height of two monolayers as shown in Fig. 2.32. The calculated WL band edge energies are given in Tab. 2.8.

e_1^{WL} [eV]	h_1^{WL} [eV]
1.4676	0.0629

Table 2.8.: Calculated band-edge energies of the InAs WL system which are used as reference to decide between bound and unbound QD-states.

As stated above, these energies are subject to the band offsets, the valence force field parametrization and, of course, the tight-binding parametrization.

In Fig. 2.33 the occupation probability for the ground hole WL state are visualized as cuts through the supercell representation in side-view. As expected, the probabilities reflect the translational symmetry of the WL perpendicular to growth direction and are symmetric around the WL center in growth direction.

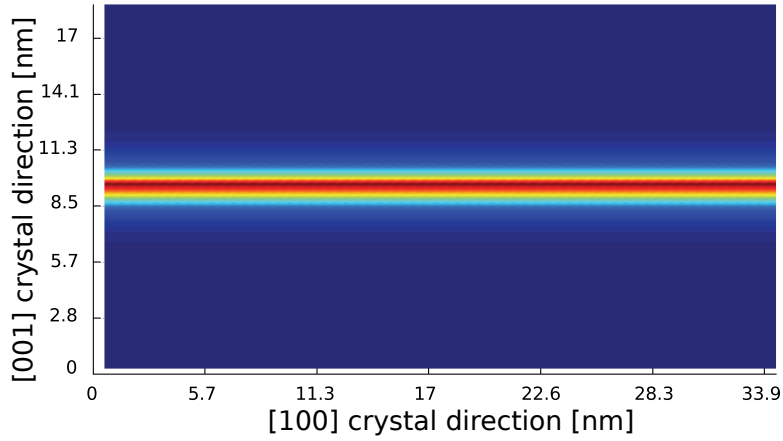


Figure 2.33.: Exemplary visualization of the occupation probability of the hole WL ground state in side-view (along the [010] crystal direction). Blue and red colors correspond to low and high occupation probability, respectively.

Having calculated the reference energies of the WL, the binding energies for different Indium concentrations of the QD were extracted. Results are presented in Tab. 2.9 for electrons and Tab. 2.10 for holes, respectively. Each listed energy represents a twofold spin degenerate bound state. Empty cells represent the onset of the continuum of delocalized states.

Quite intuitively, we observe that the number of bound states increases for larger Indium concentration, i.e. for a deeper confinement potential. For a typical QD as observed in experiments having an average Indium concentration of 20%, due to our calculations three electrons and five holes are expected to be bound. Experiments show typical number of bound states of one to four spin-degenerate energy levels [177]. For smaller QD Indium concentrations than 15% only one electron and hole are expected to be bound, having an energy approaching the WL band edges for

conc. [%]	E_{Gap} [eV]	e_1	e_2	e_3	e_4	e_5	e_6
15	1.3667	26.3	3.3	2.4			
17.5	1.3565	33.4	8.9	6.2			
20	1.3444	41.7	14.6	13.5			
22.5	1.3312	50.5	22.0	20.8			
25	1.3175	59.1	29.7	28.0	3.9	1.9	
30	1.2924	78.01	45.01	41.51	15.11	11.41	9.91

Table 2.9.: Electron binding energies and single-particle energy gap as a function of InGaAs QD Indium concentration. All energies are given in units of meV unless stated otherwise.

conc. [%]	h_1	h_2	h_3	h_4	h_5	h_6
15	10.644	4.144	2.894			
17.5	13.704	7.014	5.614	0.734		
20	17.534	10.104	8.514	3.024	1.144	
22.5	21.974	14.564	13.054	7.074	4.474	3.764
25	27.014	19.454	16.934	10.874	8.034	6.814
30	34.19	24.52	22.56	15.68	13.31	12.16

Table 2.10.: Hole binding energies as a function of InGaAs QD Indium concentration. All energies are given in units of meV unless stated otherwise.

Indium concentrations approaching zero.

From the calculated energies we can extract the following trends. Electron binding energies are growing faster than hole binding energies with increasing Indium concentration due to their lower effective mass. While splitting between the first and the second bound state (s - and p -like symmetries) gets larger with increasing Indium concentration, the splittings between the two nearly degenerate states with both p -like symmetry remain approximately constant for both electrons and holes.

3. Many-particle theory

Contents

3.1. Full Configuration Interaction	73
3.1.1. Coulomb matrix elements from TB wave functions	76
3.1.2. Many-particle states	78
3.1.3. Dipole matrix elements from TB wave functions	79
3.1.4. Excitonic spectrum	84
3.2. Excitonic fine-structure splitting	86

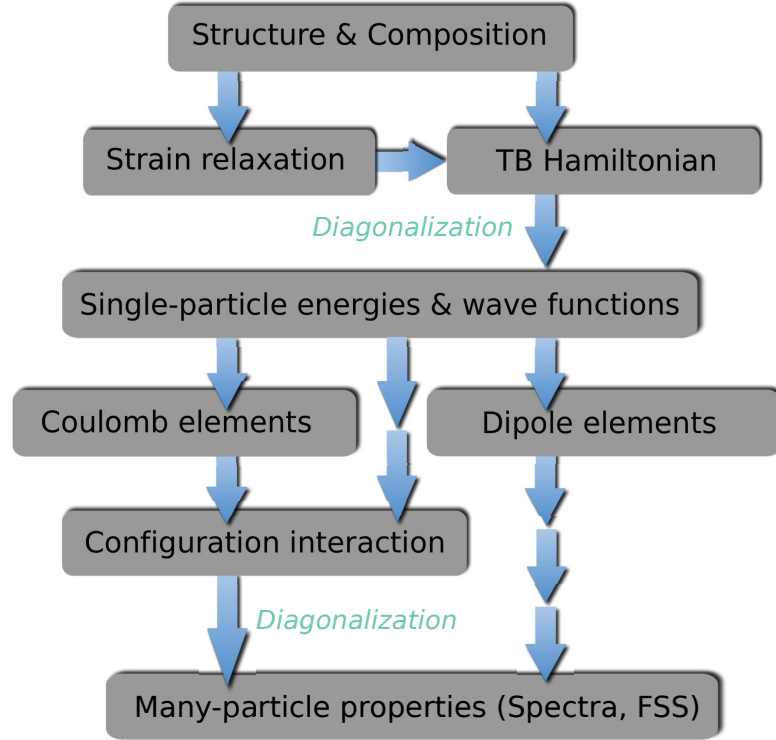


Figure 3.1.: Scheme of the computational flow in order to calculate many-particle properties of the QD carriers. Having obtained the single-particle energies and wave functions, interaction matrix elements can be calculated and many-particle properties are accessible via diagonalization of the configuration interaction Hamiltonian.

Single-particle energies and wave functions capture all structural properties of the QDs such as the shape, composition, strain distribution and microscopic realization. Therefore, single-particle properties are often used to describe the physical behaviour of semiconductor systems. On the other hand, in experiments the physical properties are determined by the many-particle interactions since usually there is more than only one particle bound in the QD. To be able to calculate optical emission and absorption spectra showing many-particle states like the exciton, trion, biexciton and others, it is necessary to allow for the carriers to interact with each other via Coulomb interaction on the one hand, and to couple the electronic system with the light field on the other hand. Those interactions can be accounted for in the so-called "Full Configuration Interaction" approach (FCI), which we base on the single-particle tight-binding energies and wave functions. Therefore we link single- and many-particle theory to comprehensively describe semiconductor quantum dots.

In this chapter the calculation of optical absorption and emission spectra via the FCI method will be introduced. In the end of the chapter we will focus on the excitonic fine-structure splitting (FSS), which is of great interest in the research field

concerning new devices for quantum information processing and quantum cryptography [178]. As shown in Fig. 3.1, the single-particle energies and wave functions calculated using the TB model are taken as input for the FCI and for the derivation of matrix elements in order to calculate optical spectra. In the following we do neglect electron-phonon interactions. Treating this interaction correctly would be topic for another thesis, see [179] for example.

3.1. Full Configuration Interaction

The most important mechanism for electrons and holes to interact is the Coulomb interaction. Two particles influence each other by renormalization of their energies and wave functions and to be precise, there is no such thing as two individual particles inside a quantum dot because their *individual* properties arise from the existence of the other particle. For example a pair of one bound electron and one bound hole form a quasiparticle called exciton because of the attraction caused by the opposite charges. Two electrons repulse each other, which also renormalizes the energies. If there is a third charge inside the dot, the quasiparticle trion plus or trion minus is built, depending on whether the third particle has positive or negative charge. Additionally, bound carriers in the QD are embedded in a matrix of bulk material with a continuum of delocalized carrier states, which gives rise to energy renormalizations due to the coupling to phonons (forming a new quasiparticle called polaron).

Since for our needs this renormalizations are of minor interest, we neglect them. For further information on carrier-phonon interaction see [179].

In the "Full Configuration Interaction" approach [180, 181] the Coulomb interaction between all bound single-particle states is taken into account. The FCI-Hamiltonian is formulated in the basis of single-particle configurations in which matrix elements for the Coulomb interaction are added. An example of these configurations is shown in Fig. 3.2, adopted from [19]. Since the Hilbert space for this problem grows exponentially with the number of states in consideration, and since in QDs showing strong carrier confinement (large QDs in size and/or QDs with a high Indium content) many bound states can be occupied by carriers, the number of states in the FCI is often reduced artificially. In this case, the Hilbert space is truncated and only the first few bound states for electrons and holes are taken into account. For such a truncation the method is called "Configuration Interaction" (CI) only.

The FCI Hamiltonian reads

$$H^{\text{FCI}} = H_0 + H_C, \quad (3.1)$$

allowing the free particles (H_0) to interact via Coulomb interaction (H_C). Intro-

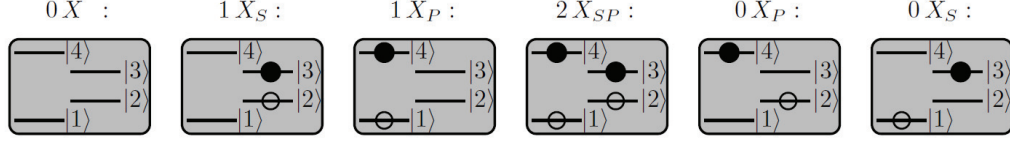


Figure 3.2.: Exemplary single-particle configurations for a QD having two confined states both for electrons and holes in the electron-hole picture, from [19]. For simplicity only one spin direction and only configurations with an even number of carriers are assumed. The s -states are labelled $|2\rangle$ and $|3\rangle$ while p -states are labelled $|1\rangle$ and $|4\rangle$. From left to right these configurations are: the empty dot; the exciton with the carriers occupying the s -shells (ground state exciton $1X_S$); the p -exciton $1X_P$; the biexciton $2X_{SP}$; the p - s -exciton $0X_P$; the s - p -exciton $0X_S$. Charged configurations with an odd number of carriers are not shown here.

ducing quasi-particle creation and annihilation operators λ_i^\dagger and λ_i where $\lambda_i^\dagger(\lambda_i)$ is either an operator on the electron- ($\lambda = e$) or hole-subspace ($\lambda = h$) creating (annihilating) an electron (hole) in the single-particle state i , the free particle part of the Hamiltonian is given by

$$H_0 = \sum_i \left(\epsilon_i^e e_i^\dagger e_i + \epsilon_i^h h_i^\dagger h_i \right). \quad (3.2)$$

Here, ϵ_i^e and ϵ_i^h are the single-particle electron and hole energies of state i as calculated by TB theory. The Hamiltonian H_C , allowing for carrier-carrier interaction between configurations, reads

$$H_C = \sum_{ijkl} V_{ijkl}^{\lambda_i \lambda_j \lambda_k \lambda_l} \lambda_i^\dagger \lambda_j^\dagger \lambda_k \lambda_l. \quad (3.3)$$

In the above equation, $V_{ijkl}^{\lambda_i \lambda_j \lambda_k \lambda_l}$ are the Coulomb matrix elements (CME) between particles in the states i, j, k and l . Depending on the operator sequence three categories of these matrix elements can be identified:

1. Band-diagonal interaction elements: $\lambda_i^\dagger \lambda_j^\dagger \lambda_k \lambda_l = e_i^\dagger e_j^\dagger e_k e_l$ or $h_i^\dagger h_j^\dagger h_k h_l$
2. Electron-hole direct interaction elements: $\lambda_i^\dagger \lambda_j^\dagger \lambda_k \lambda_l = e_i^\dagger h_j^\dagger h_k e_l$ or $h_i^\dagger e_j^\dagger e_k h_l$
3. Electron-hole exchange interaction elements: $\lambda_i^\dagger \lambda_j^\dagger \lambda_k \lambda_l = e_i^\dagger h_j^\dagger e_k h_l$ or $h_i^\dagger e_j^\dagger h_k e_l$.

The first category describes the simple repulsion between two carriers with equal charge. Following the operator notation, this process can be expressed as the annihilation of two carriers in the states k and l and the creation of two carriers in

the states i and j . The second category describes the direct attraction of carriers with different charge, where for example an electron in the state k and a hole in the state l are annihilated and an electron in state i and a hole in state j are created. The third category corresponds to the process of electrons and holes exchanging their states during the interaction. This interaction process occurs because of the undistinguishability due to the quantum nature of these particles. Although electrons and holes can be distinguished by their respective mass, these processes occur and therefore the matrix elements exist. Usually these interactions are neglected [127] because they have considerably smaller amplitude in comparison to the direct terms. Throughout this thesis these matrix elements are calculated explicitly since they are partly responsible for the excitonic fine-structure splittings. Showing all these processes as single contributions the FCI-Hamiltonian reads:

$$\begin{aligned}
H^{FCI} &= H_0 + H_C \\
&= \sum_i (\epsilon_i^e e_i^\dagger e_i + \epsilon_i^h h_i^\dagger h_i) \\
&+ \frac{1}{2} \sum_{ijkl} V_{ijkl}^{eeee} e_i^\dagger e_j^\dagger e_k e_l + \frac{1}{2} \sum_{ijkl} V_{ijkl}^{hhhh} h_i^\dagger h_j^\dagger h_k h_l \\
&- \sum_{ijkl} V_{ijkl}^{ehhe} e_i^\dagger h_j^\dagger h_k e_l - \sum_{ijkl} V_{ijkl}^{heeh} h_i^\dagger e_j^\dagger e_k h_l \\
&- \sum_{ijkl} V_{ijkl}^{eh eh} e_i^\dagger h_j^\dagger e_k h_l - \sum_{ijkl} V_{ijkl}^{he he} h_i^\dagger e_j^\dagger h_k e_l. \tag{3.4}
\end{aligned}$$

The factor of $\frac{1}{2}$ appears to avoid double counting. The minus sign in the electron-hole interactions appears due to the attractive nature of the different charges, the plus sign in the electron-electron and hole-hole interactions accounts for the repulsion between carriers of the same charge. To calculate the arising many-particle energies and wave functions, this Hamiltonian has to be diagonalized. The eigenenergies correspond to the many-particle energies as seen in experiments, the eigenstates of the Hamiltonian give the many-particle states in terms of mixing coefficients for the single-particle configurations.

3.1.1. Coulomb matrix elements from TB wave functions

In general, direct and exchange Coulomb matrix elements between carriers can be calculated by spatial integration of the corresponding carrier wave functions with the Coulomb potential:

$$V_{ijkl}^{dir} = \frac{e^2}{4\pi\epsilon\epsilon_0} \iint \frac{\psi_i^*(\mathbf{r}_1)\psi_j^*(\mathbf{r}_2)\psi_k(\mathbf{r}_2)\psi_l(\mathbf{r}_1)}{|\mathbf{r}_1 - \mathbf{r}_2|} d\mathbf{r}_1 d\mathbf{r}_2 \quad (3.5)$$

$$V_{ijkl}^{exch} = \frac{e^2}{4\pi\epsilon\epsilon_0} \iint \frac{\psi_i^*(\mathbf{r}_1)\psi_j^*(\mathbf{r}_2)\psi_k(\mathbf{r}_1)\psi_l(\mathbf{r}_2)}{|\mathbf{r}_1 - \mathbf{r}_2|} d\mathbf{r}_1 d\mathbf{r}_2. \quad (3.6)$$

Here $\psi(\mathbf{r})$ are the single-particle wave functions. The prefactor consists of the charges and the material dependent relative permittivity ϵ and the vacuum permittivity ϵ_0 (dielectric constant).

As shown in chapter 2.3.3, diagonalization of the tight-binding Hamiltonian in the basis of atomic orbitals yields the wave function coefficients in this basis. Only knowledge about the orbital symmetries, spatial orientations and energies enters the calculation, whereas no information about the basis functions is needed. Now for the calculation of the Coulomb matrix elements above, those basis functions are needed explicitly, at least in principle. However, due to the long-range nature of the Coulomb interaction, the basis functions intuitively appear less important than the overall variation of the wave function which enter the integral. Therefore, it is possible to approximately calculate the Coulomb matrix elements from the tight-binding coefficients directly. For a deeper discussion follow the appendix of [112]. We can use the tight-binding wave functions

$$\psi(\mathbf{r}) = \sum_{\tilde{\mathbf{R}}} c_{\tilde{\mathbf{R}}}(\mathbf{R}) \phi_{\tilde{\mathbf{R}}}(\mathbf{r}) \quad (3.7)$$

with the generalized index $\tilde{\mathbf{R}} = \{\mathbf{R}\alpha\nu\sigma\}$ for the calculation of the Coulomb matrix elements. $\phi_{\tilde{\mathbf{R}}}(\mathbf{r}) = \langle \mathbf{r} | \tilde{\mathbf{R}} \rangle$ are the (unknown) spatial representations of the basis orbitals. We plug Eqn. (3.7) in Eqn. (3.5), yielding:

$$V_{ijkl}^{dir} = \sum_{\tilde{\mathbf{R}}_1 \tilde{\mathbf{R}}_2 \tilde{\mathbf{R}}_3 \tilde{\mathbf{R}}_4} c_{\tilde{\mathbf{R}}_1}^{i*} c_{\tilde{\mathbf{R}}_2}^{j*} c_{\tilde{\mathbf{R}}_3}^k c_{\tilde{\mathbf{R}}_4}^l \iint d\mathbf{r}_1 d\mathbf{r}_2 V(\mathbf{r}_1 - \mathbf{r}_2) \phi_{\tilde{\mathbf{R}}_1}^*(\mathbf{r}_1) \phi_{\tilde{\mathbf{R}}_2}^*(\mathbf{r}_2) \phi_{\tilde{\mathbf{R}}_3}(\mathbf{r}_2) \phi_{\tilde{\mathbf{R}}_4}(\mathbf{r}_1) \quad (3.8)$$

with the Coulomb potential

$$V(\mathbf{r}_1 - \mathbf{r}_2) = \frac{e^2}{4\pi\epsilon\epsilon_0 |\mathbf{r}_1 - \mathbf{r}_2|}. \quad (3.9)$$

The variation of the wave functions within the interatomic distance, $\phi(\mathbf{r})$, is unknown and assumed to be of minor importance. Nevertheless, as before, it turns out

QD shape	V_{1111}^{hhhh}	V_{1111}^{eeee}	V_{1111}^{ehhe}	$V_{1111}^{eh eh}$
lens	30.37	33.57	31.66	0.25
pyramid	32.77	27.81	29.91	0.33
disk	30.34	24.69	27.02	0.26

Table 3.1.: Typical values of the Coulomb matrix elements for combinations of the s -like electron and hole states for the three standard quantum dots examined in the single-particle theory section as calculated from tight-binding wave function coefficients. All values are given in units of meV.

that Eqn. (3.8) can be approximated by using only the tight-binding wave function *coefficients*, which are defined on the discrete grid of (relaxed) atomic sites:

$$V_{ijkl}^{dir} \approx \sum_{\mathbf{R}_1 \mathbf{R}_2} c_{\mathbf{R}_1}^{i*} c_{\mathbf{R}_2}^{j*} c_{\mathbf{R}_2}^k c_{\mathbf{R}_1}^l V(\mathbf{R}_1 - \mathbf{R}_2) \quad (3.10)$$

where the potential now is a function of differences in atomic sites:

$$V(\mathbf{R}_1 - \mathbf{R}_2) = \begin{cases} \frac{e^2}{4\pi\epsilon_0|\mathbf{R}_1 - \mathbf{R}_2|} & \text{for } \mathbf{R}_1 \neq \mathbf{R}_2 \\ \frac{1}{V_{uc}} \int_{uc} d\mathbf{r}_1 d\mathbf{r}_2 \frac{e^2}{4\pi\epsilon_0|\mathbf{r}_1 - \mathbf{r}_2|} \approx V_c & \text{for } \mathbf{R}_1 = \mathbf{R}_2. \end{cases} \quad (3.11)$$

Here, V_c is a constant energy to be calculated only once and V_{uc} is the unit cell volume.

The approximation of using tight-binding wave function coefficients only is valid because of the long-ranging behaviour of the Coulomb interaction [112]. For numerical reasons the summations over lattice points for the calculation of the CMEs are carried out in the Fourier transformed basis [182]. Since the choice of the relative permittivity ϵ of the material surrounding the interacting carriers is not straightforward, we use the mean value for the materials occupying the supercell for the screening. In the case of InAs and GaAs this is a rather good choice, because the constants are quite similar: $\epsilon^{InAs} = 12.3$ and $\epsilon^{GaAs} = 10.89$ (both at room temperature [118]). In Tab. 3.1 we show typical values for the calculated Coulomb matrix elements between s -like single-particle states for the three standard QDs as defined in section 2.7 indicating the energy scales of direct and indirect Coulomb matrix elements in the InGaAs material system.

We can see that the direct Coulomb matrix elements all have the same energy scale, varying only within a few meV, while the exchange matrix elements are smaller by a factor of around 100. These values are in good agreement with typical magnitudes of the Coulomb matrix elements in the InAs/GaAs material system.

Once calculated, with these matrix elements the many-particle states can be derived from the diagonalization of the FCI-Hamiltonian. For the consecutive calculation of optical spectra featuring realistic relative peak heights, information is needed

about the strengths of optical transitions between the carrier configurations, which are represented by the dipole matrix elements.

3.1.2. Many-particle states

Having calculated the Coulomb matrix elements for carrier-carrier interaction between bound states in the quantum dot as discussed in the previous section, Coulomb-mediated many-particle states of the quantum dot can be calculated by numerical diagonalization of Eqn. (3.4). This diagonalization is carried out in the basis of single-particle configurations, giving the coefficients for linear combinations of the basis states.

For simplicity and numerical reasons we truncate the many-particle Hilbert space in two ways. Since the number of configurations scales as 2^N , with N being the number of single-particle states under consideration, the size of the Hilbert space is very large even for quantum dots with a medium confinement (medium-sized dots and/or intermediate Indium content). Only very few quantum dot experiments show confinements large enough to have more energy levels confined than the lowest levels which can be identified as s -, p - and d -like states. This is mostly due to the average Indium content being smaller than 20% in most experiments. Additionally, considering optical or electrical pumping of the quantum dot levels, the recombination times usually are fast enough to keep only the few lowest energy levels occupied with carriers.

With these considerations in mind we truncate the Hilbert space to particle numbers not exceeding 6, i.e. taking only s - and p -like states into account. With this we neglect small renormalizations of the many-particle energies because of the energetically higher lying states, but taking into account this d -like states would already enlarge the Hilbert space enormously. The other truncation of the Hilbert space we carry out is not necessary but keeps the spectra simple to interpret. We reduce the basis to configurations that conserve the number of particles in a way, that only configurations having the same number of electrons and holes form the basis. With this truncation we neglect charged excitons ($X^{1\pm}, X^{2\pm}, \dots$) but speed up the diagonalization procedure. Optical quantum dot spectra as investigated in this thesis are determined mainly by the direct excitonic transitions, as can be seen by the dipole matrix elements (to be discussed in the next section), so this second truncation appears to be a good approximation.

3.1.3. Dipole matrix elements from TB wave functions

For the calculation of optical emission and absorption spectra from semiconductor quantum dots it is necessary to describe the interaction of the quantum dot carriers with the electromagnetic field. In the literature there are elaborated methods to incorporate magnetic and electric fields directly into the tight-binding Hamiltonian [183, 184]. These methods are used for strong fields which influence the orbital energies and therefore have a direct impact on the single-particle energies. For weak fields, which vary slowly on the scale of typical quantum dot sizes, it is sufficient to treat the interaction in the widely used dipole approximation.

Within this approximation the light-matter coupling of a dipole \mathbf{d} in an electric field \mathbf{E} is given by the dipole Hamiltonian

$$H_D = -\mathbf{d}\mathbf{E}. \quad (3.12)$$

Without any loss of generality, we assume a linearly polarized electric field $\mathbf{E}(\mathbf{r}, t)$ with the direction of propagation along the wave vector \mathbf{k}

$$\mathbf{E}(\mathbf{r}, t) = \mathbf{E}_0^{[klm]} e^{i(\mathbf{k}\mathbf{r} - \omega t)} \quad (3.13)$$

with $\mathbf{E}_0^{[klm]} = (E_0^k, E_0^l, E_0^m)$ being the polarization vector with lattice parameters k, l and m and ω being the frequency. In our cases the polarization will most likely be along the $[110]$ and $[\bar{1}\bar{1}0]$ crystal directions, perpendicular to the growth direction. This results in

$$\mathbf{E}_0^{[110]} = \frac{1}{\sqrt{2}}(1, 1, 0) \quad (3.14)$$

and

$$\mathbf{E}_0^{[\bar{1}\bar{1}0]} = \frac{1}{\sqrt{2}}(1, -1, 0), \quad (3.15)$$

respectively. Considering emission from a quantum dot excitonic recombination, the absolute values of \mathbf{k} and \mathbf{r} can be estimated as

$$|\mathbf{k}| \cdot |\mathbf{r}| \approx \frac{2\pi}{\lambda} \cdot 10\text{nm} \approx \frac{2\pi}{1000\text{nm}} \cdot 10\text{nm} \approx 0.06 \ll 1. \quad (3.16)$$

Here we used a spatial distribution of the exciton wave function of 10 nm [185], which is strongly localized in a quantum dot emitting at a typical emission wavelength of around 1000 nm for InGaAs quantum dots. $|\mathbf{k}| \cdot |\mathbf{r}| \ll 1$ translates into the field varying only slowly on the QD scale, the dipole approximation can be used, which means neglecting the spatial variation of the electric field.

Writing the approximate dipole Hamiltonian gives

$$H_D = -\mathbf{d}\mathbf{E}_0^{[klm]} \quad (3.17)$$

or, in second quantization,

$$H_D = - \sum_{i=1}^{N_e} \sum_{j=1}^{N_h} [D_{ij} \underbrace{c_{e,i}^\dagger c_{h,j}^\dagger}_{\text{absorption}} + D_{ij}^* \underbrace{c_{e,i} c_{h,j}}_{\text{emission}}] \quad (3.18)$$

with N_e and N_h being the number of single-particle bound states of electrons and holes, respectively, and $c_{e,i}^\dagger$ ($c_{e,i}$) being a creation (annihilation) operator for electrons. The constants d_{ij} are the matrix elements of the dipole operator $\mathbf{d} = e_0 \hat{\mathbf{r}}$ with e_0 being the electric charge and $\hat{\mathbf{r}}$ being the position operator. They enter the Hamiltonian via $D_{ij} = d_{ij} \mathbf{E}_0^{[klm]}$. The calculation of these matrix elements has been discussed in the literature to some extent [112], because different contributions enter the matrix elements, as will be shown in the following.

In general the matrix elements of the dipole Hamiltonian in the basis of tight-binding wave functions read

$$D_{ij} = \langle \psi_{e_i} | H_D | \psi_{h_j} \rangle \quad (3.19)$$

$$= \sum_{\mathbf{R}, \alpha \nu \sigma} \sum_{\mathbf{R}', \alpha' \nu' \sigma'} c_{\mathbf{R}, \alpha \nu \sigma}^{e_i^*} c_{\mathbf{R}', \alpha' \nu' \sigma'}^{h_j} \langle \mathbf{R}, \alpha \nu \sigma | H_D | \mathbf{R}', \alpha' \nu' \sigma' \rangle \quad (3.20)$$

$$= e_0 \sum_{\mathbf{R}, \nu} \sum_{\mathbf{R}', \nu'} c_{\mathbf{R}, \nu}^{e_i^*} c_{\mathbf{R}', \nu'}^{h_j} \langle \mathbf{R}, \nu | \hat{\mathbf{r}} \mathbf{E}_0^{[klm]} | \mathbf{R}', \nu' \rangle \quad (3.21)$$

with the nomenclature used before with the spatial position \mathbf{R} , the atom type α , atomic orbitals ν and spin σ . In the last term, the spin index has been dropped because in the dipole approximation no spin-flips are allowed, so H_D is diagonal in spin. Additionally the atom type index can be dropped because $\alpha = \alpha(\mathbf{R})$.

In the tight-binding treatment, the wave functions

$$\psi = \sum_{\mathbf{R}, \alpha \nu \sigma} \underbrace{c_{\mathbf{R}, \alpha \nu \sigma}}_{\text{envelope}} \underbrace{|\mathbf{R}, \alpha \nu \sigma\rangle}_{\text{orbital}} \quad (3.22)$$

exhibit two contributions. The first is the global variation of the wave function, described by the tight-binding coefficients $c_{\mathbf{R}, \alpha \nu \sigma}$ and called the envelope part. The local variation of the wave function is given by orbitals at a certain atomic position and is called orbital part [186–188].

We can formulate the position operator with respect to these two contributions:

$$\hat{\mathbf{r}} = \sum_{\mathbf{R}, \nu} |\mathbf{R}, \nu\rangle \mathbf{R} \langle \mathbf{R}, \nu| + \sum_{\mathbf{R}, \nu} \sum_{\mathbf{R}', \nu'} |\mathbf{R}, \nu\rangle \langle \mathbf{R}, \nu| \tilde{\mathbf{r}} |\mathbf{R}', \nu'\rangle \langle \mathbf{R}', \nu'|. \quad (3.23)$$

In this expression, \mathbf{R} and \mathbf{R}' are the discrete atomic positions, whereas the space in between is described by the vector $\tilde{\mathbf{r}} = \hat{\mathbf{r}} - \mathbf{R}$ relative to these discrete positions.

Evaluating the dipole matrix elements with this operator gives the envelope part

$$\begin{aligned}
D_{ij}^{\text{env}} &= e_0 \sum_{\mathbf{R}, \nu} \sum_{\mathbf{R}', \nu'} c_{\mathbf{R}, \nu}^{e_i^*} c_{\mathbf{R}', \nu'}^{h_j} \langle \mathbf{R}, \nu | \left[\sum_{\mathbf{R}'', \nu''} |\mathbf{R}'', \nu''\rangle c_e(\mathbf{R}, \mathbf{E}_0^{[klm]}) \langle \mathbf{R}'', \nu'' | \right] | \mathbf{R}', \nu' \rangle \\
&= e_0 \sum_{\mathbf{R}, \nu} \sum_{\mathbf{R}', \nu'} \sum_{\mathbf{R}'', \nu''} c_{\mathbf{R}, \nu}^{e_i^*} c_{\mathbf{R}', \nu'}^{h_j} c_e(\mathbf{R}, \mathbf{E}_0^{[klm]}) \delta_{\mathbf{R}\mathbf{R}''} \delta_{\mathbf{R}''\mathbf{R}'} \delta_{\nu\nu''} \delta_{\nu''\nu'} \\
&= e_0 \sum_{\mathbf{R}, \nu} c_{\mathbf{R}, \nu}^{e_i^*} c_{\mathbf{R}, \nu}^{h_j} c_e(\mathbf{R}, \mathbf{E}_0^{[klm]})
\end{aligned} \tag{3.24}$$

with the scalar expression

$$c_e(\mathbf{R}, \mathbf{E}_0^{[klm]}) = \mathbf{R} \cdot \mathbf{E}_0 = R^k E_0^k + R^l E_0^l + R^m E_0^m \tag{3.25}$$

describing the dipole moment between envelope functions of the same orbitals at the same atomic site. The orbital part is

$$\begin{aligned}
D_{ij}^{\text{orb}} &= e_0 \sum_{\mathbf{R}, \nu} \sum_{\mathbf{R}', \nu'} c_{\mathbf{R}, \nu}^{e_i^*} c_{\mathbf{R}', \nu'}^{h_j} \langle \mathbf{R}, \nu | \left[\sum_{\mathbf{R}'', \nu''} \sum_{\mathbf{R}''', \nu'''} |\mathbf{R}'', \nu''\rangle \right. \\
&\quad \left. \langle \mathbf{R}'', \nu'' | \tilde{\mathbf{r}} | \mathbf{R}''', \nu''' \rangle \langle \mathbf{R}''', \nu''' | \right] | \mathbf{R}', \nu' \rangle,
\end{aligned} \tag{3.26}$$

yielding

$$\begin{aligned}
D_{ij}^{\text{orb}} &= e_0 \sum_{\mathbf{R}, \nu} \sum_{\mathbf{R}', \nu'} \sum_{\mathbf{R}'', \nu''} \sum_{\mathbf{R}''', \nu'''} c_{\mathbf{R}, \nu}^{e_i^*} c_{\mathbf{R}', \nu'}^{h_j} \langle \mathbf{R}'', \nu'' | \tilde{\mathbf{r}} | \mathbf{R}''', \nu''' \rangle \delta_{\mathbf{R}\mathbf{R}''} \delta_{\mathbf{R}''\mathbf{R}'} \delta_{\nu\nu''} \delta_{\nu''\nu'} \\
&= e_0 \sum_{\mathbf{R}, \nu} \sum_{\mathbf{R}', \nu'} c_{\mathbf{R}, \nu}^{e_i^*} c_{\mathbf{R}', \nu'}^{h_j} \langle \mathbf{R}, \nu | \tilde{\mathbf{r}} | \mathbf{R}', \nu' \rangle
\end{aligned} \tag{3.27}$$

with the matrix elements between different orbitals at different sites $\langle \mathbf{R}, \nu | \tilde{\mathbf{r}} | \mathbf{R}', \nu' \rangle$. Both parts together give

$$D_{ij} = D_{ij}^{\text{env}} + D_{ij}^{\text{orb}} \tag{3.28}$$

$$= e_0 \sum_{\mathbf{R}, \nu} \sum_{\mathbf{R}', \nu'} c_{\mathbf{R}, \nu}^{e_i^*} c_{\mathbf{R}', \nu'}^{h_j} \left[c_e(\mathbf{R}, \mathbf{E}_0^{[klm]}) \delta_{\mathbf{R}\mathbf{R}'} \delta_{\nu\nu'} + \langle \mathbf{R}, \nu | \tilde{\mathbf{r}} | \mathbf{R}', \nu' \rangle \right]. \tag{3.29}$$

The matrix elements from the orbital part read

$$\langle \mathbf{R}, \nu | \tilde{\mathbf{r}} | \mathbf{R}', \nu' \rangle = \int d^3\tilde{\mathbf{r}} \tilde{\phi}_{\mathbf{R}}^*(\tilde{\mathbf{r}}) \tilde{\mathbf{r}} \phi_{\mathbf{R}'}(\tilde{\mathbf{r}}) \tag{3.30}$$

and it is a well-known shortcoming of the empirical tight-binding approach that the explicit local basis functions $\phi_{\mathbf{R}}(\tilde{\mathbf{r}})$ are not known. Different authors employ different approximations for the orbital part: Leung et al. [188] for example neglect contributions from dipole moments from different atomic sites, stating their contribution being at least one magnitude smaller than the contributions from same-atom

dipole moments, and treat the matrix elements from different orbitals at the same atomic site as fitting parameters. Other authors [186] use atomic Slater orbitals [189] for the unknown local basis functions to calculate the matrix elements explicitly. Since using Slater orbitals is spoiled by the non-orthogonality of the orbitals at different atomic sites, numerically orthogonalized Slater orbitals have been used [112, 190]. Changes in the dipole elements were found to be small using standard or numerically orthogonalized Slater orbitals for on-site contributions [112]. However, for the system investigated in [112] the importance of the envelope contribution in comparison to the orbital contribution was pointed out by the result that the latter contributions were by a factor of 30 smaller than the first contributions. In [191], it was stated that the orbital contributions become important for intraband transitions as needed in detectors for example. In [187] it was emphasized, that the optical spectra are dominated mainly by the symmetries of the bound electron and hole wave functions. Following these arguments and considering that we are interested mainly in the electronic properties and their influences in the spectra, we calculate optical spectra by neglecting all orbital contributions to the dipole moments. This gives

$$\begin{aligned} D_{ij} &\approx D_{ij}^{\text{env}} \\ &= e_0 \sum_{\mathbf{R}, \nu} c_{\mathbf{R}, \nu}^{e_i*} c_{\mathbf{R}, \nu}^{h_j} c_e(\mathbf{R}, \mathbf{E}_0^{[klm]}). \end{aligned} \quad (3.31)$$

With these dipole matrix elements, we are able to calculate optical spectra not only by the energies occurring through the diagonalization of the many-particle Hamiltonian, but also include information about the relative peak heights, allowed and forbidden transitions as well as selection rules, all of which are contained in the dipole matrix elements. Nevertheless, the results have to be read with care because of the approximations used while deriving the matrix elements.

Typical dipole matrix elements for the standard lens-shaped pure InAs QD are shown for light field polarization along [110] and $[1\bar{1}0]$ in Figs. 3.3 and 3.4, respectively. On the left side electron states are indicated including spin index, e.g. electron state “1” is the lowest bound electron state having *s*-like symmetry and spin in one direction, while electron state “2” is the energetic degenerate *s*-like state having the same energy and opposite spin. Colors code the calculated transition strength. Due to the approximations made in the calculation of the dipole matrix elements, the absolute values of the dipole matrix elements are of minor importance, while the relative peak heights are interesting here, giving the differences in transition strengths of various recombination channels.

The matrix of dipole elements divides into three subblocks of transitions between states with the same symmetry: The first block being between electron and hole *s*-like states, the second between electron and hole *p*-like states and the third block being between all calculated *d*-like states. Transitions between states with different symmetries have very low amplitudes and therefore are unlikely to occur. From the relative values it can be seen, that in our system of an InGaAs QD the electron-hole

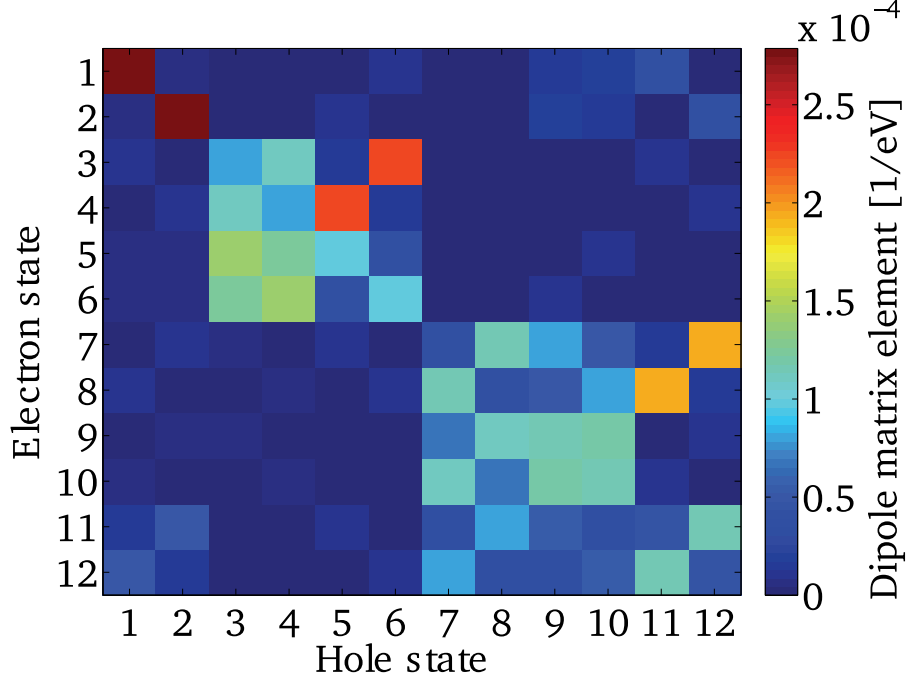


Figure 3.3.: Dipole matrix elements for the standard pure InAs QD with lens shape for polarization along [110] between the first twelve electron and hole bound states.

s -to- s transitions dominate over the p -to- p transitions, which are in turn stronger than the d -to- d transitions.

In the s -symmetry subblock it can be seen, that spin-degenerate states are perpendicular: for a given polarization only one of the electron states with a given energy has a non-vanishing transition strength with a single hole state, the transition from the other electron state is forbidden by the wave functions' symmetry properties. This leads to two dark and two bright excitonic transitions¹, discussed in the following sections. By comparison of the dipole matrix elements for the different polarizations, selection rules for different spin-combinations for the light polarization can be identified. For one polarization two excitonic transitions are bright, while for the other polarization the other two transitions appear bright, as can be seen for example in the sub-block for the first two electron and hole states in Figs. 3.3 and 3.4.

¹Excitonic here means the lowest excitonic transitions between electron and hole s -like states.

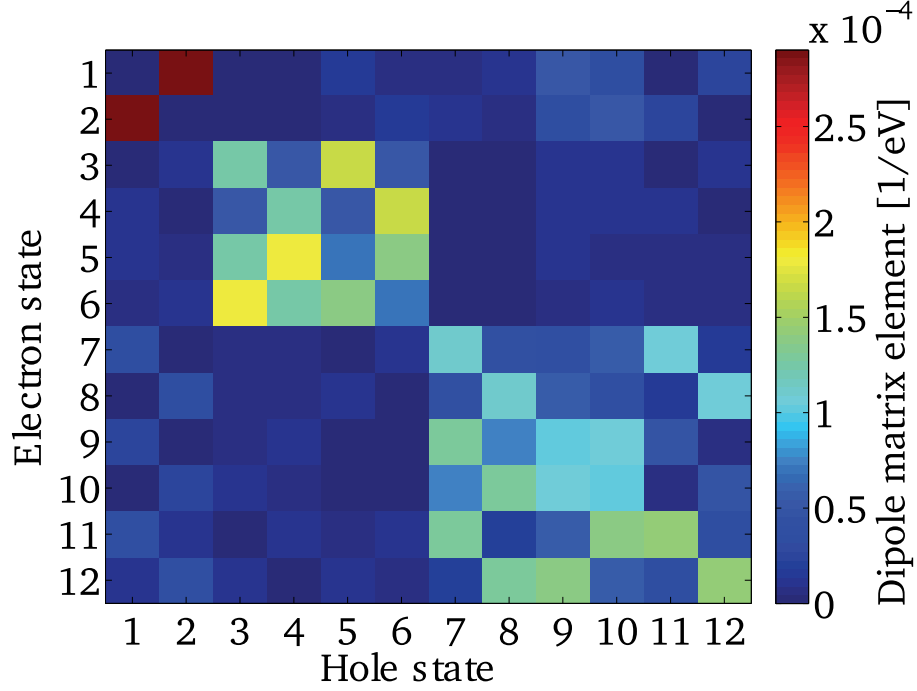


Figure 3.4.: Dipole matrix elements for the standard pure InAs QD with lens-shape for polarization along $[1\bar{1}0]$ between the first twelve electron and hole bound states.

3.1.4. Excitonic spectrum

Having obtained the many-particle states by diagonalization of H^{FCI} and the dipole matrix elements by evaluation of equation (3.31), optical spectra can be calculated. We use the perturbative approach via Fermi's golden rule [192, 193], in which the intensity I_{if} of a dipole-mediated transition between an initial many-particle state ψ_i and a final many-particle state ψ_f is given by

$$I_{if} = |\langle \psi_f | H_D | \psi_i \rangle|^2. \quad (3.32)$$

With this, the optical spectra can be calculated by evaluation of

$$\begin{aligned} I(E) &= \sum_i \sum_f I_{if} \frac{\Delta}{\Delta^2 + (E_{if} - E)^2} \\ &= \sum_i \sum_f |d_{if}|^2 \frac{\Delta}{\Delta^2 + (E_{if} - E)^2} \end{aligned} \quad (3.33)$$

where

$$E_{if} = E_i - E_f \quad (3.34)$$

is the energetic difference between initial and final state. The emission lines are homogeneously broadened with a Lorentzian (being the Fourier-tranform of the

exponential decay) of width Δ . Typical values for the broadening are $\Delta \approx 0.1$ meV for single quantum dots. Additional inhomogeneous broadening occurs in an ensemble of QDs due to size and composition fluctuations, with typical values of $\Delta_{inh} \approx 10\text{-}25$ meV.

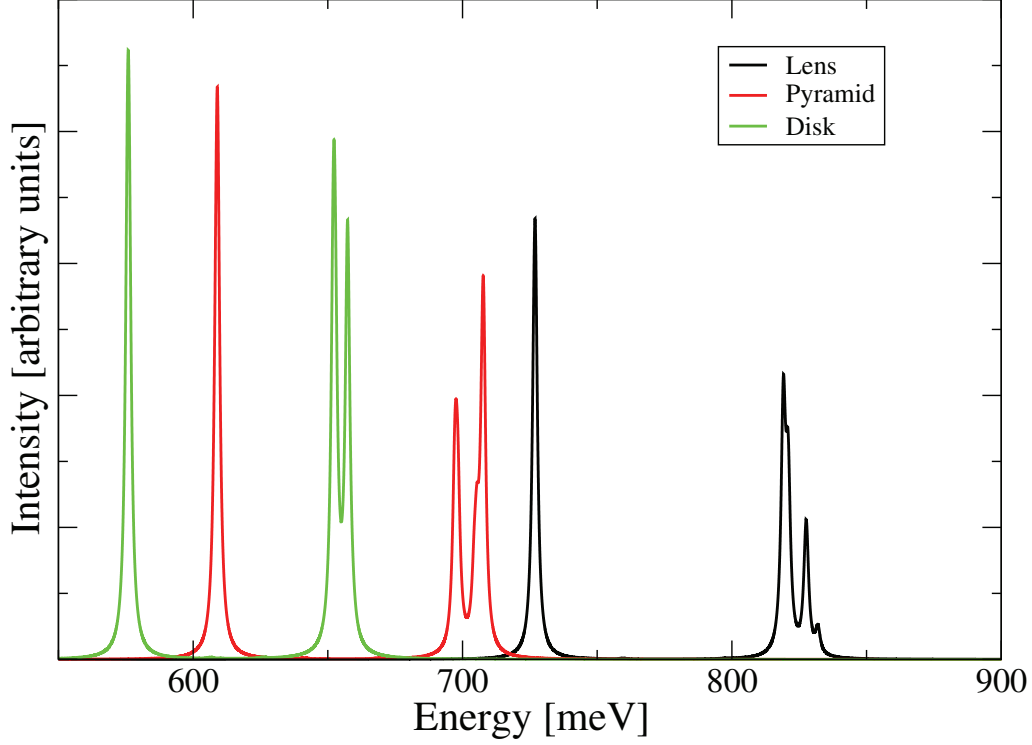


Figure 3.5.: Emission spectra of the three standard QDs for [110] polarization using a homogeneous broadening of $\Delta = 1$ meV. For each geometry transitions between *s*-like and *p*-like states can be identified.

In Fig. 3.5 the calculated emission spectra of the three standard pure InAs QDs having lens-, truncated pyramid- and disk-shape are displayed. Peak positions are renormalized by Coulomb interaction, while the relative peak heights are determined by the dipole matrix elements. A homogeneous broadening of 1 meV was assumed. Because of the large Hilbert space of the FCI, a CI featuring six electron and hole basis states was carried out. This leads to only *s*- and *p*-like excitonic transitions being visible, showing the calculated difference in peak heights: *s*-like excitonic transitions dominate the spectrum for each geometry. For clarity, only excitonic transitions are displayed, neglecting transitions from higher quasi particles like the biexciton as well as transitions from charged excitons.

3.2. Excitonic fine-structure splitting

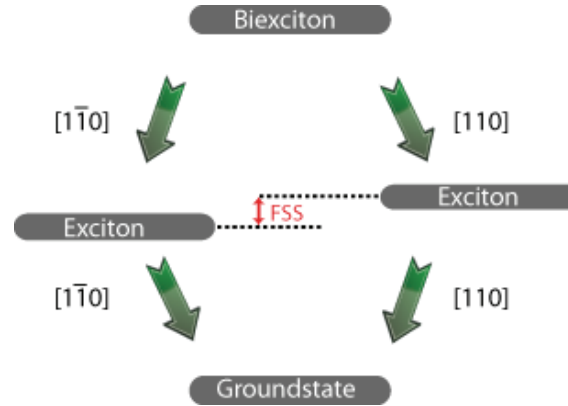


Figure 3.6.: Scheme of the cascaded decay of a biexciton into the ground state via intermediate excitonic states. Depending on the polarization of the first decay, the polarization of the second decay is fixed. The intermediate exciton states show a small energy splitting caused by electron-hole Coulomb exchange interaction, labelled FSS.

Ever since Albert Einstein’s idea of a “spooky action at a distance” [194], the concepts of indistinguishability and entanglement are subjects of discussion, though inherent in quantum physics. Two particles are indistinguishable if they coincide in all their properties, e.g. their quantum numbers. If two or more particles are correlated in such a way, that the whole system does not factorize, i.e., its density matrix has no independent subblocks, the system is in a superposition state. Here, the properties of the single particles are not distinct, unless a measurement is performed (the famous cat experiment) and the particles are called entangled. If the system consists of two photons, for example created by parametric down conversion, entanglement can be the correlation in the polarization of the two photons. Since the polarization of the initial single photon is known, and a conservation law for angular momentum exists, the sum of angular momenta of the two created photons is known as well. Therefore, if a measurement is taken on one particle, the outcome of measurement at the other particle at any subsequent time is known as well. Without a measurement being performed, entanglement is naturally degraded by dephasing processes via the interaction with the environment.

In the present case, entangled photons from semiconductor quantum dots can be created via the biexciton-exciton-groundstate cascade [195] as shown in Fig. 3.6 or in a direct two-photon emission process [196]. Here, we will concentrate on the cascaded emission process, starting from the biexciton, where two electrons and two holes are correlated by Coulomb interaction. The biexciton decays into the exciton by creation of a photon either polarized along the [110] or along the [1-10] crystal direction. Subsequently, the exciton decays into the groundstate by emission of

another photon, with a polarization defined by that of the first photon, as can be seen in Fig. 3.6. After emission of the two photons, no information about the decay path is available, if the excitonic states are energetically degenerate and therefore, the photon pair is entangled in polarization. These polarization entangled photon pairs are needed for various purposes such as quantum communication devices, quantum computing applications and quantum cryptography.

Nevertheless, in reality the two bright excitonic states are split by a small amount of energy, typically between a few and a few hundred μeV , called the excitonic fine-structure-splitting (FSS). This splitting occurs because of the Coulomb exchange interaction and gives the photons a "which-path" information, which affects the entanglement of the photons. If the FSS is smaller than or comparable to the homogeneous linewidth of the transitions, entanglement still exists, because the "which-path" information is inaccessible due to the linewidth. If the FSS is larger than the linewidth, the degree of entanglement is reduced to a value between unity and zero, corresponding to full entanglement and no entanglement, respectively.

Quantum cryptographic protocols [178, 197] based on polarization-entangled photons need a certain minimum degree of entanglement for efficient error correction and transmission of keys in the same way that long-range fiber communication or quantum computing devices need entanglement as large as possible. This is spoiled by the natural FSS.

In the last decade, large efforts were made to control the excitonic fine-structure splitting in single semiconductor quantum dots in order to achieve highly entangled photon pairs. Initially, the FSS was thought to arise from a shape asymmetry of the QDs alone, a misconception to be clarified by Bester et al. [36]. In QDs, the FSS stems from the Coulomb exchange interaction between the bound carriers inside the quantum dot as well as from the lattice asymmetry in zincblende crystals between $[110]$ - and $[\bar{1}\bar{1}0]$ -directions and the lattice distortion (symmetry lowering) by strain. Many different techniques, including the application of electric [198] and magnetic fields [199] or growth control and post selection techniques have been applied successfully to reduce the FSS. Also tuning of the FSS with application of external stress has been realized [200]. Nevertheless, in device applications external factors like electromagnetic fields are hard to integrate because each quantum dot has a unique realization in terms of mean concentrations, shapes, sizes and, of course, a unique FSS. Therefore, the search for standardized small FSSs in QDs is still not finished, although single-photon sources with near-unity indistinguishability have been reported [201].

In experiments, the FSS is measured as the energetic distance of the two excitonic peaks arising in the photoluminescence spectrum for $[110]$ - and $[\bar{1}\bar{1}0]$ -polarization, respectively [126]. In our TB-CI model the FSS can be calculated in the same way, as indicated in the following. After having calculated the Coulomb matrix elements

QD shape	$d - d$ [μeV]	$d - b$ [μeV]	FSS [μeV]	$E_B(2X)$ [meV]
lens	49.3	459.3	58.7	-3.23
pyramid	11.8	596.3	65.6	-2.87
disk	41.5	446.4	28.0	-2.43

Table 3.2.: Excitonic fine-structure splittings and biexciton binding energies $E_B(2X)$ of the three standard QDs. $d - d$ labels dark-dark exciton splitting, $d - b$ the splitting between dark and bright and FSS the splitting between the two bright exciton states.

including electron-hole exchange interaction, the excitonic spectrum can be calculated. As known from textbooks, the exciton is fourfold degenerate if Coulomb interaction is absent and is split into two doublets, called dark and bright exciton by direct Coulomb interaction. These doublets are further split by the Coulomb exchange interaction and the FSS labels the splitting between the two bright excitons. In the many-particle energy spectrum including Coulomb interaction, the splitting between the states of fourth and fifth lowest energy equals the FSS. The energetically lowest many-particle state always is the ground-state (empty QD), followed by the two dark exciton states, followed by the two bright exciton states [202]. In the same way, biexciton binding energies can be calculated as the energetic distance of the lowest biexciton many-particle state to the bright exciton states.

In Tab. 3.2 we exemplarily show the excitonic fine-structure and the biexciton binding energy $E_B(2X)$ of the three standard pure InAs QDs defined in the single-particle chapter. Each TB-realization of a QD has its very own distribution of atoms inside the supercell and with this a unique strain-distribution. Therefore, these splittings are valid for the particular realization and will differ for another unique supercell realization. Nevertheless, both fine-structure splittings and biexciton binding energies agree well with literature values [126, 203, 204]. The influence of atomic realizations on the FSS will be discussed in section 4.1.

Fig. 3.7 displays the excitonic fine-structure of a pure InAs QD having lens shape for two perpendicular light polarizations. Four lines can be identified, being the two dark excitons on the left hand side and the two bright exciton lines on the right hand side. Despite the dark excitons should be non-visible because they are dipole-forbidden, because of the approximations made during the derivation of the dipole matrix elements by neglecting the orbital part of the tight-binding wave functions, they have small oscillator strength. Nevertheless, in comparison to the bright excitons, emission from the dark excitons is negligible. The spectrum reveals a splitting between the dark excitons of $54 \mu\text{eV}$, a dark-bright splitting of $565 \mu\text{eV}$ and a splitting of the bright exciton states, the FSS, of $63 \mu\text{eV}$. Another feature in the high-resolution spectrum is the polarization anisotropy. Possible combinations of spin quantum numbers in the recombination of heavy holes and electrons result in the excitonic transitions having angular momenta of ± 1 and ± 2 , forming bright

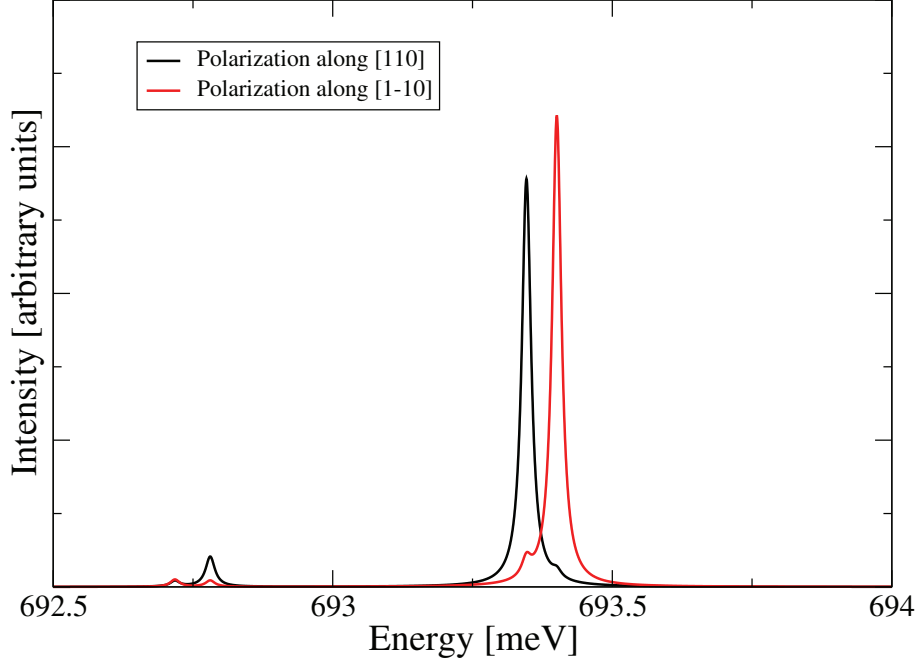


Figure 3.7.: High resolution spectrum of an InAs QD showing the excitonic fine-structure of dark and bright excitons. An artificially small broadening of $\Delta = 0.01$ meV was assumed for illustration purposes.

and dark excitons. Since the polarized electric field couples either to $+1$ or -1 for perpendicular polarizations, for each polarization one of the bright exciton states is dipole-allowed, resulting in the polarization anisotropy.

Having the fine-structure splittings in mind, which are of the order of μeV , we note that the accuracy of these splittings is not restricted by the accuracy of the TB band structure fitting parameters. Those parameters define the accuracy of the band structure up to usually around 10 meV and depend on the accuracy of experimental parameters during the fitting process themselves. On the contrary, the excitonic fine-structure splitting is a property of the wave functions, which in turn reflect the atomistic structure of the confinement potential by their spatial variation. The accuracy of this splitting therefore does not depend on the accuracy of the TB parameters. Since the magnitude of the splittings coincides very well with experimental values, our TB model seems to be a valid method. Also, no more elaborate models for the calculation of the excitonic FSS are known than pseudopotential or TB models.

After having established the theory of the calculation of single-particle energies and wave functions within the NN sp^3s^* tight-binding model we introduced the theory for calculation of many-particle energies and emission spectra within the CI approach using Coulomb and dipole matrix elements from TB wave functions. In the following Section applications of this powerful model are presented.

4. QDs in single-photon emitters and laser devices

Contents

4.1. Evolution of FSS under SRL influence	93
4.1.1. Introduction	93
4.1.2. System	94
4.1.3. Results and discussion	95
4.2. Optical gain in QD active media	99
4.2.1. Optical gain	99
4.2.2. Envelope approximation	100
4.2.3. Realistic envelopes	103
4.2.4. Negative differential gain in QD systems	107
4.2.5. Results and discussion	108
4.3. Conclusion	113

In this chapter, results using our next-neighbour sp^3s^* tight-binding model in combination with the configuration interaction treatment introduced in the previous chapters are presented. These results clearly answer the questions raised in the introduction regarding InGaAs QDs to be employed as optical components. Being closely connected to future device applications, our results can guide device design for next generation quantum dot lasers, quantum repeaters and entanglement devices.

The first section reports on InAs QDs tailored by the use of a strain-reducing layer (SRL) to emit at the telecom long-wavelength windows of 1.3 and 1.5 μm , which are favorable for long-range communication due to low fiber-absorption. The SRL is an additional InGaAs quantum well on top of the WL embedding the QD. The question is answered, whether the excitonic FSS, which must be small for entanglement purposes, depends on the Indium content of the strain-reducing layer. Results are published in [124]. The work presented in this section was done in most instances by the first author, while the other authors contributed by supplying partial program code and consultancy.

The second section concerns InGaAs QDs being the active medium of a semiconductor laser. Theoretically predicted by means of quantum-kinetic models and experimentally observed recently, a reduction of the optical peak gain (the amplification of the light field due to stimulated emission during passing the active medium) with high excitation values can be observed. We give a short introduction into the theoretical background and discuss the effect in detail using realistic modelling of the bound state energies and wave functions via our sp^3s^* tight-binding model. Different regimes for the emergence of the effect are discussed with respect to structural QD properties. Results regarding this section can be found in [205]. This work was done in equal parts by the first two authors, while the other authors contributed by consultancy. The first author contributed by carrying out the single-particle calculations in the tight-binding model as well as the fitting of the obtained TB wave functions to their analytical counterparts, while the second author contributed by the calculation of the optical gain spectra based on these wave functions via solution of the semiconductor Bloch equations. Parts of the text passage regarding the gain theory were formulated by the second author.

4.1. Evolution of FSS under SRL influence

In this section, the variation of the excitonic fine-structure splitting (FSS) is studied for semiconductor quantum dots under the influence of a strain-reducing layer, utilized to shift the emission wavelength of the excitonic transition into the telecom-wavelength regime of $1.3\text{-}1.5\mu\text{m}$. By means of a sp^3s^* -tight-binding model and configuration interaction we calculate wavelength shifts and fine-structure splittings for various quantum dot geometries. We find the splittings remaining small and even decreasing with strain-reducing layer composition for quantum dots with large height. Combined with an observed increased emission efficiency, the applicability of InAs QDs in SRL geometry for generation of entangled photons is persistent.

4.1.1. Introduction

QD photons as components for the use in quantum cryptography and quantum teleportation applications must have specific properties. On the one hand, for long-range transmission it is crucial to have photon emission at wavelengths for which the fiber absorption is minimal. On the other hand, high-degree polarization entanglement is essential in quantum cryptography protocols [178].

Emission via the biexciton-exciton cascade of a single QD has been identified as a promising candidate producing distinctive entangled photons [195]. The degree of entanglement is directly related to the intrinsic excitonic fine-structure splitting (FSS) which spoils the entanglement with increasing absolute value [206] as discussed in the previous section. Various successful attempts have been made to minimize the FSS: post-growth selection, application of external stress [200] or of external fields [198]. Still, the FSS is a property receiving considerable attention.

The InAs/GaAs material system provides good growth control and is a popular material system for many QD applications. Typical emission wavelengths of the ground state emission are $< 1.0\mu\text{m}$, as can be seen in Chapter 2, which is far from telecom low-absorption windows at $1.3\mu\text{m}$ and $1.5\mu\text{m}$. Among other possibilities to overcome this problem, the concept of a strain-reducing layer (SRL) was introduced [207, 208]. The SRL consists of an $\text{In}_x\text{Ga}_{1-x}\text{As}$ quantum well on top of the QD which relieves compressive strain inside the QD and brings bound electron and hole states closer together, resulting in a longer emission wavelength [209, 210]. Moreover, the longer emission wavelength is also driven by material deposition on the QD [209]. A cross-sectional scanning electron microscopy (SEM) image from [210] of an InAs QD embedded in an InGaAs SRL is shown in Fig. 4.1.

For device integration, small FSS and emission at telecom wavelengths have to be realized simultaneously. We theoretically study the interplay between SRL Indium concentration x (SRL- x) and the excitonic FSS in these SRL-QD-structures. For

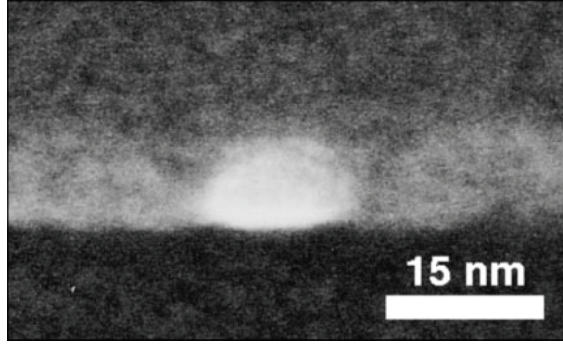


Figure 4.1.: Exemplary scanning electron microscopy image of an InAs QD embedded in an additional InGaAs quantum well, acting as the strain-reducing layer.

this purpose, we use an atomistic description of the structure based on a semi-empirical tight-binding model. This gives us the possibility to model random atomic realizations in the SRL, which is a clear advantage over continuum models.

4.1.2. System

The system under consideration is depicted in Fig. 4.2(a). An InAs QD grown along the [001] direction is situated on a wetting layer (WL) of two atomic layers resting on a GaAs buffer. To rule out the effect of reduction of point group symmetry caused by a reduced Indium concentration inside the QD or elongation, we consider pure InAs QDs having circular lens-shape. The QD is overgrown by an $\text{In}_x\text{Ga}_{1-x}\text{As}$ SRL (Fig. 4.2(b)). Most reported values of the SRL Indium concentration are $0 < x < 0.3$ [203, 204, 208, 209]. The peak value of x , estimated as 0.45 in [210], is a result of QD disassembling at higher x [211]. The whole system is embedded in a GaAs host matrix.

The shift of emission wavelength is driven by two mechanisms: the deposition of Indium atop the QD results (i) in local strain reduction lowering (raising) electron (hole) energies [212, 213] and (ii) in QD size changes in height, $\Delta h(x)$, and diameter, $\Delta d(x)$, due to the material attachment [209]. We model this size change by comparing the slope of the emission wavelength with SRL- x to experiment [203]. This results in the size changes indicated in Fig. 4.2(c). For the setup of the alloyed SRL we use a random realization scheme. For each realization, the following steps are used: (i) The appropriate number of In atoms is randomly placed within the considered supercell, allowing for random clustering of atoms. (ii) The resulting individual strain profile is used in the diagonalization of the TB matrix. (iii) Interaction matrix elements and optical properties are determined for the particular realization.

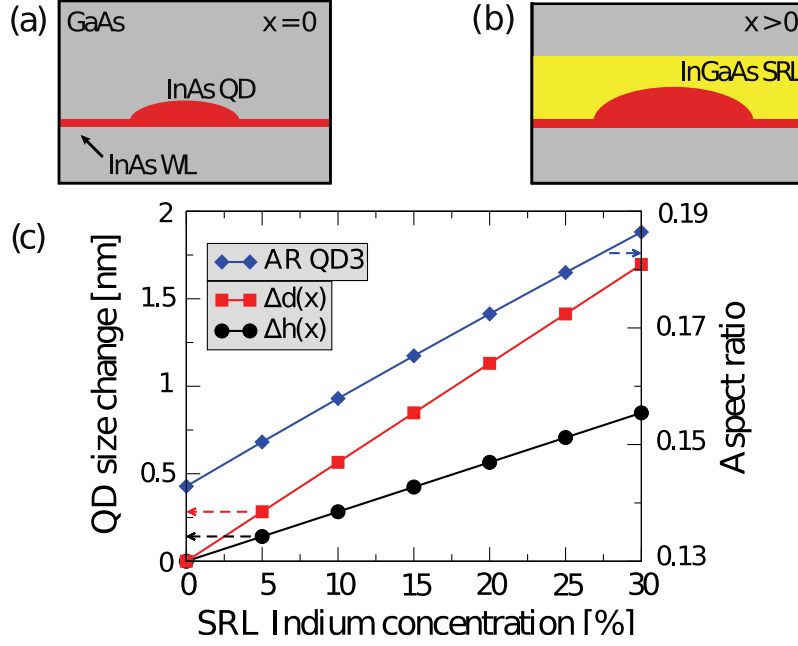


Figure 4.2.: (a) System without SRL, consisting of an InAs QD on an InAs WL embedded in a GaAs host matrix. (b) System for nonzero SRL- x exaggerating size change for illustration reasons. (c) QD size changes with SRL Indium concentration reproducing the experimental emission wavelength slope from [203] and resulting change in aspect ratio (AR) for QD3.

In our calculations for the excitonic FSS we employ our NN sp^3s^* -TB model with the parametrization from Ref. [107] and a valence-band offset between InAs and GaAs of 0.05 meV [214]. Strain-relaxation with the Keating potential is carried out utilizing the implementation from Ref. [61]. For the scaling with strain we use the value of $\eta = 2.9$ for all off-diagonal matrix elements, as suggested in Ref. [77].

4.1.3. Results and discussion

Calculations of the emission wavelength were performed for a fixed QD diameter of 15.82 nm and four different QD heights: 1.13 nm (QD1), 1.69 nm (QD2), 2.26 nm (QD3) and 3.39 nm (QD4). Both diameter and height are subject to a linear increase with SRL- x due to additional material deposition. We benchmark the slope of the groundstate emission wavelength with SRL- x with experimental data from Ref. [203], resulting in the size changes shown in Fig. 4.2(c). Fig. 4.3 shows the increase of the emission wavelength with SRL- x . QD1 provides a good match with the experimental data. For comparison, results for QD2 without any QD size increase are shown in Fig. 4.3, covering the strain-induced shift in emission wavelength alone, resulting in a much smaller slope (dashed line).

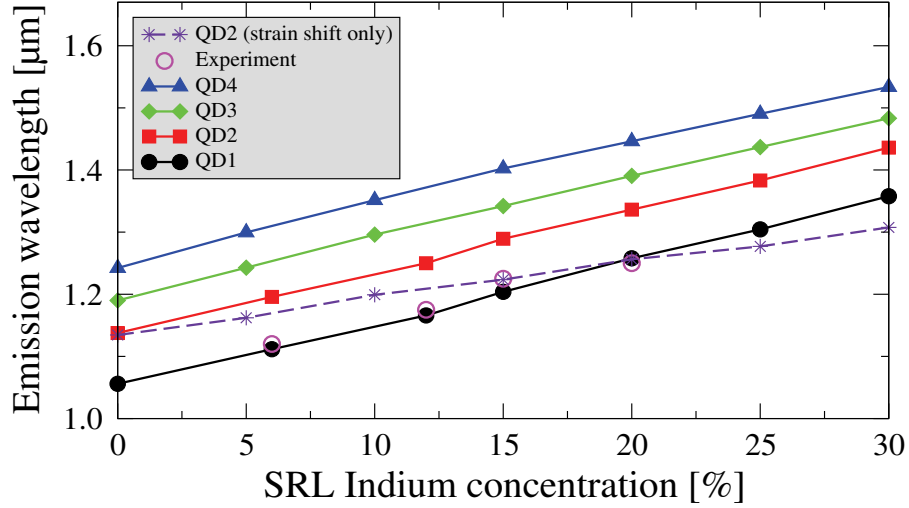


Figure 4.3.: Shift of excitonic emission wavelength with SRL Indium concentration for QDs of different height. Comparison with experimental values and with QDs lacking size increase.

The shift of emission wavelength with SRL- x desired for long-wavelength communication is reproduced, reaching the value of $1.53 \mu\text{m}$ for the largest QDs covered by an $\text{In}_{0.3}\text{Ga}_{0.7}\text{As}$ SRL driven by both strain relieve and additional material deposition.

The trend of increasing emission wavelength with increasing height at a fixed value of SRL- x can be understood in a simple particle-in-a-box picture, where the QD-height corresponds to the box-width. Enlarging the width causes the electron (hole) energy levels to drop (raise), reducing the recombination energy.

Having benchmarked our model with the experimental data we calculate the FSS for the considered QDs. Even without a SRL, the FSS exhibits statistical fluctuations due to symmetry reduction by QD structure and composition fluctuations and resulting individual strain profiles [215, 216]. With the SRL present, the symmetry is further reduced by the statistical distribution of atoms in the $\text{In}_x\text{Ga}_{1-x}\text{As}$ alloy. In Fig. 4.4 the statistical fluctuation of the calculated FSS with the emission wavelength is shown.

All calculated values of the FSS spread between the smallest calculated value of $6 \mu\text{eV}$ and $119 \mu\text{eV}$, which is in very good agreement with experiments for InAs QDs [126, 203, 204]. A general trend of increasing FSS with increasing emission wavelength can be seen in Fig. 4.4 and is consistent with experimental and theoretical trends for both single QDs and SRL samples [126, 217–219]. A linear fit is provided as a guide to the eye.

In Fig. 4.5 the variation of the FSS with SRL- x is shown for the four different QDs. For each QD-height/SRL- x combination five realizations were averaged, giving the

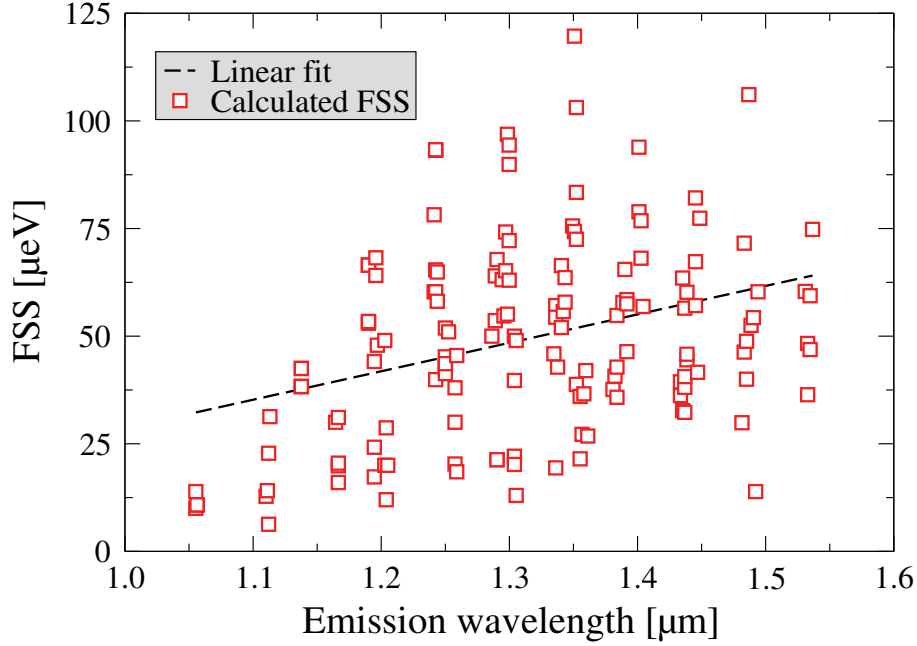


Figure 4.4.: Statistical scattering of the calculated FSS with excitonic emission wavelength and linear fit.

depicted data. Error bars show the standard deviation of the FSS for each data point. For small SRL- x , all QDs show an increase of the FSS. From an intuitive point of view the initial increase in FSS can be understood by symmetry lowering via the inclusion of Indium atoms in the SRL, but in this picture the increase with SRL- x should carry on over the whole range of x , resulting in an overall increase of FSS. The initial increase is continued for QD1 until high SRL- x values, where saturation can be seen. For the larger QDs (QD2–QD4) at small SRL- x already a reduction of the FSS is calculated. The data suggests a trend that in larger QDs the possible reduction of the FSS occurs already at lower In concentrations. For large SRL- x of 0.3, the FSS for all QDs tends to take intermediate values in the range of $45 \pm 15 \mu\text{eV}$.

With these results we demonstrate that utilizing a SRL for wavelength-shifting does not compromise the applicability of QD-SRL samples by unintentionally raising the FSS. Moreover, for some geometries the FSS is even reduced, maintaining the possibility of post-growth minimization of FSS.

Following the argumentation of Ref. [219], a reduction of the FSS is caused by a delocalization of electronic wave functions. We demonstrate that growing an SRL on the QD can lower the FSS due to the same reasons: the SRL weakens the confinement potential in growth direction, leading to a small spread of wave function into the SRL region and a reduction of the electron-hole exchange matrix element.

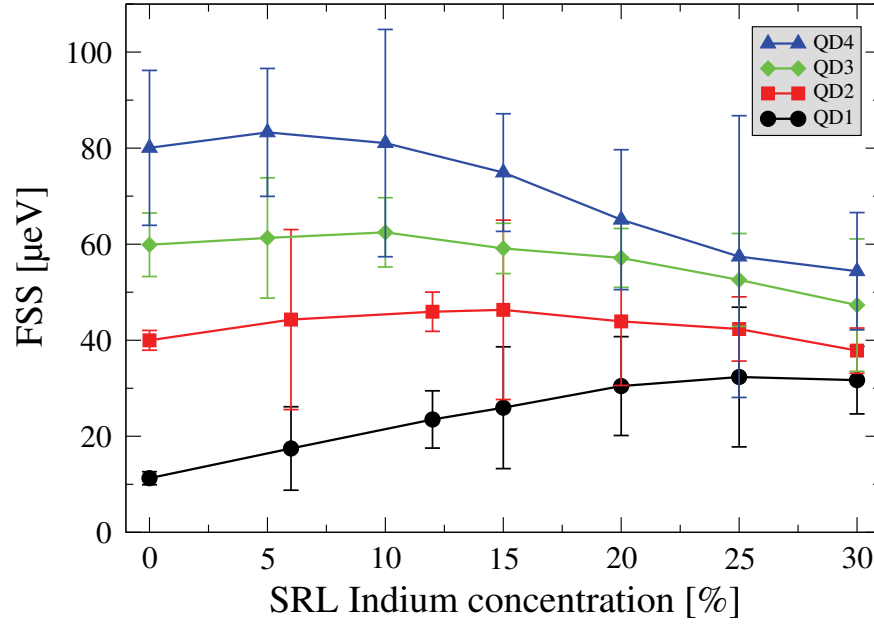


Figure 4.5.: Variation of the FSS as a function of SRL Indium concentration for different QD height from averaging over FSSs for each QD height and SRL- x . The initial increase in FSS for all QDs in regions of small SRL- x is counteracted by a reduction for larger SRL- x . A convergence of FSS to mediate values of around $45\mu\text{eV}$ can be seen.

Simultaneously, the recombination energy of the exciton is decreased due to larger QD-size with SRL- x and the modified strain profile. This effect seems to overtake the effect of symmetry lowering the earlier, the larger the QD height.

For device integration the emission efficiency is an important quantity. In Fig. 4.6 we show the squared dipole matrix element of the excitonic transition with polarization along $[110]$ crystal direction $D_X([110])^2$, plotted versus the SRL Indium concentration. It can be observed, that both increasing the QD height or the SRL- x strengthens the excitonic dipole transition, which is beneficial for device applications.

In conclusion, we have presented tight-binding and CI calculations of the FSS in InAs/GaAs QDs emitting at telecom wavelengths suited for long-range quantum communication. Our data emphasizes the possible use of the QD-SRL system for device application because operation at telecom wavelengths can be reached while excitonic transitions are strengthened with SRL- x . Counterintuitively, the FSS does not increase persistantly, but shows reduction and saturation, making the system feasible for the generation of entangled photon pairs.

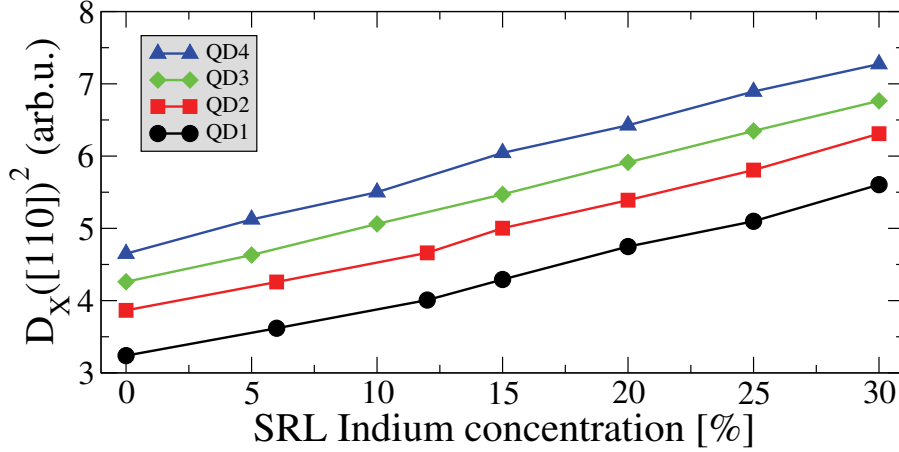


Figure 4.6.: Plot of squared excitonic dipole transition matrix element versus the SRL Indium concentration for QD1-QD4. With larger QD height and with larger SRL- x transitions become more efficient.

4.2. Optical gain in QD active media

Now we turn to a different property of QD emitters: the optical gain in the presence of excited carriers residing in the QD and WL states [220]. The saturation behaviour of optical gain with increasing excitation density is an important factor for laser device performance. For active materials based on self-organized InGaAs/GaAs quantum dots we study the interplay between structural properties of the quantum dots and many-body effects of excited carriers in the optical properties via a combination of tight-binding and quantum-kinetic calculations in this section. In this section we first introduce the optical gain, the envelope approximation and the fitting procedure of TB wave functions onto their analytical envelope counterparts. Then we link these wave functions with quantum-kinetic calculation of the optical gain spectra.

4.2.1. Optical gain

We employ a quantum-kinetic theory for the optical gain, that accounts for non-Markovian effects and self-consistent QD energy renormalizations. The calculations are based on the semiconductor Bloch equation (SBE, [221]) for the interband transition amplitudes $\psi_\alpha = \langle e_\alpha h_\alpha \rangle$, which are formulated in the frequency domain [222]

$$\begin{aligned}
 (\hbar\omega - \varepsilon_\alpha^{e,\text{HF}} - \varepsilon_\alpha^{h,\text{HF}})\psi_\alpha(\omega) + [1 - f_\alpha^e - f_\alpha^h] \Omega_\alpha^{\text{HF}}(\omega) \\
 = S_\alpha^c(\omega) + S_\alpha^p(\omega) .
 \end{aligned}
 \tag{4.1}$$

The single-particle energies $\varepsilon_\alpha^{a,\text{HF}} = e_\alpha^a + \Sigma_\alpha^{a,\text{HF}}$ with $a = e, h$ contain the TB energies e_α^a and $\Sigma_\alpha^{a,\text{HF}} = \sum_\beta (V_{\alpha\beta\beta\alpha} - V_{\alpha\beta\alpha\beta}) f_\beta^a$ combines the Hartree and exchange Coulomb self-energy. The Coulomb exchange contributions to the interband Rabi energy $\Omega_\alpha^{\text{HF}}(\omega) = \mathbf{d} \cdot \mathbf{E}(\omega) + \sum_\beta V_{\alpha\beta\alpha\beta} \psi_\beta(\omega)$ give rise to the excitonic resonance of the WL and to excitonic renormalizations of the QD transitions. Additionally, $S_\alpha^c(\omega)$ and $S_\alpha^p(\omega)$ describe the carrier-carrier and carrier-phonon correlations, that are evaluated in the Born approximation and random-phase approximation, respectively [223]. These lead to interaction-induced dephasing of the interband transition amplitudes ψ_α in the time domain, which results in line-broadening as well as additional line shifts in the frequency domain. Because of the discrete energy level structure in QD systems, two factors complicate the numerical evaluation. First, memory effects are non-negligible, so that the Markov approximation should no longer be used [222]. As described above, we circumvent this problem by evaluating the SBE and correlation integrals in the frequency domain, and it is the frequency dependence of the correlation contributions $S_\alpha^c(\omega)$ and $S_\alpha^p(\omega)$ that is expression of the non-Markovian memory effects [222]. Moreover, it is important to properly evaluate the scattering integrals by using self-consistently renormalized energies rather than the free single-particle energies.

Both carrier-phonon interaction using the polaron picture and carrier-carrier interaction can be cast into the form

$$S_\alpha^{c,p}(\omega) = -\Gamma_\alpha^{\text{DD}}(\omega)\psi_\alpha(\omega) + \sum_\beta \Gamma_{\alpha\beta}^{\text{OD}}(\omega)\psi_\beta(\omega). \quad (4.2)$$

One can identify contributions which are diagonal in the state index α (s , p , or WL) for the transition amplitude (diagonal dephasing Γ^{DD}) and off-diagonal parts (Γ^{OD}) which connect the interband transition amplitudes for various states.

We consider the linear optical response to a weak probe field E , and use for $f_\alpha^{e(h)}$ Fermi-Dirac functions with total carrier densities

$$N = 2N_{\text{dot}} \sum_\alpha f_\alpha^{e(h)} + 2A^{-1} \sum_k f_k^{e(h)}. \quad (4.3)$$

In all examples, a temperature of 300 K is assumed. In the above equation, N_{dot} is the 2-dimensional QD density and A is the active layer area. The solution to Eq. (4.1) provides the intrinsic material gain.

4.2.2. Envelope approximation

In Ref. [224] it has been shown that for lens-shaped QDs with small height to diameter ratio, the wave functions separate in good approximation into in-plane and z -components. We utilize this property by mapping the full three-dimensional

wave functions from the TB calculation onto analytical counterparts for the in-plane and z-components to determine the interaction matrix elements as described in [223]. This way we connect the many-body gain calculation to realistic QD size and composition properties.

Simple but widely used models for the calculation of electron and hole bound states in semiconductor nanostructures are based on the envelope approximation, in close connection to the effective mass approximation [225]. Following the discussion in [226], in the envelope approximation the n -th bound wave function in a semiconductor nanostructure is represented by the product of a slowly oscillating envelope part $f_n(\mathbf{r})$ and a fast oscillating part $u_0(\mathbf{r})$:

$$\psi_n(\mathbf{r}) = f_n(\mathbf{r})u_0(\mathbf{r}). \quad (4.4)$$

Here, $u_0(\mathbf{r})$ is the Bloch function for $\mathbf{k} = 0$ that oscillates with the lattice periodicity. It can be shown for quantum wells, that the envelope function $f_n(\mathbf{r})$ factorizes into a part along the growth axis (z -axis) and a perpendicular part:

$$f_n(\rho, z) = \phi(\rho)\chi_n(z) \quad (4.5)$$

where ρ and z give the position in cylindrical coordinates. This factorization has been shown to hold even for flat quantum dots with small height to diameter ratio in [224]. The in-plane part $\phi(\rho)$ can be described by a plane wave due to the translational symmetry throughout the quantum well. The actual form of the function $\chi_n(z)$ depends on the choice of model for the quantum well. For analytical solutions, the quantum well is modelled as a potential well in z -direction with either infinite or finite height, ranging from $-\frac{L}{2}$ to $\frac{L}{2}$. Here, L is the quantum well extension in growth direction. For the infinite well the lowest bound state is given by

$$\chi_1^{inf}(z) = \sqrt{\frac{2}{L}} \cos\left(\frac{\pi}{L}z\right). \quad (4.6)$$

As shown in Fig. 4.7 the infinite potential well is a rather bad choice because quantum mechanical wave functions penetrate into the barrier material. The infinite potential well does not account for this behaviour. For a potential well of finite height the lowest bound state is given by

$$\chi_1^{fin}(z) = \alpha \begin{cases} \exp(\kappa z), & \text{for } -\infty < z \leq -\frac{L}{2} \\ \frac{\exp(-\kappa L/2)}{\exp(kL/2)} \cos(kz), & \text{for } -\frac{L}{2} < z < \frac{L}{2} \\ \exp(-\kappa z), & \text{for } \frac{L}{2} \leq z < \infty. \end{cases} \quad (4.7)$$

The prefactor α is given by

$$\alpha = e^{kL/2} \left[\left(1 + \frac{\kappa^2}{k^2}\right) \left(\frac{L}{2} + \frac{1}{\kappa}\right) \right]^{-\frac{1}{2}}, \quad (4.8)$$

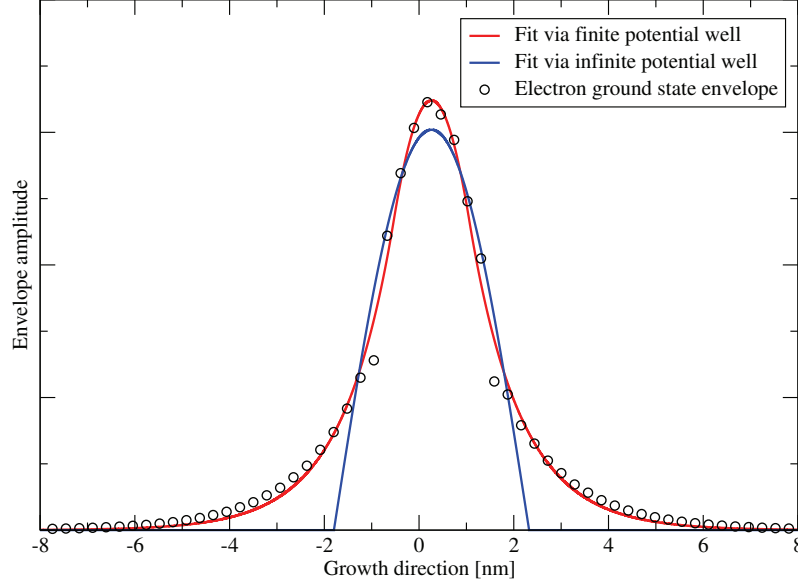


Figure 4.7.: Comparison between the models of infinite and finite height of the potential well in envelope function approximation for the standard lens-shaped QD of the previous sections. Due to the penetration of the envelope wave function into the buffer the infinite potential well is not suited for fitting the envelope functions accurately.

with k and κ obeying

$$k \cdot \tan\left(k \frac{L}{2}\right) = \kappa. \quad (4.9)$$

As shown in Fig. 4.7, this is a more realistic description of the wave function in z -direction, as intuitively understood.

Turning to quantum dots, this model has been used for the calculation of electronic states of flat dots with rotational symmetry. In growth direction it appears natural to see the dot as a quantum well, but this picture is spoiled for the in-plane part. In the ρ -plane the wave functions $\phi(\rho)$ cannot be described by plane waves because the confinement degrades the translational symmetry. They can rather be approximated by the eigenfunctions of a quantum harmonic oscillator [220, 227]. For this model the ground state is given by a gaussian envelope

$$\phi_s(\rho - \mathbf{R}) = \frac{\beta}{\sqrt{\pi}} e^{-\frac{\beta^2}{2} |\rho - \mathbf{R}|^2}, \quad (4.10)$$

where \mathbf{R} denotes the center of the quantum dot in the ρ -plane. The parameter β is referred to as the inverse oscillator length:

$$\beta = \frac{\sqrt{m\Delta E}}{\hbar}. \quad (4.11)$$

The factor ΔE accounts for the equidistant energy splitting in the quantum harmonic oscillator model and \hbar is Planck's constant.

4.2.3. Realistic envelopes

On the one hand we are able to calculate the atomistic single-particle wave functions by means of our tight-binding model on a very involved level. On the other hand for subsequent calculations, e.g. solving for the density matrix time evolution including reservoirs or quantum-kinetic calculations, the envelope function model is the only chance to include single-particle properties in the calculation: due to the problem size the wave functions can only be dealt with properly via the factorization into in-plane and z-parts. To steer a middle course and use at least the best parameters available for the envelope function approximation, we fit the functions $\phi_s(\rho - \mathbf{R})$ and $\chi_1^{fin}(z)$ of Eqns. (4.10) and (4.7), respectively, to the full three-dimensional tight-binding wave functions. Doing so, we integrate the wave functions over a perpendicular spatial direction as shown exemplarily in Fig. 4.8. For a fit of the

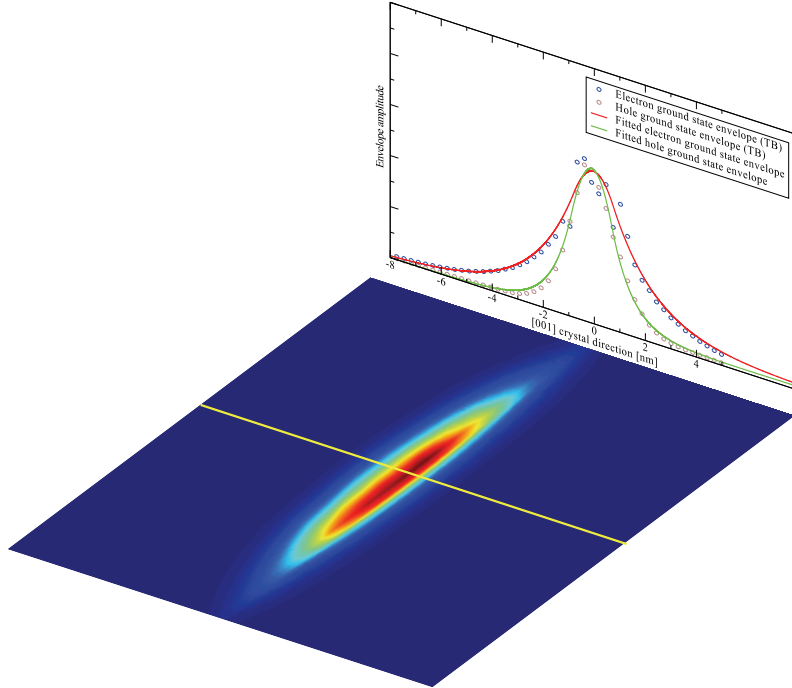


Figure 4.8.: Visualization of the fits in growth direction for the gain calculations. The lower part shows the ground hole wave function of QD 2 in side-view, integrated along [010]. In the upper part an exemplary envelope fit is shown. The fitting is done with respect to the yellow line, i.e. along the growth direction and through the quantum dot center.

z -part ([001]) we integrate over ρ and use k and L as fitting targets. For the fit of

the ρ -part we integrate over x ([100]) or y ([010]) to account for the QD shape from two different sides and use the inverse oscillator length β as the fitting target. To account for the three-dimensional structure of the QD we average the fitting results for the x - and y -directions. The obtained fitting parameters are shown in Tab. 4.1 for two realistic quantum dots having lens-shape, mean Indium concentrations of 30% and 40% and a height and diameter of 2.2 nm and 25 nm (QD 1) and 2.0 nm and 15 nm (QD 2), respectively.

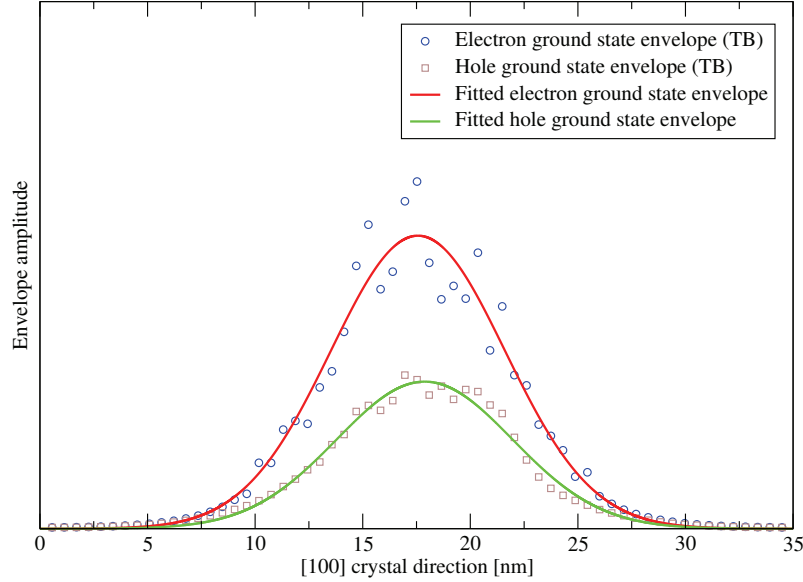


Figure 4.9.: [100]-dependence of the envelopes of the wave functions as calculated by TB for the ground states of electrons and holes, respectively, as well as their fitted analytical counterparts. QD 2 as defined in the text was used. Due to the reduced Indium content in the quantum dot, wave functions spread layerwise.

A few trends appear intuitively: Modelling the quantum confinement in growth direction as a quantum well and in the perpendicular plane as a harmonic oscillator potential is a better choice the higher the Indium content of the QD is. For a pure QD, the dot appears as a quantum well when seen only in a small region of a few nm . For QDs with low Indium content the actual atomic realization becomes more important and spoils the envelope function approximation, as shown in Figs. 4.9 and 4.10. Here, a QD having lens-shape with height and diameter of 2,0 and 15 nm, respectively, being composed of $In_{0.4}Ga_{0.6}As$, was used. For a pure $InAs$ -QD as in Fig. 4.7 the envelope function approximation is quite good for electrons, as can be seen in comparison with the results of section 2.7, where the nearly equidistant energy spacing of bound electron states was observed. For holes, nevertheless, the energies never appear in such an equidistant alignment. Therefore the obtained fit is worse for holes than for electrons. Often it is assumed for electrons and holes to have equal envelopes, although not implied by the envelope function definition or

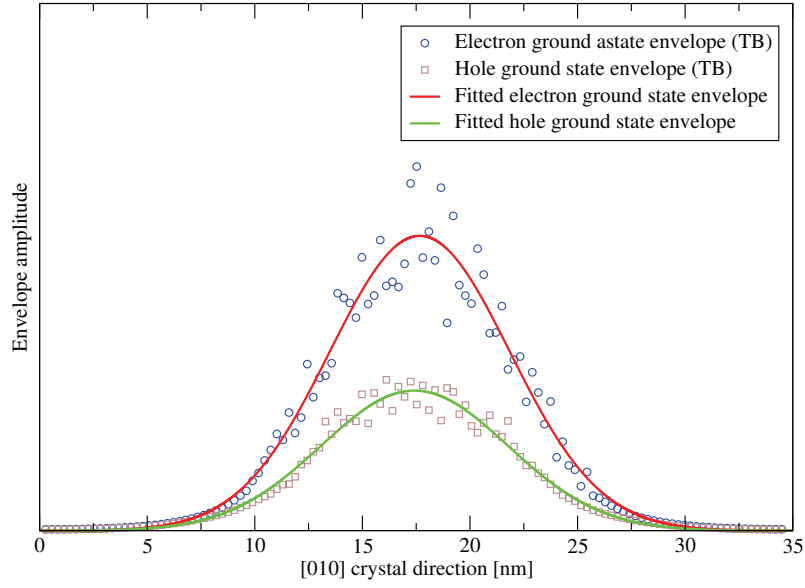


Figure 4.10.: [010]-dependence of the envelopes of the wave functions as calculated by TB for the ground states of electrons and holes, respectively, as well as their fitted analytical counterparts. QD 2 as defined in the text was used. Due to the reduced Indium content in the quantum dot, wave functions spread layerwise.

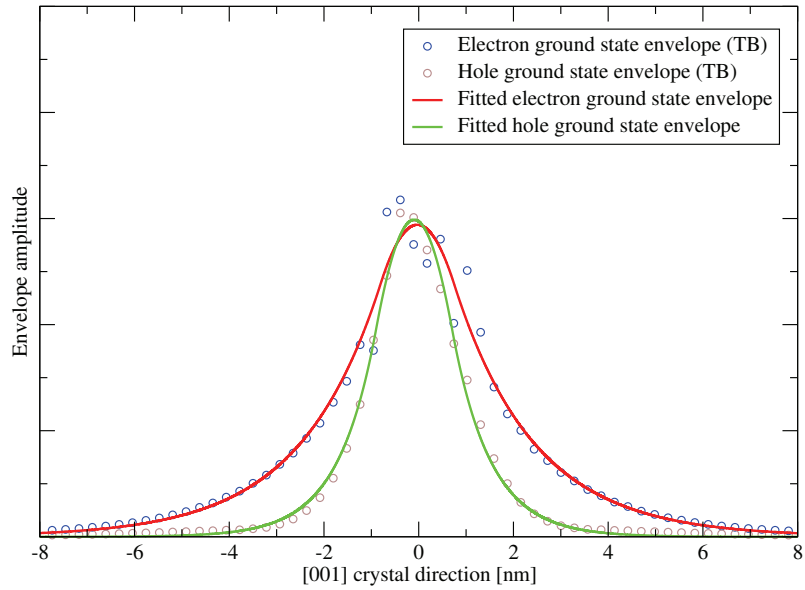


Figure 4.11.: [001]-dependence of the envelopes of the wave functions as calculated by TB for the ground states of electrons and holes, respectively, as well as their fitted analytical counterparts. QD 2 as defined in the text was used. The asymmetry of wave functions is caused by the influence of the wetting layer.

QD	k_e	L_e	β_e	k_h	L_h	β_h
1	0.,725	1.691	0.275	1.049	1.262	0.260
2	0.,806	1.502	0.343	1.068	1.411	0.336

Table 4.1.: Fitted values for factor k , the well width L and inverse oscillator length β for both electrons and holes.

the calculated tight-binding wave functions. The differences of the electron and hole wave function envelopes can be seen in Figs. 4.9 to 4.11.

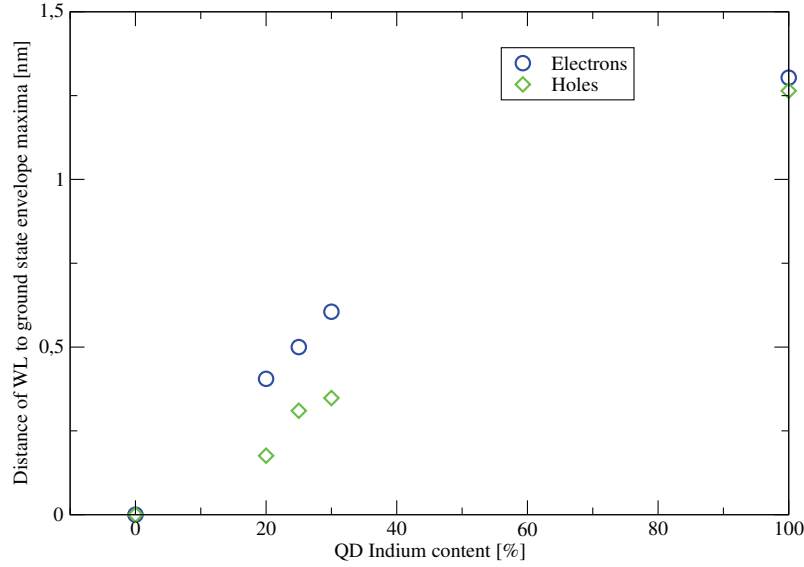


Figure 4.12.: Spatial distances in growth direction ([001]) of the center of electron and hole ground state envelope functions to the WL band edges as a function of the QD Indium content. Increasing the carrier confinement due to increased Indium content causes the wave function center to shift away from the wetting layer.

In the subsequent evaluations of scattering integrals entering the gain calculations the spatial distance in growth direction, i.e. the wave function overlap in [001]-direction, determines the scattering efficiency. We visualize in Fig. 4.12 the evolution of this overlap as a function of the QD Indium content for QD 1. The spatial distances are derived as the difference of the centers of the respective fitted envelope functions for electrons and holes to the centers of the WL electron and hole band edges. As a general trend it can be seen, that because of the increasing confinement due to the increasing QD Indium content, the QD envelope functions are drawn away from the WL. Due to the different envelopes, this behaviour differs for electrons and holes, although the general trend holds. For hole envelope functions, the distance appears smaller than for electron envelope functions due to the shallower confinement at the valence bands.

4.2.4. Negative differential gain in QD systems

Gain properties play a central role in the design and performance of optoelectronic devices. For semiconductor active materials, the single-particle electronic states are defined by structural properties such as material composition, quantum confinement and strain. Optical properties are additionally influenced by many-body effects of the excited carriers. The excitation dependence of the optical gain is determined by the interplay of phase-space filling, energy renormalization (e.g. gap shrinkage), dephasing, and screening of the Coulomb interaction. Of particular importance for device applications is the saturation behavior of the optical gain with increasing excitation density. For semiconductor quantum wells the excitation dependence of gain spectra is dominated by phase-state filling (PSF) and energy renormalizations. Coulomb enhancement of interband transitions and homogeneous line broadening additionally contribute to magnitude and spectral distribution of the gain [221, 228–231]. Semiconductor QDs behave quite differently in this respect due to the presence of localized electronic states with discrete energies. For semiconductor QDs the gain saturation is predominantly influenced by the interplay of PSF and excitation-induced dephasing (EID). Assuming quasi-equilibrium carrier populations for the excited electrons and holes, state filling is governed by the respective Fermi-functions. Naturally, the inversion of the lowest QD interband transition increases with excitation density and saturates when the corresponding states are fully populated. EID is provided by carrier-carrier Coulomb scattering and carrier-phonon scattering processes, which have been extensively studied in the past for QD systems [177, 222, 232–236]. Part of the excited carriers reside in delocalized wetting-layer (WL) and barrier states being coupled to the QD states via scattering processes. Mostly due to the availability of additional scattering partners, EID also increases with excited carrier density [177]. The corresponding broadening reduces the optical peak gain. As a result, two scenarios can occur. Usually PSF increases faster than EID and the optical gain saturates for high excitation densities. In the other scenario, EID and the corresponding broadening of the QD resonances increases faster than the PSF, thus leading to a *negative* differential gain, i.e., a reduction of the peak gain with increasing excitation density. This behavior has been predicted theoretically [176, 237, 238] and was recently observed [239] using gain spectra obtained via the Hakki-Paoli technique [240] at elevated temperatures. In what follows, we identify regimes in which the respective scenarios occur for realistic QD structures and investigate the influence of structural properties on the gain saturation.

We consider an ensemble of InGaAs QDs, taking into account the two lowest confined shells for electrons and holes, labeled *s*- and *p*-states, respectively, as well as the quasi-continuum of WL states. Single-particle energies and wave functions of these lowest QD shells are extracted from atomistic tight-binding (TB) calculations as discussed above in Chapter 2 using the sp^3s^* -model with nearest neighbors and

spin-orbit coupling as well as including strain calculated via valence force field minimization of the total strain energy. As described above, we link the results from the calculation of the single-particle properties to their analytical counterparts to enter the gain-calculation.

4.2.5. Results and discussion

To illustrate the emergence of the two aforementioned regimes of gain saturation, we investigate two exemplary QDs, each representing either dominant PSF or EID. QD 1 is lens-shaped with diameter and height of 25 nm and 2.2 nm, respectively, being composed of $\text{In}_{0.3}\text{Ga}_{0.7}\text{As}$. Excitation dependent optical gain spectra in Fig. 4.13 exhibit the peak gain saturation with increasing excitation due to PSF, accompanied by EID and a redshift of the s -shell absorption due to the Coulomb interaction of QD and WL carriers. The calculated EID of the lowest QD transition saturates at elevated carrier densities and is even slightly reduced for $1 \times 10^{12} \text{cm}^{-2}$. It is the saturation of the population inversion, which dominates the density dependence of the peak gain, except for the highest considered carrier density, where the reduced broadening leads to a slightly increased peak gain.

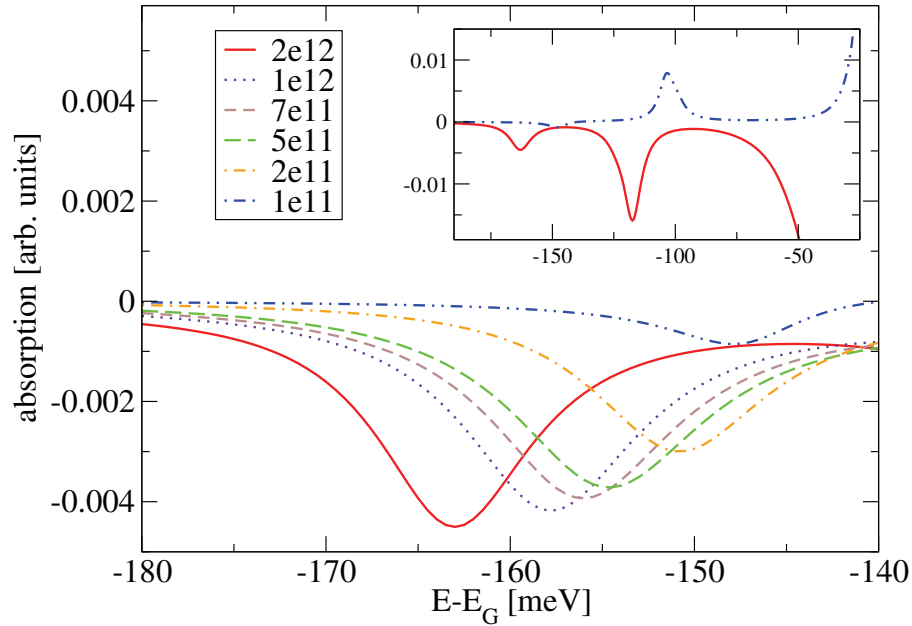


Figure 4.13.: Low-energy part of the optical spectra for QD 1 with 30% In content and various excitation densities (in cm^{-2}) as a function of energy relative to the WL energy gap E_G . The inset shows optical spectra for low and high excitation density covering s -shell, p -shell and the WL absorption edge.

Small changes of the structural properties can significantly alter this behaviour,

as is demonstrated by our second example. QD 2 is lens-shaped with a diameter and height of 15 nm and 2.0 nm, respectively, being composed of $\text{In}_{0.4}\text{Ga}_{0.6}\text{As}$. In the excitation dependent optical gain spectra of Fig. 4.14, the dominant role of dephasing can be identified, as the s -shell transition is strongly broadened with increasing excitation density. As a result, only for weak excitation the peak gain increases with carrier density. As soon as the EID increases faster than the inversion, the peak gain is reduced and the regime of negative differential gain is reached. We note that the increasing EID in a situation where the QD inversion saturates is a direct consequence of the electronically coupled 0D+2D (QD+WL) system.

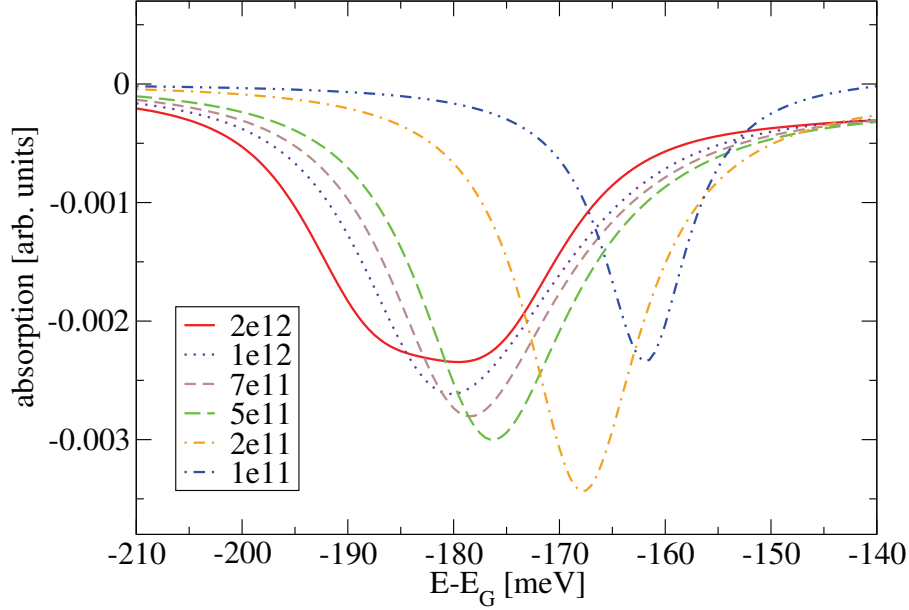


Figure 4.14.: Low-energy part of the optical spectra for QD 2 and 40% In content for various excitation densities (in cm^{-2}) as a function of energy relative to the WL energy gap.

To investigate the interplay between structural properties on the one hand and EID and PSF on the other, the carrier density dependence of the peak gain is shown in Fig. 4.15 for QD 1 (solid line), QD 2 (dashed line), as well as for the same geometries and reduced Indium content. For QD 1 the peak gain slowly saturates while for QD 2 at elevated carrier densities a negative differential gain is obtained. If we lower the Indium content in QD 1 (dash-dotted line), the overall peak gain is reduced and the onset of saturation is shifted to higher carrier densities due to shallower confinement. For QD 2 a reduced Indium content (dotted line) leads to a gradual disappearance of negative differential gain.

These rather involved dependencies can be understood from Fig. 4.16, where the spectral broadening (a) and the inversion (b) of the s -shell transition are shown. A substantial difference in the excitation dependence of the spectral broadening

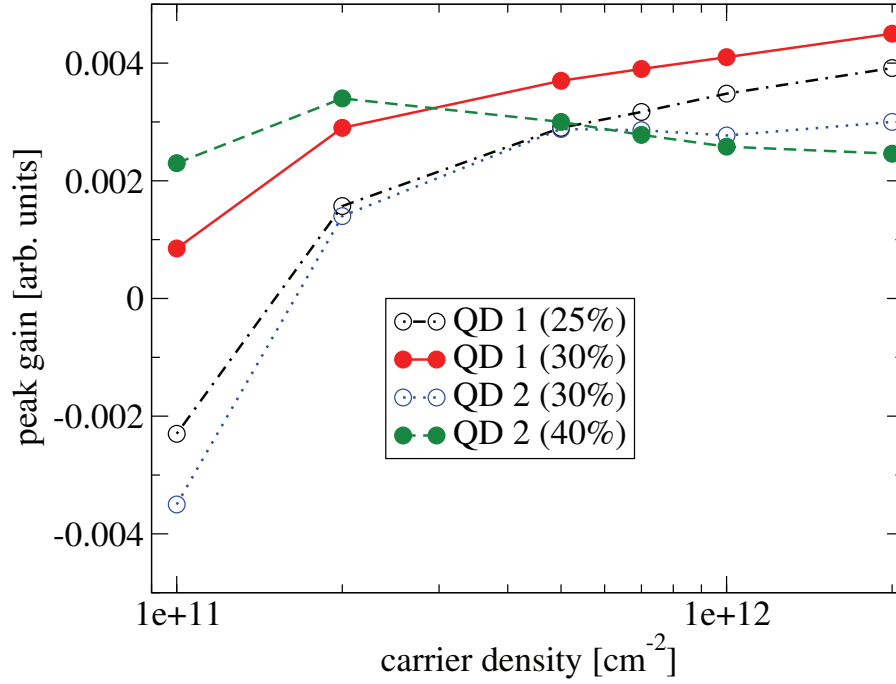


Figure 4.15.: Excitation density dependence of the peak gain for selected QD geometries, with given In content. QD 1 (30%) and QD 2 (40%) correspond to Figs. 4.13 and 4.14, respectively.

between QD 1 and QD 2 can be observed. In all cases, the broadening increases with carrier density in a comparable way for low excitation densities. In QD 1 with 30% Indium content (solid line) the broadening saturates and is even reduced for large excitation densities due to a combination of QD single-particle shifts (increasing the energetic distance of QD and WL scattering partners), state filling (leading to Pauli blocking of scattering channels), and screening (reducing the Coulomb interaction). In contrast, the broadening in QD 2 (dashed line) increases monotonously also in a regime where the inversion has already saturated, see Fig. 4.16 (b), thus leading to negative differential gain.

For the regime of dominant dephasing, that depends on the dephasing increasing with excitation density, we can identify a connection to structural properties. QD 1 with 25% Indium content has the shallowest confinement and the strongest reduction of EID at high carrier densities. For QD 1 and 30% Indium content, the deeper QD confinement reduces the dephasing itself and the density dependent quenching of the dephasing is less pronounced. QD 2 with 30% Indium content has an even deeper confinement as QD 1 due to its reduced size. Here, no reduction of EID is observed, but only a saturation. Finally, QD 2 with 40% Indium content has the deepest confinement and shows a monotonous increase of dephasing.

To provide further insight from the viewpoint of the microscopic calculation, we

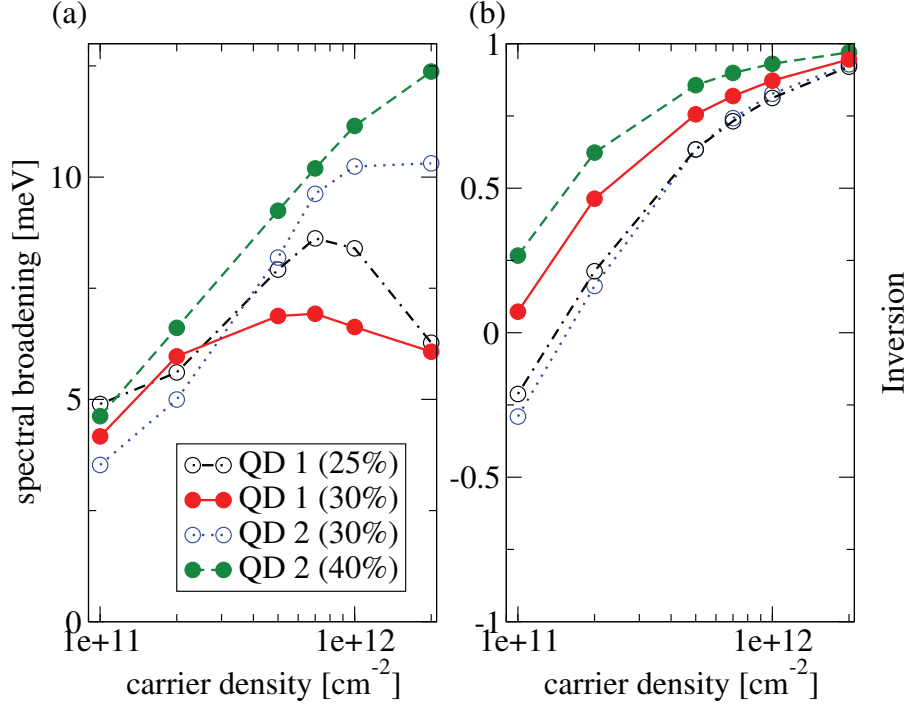


Figure 4.16.: Excitation density dependence of *s*-shell broadening (a) and inversion (b) for various QD geometries and Indium contents.

compare in Fig. 4.17 the different diagonal and off-diagonal dephasing contributions $\Gamma_{\alpha}^{\text{DD}}(\omega_p)$ and $\Gamma_{\alpha\beta}^{\text{OD}}(\omega_p)$ due to carrier-carrier scattering at peak gain energy $\hbar\omega_p$. Quite counterintuitively, both diagonal and off-diagonal *s*-shell dephasing components are reduced with increasing carrier density due to a combination of increased QD level shifts and screening of the Coulomb interaction. However, the *difference* of both contributions increases with carrier density, and this determines the net diagonal dephasing, cf. Eq. (4.2). Additionally, in Fig. 4.17 we provide the Γ_{sp}^{OD} -component, which is stronger for QD 2 than for QD 1. As a result of many-body compensation effects, Γ_{sp}^{OD} reduces the dephasing according to Eq. (4.2). Hence the reduction of Γ_{sp}^{OD} with increasing carrier density leads to a net increase of the total dephasing. Since the role of Γ_{sp}^{OD} is stronger in QD 2, the off-diagonal dephasing supports for QD 2 the prevailing dephasing regime.

In conclusion we can identify two regimes in which either excitation-induced dephasing or phase-space filling dominates the evolution of the QD peak gain with excitation density. It is shown that high Indium contents or small QD sizes lead to a faster saturation of the QD inversion. In this case, further increasing dephasing can result in negative differential gain. Moreover, smaller QDs show a different density dependence of the ratio between diagonal and off-diagonal dephasing, also fostering the dominant role of broadening in high-density gain spectra. These findings should support further experimental investigations or applications of negative

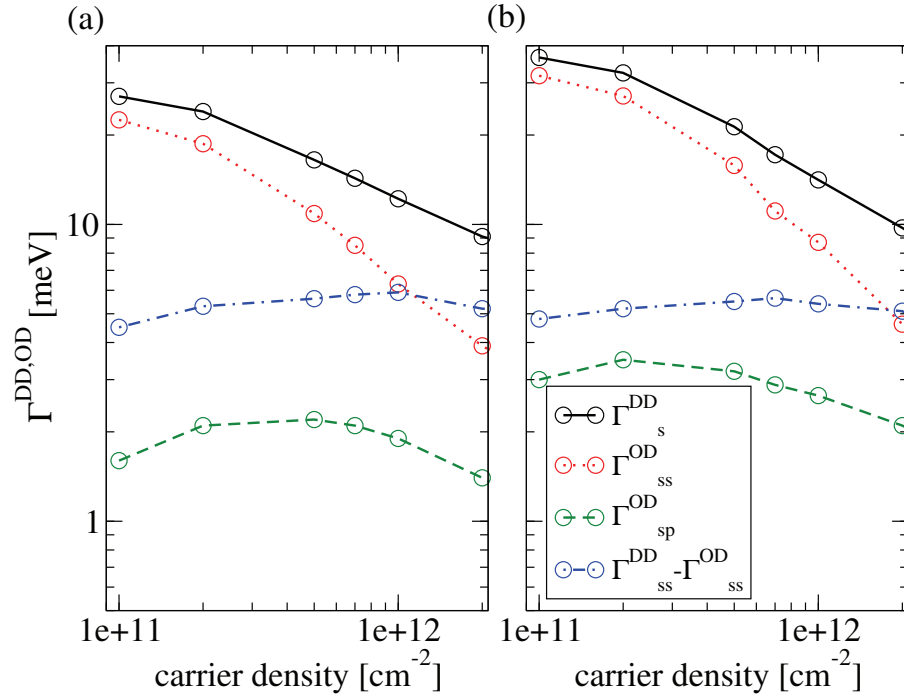


Figure 4.17.: Excitation density dependence of diagonal (DD) and off-diagonal (OD) dephasing contributions for (a) the dominant phase-state filling regime of QD 1 (30%) and (b) the dominant dephasing regime of QD 2 (40%).

differential gain in QD systems.

4.3. Conclusion

Devices based on self-assembled InGaAs/GaAs quantum dots are close to market-ready, although some difficulties have to be circumvented. In the previous sections of this chapter we presented studies concerning some of these difficulties, guiding the way towards self-organized QDs as optical components in device applications a few steps.

Concerning section 4.1, these devices include various light emitters for quantum computing and communication [241], ranging from LEDs at telecom wavelengths for conventional fiber transport of information to devices emitting polarization entangled photon pairs, such as quantum repeaters [242–244] for long-range fiber transport of information encrypted by protocols using entanglement-based schemes or write and read-out devices for generation of quantum keys for quantum key distribution [245, 246]. Regarding the need for a vanishing fine-structure splitting, application of electromagnetic fields or combined external stresses as well as QD pre-selection are promising ways to minimize the FSS, as stated above. Nevertheless, for reliable fabrication of InGaAs QDs with vanishing FSS, growth-control-based approaches like growth at a SRL seem to be the best way to integrate QDs into devices. In this respect, further research is needed optimizing the SRL influence and FSS reduction at the same time. Recently, QDs in the InAs(P)/InP material system have been shown to be promising candidates exhibiting smaller FSS and a smaller bandwidth of FSS with individual QD realizations [33, 216, 247].

In section 4.2 different regimes for the emergence of a negative differential gain in QD based active media were discussed. Those active media are to be integrated into next generation LED and laser devices, where the different physical behaviour of QDs compared with QWs leads to the emergence of devices with superior performance [238, 248]. For these devices gain saturation behaviour with increasing excitation is important for the high-excitation regime, directly influencing the performance. Direct implementation of the negative differential gain effect could take place in gain-lever lasers [249, 250], allowing for new operational regimes, or in quantum dot optical amplifiers [251]. Also, directly modulated lasers exhibiting a negative chirp could be realized employing negative differential gain [252].

5. Summary and outlook

Summary

After an introduction into the vivid field of research on semiconductor quantum dots, we presented full details about the tight-binding theory for the calculation of electron and hole bound states and energies, respectively. We introduced the differences in modelling semiconductor bulk band structures and bound states in nanostructures like quantum wells and quantum dots and, after introducing and discussing all relevant influences like spin-orbit coupling, strain and piezoelectricity, we presented a summary of common quantum dot structures from literature. Three typical geometries and concentrations were identified and the corresponding single-particle energies and wave functions were presented as well as benchmarks for our next-neighbour sp^3s^* tight-binding model. Subsequently we studied the influence of the variation of QD height, diameter and Indium concentration on single-particle energies and the fundamental energy gap. Attention was paid to the influence of the choice of the energy band alignment as expressed through the valence band offset between the two semiconductor materials and the number of bound states with respect to the QD geometry.

After this comprehensive introduction into single-particle tight-binding theory, we presented the calculation of many-particle properties of charge carriers in QDs via the configuration-interaction method. The derivation of Coulomb and dipole matrix elements from tight-binding coefficients was discussed as well as the subsequent calculation of the excitonic emission and absorption spectra. Special attention was paid to the excitonic fine-structure splitting of bright exciton states.

Based on this theoretical foundation we presented results of our calculations as summarized roughly in the following:

In section 4.1 we have shown tight-binding and configuration interaction calculations of the excitonic fine-structure splitting in InAs/GaAs QDs emitting at telecom wavelengths suited for long-range quantum communication by means of overgrowth of the QD by a strain-reducing layer. Our data emphasizes the possible use of the QD-SRL system for device application because operation at telecom wavelengths can be reached while excitonic transitions are strengthened with SRL- x . The dependence of the FSS on the SRL Indium content was derived by statistically averaging over different atomic realizations per SRL- x for different QD geometries. Slopes of the QD emission wavelength with SRL- x were calculated in excellent agreement with experimental data by allowing for the QD size to rise due to additional material provided by the SRL. Counterintuitively, the FSS does not increase persistently, but shows reduction and saturation, making the system feasible for the generation of entangled photon pairs.

In section 4.2 we examined the interplay of structural properties and many-body effects on the optical gain spectra of active materials based on InGaAs/GaAs quantum

dots. For this we combined the single-particle energies and wave functions obtained from our tight-binding model, which account for the structural QD properties, with quantum-kinetic calculations of the optical gain. We could identify two regimes in which either excitation-induced dephasing or phase-space filling dominates the evolution of the QD peak gain with excitation density. It was shown that high Indium contents or small QD sizes lead to a faster saturation of the QD inversion. In this case, further increasing dephasing can result in negative differential gain. Moreover, smaller QDs show a different density dependence of the ratio between diagonal and off-diagonal dephasing, also fostering the dominant role of broadening in high-density gain spectra. These findings should support further experimental investigations or applications of negative differential gain in QD systems and will guide device design for semiconductor lasers.

Outlook

Technically, the utilized tight-binding model could be expanded in several ways to make it more accurate or to integrate further physical aspects into the calculation. Depending on the desired application expanding the basis from sp^3s^* to $sp^3d^5s^*$ is an obvious expansion of the model. As mentioned earlier, this expanded basis is needed for applications far away from the Γ -point, where the sp^3s^* -basis fails to accurately reproduce the effective masses of the energy bands. If the ongoing discussion in the tight-binding and pseudopotential community about the correct incorporation of piezoelectric effects comes to an end, this could be another improvement of the model. Also, accounting for the effect of strain onto atomic orbitals (diagonal corrections in the TB Hamiltonian) could be beneficial. To paint an even more realistic picture of epitaxially grown nanostructures, material segregation at boundary interfaces between different materials, such as the boundary between QD and the buffer or the SRL and the buffer should be incorporated into the model via concentration gradients. To enhance the agreement of optical spectra with experiments, dipole matrix elements could be calculated using orthogonalized Slater orbitals or using explicit basis functions obtained by DFT. From the latter, also TB parametrizations could be adopted to further increase the quality of the TB band structures.

Those expansions will not alter physical behaviour principally but allow for different physical properties to investigate. From the physical point of view there are also several possibilities for further work. For the evolution of the fine-structure splitting with the Indium content of the strain-reducing layer, comparison to recent experiments is intended. Indeed, finding a way to a systematical reduction of the FSS is necessary. Our results suggest that using the SRL geometry could be a possible way, at least towards a fixed FSS, not a vanishing FSS. Also, varying the SRL structure, i.e. the position of the SRL or the concentration gradients, will be worth studying. A first step towards this direction will be using results of TEM, AFM and

PL measurements as inputs for the TB-modelling of the SRL-QD structures [253].

Besides further work on the topics presented in this thesis, research on other material systems, such as InAsP/InP would be of great interest. In the InAsP/InP material system very small FSS was predicted [33] as well as QD emission at large wavelengths [247]. Also other applications of the TB model, for example to study QD molecules (laterally or vertically coupled QDs) are possible. Here, the optical properties are not only defined by the geometrical aspects but also by the distance of the QDs, which allows for tuning of the emission spectra with the distance between QDs. Interesting other systems are for example nanoplatelets, which are II-VI semiconductor plates with thickness of only a few monolayers and large lateral dimensions. Also, new thin-layered graphene-like materials such as MoS₂ and other transition chalcogenides appear interesting. Both nanoplatelets and thin-layered transition dichalcogenides offer unique properties like large excitonic binding energies of up to several hundred meV.

However, due to the persistent trend of miniaturization, low-dimensional semiconductor structures with superior properties will proceed to conquer everyday optical and electronic devices. With up-to-date and next generation computers, i.e. as long as density functional theory can only allow for the inclusion of hundreds of atoms in the calculations, the empirical tight-binding method for the description of the electronic and optical properties of these devices will be one of the methods of choice.

A. Appendix

A.1. Quantum dot growth

In this section we give a short introduction to the epitaxial growth modes in which semiconductor quantum dots can be manufactured. For semiconductor heterostructures, there are in general three common growth modes, as sketched in Fig. A.1 differing mainly in the adhesion of provided atoms on a new grown layer in comparison to the bulk interface layer adhesion. With adhesion, the tendency of particles of different kinds to cling to one another is meant. If the adhesion on the new surface is similar to the bulk adhesion, the Frank-van-der-Merve-growth [254–256] takes place which leads to the consecutive growth of monolayers on top of each other. If the adhesion on the new surface is much higher than the bulk adhesion, the so-called Volmer-Weber growth [257] happens, where due to the different adhesions high islands of the material to grow build up. In between these two extremal conditions, the Stranski-Krastanov growth [258] occurs, widely used for the fabrication of quantum dots. In the Stranski-Krastanov growth mode first one or a small number of monolayers of the deposited material is built, called the wetting layer. After the buildup of a critical number of monolayers, islands formation on top of the wetting layer is favoured energetically due to strain from lattice mismatch. Those islands form the quantum dots.

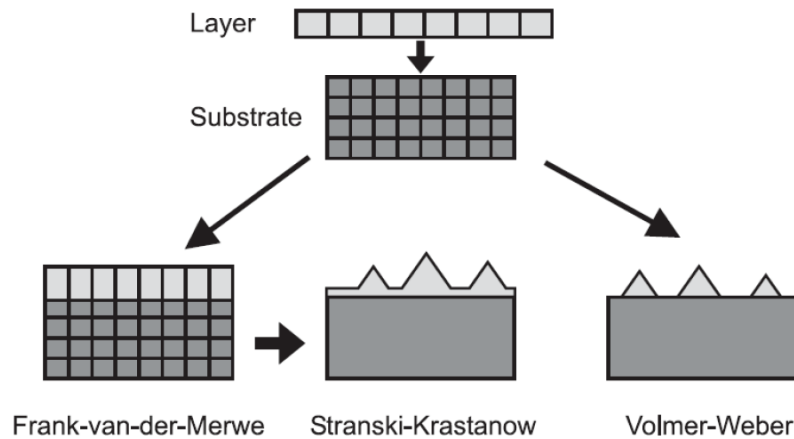


Figure A.1.: Scheme of the different growth modes described in the text. Picture from [259].

There are two technical realizations of Stranski-Krastanov growth, called molecular beam epitaxy (MBE) and metal organic vapor phase epitaxy (MOVPE). MBE growth is used to grow high quality quantum wells, wires and dots of different semiconductor materials on top of a substrate located in ultra high vacuum. Materials to grow are stored in effusion cells, which can be opened and closed to adjust the rate of material flow, and are heated to form a molecular beam of material to adsorb at the surface of the substrate. With this technique of opening and closing shutters for effusion cells containing different materials complicated heterostructures can be

formed, including monolayer growth, doping and overgrowth of structures. MBE growth can be controlled and monitored by in-situ diffraction techniques to probe the growing surface such as RHEED (reflection high energy electron diffraction). Due to requirement of ultra high vacuum and because of slow growth rates, MBE growth is relatively expensive.

In difference to MBE, in the MOVPE growth mode no vacuum is needed because reactant materials (such as Trimethylgallium, Trimethylindium and Arsine for InGaAs-heterostructures) are heated and pass the substrate in the vapor phase at moderate pressure. Here, the growth does take place because of the chemical reaction of the vaporized materials with the substrate's surface. This enables a faster and cheaper growth of semiconductor heterostructures but produces less pure results than using MBE growth. MOVPE has become the most used growth technique for mass production of optoelectronic devices, especially for Nitride-based components.

A.2. LAMMPS best practice parameters

Since no compendium for the choice of LAMMPS internal parameters is available, we report on the parameters used for the calculations in this thesis. We define the size of the simulation box (supercell) via the `xlo xhi` (in x-direction) keywords in the LAMMPS data file. We read out the values of the extremal atom positions and add half a lattice constant $\frac{a_{GaAs}}{2}$ of the host crystal at each interface to be able to account for the periodicity of the host crystal. To avoid artefacts, it turned out to be fruitful to add an additional space of 10^{-5} nm at each side of the simulation domain due to numerical reasons. In the LAMMPS input file for the minimization we use the specifications `units metal`, `atom_style atomic` and periodic boundary conditions via `boundary p p p`. It turned out, that for more symmetric problems, e.g. calculations with only a wetting layer in the supercell, the 'Hessian-free truncated Newton' (hftn) minimization method is the best choice (`min_style hftn`). For the calculations including a quantum dot with or without disorder, the 'conjugent gradient' (cg) method is the fastest and most robust algorithm for the minimization of the potential energy (`min_style cg`). While using the conjugent gradient algorithm it is a good choice to reduce the 'step-size' via `min_modify dmax 0.0005` to achieve a robust computation. `dmax` limits the maximal spatial displacement of a single atom in one iteration of the minimization and therefore acts as a damping in the subsequent calculation steps. As a criterion for the minimization to terminate we use an energy tolerance of `etol = 1e-12` or a force norm tolerance of `ftol = 1e-1`, both being the difference between two consecutive steps in energy and the norm of the global force vector, respectively.

A.3. PETSc/SLEPc best practice parameters

In PETSc, the environment for the solution of eigenvalue problems is called EPS (Eigenvalue Problem Solver). All optional arguments for the actual problem can be defined as properties of this environment. For our standard calculations containing a diagonalization domain of around one million atoms and searching for a handful of interior eigenpairs per electrons and holes, the following options turned out to suit the problem best.

The best solver for our quantum dot calculations turned out to be the Krylov Schur algorithm which can be set via `-eps_type krylovschur`. Find an overview over Krylov projection methods and the original references in [162].

We set the diagonalization accuracy via `-eps_tol 1e-10` where the accuracy is measured relative to the eigenvalue:

$$\text{eps_tol} \stackrel{!}{\leq} \frac{\|Ax - kx\|}{\|kx\|}. \quad (\text{A.1})$$

A is the matrix to be diagonalized, k the approximate eigenvalue and x the approximate eigenstate. The value of `1e-10` is needed for the calculation to converge to the physically correct twofold Kramers degeneracy of the eigenstates due to spin degeneracy. For lower values, the computational time is shorter but p - and d -like states show no degeneracy; although of course the eigenvalues differ only by a small fraction. For a quick diagonalization in search of only the energy levels a tolerance of `1e-5` is enough, but if one wants to calculate optical properties via CI the degeneracies have to be taken into account in order to resolve fine-structure splittings and polarization anisotropy.

As pointed out we are interested in highly accurate results, so we set the number of maximum iterations to a very large value via `-eps_max_it 20000000`. To accelerate the computation we provide some basic mathematical properties of the matrix to the solver: the TB-Hamiltonian matrix is hermitian `-eps_hermitian` and therefore has real eigenvalues. `-eps_target_real` sets the eigenvalue search to happen along the real axis only.

The number of eigenpairs to be computed can be set via `-eps_nev N` where each state is counted individually, so choosing $N = 2$ will give the two s -like states and so on.

To calculate eigenpairs in the interior of the spectrum, as it is needed here because only eigenpairs around the band gap are of interest, we choose the computation to search for eigenpairs closest to a target value via: `-eps_target 1.0`. The value is in eV and should be as close as possible to the actual eigenvalues for fast convergence.

To further improve the convergence speed it turned out useful to use the harmonic

Ritz extraction algorithm: `-eps_harmonic`. This changes how the spectral information gets extracted from the single subspaces built from the original matrix in the diagonalization process. The maximum dimension of these subspaces to be used by the solver can be set by using: `-eps_ncv 100`. The fixed value of 100 turned out to be a good value for $nev \approx 10$. For monitoring the progress of these computations we use `-eps_monitor` for the convergence steps and `-eps_view` for a printout of all properties of the eigenproblem solver object. A typical output of `-eps_view` looks like

```
0: EPS Object:
0: problem type: hermitian eigenvalue problem
0: method: krylovschur
0: extraction type: harmonic Ritz
0: selected portion of the spectrum: closest to target: 1+0i (along
the real axis)
0: number of eigenvalues (nev): 8
0: number of column vectors (ncv): 100
0: maximum dimension of projected problem (mpd): 100
0: maximum number of iterations: 20000000
0: tolerance: 1e-10
0: convergence test: relative to the eigenvalue
0: estimates of matrix norms (constant): norm(A)=1
0: IP Object:
0: orthogonalization method: classical Gram-Schmidt
0: orthogonalization refinement: if needed (eta: 0.707100)
0: ST Object:
0: type: shift
0: shift: 0+0 i
0: Elapsed Time: 5941.153749
0: Number of iterations of the method: 83
0: Solution method: krylovschur
0:
0: Number of requested eigenvalues: 8
0: Stopping condition: tol=1e-10, maxit=20000000
0: Number of converged approximate eigenpairs: 9
0:
0: k ||Ax-kx||/||kx||
0: -----
0: 1.1192190630 +0.0000000000 i 2.53797e-11
0: 1.1192190630 +0.0000000000 i 8.39935e-11
0: 1.1926452383 -0.0000000000 i 4.63115e-11
0: 1.1926452383 -0.0000000000 i 2.07435e-11
0: 1.1994611374 -0.0000000000 i 6.69836e-11
```

```
0:  1.1994611374 -0.0000000000 i 1.31763e-11
0:  1.2660478656 -0.0000000000 i 7.9943e-11
0:  1.2660478656 +0.0000000000 i 3.44358e-12
0:  1.2695011837 +0.0000000000 i 2.66525e-11
```

Although in general when dealing with large matrices not conditioned in particular a preconditioner should help accelerating the diagonalization process, in our case all preconditioners turned out to be very memory demanding and slow in terms of convergence. Therefore no preconditioners were applied to the Hamiltonian matrices throughout the calculations presented in this thesis.

A.4. TB parametrizations

In our quantum dot model using a next-neighbour sp^3s^* model including spin-orbit coupling we use the band structure parametrization from [107]. The given parameters reproduce low temperature bulk band gaps at the Γ -point of 1,511 eV for GaAs and 0,4152 eV for InAs, respectively. The literature values for these band gaps are 1,519 eV for bulk GaAs and 0,415 eV for bulk InAs, respectively, at low temperatures [118]. In the literature there are many tight-binding parametrizations present, differing in basis, number of neighbours considered, temperature dependence of target values and physical purpose, i.e. optical properties or electronic transport. A good overview of parametrizations can be found in [48]. Selected parametrizations for GaAs and InAs in the next neighbour spin-orbit sp^3s^* model as used in this thesis are reported in Tab. A.1.

Using the variety of parametrizations we can choose the appropriate parametrization for experiments with different temperatures. The evolution of the single-particle band gap with temperature is nonlinear and can be described by [118]

$$E_{Gap}^{GaAs}(T) = 1.519 - 5.405 \cdot 10^{-4} \frac{T^2}{(T + 204)} \quad (A.2)$$

$$E_{Gap}^{InAs}(T) = 0.415 - 2.760 \cdot 10^{-4} \frac{T^2}{(T + 83)}. \quad (A.3)$$

The formula provides the temperature dependent values of the band gap as shown in Tab. A.2 to compare the results employing the different TB-parametrization against. Because of the small gradient of the single-particle band gap at small temperatures in both InAs and GaAs, the 77 K-parametrization still is suitable for low temperature calculations because the band gap values differ only in the order of meV to the 0 K case.

	Wei et al. [107]		Priester et al. [108]		Klimeck et al. [106]	
T [K]	77		300		300	
	GaAs	InAs	GaAs	InAs	GaAs	InAs
E_{Gap}	1.511	0.4152	1.5499	0.429	1.424	0.3868
E_{sA}	-9.2664	-9.3562	-8.3431	-9.5381	-3.53284	-9.21537
E_{sC}	-4.3504	-3.9611	-2.6569	-2.7219	-8.11499	-2.21525
E_{pA}	+1.4866	+1.8201	+0.9252	+0.7733	+0.27772	+0.02402
E_{pC}	+3.2136	+3.1842	+3.5523	+3.5834	+4.57341	+4.64241
E_{s^*A}	+8.7826	+7.0432	+7.4249	+7.2730	+12.3393	+7.44461
E_{s^*C}	+5.8765	+6.1232	+6.6235	+6.6095	+4.31241	+4.12648
V_{sAsC}	-7.9480	-6.5393	-6.4513	-5.6052	-6.87653	-5.06858
V_{sAxC}	+2.7777	+4.3607	+4.4607	+3.0205	+2.85929	+2.51793
V_{xAsC}	+10.005	+7.0849	+5.7413	+5.3894	+11.09774	+6.18038
V_{s^*AxC}	+3.6271	+3.0007	+4.3083	+3.2191	+6.31619	+3.79662
V_{xAs^*C}	+7.0071	+5.4020	+6.6473	+3.7234	+5.02335	+2.45537
V_{xAxC}	+2.3069	+2.5491	+1.9546	+1.8398	+1.33572	+0.84908
V_{xAyC}	+5.0305	+5.4700	+5.0178	+4.3977	+5.07596	+4.68538
Δ_A	+0.420	+0.420	+0.4014	+0.4155	+0.32703	+0.38159
Δ_C	+0.174	+0.393	+0.1659	+0.387	+0.12000	+0.37518

Table A.1.: Material parameters for GaAs and InAs. The temperature denotes at which temperature the band structure was fitted. E_{Gap} gives the single-particle gap calculated using the actual parametrization. E are the orbital energies, V are the hopping matrix elements, s, s^* denote the s and s^* orbitals while x and y are abbreviations for the p_x and p_y orbitals. A and C denote anion and cation sites, respectively. $\Delta_{A/C}$ corresponds to the spin-orbit-splitting parameters via $\Delta_{A/C} = 3\lambda_{A/C}$. All parameters are given in eV unless stated otherwise.

	GaAs	InAs
0 K	1.519	0.415
77 K	1.5075	0.4047
300 K	1.4224	0.354

Table A.2.: Single-particle bulk band gaps in eV at selected temperatures for InAs and GaAs.

Publications and conference contributions

Parts of this work have been published in journals:

- *Negative differential gain in quantum dot systems: Interplay of structural properties and many-body effects*
Applied Physics Letters, **104**, 24, 242108 (2014)
Elias Goldmann, Michael Lorke, Thomas Frauenheim, and Frank Jahnke
- *Excitonic fine-structure splitting in telecom-wavelength InAs/GaAs quantum dots: Statistical distribution and height-dependence*
Applied Physics Letters, **103**, 24, 242102 (2013)
Elias Goldmann, Stefan Barthel, Matthias Florian, Kolja Schuh, and Frank Jahnke
- *Structural and emission properties of MOVPE-grown InGaAs/GaAs telecom quantum dots with bimodal height distribution*
Submitted to Applied Physics Letters (2014)
Elias Goldmann, Matthias Paul, Florian Krause, Jan Kettler, Thorsten Mehrrens, Knut Müller, Andreas Rosenauer, Michael Jetter, Peter Michler, and Frank Jahnke

Parts of this work have been presented as talks and posters at conferences:

- *Structural analysis, wavelength engineering and excitonic fine-structure splitting in telecom quantum dots as quantum light emitters*
BMBF Q.com status seminar I, Bad Honnef (2014)
Elias Goldmann, Stefan Barthel, Matthias Florian, Kolja Schuh, Frank Jahnke, Matthias Paul, Michael Jetter, Peter Michler, Florian Krause, Knut Müller, and Andreas Rosenauer
- *Structure and optical properties of InGaAs telecom quantum dots*
Solid state seminary, Bremen (2014)
Elias Goldmann, Matthias Paul, Knut Müller, and Frank Jahnke
- *Atom-by-atom modeling of QDs*
Solid-state workshop University of Bremen, Bad Bederkesa (2013)
Elias Goldmann and Frank Jahnke
- *Tight-binding model of strain-reducing layers in semiconductor quantum dots*
DPG spring meeting condensed matter section, Berlin (2012)
Elias Goldmann, Stefan Barthel, Kolja Schuh, Gerd Czycholl, and Frank Jahnke
- *Tight-binding model of strain-reducing layers in semiconductor quantum dots*
BMBF Quantum Repeater status seminar II, Bad Honnef (2012)
Elias Goldmann, Stefan Barthel, Kolja Schuh, Gerd Czycholl, and Frank Jahnke
- *The Single QD laser - From Weak To High Excitation*
FOPS at Lake Junaluska, North Carolina, USA (2011)
Christopher Gies, Matthias Florian, Paul Gartner, Elias Goldmann, Alexander Steinhoff, Kolja Schuh und Frank Jahnke,
- *Atomistic tight-binding models of semiconductor quantum dots*
DPG spring meeting condensed matter section, Dresden (2011):
Elias Goldmann, Stefan Barthel, and Frank Jahnke

Bibliography

- [1] Katherine Sanderson. Quantum dots go large. *Nature*, 459(7248):760, 2009.
- [2] R. Dingle, W. Wiegmann, and C. Henry. Quantum states of confined carriers in very thin $\text{Al}_x\text{Ga}_{1-x}\text{As}$ -GaAs- $\text{Al}_x\text{Ga}_{1-x}\text{As}$ heterostructures. *Physical Review Letters*, 33(14):827, 1974.
- [3] A. I. Ekimov and A. A. Onushchenko. Size quantization of the electron energy spectrum in a microscopic semiconductor crystal. *JETP Letters*, 40(8):1136–1139, 1984.
- [4] C. Murray, D. J. Norris, and M. G. Bawendi. Synthesis and characterization of nearly monodisperse CdE (E= sulfur, selenium, tellurium) semiconductor nanocrystallites. *Journal of the American Chemical Society*, 115(19):8706–8715, 1993.
- [5] A. Luque, A. Marti, and C. Stanley. Understanding intermediate-band solar cells. *Nature Photonics*, 6, 2012.
- [6] K. Bourzac. Quantum dots go on display. *Nature*, 493(7432):283–283, 2013.
- [7] F. Meinardi, A. Colombo, K. A. Velizhanin, R. Simonutti, M. Lorenzon, L. Beverina, R. Viswanatha, V. I. Klimov, and S. Brovelli. Large-area luminescent solar concentrators based on “Stokes-shift-engineered” nanocrystals in a mass-polymerized PMMA matrix. *Nature Photonics*, Advance online publication:1749–4893, 2014.
- [8] X. Gao, Y. Cui, R. M. Levenson, L. W. K. Chung, and S. Nie. In vivo cancer targeting and imaging with semiconductor quantum dots. *Nature Biotechnology*, 22:969, 2004.
- [9] M. V. Yezhelyev, L. Qi, R. M. O’Regan, S. Nie, and Xi. Gao. Proton-sponge coated quantum dots for sirna delivery and intracellular imaging. *Journal of the American Chemical Society*, 130(28):9006–9012, 2008.
- [10] M. Cheki, M. Moslehi, and M. Assadi. Marvelous applications of quantum dots. *European review for medical and pharmacological sciences*, 17(9):1141–1148, 2013.
- [11] J. M. Moison, F. Houzay, F. Barthe, L. Leprince, E. Andre, and O. Vatel.

- Self-organized growth of regular nanometer-scale InAs dots on GaAs. *Applied Physics Letters*, 64:196, 1994.
- [12] F. Houzay, C. Guille, J.M. Moison, P. Henoc, and F. Barthe. First stages of the MBE growth of InAs on (001)GaAs. *Journal of Crystal Growth*, 81(1-4):67–72, 1987.
- [13] S. Franchi, G. Trevisi, L. Seravalli, and P. Frigeri. Quantum dot nanostructures and molecular beam epitaxy. *Progress in Crystal Growth and Characterization of Materials*, 47(2):166–195, 2003.
- [14] J. Márquez, L. Geelhaar, and K. Jacobi. Atomically resolved structure of InAs quantum dots. *Applied Physics Letters*, 78(16):2309–2311, 2001.
- [15] S. Anders, C. S. Kim, B. Klein, Mark W. Keller, R. P. Mirin, and A. G. Norman. Bimodal size distribution of self-assembled $In_xGa_{1-x}As$ quantum dots. *Physical Review B*, 66:125309, 2002.
- [16] Y. Arakawa and H. Sakaki. Multidimensional quantum well laser and temperature dependence of its threshold current. *Applied Physics Letters*, 40:939, 1982.
- [17] D. Bimberg and U. W. Pohl. Quantum dots: promises and accomplishments. *Materials Today*, 14(9):388–397, 2011.
- [18] Y. Mu and C. M. Savage. One-atom lasers. *Physical Review A*, 46(9):5944, 1992.
- [19] S. Ritter, P. Gartner, C. Gies, and F. Jahnke. Emission properties and photon statistics of a single quantum dot laser. *Optics Express*, 18(10):9909–9921, 2010.
- [20] J. McKeever, A. Boca, A. D. Boozer, J. R. Buck, and H. J. Kimble. Experimental realization of a one-atom laser in the regime of strong coupling. *Nature*, 425(6955):268–271, 2003.
- [21] C. Kruse, H. Lohmeyer, K. Sebald, J. Gutowski, D. Hommel, J. Wiersig, and F. Jahnke. Green laser emission from monolithic II-VI-based pillar microcavities near room temperature. *Applied Physics Letters*, 92(3), 2008.
- [22] M. Nomura, N. Kumagai, S. Iwamoto, Y. Ota, and Y. Arakawa. Laser oscillation in a strongly coupled single-quantum-dot-nanocavity system. *Nature Physics*, 6(4):279–283, 2010.
- [23] T. Nowozin, D. Bimberg, K. Daqrouq, M. Ajour, and M. Awedh. Materials for future quantum dot-based memories. *Journal of Nanomaterials*, 2013, 2013.
- [24] A. Marent, T. Nowozin, M. Geller, and D. Bimberg. The QD-flash: a

- quantum dot-based memory device. *Semiconductor Science and Technology*, 26(1):014026, 2011.
- [25] M. Hayne, R. J. Young, E. P. Smakman, T. Nowozin, P. Hodgson, J. K. Garleff, P. Rambabu, P. M. Koenraad, A. Marent, L. Bonato, A. Schliwa, and D. Bimberg. The structural, electronic and optical properties of GaSb/GaAs nanostructures for charge-based memory. *Journal of Physics D: Applied Physics*, 46(26):264001, 2013.
- [26] P. Y. Yu and M. Cardona. *Fundamentals of semiconductors: physics and materials properties*. Springer, Berlin, 1999.
- [27] O. Stier. *Electronic and optical properties of quantum dots and wires*. PhD thesis, Technische Universität Berlin, 2000.
- [28] O. Stier, M. Grundmann, and D. Bimberg. Electronic and optical properties of strained quantum dots modeled by 8-band $\mathbf{k}\cdot\mathbf{p}$ theory. *Physical Review B*, 59:5688–5701, 1999.
- [29] A. Schliwa, M. Winkelnkemper, and D. Bimberg. Impact of size, shape, and composition on piezoelectric effects and electronic properties of InGaAs/GaAs quantum dots. *Physical Review B*, 76:205324, 2007.
- [30] J. C. Phillips. Energy-band interpolation scheme based on a pseudopotential. *Phys. Rev.*, 112:685–695, 1958.
- [31] Marvin L. Cohen and T. K. Bergstresser. Band structures and pseudopotential form factors for fourteen semiconductors of the diamond and zinc-blende structures. *Phys. Rev.*, 141:789–796, 1966.
- [32] J. Chelikowsky and M. Cohen. Nonlocal pseudopotential calculations for the electronic structure of eleven diamond and zinc-blende semiconductors. *Physical Review B*, 14(2):556–582, 1976.
- [33] R. Singh and G. Bester. Nanowire quantum dots as an ideal source of entangled photon pairs. *Physical Review Letters*, 103:063601, 2009.
- [34] A. Franceschetti, H. Fu, L. W. Wang, and A. Zunger. Many-body pseudopotential theory of excitons in InP and CdSe quantum dots. *Physical Review B*, 60:1819–1829, 1999.
- [35] A. J. Williamson, L. W. Wang, and A. Zunger. Theoretical interpretation of the experimental electronic structure of lens-shaped self-assembled InAs/GaAs quantum dots. *Physical Review B*, 62:12963–12977, 2000.
- [36] G. Bester, S. Nair, and A. Zunger. Pseudopotential calculation of the excitonic fine structure of million-atom self-assembled InGaAs/GaAs quantum dots. *Physical Review B*, 67:161306, 2003.

- [37] L. W. Wang and A. Zunger. Electronic structure pseudopotential calculations of large (approx. 1000 atoms) Si quantum dots. *The Journal of Physical Chemistry*, 98(8):2158–2165, 1994.
- [38] G. Bester. Electronic excitations in nanostructures: an empirical pseudopotential based approach. *Journal of Physics: Condensed Matter*, 21(2):023202, 2009.
- [39] P. Vogl, H. Hjalmarson, and J. Dow. A semi-empirical tight-binding theory of the electronic structure of semiconductors. *J. Phys. Chem. Solids*, 44(5):365–378, 1983.
- [40] R. Santoprete, B. Koiller, R. B. Capaz, P. Kratzer, Q. K. K. Liu, and M. Scheffler. Tight-binding study of the influence of the strain on the electronic properties of InAs/GaAs quantum dots. *Physical Review B*, 68:235311, 2003.
- [41] P.-O. Löwdin. On the non-orthogonality problem connected with the use of atomic wave functions in the theory of molecules and crystals. *The Journal of Chemical Physics*, 18(3):365–375, 1950.
- [42] B. A. McKinnon and T. C. Choy. Significance of nonorthogonality in tight-binding models. *Physical Review B*, 52:14531–14538, 1995.
- [43] G. Seifert. Tight-binding density functional theory: An approximate Kohn-Sham DFT scheme. *The Journal of Physical Chemistry A*, 111(26):5609–5613, 2007.
- [44] S. Schulz and G. Czycholl. Tight-binding model for semiconductor nanostructures. *Physical Review B*, 72:165317, 2005.
- [45] D. J. Chadi and M. L. Cohen. Tight-binding calculations of the valence bands of diamond and zincblende crystals. *physica status solidi (b)*, 68(1):405–419, 1975.
- [46] J.-M. Jancu, R. Scholz, F. Beltram, and F. Bassani. Empirical spds* tight-binding calculation for cubic semiconductors: General method and material parameters. *Physical Review B*, 57:6493–6507, 1998.
- [47] R. Viswanatha, S. Sapra, T. Saha-Dasgupta, and D. D. Sarma. Electronic structure of and quantum size effect in III-V and II-VI semiconducting nanocrystals using a realistic tight binding approach. *Physical Review B*, 72:045333, 2005.
- [48] A. Di Carlo. Microscopic theory of nanostructured semiconductor devices: beyond the envelope-function approximation. *Semiconductor Science and Technology*, 18(1):R1, 2003.

- [49] J. C. Slater and G. F. Koster. Simplified LCAO method for the periodic potential problem. *Phys. Rev.*, 94(6):1498–1524, 1954.
- [50] T. Boykin. More complete treatment of spin-orbit effects in tight-binding models. *Physical Review B*, 57:1620–1625, 1998.
- [51] R. Maranganti and P. Sharma. *Handbook of Theoretical and Computational Nanotechnology*, volume 118. Forschungszentrum Karlsruhe, Germany, 2006.
- [52] G. R. Liu and S. S. Q. Jerry. A finite element study of the stress and strain fields of InAs quantum dots embedded in GaAs. *Semiconductor Science and Technology*, 17(6):630, 2002.
- [53] T. Benabbas, P. Francois, Y. Androussi, and A. Lefebvre. Stress relaxation in highly strained InAs/GaAs structures as studied by finite element analysis and transmission electron microscopy. *Journal of Applied Physics*, 80(5):2763–2767, 1996.
- [54] G. Muralidharan. Strains in InAs quantum dots embedded in GaAs: A finite element study. *Japanese Journal of Applied Physics*, 39:658, 2000.
- [55] S. Christiansen, M. Albrecht, H. P. Strunk, and H. J. Maier. Strained state of Ge(Si) islands on Si: Finite element calculations and comparison to convergent beam electron-diffraction measurements. *Applied Physics Letters*, 64(26):3617–3619, 1994.
- [56] A. S. Saada. *Elasticity: theory and applications*. J. Ross Publishing, 2009.
- [57] M. J. P. Musgrave and J. A. Pople. A general valence force field for diamond. *Proceedings of the Royal Society of London. Series A. Mathematical and Physical Sciences*, 268(1335):474–484, 1962.
- [58] P. N. Keating. Effect of invariance requirements on the elastic strain energy of crystals with application to the diamond structure. *Physical Review*, 145:637–645, 1966.
- [59] R. M. Martin. Elastic properties of ZnS structure semiconductors. *Physical Review B*, 1:4005–4011, 1970.
- [60] J. Martins and A. Zunger. Bond lengths around isovalent impurities and in semiconductor solid solutions. *Physical Review B*, 30:6217–6220, 1984.
- [61] M. Schowalter, K. Muller, and A. Rosenauer. Scattering amplitudes and static atomic correction factors for the composition-sensitive 002 reflection in sphalerite ternary iii-v and ii-vi semiconductors. *Acta Crystallographica Section A: Foundations of Crystallography*, 68(1):68–76, 2011.
- [62] O. Rubel, I. Németh, W. Stolz, and K. Volz. Modeling the compositional

- dependence of electron diffraction in dilute GaAs- and GaP-based compound semiconductors. *Physical Review B*, 78:075207, 2008.
- [63] S. Adachi. GaAs, AlAs, and $Al_xGa_{1-x}As$: Material parameters for use in research and device applications. *Journal of Applied Physics*, 58(3):R1–R29, 1985.
- [64] Y.A. Burenkov, S.Y. Davydov, and S.P. Nikanorov. Elastic properties of InAs. *Sov. Phys. Solid State*, 17:1446, 1975.
- [65] M. Zielinski. Including strain in atomistic tight-binding Hamiltonians: An application to self-assembled InAs/GaAs and InAs/InP quantum dots. *Physical Review B*, 86:115424, 2012.
- [66] M. A. Migliorato, A. G. Cullis, M. Fearn, and J. H. Jefferson. Atomistic simulation of strain relaxation in InGaAs/GaAs quantum dots with nonuniform composition. *Physical Review B*, 65:115316, 2002.
- [67] F. H. Stillinger and T. A. Weber. Computer simulation of local order in condensed phases of silicon. *Physical Review B*, 31:5262–5271, 1985.
- [68] S. Plimpton. Fast parallel algorithms for short-range molecular dynamics. *Journal of Computational Physics*, 117(1):1–19, 1995.
- [69] R. Dembo and T. Steihaug. Truncated-Newton algorithms for large-scale unconstrained optimization. *Mathematical Programming*, 26:190–212, 1983.
- [70] S. Nash. Preconditioning of truncated-Newton methods. *SIAM Journal on Scientific and Statistical Computing*, 6(3):599–616, 1985.
- [71] D. P. O’Leary. A discrete Newton algorithm for minimizing a function of many variables. *Mathematical Programming*, 23:20–33, 1982.
- [72] M. R. Hestenes and E. Stiefel. *Methods of conjugate gradients for solving linear systems*, volume 49. NBS, 1952.
- [73] J.-M. Jancu, R. Scholz, F. Beltram, and F. Bassani. Empirical $spds^*$ tight-binding calculation for cubic semiconductors: General method and material parameters. *Physical Review B*, 57(11):6493–6507, 1998.
- [74] T. B. Boykin, G. Klimeck, R. C. Bowen, and F. Oyafuso. Diagonal parameter shifts due to nearest-neighbor displacements in empirical tight-binding theory. *Physical Review B*, 66:125207, 2002.
- [75] M. Zielinski, M. Korkusiński, and P. Hawrylak. Atomistic tight-binding theory of multiexciton complexes in a self-assembled InAs quantum dot. *Physical Review B*, 81:085301, 2010.
- [76] S. Froyen and W. A. Harrison. Elementary prediction of linear combination

- of atomic orbitals matrix elements. *Physical Review B*, 20:2420–2422, 1979.
- [77] W. Jaskolski, M. Zielinski, Garnett W. Bryant, and J. Aizpurua. Strain effects on the electronic structure of strongly coupled self-assembled InAs/GaAs quantum dots: Tight-binding approach. *Physical Review B*, 74:195339, 2006.
- [78] E. P. O'Reilly, A. Lindsay, S. Tomic, and M. Kamal-Saadi. Tight-binding and $\mathbf{k} \cdot \mathbf{p}$ models for the electronic structure of Ga(In)NAs and related alloys. *Semiconductor Science and Technology*, 17(8):870, 2002.
- [79] M. C. Munoz and G. Armelles. X-point deformation potentials of III-V semiconductors in a tight-binding approach. *Physical Review B*, 48:2839–2842, 1993.
- [80] S. Lee, O. L. Lazarenkova, P. von Allmen, F. Oyafuso, and G. Klimeck. Effect of wetting layers on the strain and electronic structure of InAs self-assembled quantum dots. *Physical Review B*, 70:125307, 2004.
- [81] J. E. Bernard and A. Zunger. Is there an elastic anomaly for a (001) monolayer of InAs embedded in GaAs? *Applied Physics Letters*, 65(2):165–167, 1994.
- [82] C. Pryor, J. Kim, L. W. Wang, A. J. Williamson, and A. Zunger. Comparison of two methods for describing the strain profiles in quantum dots. *Journal of Applied Physics*, 83(5):2548–2554, 1998.
- [83] K. Müller, M. Schowalter, A. Rosenauer, O. Rubel, and K. Volz. Effect of bonding and static atomic displacements on composition quantification in In-GaNAs. *Physical Review B*, 81:075315, 2010.
- [84] W. G. Cady. *Piezoelectricity*. McGraw-Hill, 1946.
- [85] L. De Caro and L. Tapfer. Elastic lattice deformation of semiconductor heterostructures grown on arbitrarily oriented substrate surfaces. *Physical Review B*, 48:2298–2303, 1993.
- [86] M. Grundmann, O. Stier, and D. Bimberg. InAs/GaAs pyramidal quantum dots: Strain distribution, optical phonons, and electronic structure. *Physical Review B*, 52:11969–11981, 1995.
- [87] D. L. Smith and C. Mailhot. Theory of semiconductor superlattice electronic structure. *Rev. Mod. Phys.*, 62:173–234, 1990.
- [88] A. D. Andreev and E. P. O'Reilly. Theory of the electronic structure of GaN/AlN hexagonal quantum dots. *Physical Review B*, 62:15851–15870, 2000.
- [89] M. Holm, M.-E. Pistol, and C. Pryor. Calculations of the electronic structure of strained InAs quantum dots in InP. *Journal of Applied Physics*, 92(2):932–936, 2002.

- [90] W. Sheng and J.-P. Leburton. Absence of correlation between built-in electric dipole moment and quantum stark effect in single InAs/GaAs self-assembled quantum dots. *Physical Review B*, 67:125308, 2003.
- [91] V. Ranjan, G. Allan, C. Priester, and C. Delerue. Self-consistent calculations of the optical properties of GaN quantum dots. *Physical Review B*, 68:115305, 2003.
- [92] M. A. Migliorato, D. Powell, S. L. Liew, A. G. Cullis, P. Navaretti, M. J. Steer, M. Hopkinson, M. Fearn, and J. H. Jefferson. Influence of composition on the piezoelectric effect and on the conduction band energy levels of $\text{In}_x\text{Ga}_{1-x}\text{As}/\text{GaAs}$ quantum dots. *Journal of Applied Physics*, 96(9):5169–5172, 2004.
- [93] G. Bester and A. Zunger. Cylindrically shaped zinc-blende semiconductor quantum dots do not have cylindrical symmetry: atomistic symmetry, atomic relaxation, and piezoelectric effects. *Physical Review B*, 71:045318, 2005.
- [94] G. Bester, X. Wu, D. Vanderbilt, and A. Zunger. Importance of second-order piezoelectric effects in zinc-blende semiconductors. *Physical Review Letters*, 96:187602, 2006.
- [95] M. A. Migliorato, D. Powell, A. G. Cullis, T. Hammerschmidt, and G. P. Srivastava. Composition and strain dependence of the piezoelectric coefficients in InGaAs alloys. *Physical Review B*, 74:245332, 2006.
- [96] G. Bester, A. Zunger, X. Wu, and D. Vanderbilt. Effects of linear and non-linear piezoelectricity on the electronic properties of InAs/GaAs quantum dots. *Physical Review B*, 74:081305, 2006.
- [97] V. A. Fonoberov and A. A. Balandin. Excitonic properties of strained wurtzite and zinc-blende GaN/ $\text{Al}_x\text{Ga}_{1-x}\text{N}$ quantum dots. *Journal of Applied Physics*, 94(11):7178–7186, 2003.
- [98] T. Saito and Y. Arakawa. Electronic structure of piezoelectric $\text{In}_{0.2}\text{Ga}_{0.8}\text{N}$ quantum dots in GaN calculated using a tight-binding method. *Physica E: Low-dimensional Systems and Nanostructures*, 15(3):169 – 181, 2002.
- [99] S. Cho, A. Majerfeld, A. Sanz-Hervás, J. J. Sánchez, J. L. Sánchez-Rojas, and I. Izpura. Determination of the pyroelectric coefficient in strained InGaAs/GaAs quantum wells grown on (111)B GaAs substrates. *Journal of Applied Physics*, 90(2):915–917, 2001.
- [100] J. J. Sanchez, J. I. Izpura, J. M. G. Tijero, E. Munoz, S. Cho, and A. Majerfeld. Confirmation of the pyroelectric coefficient of strained $\text{In}_x\text{Ga}_{1-x}\text{As}/\text{GaAs}$ quantum well structures grown on (111)B GaAs by differential photocurrent spectroscopy. *Journal of Applied Physics*, 91(5):3002–3006, 2002.

- [101] R. M. Martin. Piezoelectricity. *Physical Review B*, 5:1607–1613, 1972.
- [102] L. Nordheim. Zur Elektronentheorie der Metalle. I. *Annalen der Physik*, 401(5):607–640, 1931.
- [103] D. Mourad. *Empirische Tight-Binding-Modellierung geordneter und ungeordneter Halbleiterstrukturen*. PhD thesis, Universität Bremen, 2010.
- [104] T. Boykin, G. Klimeck, R. Bowen, and R. Lake. Effective-mass reproducibility of the nearest-neighbor sp^3s^* models: Analytic results. *Physical Review B*, 56(7):4102–4107, 1997.
- [105] A. Kobayashi, O. Sankey, and J. Dow. Chemical trends for defect energy levels in $Hg_{(1-x)}Cd_xTe$. *Physical Review B*, 25(10):6367–6379, 1982.
- [106] G. Klimeck, C. R. Bowen, T.B. Boykin, and T.A. Cwik. sp^3s^* tight-binding parameters for transport simulations in compound semiconductors. *Superlattices and Microstructures*, 27(5):519–524, 2000.
- [107] Y. Wei and M. Razeghi. Modeling of type-II InAs/GaSb superlattices using an empirical tight-binding method and interface engineering. *Physical Review B*, 69:085316, 2004.
- [108] C. Priester, G. Allan, and M. Lannoo. Band-edge deformation potentials in a tight-binding framework. *Physical Review B*, 37(14):8519–8522, 1988.
- [109] J. G. Mencherro, T. G. Dargam, and B. Koiller. Tight-binding description of the band-edge states in GaAs/AlAs quantum wells and superlattices. *Physical Review B*, 61:13021–13025, 2000.
- [110] S. Barthel. Simulation von Wurtzit-Nanostrukturen im Effective-Bond-Orbital Modell. Diploma thesis, Universität Bremen, 2009.
- [111] H. Dierks and G. Czycholl. Tight-binding calculations of the subband structures of zincblende-semiconductor [001] quantum wells. *Zeitschrift für Physik B Condensed Matter*, 99:207–217, 1995.
- [112] S. Schulz. *Electronic and optical properties of quantum dots: a tight-binding approach*. PhD thesis, Universität Bremen, 2007.
- [113] S. H. Wei and A. Zunger. Calculated natural band offsets of all II–VI and III–V semiconductors: Chemical trends and the role of cation d orbitals. *Applied Physics Letters*, 72(16):2011–2013, 1998.
- [114] M. Cardona and N. E. Christensen. Acoustic deformation potentials and heterostructure band offsets in semiconductors. *Physical Review B*, 35:6182–6194, 1987.
- [115] Craig Pryor. Eight-band calculations of strained InAs/GaAs quantum dots

- compared with one-, four-, and six-band approximations. *Physical Review B*, 57:7190–7195, 1998.
- [116] S. P. Kowalczyk, W. J. Schaffer, E. A. Kraut, and R. W. Grant. Determination of the InAs–GaAs(100) heterojunction band discontinuities by x-ray photoelectron spectroscopy (XPS). *Journal of Vacuum Science and Technology*, 20(3):705–708, 1982.
- [117] I. Vurgaftman, J. R. Meyer, and L. R. Ram-Mohan. Band parameters for III–V compound semiconductors and their alloys. *Journal of Applied Physics*, 89(11):5815–5875, 2001.
- [118] Nsm archive, 2013. Online database at <http://www.ioffe.rssi.ru/SVA/-NSM/Semicond/>.
- [119] R. Leon, S. Fafard, P. G. Piva, S. Ruvimov, and Z. Liliental-Weber. Tunable intersublevel transitions in self-forming semiconductor quantum dots. *Physical Review B*, 58(8):R4262, 1998.
- [120] H. Eisele, A. Lenz, R. Heitz, R. Timm, M. Dahne, Y. Temko, T. Suzuki, and K. Jacobi. Change of inas/gaas quantum dot shape and composition during capping. *Journal of Applied Physics*, 104(12):124301–124301, 2008.
- [121] P. B. Joyce, T. J. Krzyzewski, G. R. Bell, B. A. Joyce, and T. S. Jones. Composition of InAs quantum dots on GaAs (001): Direct evidence for (In, Ga) As alloying. *Physical Review B*, 58(24):R15981, 1998.
- [122] V. Mlinar, M. Bozkurt, J. M. Ulloa, M. Ediger, G. Bester, A. Badolato, P. M. Koenraad, R. J. Warburton, and A. Zunger. Structure of quantum dots as seen by excitonic spectroscopy versus structural characterization: Using theory to close the loop. *Physical Review B*, 80(16):165425, 2009.
- [123] V. Mlinar and A. Zunger. Spectral barcoding of quantum dots: Deciphering structural motifs from the excitonic spectra. *Physical Review B*, 80(3):035328, 2009.
- [124] E. Goldmann, S. Barthel, M. Florian, K. Schuh, and F. Jahnke. Excitonic fine-structure splitting in telecom-wavelength InAs/GaAs quantum dots: Statistical distribution and height-dependence. *Applied Physics Letters*, 103(24):242102, 2013.
- [125] C. Y. Ngo, S. F. Yoon, C. Z. Tong, W. K. Loke, and S. J. Chua. An investigation of growth temperature on the surface morphology and optical properties of 1.3 μm InAs/InGaAs/GaAs quantum dot structures. *Nanotechnology*, 18(36):365708, 2007.
- [126] R. Seguin, A. Schliwa, S. Rodt, K. Pötschke, U. W. Pohl, and D. Bimberg.

- Size-dependent fine-structure splitting in self-organized InAs/GaAs quantum dots. *Physical Review Letters*, 95:257402, 2005.
- [127] M. Korkusinski, W. Sheng, and P. Hawrylak. Designing quantum systems in self-assembled quantum dots. *physica status solidi (b)*, 238(2):246–249, 2003.
- [128] M. Korkusinski, M. Zielinski, and P. Hawrylak. Multiexciton complexes in InAs self-assembled quantum dots. *Journal of Applied Physics*, 105(12):122406–122406–6, 2009.
- [129] T. Walther, A. G. Cullis, D. J. Norris, and M. Hopkinson. Nature of the Stranski-Krastanow transition during epitaxy of InGaAs on GaAs. *Physical Review Letters*, 86:2381–2384, 2001.
- [130] I. Kegel, T. H. Metzger, A. Lorke, J. Peisl, J. Stangl, G. Bauer, K. Nordlund, W. V. Schoenfeld, and P. M. Petroff. Determination of strain fields and composition of self-organized quantum dots using x-ray diffraction. *Physical Review B*, 63:035318, 2001.
- [131] M. Bayer, G. Ortner, O. Stern, A. Kuther, A. A. Gorbunov, A. Forchel, P. Hawrylak, S. Fafard, K. Hinzer, T. L. Reinecke, S. N. Walck, J. P. Reithmaier, F. Kloppe, and F. Schäfer. Fine structure of neutral and charged excitons in self-assembled In(Ga)As/(Al)GaAs quantum dots. *Physical Review B*, 65:195315, 2002.
- [132] M. Korkusinski, P. Hawrylak, M. Bayer, G. Ortner, A. Forchel, S. Fafard, and Z. Wasilewski. Entangled states of electron-hole complex in a single InAs/GaAs coupled quantum dot molecule. *Physica E: Low-dimensional Systems and Nanostructures*, 13(2–4):610 – 615, 2002.
- [133] J.P. Reithmaier, G. Sek, A. Löffler, C. Hofmann, S. Kuhn, S. Reitzenstein, L.V. Keldysh, V.D. Kulakovskii, T.L. Reinecke, and A. Forchel. Strong coupling in a single quantum dot-semiconductor microcavity system. *Nature*, 432, 2004.
- [134] G. Ortner, M. Schwab, M. Bayer, R. Pässler, S. Fafard, Z. Wasilewski, P. Hawrylak, and A. Forchel. Temperature dependence of the excitonic band gap in InGaAs/GaAs self-assembled quantum dots. *Physical Review B*, 72:085328, 2005.
- [135] K. H. Schmidt, M. Versen, U. Kunze, D. Reuter, and A. D. Wieck. Electron transport through a single InAs quantum dot. *Physical Review B*, 62:15879–15887, 2000.
- [136] G. Bester, D. Reuter, L. He, A. Zunger, P. Kailuweit, A. D. Wieck, U. Zeitler, J. C. Maan, O. Wibbelhoff, and A. Lorke. Experimental imaging and atomistic modeling of electron and hole quasiparticle wave functions in InAs/GaAs

- quantum dots. *Physical Review B*, 76:075338, 2007.
- [137] I. A. Yugova, A. Greilich, E. A. Zhukov, D. R. Yakovlev, M. Bayer, D. Reuter, and A. D. Wieck. Exciton fine structure in InGaAs/GaAs quantum dots revisited by pump-probe faraday rotation. *Physical Review B*, 75:195325, 2007.
 - [138] M. Mehta, D. Reuter, A. Melnikov, A. D. Wieck, S. Michaelis de Vasconcellos, T. Baumgarten, A. Zrenner, and C. Meier. Intentionally positioned self-assembled InAs quantum dots in an electroluminescent p-i-n junction diode. *Physica E: Low-dimensional Systems and Nanostructures*, 42(10):2749 – 2752, 2010.
 - [139] A. Schliwa, M. Winkelnkemper, A. Lochmann, E. Stock, and D. Bimberg. In(Ga)As/GaAs quantum dots grown on a (111) surface as ideal sources of entangled photon pairs. *Physical Review B*, 80:161307, 2009.
 - [140] S. Rodt, A. Schliwa, K. Pötschke, F. Guffarth, and D. Bimberg. Correlation of structural and few-particle properties of self-organized InAs/GaAs quantum dots. *Physical Review B*, 71:155325, 2005.
 - [141] S. Rodt, R. Seguin, A. Schliwa, F. Guffarth, K. Pötschke, U.W. Pohl, and D. Bimberg. Size-dependent binding energies and fine-structure splitting of excitonic complexes in single InAs/GaAs quantum dots. *Journal of Luminescence*, 122–123(0):735 – 739, 2007.
 - [142] W. Sheng, S.-J. Cheng, and P. Hawrylak. Multiband theory of multi-exciton complexes in self-assembled quantum dots. *Physical Review B*, 71:035316, 2005.
 - [143] W. Sheng, M. Korkusinski, and P. Hawrylak. Microscopic approach to many-exciton complexes in self-assembled InGaAs/GaAs quantum dots. *Physica E: Low-dimensional Systems and Nanostructures*, 26(1-4):267 – 270, 2005.
 - [144] S. Raymond, S. Studenikin, A. Sachrajda, Z. Wasilewski, S. J. Cheng, W. Sheng, P. Hawrylak, A. Babinski, M. Potemski, G. Ortner, and M. Bayer. Excitonic energy shell structure of self-assembled InGaAs/GaAs quantum dots. *Physical Review Letters*, 92:187402, 2004.
 - [145] S. Awirothananon, S. Raymond, S. Studenikin, M. Vachon, W. Render, A. Sachrajda, X. Wu, A. Babinski, M. Potemski, S. Fafard, S. J. Cheng, M. Korkusinski, and P. Hawrylak. Single-exciton energy shell structure in InAs/GaAs quantum dots. *Physical Review B*, 78:235313, 2008.
 - [146] M. Korkusinski, P. Hawrylak, M. Zielinski, W. Sheng, and G. Klimeck. Building semiconductor nanostructures atom by atom. *Microelectronics Journal*, 39(3-4):318 – 326, 2008.

- [147] G. Ortner, M. Bayer, A. Larionov, V. B. Timofeev, A. Forchel, Y. B. Lyanda-Geller, T. L. Reinecke, P. Hawrylak, S. Fafard, and Z. Wasilewski. Fine structure of excitons in InAs/GaAs coupled quantum dots: A sensitive test of electronic coupling. *Physical Review Letters*, 90:086404, 2003.
- [148] G. Ortner, D. R. Yakovlev, M. Bayer, S. Rudin, T. L. Reinecke, S. Fafard, Z. Wasilewski, and A. Forchel. Temperature dependence of the zero-phonon linewidth in InAs/GaAs quantum dots. *Physical Review B*, 70:201301, 2004.
- [149] Y. Arakawa. Personal communication.
- [150] N. Baer, C. Gies, J. Wiersig, and F. Jahnke. Luminescence of a semiconductor quantum dot system. *The European Physical Journal B-Condensed Matter and Complex Systems*, 50(3):411–418, 2006.
- [151] M. Schwab, H. Kurtze, T. Auer, T. Berstermann, M. Bayer, J. Wiersig, N. Baer, C. Gies, F. Jahnke, J. P. Reithmaier, A. Forchel, M. Benyoucef, and P. Michler. Radiative emission dynamics of quantum dots in a single cavity micropillar. *Physical Review B*, 74(4):045323, 2006.
- [152] M. Usman, T. Inoue, Y. Harda, G. Klimeck, and T. Kita. Experimental and atomistic theoretical study of degree of polarization from multilayer InAs/GaAs quantum dot stacks. *Physical Review B*, 84(11):115321, 2011.
- [153] V.G. Dubrovskii, G.E. Cirlin, P.A. Brunkov, U. Perimetti, and N. Akopyan. Ultra-low density InAs quantum dots. *Semiconductors*, 47(10):1324–1327, 2013.
- [154] A. Strittmatter, A. Holzbecher, A. Schliwa, J.-H. Schulze, D. Quandt, T. D. Germann, A. Dreismann, O. Hitzemann, E. Stock, I. A. Ostapenko, S. Rodt, W. Unrau, U. W. Pohl, A. Hoffmann, D. Bimberg, and V. Haisler. Site-controlled quantum dot growth on buried oxide stressor layers. *physica status solidi (a)*, 209(12):2411–2420, 2012.
- [155] S. Lee, F. Oyafuso, P. von Allmen, and G. Klimeck. Boundary conditions for the electronic structure of finite-extent embedded semiconductor nanostructures. *Physical Review B*, 69(4):045316, 2004.
- [156] G. H. Golub and H. A. van der Vorst. Eigenvalue computation in the 20th century. *Journal of Computational and Applied Mathematics*, 123(1-2):35 – 65, 2000.
- [157] V. Hernandez, J. E. Roman, A. Tomas, and V. Vidal. *A Survey of Software for Sparse Eigenvalue Problems*, 2009. Available at <http://www.grycap.upv.es/slepc/>.
- [158] V. Hernandez, J. Roman, and V. Vidal. SLEPc: A scalable and flexible toolkit

- for the solution of eigenvalue problems. *ACM Transactions on Mathematical Software*, 31(3):351–362, 2005.
- [159] S. Balay, J. Brown, K. Buschelman, W. D. Gropp, D. Kaushik, M.G. Knepley, L. C. McInnes, B. F. Smith, and H. Zhang. *PETSc Web page*, 2012. <http://www.mcs.anl.gov/petsc/>.
- [160] S. Balay, J. Brown, K. Buschelman, V. Eijkhout, W. D. Gropp, D. Kaushik, M. G. Knepley, L. Curfman McInnes, B. F. Smith, and H. Zhang. *PETSc Users Manual*, 2012.
- [161] S. Balay, W. D. Gropp, L. Curfman McInnes, and B. F. Smith. *Efficient Management of Parallelism in Object Oriented Numerical Software Libraries*. Birkhäuser Press, 1997.
- [162] V. Hernandez, J. E. Roman, A. Tomas, and V. Vidal. Krylov-Schur methods in SLEPc. Technical Report STR-7, Universitat Politècnica de València, 2009. Available at <http://www.grycap.upv.es/slepc/>.
- [163] R. B. Morgan and M. Zeng. A harmonic restarted Arnoldi algorithm for calculating eigenvalues and determining multiplicity. *Linear Algebra and its Applications*, 415(1):96 – 113, 2006.
- [164] V. Hernandez, J. E. Roman, A. Tomas, and V. Vidal. Practical implementation of harmonic Krylov-Schur. Technical Report STR-9, Universitat Politècnica de València, 2009. Available at <http://www.grycap.upv.es/slepc/>.
- [165] R. Benchamekh, M. Nestoklon, J.-M. Jancu, and P. Voisin. *Theory and Modeling for the Nanoscale: The spds* Tight Binding Approach*, page 19. Springer, 2012.
- [166] L. He and A. Zunger. Multiple charging of InAs/GaAs quantum dots by electrons or holes: Addition energies and ground-state configurations. *Physical Review B*, 73:115324, 2006.
- [167] M. Fricke, A. Lorke, J. P. Kotthaus, G. Medeiros-Ribeiro, and P. M. Petroff. Shell structure and electron-electron interaction in self-assembled InAs quantum dots. *Europhysics Letters*, 36(3):197, 1996.
- [168] R. J. Warburton, B. T. Miller, C. S. Dürr, C. Bödefeld, K. Karrai, J. P. Kotthaus, G. Medeiros-Ribeiro, P. M. Petroff, and S. Huant. Coulomb interactions in small charge-tunable quantum dots: A simple model. *Physical Review B*, 58:16–221, 1998.
- [169] F. Oyafuso, G. Klimeck, R. C. Bowen, T. Boykin, and P. von Allmen. Disorder induced broadening in multimillion atom alloyed quantum dot systems. *physica status solidi (c)*, 0(4):1149–1152, 2003.

- [170] R. Leon, S. Marcinkevičius, X. Z. Liao, J. Zou, D. J. H. Cockayne, and S. Fafard. Ensemble interactions in strained semiconductor quantum dots. *Physical Review B*, 60:R8517–R8520, 1999.
- [171] C. Lobo, R. Leon, S. Fafard, and P. G. Piva. Intermixing induced changes in the radiative emission from III-V quantum dots. *Applied Physics Letters*, 72(22):2850–2852, 1998.
- [172] J. O. McCaldin, T. C. McGill, and C. A. Mead. Correlation for III-V and II-VI semiconductors of the Au schottky barrier energy with anion electronegativity. *Physical Review Letters*, 36:56–58, 1976.
- [173] W. R. Frensley and H. Kroemer. Theory of the energy-band lineup at an abrupt semiconductor heterojunction. *Physical Review B*, 16:2642–2652, 1977.
- [174] J. Tersoff. Band lineups at II-VI heterojunctions: Failure of the common-anion rule. *Physical Review Letters*, 56:2755–2758, 1986.
- [175] E. T. Yu, J. O. McCaldin, and T. C. McGill. *Band Offsets in Semiconductor Heterojunctions*, volume 46. Academic Press, 1992.
- [176] M. Lorke, W.W. Chow, T. R. Nielsen, J. Seebeck, P. Gartner, and F. Jahnke. Anomaly in the excitation dependence of optical gain in semiconductor quantum dots. *Physical Review B*, 74:035334, 2006.
- [177] A. Steinhoff, H. Kurtze, P. Gartner, M. Florian, D. Reuter, A. D. Wieck, M. Bayer, and F. Jahnke. Combined influence of coulomb interaction and polarons on the carrier dynamics in InGaAs quantum dots. *Physical Review B*, 88:205309, 2013.
- [178] T. Jennewein, C. Simon, G. Weihs, H. Weinfurter, and A. Zeilinger. Quantum cryptography with entangled photons. *Physical Review Letters*, 84:4729–4732, 2000.
- [179] J. Seebeck. *Carrier-Phonon Interaction in Semiconductor Quantum Dots*. PhD thesis, Universität Bremen, 2009.
- [180] N. Baer, P. Gartner, and F. Jahnke. Coulomb effects in semiconductor quantum dots. *The European Physical Journal B - Condensed Matter and Complex Systems*, 42:231–237, 2004.
- [181] A. Barenco and M. A. Dupertuis. Quantum many-body states of excitons in a small quantum dot. *Physical Review B*, 52:2766–2778, 1995.
- [182] K. Schuh. Polaronen in Halbleiter-Quantenpunkten, Diploma thesis, Universität Bremen, 2008.
- [183] M. Graf and P. Vogl. Electromagnetic fields and dielectric response in empirical

- tight-binding theory. *Physical Review B*, 51:4940–4949, 1995.
- [184] R. Peierls. Zur Theorie des Diamagnetismus von Leitungselektronen. *Zeitschrift für Physik*, 80(11-12):763–791, 1933.
 - [185] R. K. Willardson, E. R. Weber, and M. Sugawara. *Self-Assembled In-GaAs/GaAs Quantum Dots*, volume 60. Academic Press, 1999.
 - [186] S. Lee, J. Kim, L. Jönsson, J. W. Wilkins, G. W. Bryant, and G. Klimeck. Many-body levels of optically excited and multiply charged InAs nanocrystals modeled by semiempirical tight binding. *Physical Review B*, 66:235307, 2002.
 - [187] G. W. Bryant and W. Jaskólski. Tight-binding theory of quantum-dot quantum wells: single-particle effects and near-band-edge structure. *Physical Review B*, 67:205320, 2003.
 - [188] K. Leung and K. B. Whaley. Electron-hole interactions in silicon nanocrystals. *Physical Review B*, 56:7455–7468, 1997.
 - [189] J. C. Slater. Atomic shielding constants. *Physical Review*, 36:57–64, 1930.
 - [190] N. Baer, S. Schulz, S. Schumacher, P. Gartner, G. Czycholl, and F. Jahnke. Optical properties of self-organized wurtzite InN/GaN quantum dots: A combined atomistic tight-binding and full configuration interaction calculation. *Applied Physics Letters*, 87(23):231114, 2005.
 - [191] H. Jiang and J. Singh. Self-assembled semiconductor structures: electronic and optoelectronic properties. *IEEE Journal of Quantum Electronics*, 34(7):1188–1196, 1998.
 - [192] P. A. M. Dirac. The quantum theory of the emission and absorption of radiation. *Proceedings of the Royal Society of London. Series A*, 114(767):243–265, 1927.
 - [193] E. Fermi. *Nuclear physics*. University of Chicago Press, Chicago, 1950.
 - [194] A. Einstein, B. Podolsky, and N. Rosen. Can quantum-mechanical description of physical reality be considered complete? *Physical Review*, 47:777–780, 1935.
 - [195] O. Benson, C. Santori, M. Pelton, and Y. Yamamoto. Regulated and entangled photons from a single quantum dot. *Physical Review Letters*, 84:2513–2516, 2000.
 - [196] S. Schumacher, J. Förstner, A. Zrenner, M. Florian, C. Gies, P. Gartner, and F. Jahnke. Cavity-assisted emission of polarization-entangled photons from biexcitons in quantum dots with fine-structure splitting. *Optics Express*, 20(5):5335–5342, 2012.
 - [197] C. H. Bennett and D. P. DiVincenzo. Quantum information and computation.

- Nature*, 404(6775):247–255, 2000.
- [198] B. D. Gerardot, S. Seidl, P. A. Dalgarno, R. J. Warburton, D. Granados, J. M. Garcia, K. Kowalik, O. Krebs, K. Karrai, A. Badolato, and P. M. Petroff. Manipulating exciton fine structure in quantum dots with a lateral electric field. *Applied Physics Letters*, 90(4):041101–041101, 2007.
- [199] R. M. Stevenson, R. J. Young, P. See, D. G. Gevaux, K. Cooper, P. Atkinson, I. Farrer, D. A. Ritchie, and A. J. Shields. Magnetic-field-induced reduction of the exciton polarization splitting in InAs quantum dots. *Physical Review B*, 73:033306, 2006.
- [200] S. Seidl, M. Kroner, A. Hoge, K. Karrai, R. J. Warburton, A. Badolato, and P. M. Petroff. Effect of uniaxial stress on excitons in a self-assembled quantum dot. *Applied Physics Letters*, 88(20):203113–203113, 2006.
- [201] Y.-M. He, Y. He, Y.-J. Wei, D. Wu, M. Atatüre, C. Schneider, S. Höfling, M. Kamp, C.-Y. Lu, and J.-W. Pan. On-demand semiconductor single-photon source with near-unity indistinguishability. *Nature nanotechnology*, 8(3):213–217, 2013.
- [202] V. Mlinar and A. Zunger. Internal electronic structure and fine structure of multiexcitons in semiconductor quantum dots. *Physical Review B*, 80:205311, 2009.
- [203] A. I. Tartakovskii, R. S. Kolodka, H. Y. Liu, M. A. Migliorato, M. Hopkinson, M. N. Makhonin, D. J. Mowbray, and M. S. Skolnick. Exciton fine structure splitting in dot-in-a-well structures. *Applied Physics Letters*, 88(13):131115–131115, 2006.
- [204] L. Sapienza, R. N. E. Malein, C. E. Kuklewicz, P. E. Kremer, K. Srinivasan, A. Griffiths, E. Clarke, R. J. Warburton, and B. D. Gerardot. Exciton fine-structure splitting of telecom-wavelength single quantum dots: Statistics and external strain tuning. *Physical Review B*, 88(15):155330, 2013.
- [205] E. Goldmann, M. Lorke, T. Frauenheim, and F. Jahnke. Negative differential gain in quantum dot systems: Interplay of structural properties and many-body effects. *Applied Physics Letters*, 104(24):242108, 2014.
- [206] P. Michler. *Single semiconductor quantum dots*. Springer, 2009.
- [207] K. Nishi, H. Saito, S. Sugou, and J.-S. Lee. A narrow photoluminescence linewidth of 21 meV at 1.35 μm from strain-reduced InAs quantum dots covered by $\text{In}_{0.2}\text{Ga}_{0.8}\text{As}$ grown on GaAs substrates. *Applied Physics Letters*, 74(8):1111–1113, 1999.
- [208] V. M. Ustinov, N. A. Maleev, A. E. Zhukov, A. R. Kovsh, A. Y. Egorov, A. V.

- Lunev, B. V. Volovik, I. L. Krestnikov, Y. G. Musikhin, N. A. Bert, P. S. Kopev, Z. I. Alferov, N. N. Ledentsov, and D. Bimberg. InAs/InGaAs quantum dot structures on GaAs substrates emitting at $1.3\ \mu\text{m}$. *Applied Physics Letters*, 74(19):2815–2817, 1999.
- [209] H. Y. Liu, M. Hopkinson, C. N. Harrison, M. J. Steer, R. Frith, I. R. Sellers, D. J. Mowbray, and M. S. Skolnick. Optimizing the growth of $1.3\ \mu\text{m}$ InAs/InGaAs dots-in-a-well structure. *Journal of Applied Physics*, 93(5):2931–2936, 2003.
- [210] J. Tatebayashi, M. Nishioka, and Y. Arakawa. Over $1.5\ \mu\text{m}$ light emission from InAs quantum dots embedded in InGaAs strain-reducing layer grown by metalorganic chemical vapor deposition. *Applied Physics Letters*, 78(22):3469–3471, 2001.
- [211] A. Lenz, H. Eisele, R. Timm, L. Ivanova, R. L. Sellin, H.-Y. Liu, M. Hopkinson, U. W. Pohl, D. Bimberg, and M. Dähne. Limits of In(Ga)As/GaAs quantum dot growth. *physica status solidi (b)*, 246(4):717–720, 2009.
- [212] M. Richter, D. Reuter, J.-Y. Duboz, and A. D. Wieck. Influence of $\text{In}_{0.15}\text{Ga}_{0.85}\text{As}$ capping layers on the electron and hole energy levels of InAs quantum dots. *Physica E: Low-dimensional Systems and Nanostructures*, 40(6):1891–1893, 2008.
- [213] M. Usman, H. Ryu, I. Woo, D. S. Ebert, and G. Klimeck. Moving toward nano-TCAD through multimillion-atom quantum-dot simulations matching experimental data. *IEEE Transactions on Nanotechnology*, 8(3):330–344, 2009.
- [214] S.-H. Wei and A. Zunger. Calculated natural band offsets of all II–VI and III–V semiconductors: Chemical trends and the role of cation d orbitals. *Applied Physics Letters*, 72(16):2011–2013, 1998.
- [215] V. Mlinar and A. Zunger. Effect of atomic-scale randomness on the optical polarization of semiconductor quantum dots. *Physical Review B*, 79(11):115416, 2009.
- [216] L. He, M. Gong, C.-F. Li, G.-C. Guo, and A. Zunger. Highly reduced fine-structure splitting in InAs/InP quantum dots offering an efficient on-demand entangled $1.55\text{-}\mu\text{m}$ photon emitter. *Physical Review Letters*, 101(15):157405, 2008.
- [217] H. Y. Ramirez, C. H. Lin, C. C. Chao, Y. Hsu, W. T. You, S. Y. Huang, Y. T. Chen, H. C. Tseng, W. H. Chang, S. D. Lin, and S. J. Cheng. Optical fine structures of highly quantized InGaAs/GaAs self-assembled quantum dots. *Physical Review B*, 81:245324, 2010.
- [218] A. I. Tartakovskii, M. N. Makhonin, I. R. Sellers, J. Cahill, A. D. Andreev,

- D. M. Whittaker, J-P. R. Wells, A. M. Fox, D. J. Mowbray, M. S. Skolnick, K. M. Groom, M. J. Steer, H. Y. Liu, and M. Hopkinson. Effect of thermal annealing and strain engineering on the fine structure of quantum dot excitons. *Physical Review B*, 70:193303, 2004.
- [219] R. J. Young, R. M. Stevenson, A. J. Shields, P. Atkinson, K. Cooper, D. A. Ritchie, K. M. Groom, A. I. Tartakovskii, and M. S. Skolnick. Inversion of exciton level splitting in quantum dots. *Physical Review B*, 72:113305, 2005.
- [220] M. Lorke. *Optical gain and laser properties of semiconductor quantum-dot systems*. PhD thesis, Universität Bremen, 2008.
- [221] W.W. Chow and S.W. Koch. *Semiconductor-Laser Fundamentals*. Springer-Verlag, Berlin, 1st edition, 1999.
- [222] H. C. Schneider, S. W. Koch, and W.W. Chow. Excitation-induced dephasing in semiconductor quantum dots. *Physical Review B*, 70:235308, 2004.
- [223] M. Lorke, T.R. Nielsen, J. Seebeck, P. Gartner, and F. Jahnke. Influence of carrier-carrier and carrier-phonon correlations on optical absorption and gain in quantum-dot systems. *Physical Review B*, 73:85324, 2006.
- [224] A. Wojs, P. Hawrylak, S. Fafard, and L. Jacak. Electronic structure and magneto-optics of self-assembled quantum dots. *Physical Review B*, 54:5604, 1996.
- [225] G. Bastard. *Wave mechanics applied to semiconductor heterostructures*. Monographies de physique. Les Éditions de Physique, 1988.
- [226] A. Steinhoff. Mikroskopische Beschreibung des Ladungsträgereinfangs in Halbleiter-Heterostrukturen durch Elektron-Phonon-Wechselwirkung. Master's thesis, Universität Bremen, 2011.
- [227] T. Nielsen. *Carrier-Carrier and Carrier-Phonon Scattering in Self-Assembled Quantum Dots*. PhD thesis, Universität Bremen, 2005.
- [228] H. Haug and S.W. Koch. *Quantum Theory of the Optical and Electronic Properties of Semiconductors*. World Scientific Publ., Singapore, 4. edition, 2004.
- [229] W. W. Chow, P. M. Smowton, P. Blood, A. Girndt, F. Jahnke, and S. W. Koch. Comparison of experimental and theoretical GaInP quantum well gain spectra. *Applied physics letters*, 71(2):157–159, 1997.
- [230] A. Girndt, F. Jahnke, A. Knorr, S. W. Koch, and W. W. Chow. Multi-band bloch equations and gain spectra of highly excited II–VI semiconductor quantum wells. *physica status solidi (b)*, 202(2):725–739, 1997.

- [231] G. Manzke and K. Henneberger. Quantum-kinetic effects in the linear optical response of GaAs quantum wells. *physica status solidi (b)*, **234**:233, 2002.
- [232] U. Bockelmann and T. Egeler. Electron relaxation in quantum dots by means of Auger processes. *Physical Review B*, **46**:15574, 1992.
- [233] I. Magnusdottir, S. Bischoff, A. V. Uskov, and J. Mørk. Geometry dependence of Auger carrier capture rates into cone-shaped self-assembled quantum dots'. *Physical Review B*, **67**:205326, 2003.
- [234] J. Seebeck, T.R. Nielsen, P. Gartner, and F. Jahnke. Polarons in semiconductor quantum dots and their role in the quantum kinetics of carrier relaxation. *Physical Review B*, **71**:125327, 2005.
- [235] J. Gomis-Bresco, S. Dommers, V. V. Temnov, U. Woggon, M. Laemmlin, D. Bimberg, E. Malic, M. Richter, E. Schöll, and A. Knorr. Impact of coulomb scattering on the ultrafast gain recovery in InGaAs quantum dots. *Physical Review Letters*, 101:256803, 2008.
- [236] N. Majer, K. Lüdge, J. Gomis-Bresco, S. Dommers-Völkel, U. Woggon, and E. Schöll. Impact of carrier-carrier scattering and carrier heating on pulse train dynamics of quantum dot semiconductor optical amplifiers. *Applied Physics Letters*, 99(13):131102, 2011.
- [237] M. Lorke, F. Jahnke, and W.W. Chow. Excitation dependence of gain and carrier induced refractive index changes in quantum dots. *Applied Physics Letters*, **90**:51112, 2007.
- [238] W. W. Chow, M. Lorke, and F. Jahnke. Will quantum dots replace quantum wells as the active medium of choice in future semiconductor lasers? *IEEE Journal of Selected Topics in Quantum Electronics*, 17:1349, 2011.
- [239] H. Shahid, D. T. D. Childs, B. J. Stevens, and R. A. Hogg. Negative differential gain due to many body effects in self-assembled quantum dot lasers. *Applied Physics Letters*, 99(6):061104, 2011.
- [240] B. W. Hakki and T. L. Paoli. Gain spectra in GaAs double-heterostructure injection lasers. *Journal of Applied Physics*, 46(3):1299–1306, 1975.
- [241] H. J. Kimble. The quantum internet. *Nature*, 453(7198):1023–1030, 2008.
- [242] D. Bouwmeester, A. Ekert, and A. Zeilinger. *The physics of quantum information*, volume 38. Springer, Berlin, 2000.
- [243] H.-J. Briegel, W. Dür, J. I. Cirac, and P. Zoller. Quantum repeaters: The role of imperfect local operations in quantum communication. *Physical Review Letters*, 81:5932–5935, 1998.

- [244] Z. Zhao, T. Yang, Y.-Av Chen, A.-N. Zhang, and J.-W. Pan. Experimental realization of entanglement concentration and a quantum repeater. *Physical Review Letters*, 90(20):207901, 2003.
- [245] C. H. Bennett and G. Brassard. Quantum cryptography: Public key distribution and coin tossing. *Proceedings of IEEE International Conference on Computers, Systems and Signal Processing*, 175(150):8, 1984.
- [246] P. M. Intallura, M. B. Ward, O. Z. Karimov, Z. L. Yuan, P. See, A. J. Shields, P. Atkinson, and D. A. Ritchie. Quantum key distribution using a triggered quantum dot source emitting near 1.3 μm . *Applied Physics Letters*, 91(16):161103–161103, 2007.
- [247] M. Yacob, J. P. Reithmaier, and M. Benyoucef. Low-density InP-based quantum dots emitting around the 1.5 μm telecom wavelength range. *Applied Physics Letters*, 104(2):022113, 2014.
- [248] S. Strauf and F. Jahnke. Single quantum dot nanolaser. *Laser & Photonics Reviews*, 5(5):607–633, 2011.
- [249] K. J. Vahala, M. A. Newkirk, and T. R. Chen. The optical gain lever: A novel gain mechanism in the direct modulation of quantum well semiconductor lasers. *Applied Physics Letters*, 54(25):2506–2508, 1989.
- [250] Y. Li, N. A. Naderi, V. Kovanis, and L. F. Lester. Enhancing the 3-db bandwidth via the gain-lever effect in quantum-dot lasers. *Photonics Journal, IEEE*, 2(3):321–329, 2010.
- [251] T. Akiyama, M. Sugawara, and Y. Arakawa. Quantum-dot semiconductor optical amplifiers. *Proceedings of the IEEE*, 95(9):1757–1766, 2007.
- [252] J. A. J. Fells, M. A. Gibbon, I. H. White, G. H. B. Thompson, R. V. Penty, C. J. Armistead, E. M. Kimber, D. J. Moule, and E. J. Thrush. Transmission beyond the dispersion limit using a negative chirp electroabsorption modulator. *Electronics Letters*, 30(14):1168–1169, 1994.
- [253] E. Goldmann, M. Paul, F. Krause, J. Kettler, T. Mehrtens, K. Müller, A. Rosenauer, M. Jetter, P. Michler, and F. Jahnke. Structural and emission properties of MOVPE-grown InGaAs/GaAs telecom quantum dots with bimodal height distribution. Submitted to *Applied Physics Letters*, 2014.
- [254] F. C. Frank and J. H. van der Merwe. One-dimensional dislocations. I. static theory. *Proceedings of the Royal Society of London. Series A, Mathematical and Physical Sciences*, 198(1053):205–216, 1949.
- [255] F. C. Frank and J. H. van der Merwe. One-dimensional dislocations. II. misfitting monolayers and oriented overgrowth. *Proceedings of the Royal Society*

- of London. Series A, Mathematical and Physical Sciences*, 198(1053):216–225, 1949.
- [256] F. C. Frank and J. H. van der Merwe. One-dimensional dislocations. III. influence of the second harmonic term in the potential representation, on the properties of the model. *Proceedings of the Royal Society of London. Series A, Mathematical and Physical Sciences*, 200(1060):125–134, 1949.
- [257] M. Volmer and A. Weber. Keimbildung in übersättigten Gebilden. *Zeitschrift für physikalische Chemie*, 119:277–301, 1926.
- [258] I.N. Stranski and L. Krastanov. Zur Theorie der orientierten Ausscheidung von Ionenkristallen aufeinander. *Sitzungsber. Akad. Wiss. Wien, Math. Naturwiss.*, 146:797, 1938.
- [259] D. Richter. *Herstellung und Charakterisierung von InAs Quantenpunkten zur Verwendung von InP/InAs Quantengattern*. PhD thesis, Universität Stuttgart, 2009.

List of Figures

1.1.	Reduction of translational degrees of freedom affects the electronic density of states. In bulk semiconductors, the DOS is square-root like and becomes a step function for quantum wells. For consecutive loss of translational symmetry (three-dimensionally confined nanostructures) the DOS becomes δ -like, resulting in discrete energy levels.	2
1.2.	Fluorescence signals from functionalized CdSe nanocrystallites for in-vivo tumor targeting. Different colors show different nanocrystallite sizes, used to encode different functionalizations, which target cancer cells. Picture adopted from [8].	3
1.3.	Atomic force microscope (AFM) picture of a quantum dot layer before overgrowth, from [13]. The area is $500 \times 500 \text{ nm}^2$. Brighter colors translate to higher QD elevation.	4
1.4.	a) Scanning electron microscope (SEM) picture of an InAs QD on a GaAs substrate before overgrowth, from [14]. b) Transmission electron microscope (TEM) picture of a GaAs-overgrown InAs QD in cross section view (Courtesy of Gilles Patriarche, CNRS). c) TEM-picture of an overgrown alloyed InGaAs QD, from [15].	5
2.1.	Representations of atomic orbitals via the angular parts of the spherical harmonics. First line: orbital with s -symmetry; second line: orbitals with p -symmetry; last line: orbitals with d -symmetry.	17
2.2.	a) Definition of the vectors. b) Decomposition of a p -like atomic orbital into σ and π parts, weighted by the projection of \mathbf{e}_i onto the bond-parallel and bond-normal vectors, respectively.	18
2.3.	Different types of bonds between orbitals in projection view. Red/green colors describe negative/positive sign of the wave function. a) $ss\sigma$ bond, b) $sp\sigma$, c) $pp\sigma$, d) $pp\pi$, e) $sd\sigma$, f) $pd\sigma$, g) $pd\pi$, h) $dd\sigma$, i) $dd\pi$, j) $dd\delta$.	19
2.4.	Example for atomic displacements due to lattice-mismatch-induced strain. Shown is a small part of the many-million atom supercell containing the WL and the QD, cut vertically through the middle of the QD and seen from the side of the supercell. Colors correspond to absolute value (blue = small, red = large) of displacement with respect to the GaAs bulk nearest-neighbour distance.	22

2.5. Example for atomic displacements due to strain for a reduced quantum dot Indium content of 20%. The color scale for the displacements does not correspond to the scale in Fig. 2.4.	23
2.6. Scheme of the empty supercell representing the bulk system, provided that periodic boundary conditions are applied.	31
2.7. Sketch of the zincblende lattice structure, which is the superposition of two face-centered lattices for anions and cations. Large spheres indicate cations, small spheres the anions. Picture taken from http://nano-physics.pbworks.com/	34
2.8. Brillouin zone and high-symmetry points of the zincblende lattice. Image from IPV Stuttgart (http://www.ipv.uni-stuttgart.de/lehre/vorlesungen/festkoerperelektronik.html).	35
2.9. The left-hand figure shows the bulk band structure in the sp^3s^* TB model for GaAs. Right-hand figures show the corresponding DOS.	37
2.10. The left-hand figure shows the bulk band structure in the sp^3s^* model for InAs.	38
2.11. Scheme of the supercell representing a quantum well. Periodic boundary conditions have to be applied in all spatial directions, taking care of a minimal distance of layers in growth direction.	38
2.12. Sub-bands for GaAs bulk material from the diagonalization of the QW Hamiltonian for $N = 11$ layers. Colored in red are the bulk bands as calculated in the previous chapter. Deviations from the bulk bands stem from the different paths through the Brillouin-zone as indicated by L^\perp and X^\perp	41
2.13. Energy bands of an InAs quantum well of three monolayers (green) in GaAs bulk material (red bands and grey sub-bands).	44
2.14. As above, but a narrowed energy scale around energy zero is shown to emphasize the InAs quantum well bound energy bands (green) in the vicinity of the Γ -point.	44
2.15. Occupation probability at the Γ -point for bound electron and hole states of an InAs QW in a GaAs host matrix.	45
2.16. Scheme of a three-dimensionally confined area of material in the supercell, representing the QD.	46
2.17. Exemplary supercell realization of a pure lens-shaped InAs QD. Red dots indicate Indium atoms, small blue dots indicate atoms belonging to the GaAs buffer.	46
2.18. Scheme representing the workflow for the calculation of electronic single-particle states. After having setup the geometry and composition, the structure is relaxed in order to find the strained equilibrium atomic positions. This information enters the TB-Hamiltonian, the eigenenergies and eigenstates of which give the electron and hole single-particle energies and wave functions by diagonalization.	49

2.19. Atomistic supercell representation of a lens-shaped QD of pure InAs on top of a wetting layer, consisting of two monolayers InAs. Red and blue atoms are Indium and Arsenic atoms, respectively. Atoms belonging to the GaAs buffer are not shown for illustration purposes and only a small part of the original supercell is shown.	52
2.20. Atomistic supercell representation of a truncated pyramid-shaped QD of pure InAs on top of a wetting layer, consisting of two monolayers InAs. Atoms belonging to the GaAs buffer are not shown for illustration purposes. Only a small part of the original supercell is shown.	52
2.21. Atomistic supercell representation of a disk-shaped QD of pure InAs on top of a wetting layer, consisting of two monolayers InAs. Atoms belonging to the GaAs buffer are not shown for illustration purposes. Only a small part of the original supercell is shown.	53
2.22. GaAs band structure fits using different basis sizes in the empirical tight-binding model, from [165]. Red and green circles show discrepancy and agreement with experiment, respectively. The $sp^3d^5s^*$ model clearly resembles the band structure best, but for applications happening mainly at the Γ -point, the sp^3s^* -basis is already sufficient.	55
2.23. Atomistic representation of the pure InAs QD exhibiting lens-shape used to benchmark our TB model. From [75] for comparison.	56
2.24. Squared wave functions of the first 12 bound electrons (top) and holes (bottom) for a pure lens-shaped InAs QD. Each state is twofold degenerate due to spin degree of freedom. Yellow lines indicate QD geometry.	57
2.25. Squared wave functions of the first 12 bound electrons (top) and holes (bottom) for a pure InAs QD with the shape of a truncated pyramid. Each state is twofold degenerate due to spin degree of freedom. Yellow lines indicate QD geometry.	60
2.26. Squared wave functions of the first 12 bound electrons (top) and holes (bottom) for a pure disk-shaped InAs QD. Each state is twofold degenerate due to spin degree of freedom. Yellow lines indicate QD geometry.	61
2.27. Variation of electron and hole single-particle total energies with QD diameter (left hand and middle panel). In the right hand panel the variation of the single-particle energy gap $E_{Gap} = e_1 - h_1$ is depicted.	62
2.28. Variation of electron and hole single-particle energies with QD height (left hand and middle panel). In the right hand panel the variation of the single-particle energy gap $E_{Gap} = e_1 - h_1$ is depicted.	63
2.29. Variation of electron and hole single-particle energies with QD Indium concentration (upper and middle panel). In the lower panel the variation of the single-particle energy gap is depicted.	64

2.30. Schematic energy diagram showing the band alignment at interfaces between GaAs and InAs by means of the valence band offset ΔE_v . The vertical axis labels energy, horizontal axis labels a spatial dimension, e.g. growth direction.	66
2.31. Dependence of electron and hole single-particle energies (left hand and middle panel) and energy gap (right hand panel) on the choice of valence band offset ΔE_v	67
2.32. WL system consisting of two monolayers of InAs. Anions and cations of InAs are shown red and blue, while atoms belonging to the GaAs buffer are not shown for illustration.	68
2.33. Exemplary visualization of the occupation probability of the hole WL ground state in side-view (along the [010] crystal direction). Blue and red colors correspond to low and high occupation probability, respectively.	69
3.1. Scheme of the computational flow in order to calculate many-particle properties of the QD carriers. Having obtained the single-particle energies and wave functions, interaction matrix elements can be calculated and many-particle properties are accessible via diagonalization of the configuration interaction Hamiltonian.	72
3.2. Exemplary single-particle configurations for a QD having two confined states both for electrons and holes in the electron-hole picture, from [19]. For simplicity only one spin direction and only configurations with an even number of carriers are assumed. The s -states are labelled $ 2\rangle$ and $ 3\rangle$ while p -states are labelled $ 1\rangle$ and $ 4\rangle$. From left to right these configurations are: the empty dot; the exciton with the carriers occupying the s -shells (ground state exciton $1X_S$); the p -exciton $1X_P$; the biexciton $2X_{SP}$; the p - s -exciton $0X_P$; the s - p -exciton $0X_S$. Charged configurations with an odd number of carriers are not shown here.	74
3.3. Dipole matrix elements for the standard pure InAs QD with lens shape for polarization along [110] between the first twelve electron and hole bound states.	83
3.4. Dipole matrix elements for the standard pure InAs QD with lens-shape for polarization along $[1\bar{1}0]$ between the first twelve electron and hole bound states.	84
3.5. Emission spectra of the three standard QDs for [110] polarization using a homogeneous broadening of $\Delta = 1$ meV. For each geometry transitions between s -like and p -like states can be identified.	85

3.6.	Scheme of the cascaded decay of a biexciton into the ground state via intermediate excitonic states. Depending on the polarization of the first decay, the polarization of the second decay is fixed. The intermediate exciton states show a small energy splitting caused by electron-hole Coulomb exchange interaction, labelled FSS.	86
3.7.	High resolution spectrum of an InAs QD showing the excitonic fine-structure of dark and bright excitons. An artificially small broadening of $\Delta = 0.01$ meV was assumed for illustration purposes.	89
4.1.	Exemplary scanning electron microscopy image of an InAs QD embedded in an additional InGaAs quantum well, acting as the strain-reducing layer.	94
4.2.	(a) System without SRL, consisting of an InAs QD on an InAs WL embedded in a GaAs host matrix. (b) System for nonzero SRL- x exaggerating size change for illustration reasons. (c) QD size changes with SRL Indium concentration reproducing the experimental emission wavelength slope from [203] and resulting change in aspect ratio (AR) for QD3.	95
4.3.	Shift of excitonic emission wavelength with SRL Indium concentration for QDs of different height. Comparison with experimental values and with QDs lacking size increase.	96
4.4.	Statistical scattering of the calculated FSS with excitonic emission wavelength and linear fit.	97
4.5.	Variation of the FSS as a function of SRL Indium concentration for different QD height from averaging over FSSs for each QD height and SRL- x . The initial increase in FSS for all QDs in regions of small SRL- x is counteracted by a reduction for larger SRL- x . A convergence of FSS to mediate values of around $45\mu\text{eV}$ can be seen.	98
4.6.	Plot of squared excitonic dipole transition matrix element versus the SRL Indium concentration for QD1-QD4. With larger QD height and with larger SRL- x transitions become more efficient.	99
4.7.	Comparison between the models of infinite and finite height of the potential well in envelope function approximation for the standard lens-shaped QD of the previous sections. Due to the penetration of the envelope wave function into the buffer the infinite potential well is not suited for fitting the envelope functions accurately.	102
4.8.	Visualization of the fits in growth direction for the gain calculations. The lower part shows the ground hole wave function of QD 2 in side-view, integrated along [010]. In the upper part an exemplary envelope fit is shown. The fitting is done with respect to the yellow line, i.e. along the growth direction and through the quantum dot center. . .	103

4.9. [100]-dependence of the envelopes of the wave functions as calculated by TB for the ground states of electrons and holes, respectively, as well as their fitted analytical counterparts. QD 2 as defined in the text was used. Due to the reduced Indium content in the quantum dot, wave functions spread layerwise.	104
4.10. [010]-dependence of the envelopes of the wave functions as calculated by TB for the ground states of electrons and holes, respectively, as well as their fitted analytical counterparts. QD 2 as defined in the text was used. Due to the reduced Indium content in the quantum dot, wave functions spread layerwise.	105
4.11. [001]-dependence of the envelopes of the wave functions as calculated by TB for the ground states of electrons and holes, respectively, as well as their fitted analytical counterparts. QD 2 as defined in the text was used. The asymmetry of wave functions is caused by the influence of the wetting layer.	105
4.12. Spatial distances in growth direction ([001]) of the center of electron and hole ground state envelope functions to the WL band edges as a function of the QD Indium content. Increasing the carrier confinement due to increased Indium content causes the wave function center to shift away from the wetting layer.	106
4.13. Low-energy part of the optical spectra for QD 1 with 30% In content and various excitation densities (in cm^{-2}) as a function of energy relative to the WL energy gap E_G . The inset shows optical spectra for low and high excitation density covering s -shell, p -shell and the WL absorption edge.	108
4.14. Low-energy part of the optical spectra for QD 2 and 40% In content for various excitation densities (in cm^{-2}) as a function of energy relative to the WL energy gap.	109
4.15. Excitation density dependence of the peak gain for selected QD geometries, with given In content. QD 1 (30%) and QD 2 (40%) correspond to Figs. 4.13 and 4.14, respectively.	110
4.16. Excitation density dependence of s -shell broadening (a) and inversion (b) for various QD geometries and Indium contents.	111
4.17. Excitation density dependence of diagonal (DD) and off-diagonal (OD) dephasing contributions for (a) the dominant phase-state filling regime of QD 1 (30%) and (b) the dominant dephasing regime of QD 2 (40%).	112
A.1. Scheme of the different growth modes described in the text. Picture from [259].	120

List of Tables

2.1.	Stiffness parameters used in this thesis, scaled by $10^{11} \cdot \text{dyn}/(\text{cm}^2)$. .	25
2.2.	Points of high symmetry in the Brillouin zone of the zincblende lattice structure. a is the lattice constant and reciprocal vectors read (k_x, k_y, k_z) . 34	
2.3.	Benchmark of our sp^3s^* TB model with results from different other calculations (EPP 1, EPP 2, TB 1, TB 2) and with experimental data. Splittings between bound electron ($e_1..e_4$) and hole states ($h_1..h_4$) are compared as well as the single-particle energy gap $E_{Gap} = e_1 - h_1$. All values are given in meV.	56
2.4.	In the left hand table the binding energies of the ground and first few excited bound electron and hole states for the standard lens-shaped pure InAs QD are shown. The index n corresponds to electrons ($n = e$) and holes ($n = h$). The right hand table shows the intraband splittings. Additionally the single-particle energy gap $E_{Gap} = e_1 - h_1$ is given. All energies are in units of meV.	59
2.5.	In the left hand table the binding energies of the lowest bound electron and highest bound hole states for the standard pure InAs QD with truncated pyramid-shape are shown. The index n corresponds to electrons ($n = e$) and holes ($n = h$). The right hand table shows the intraband splittings. Additionally the single-particle energy gap $E_{Gap} = e_1 - h_1$ is given. All energies are in units of meV.	60
2.6.	In the left hand table the binding energies of the lowest bound electron and highest bound hole states for the standard disk-shaped pure InAs QD are shown. The index n corresponds to electrons ($n = e$) and holes ($n = h$). The right hand table shows the intraband splittings. Additionally the single-particle energy gap $E_{Gap} = e_1 - h_1$ is given. All energies are in units of meV.	62
2.7.	Influence of alloy fluctuations on lowest electron and hole binding energies ($E_B(e_1)$ and $E_B(h_1)$), the single-particle energy gap $e_1 - h_1$ and the interband splittings. All values are in meV.	65
2.8.	Calculated band-edge energies of the InAs WL system which are used as reference to decide between bound and unbound QD-states.	69
2.9.	Electron binding energies and single-particle energy gap as a function of InGaAs QD Indium concentration. All energies are given in units of meV unless stated otherwise.	70

2.10. Hole binding energies as a function of InGaAs QD Indium concentration. All energies are given in units of meV unless stated otherwise.	70
3.1. Typical values of the Coulomb matrix elements for combinations of the s -like electron and hole states for the three standard quantum dots examined in the single-particle theory section as calculated from tight-binding wave function coefficients. All values are given in units of meV.	77
3.2. Excitonic fine-structure splittings and biexciton binding energies $E_B(2X)$ of the three standard QDs. $d-d$ labels dark-dark exciton splitting, $d-b$ the splitting between dark and bright and FSS the splitting between the two bright exciton states.	88
4.1. Fitted values for factor k , the well width L and inverse oscillator length β for both electrons and holes.	106
A.1. Material parameters for GaAs and InAs. The temperature denotes at which temperature the band structure was fitted. E_{Gap} gives the single-particle gap calculated using the actual parametrization. E are the orbital energies, V are the hopping matrix elements, s, s^* denote the s and s^* orbitals while x and y are abbreviations for the p_x and p_y orbitals. A and C denote anion and cation sites, respectively. $\Delta_{A/C}$ corresponds to the spin-orbit-splitting parameters via $\Delta_{A/C} = 3\lambda_{A/C}$. All parameters are given in eV unless stated otherwise.	127
A.2. Single-particle bulk band gaps in eV at selected temperatures for InAs and GaAs.	127

Acknowledgements

By the end of my thesis i would like to thank:

Prof. Frank Jahnke for not only being my advisor but also for helping me during
this thesis with words and deeds,
Prof. Gerd Czycholl, Prof. Thomas Frauenheim and Prof. Andreas Rosenauer for
being my second advisor and my defense examiners,
Dr. Michael Lorke for the fruitful collaboration on the gain reduction topic,
Dr. Stefan Barthel and Dr. Kolja Schuh for providing parts of CI and CME code
and patiently explaining to me how to use and adopt it,
and finally Agnete Goldmann, Albrecht Goldmann, and Alexander Steinhoff for
proof-reading my thesis and cherry-picking all those tiny typos and wrong indices.

On a personal level i owe my thanks to:

my wonderful wife Sonja
for always, always supporting, encouraging and pushing me,
my Mom for always having my back,
my Dad for not pushing me into physics,
the office crew Christopher Gies, Alexander Steinhoff and Matthias Florian for
extensive camera-, carpentry-, baking-, german music-, series-
and kids-related diversion,
Christina Schwenk for deeply needed moral support,
and all the people always reminding me how crazy theoretical physics is.

Thank you!